

## Meshless numerical methods applied to multiphysics and multiscale problems

Lukyanov, Alexander

**DOI**

[10.4233/uuid:19e3bd77-d4cb-48a5-9b6a-4e96d95f39ec](https://doi.org/10.4233/uuid:19e3bd77-d4cb-48a5-9b6a-4e96d95f39ec)

**Publication date**

2019

**Document Version**

Final published version

**Citation (APA)**

Lukyanov, A. (2019). Meshless numerical methods applied to multiphysics and multiscale problems. <https://doi.org/10.4233/uuid:19e3bd77-d4cb-48a5-9b6a-4e96d95f39ec>

**Important note**


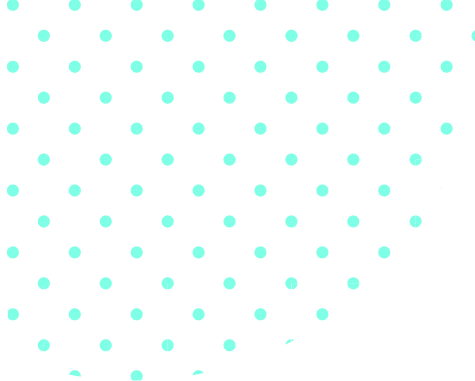
To cite this publication, please use the final published version (if applicable). Please check the document version above.

**Copyright**

Other than for strictly personal use, it is not permitted to download, forward or distribute the text or part of it, without the consent of the author(s) and/or copyright holder(s), unless the work is under an open content license such as Creative Commons.

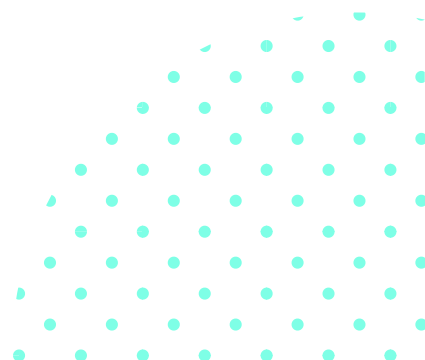
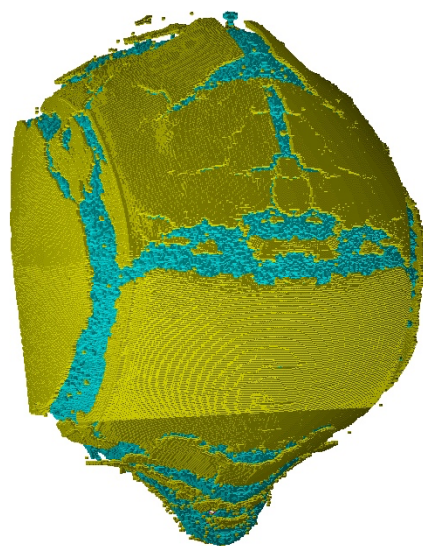
**Takedown policy**

Please contact us and provide details if you believe this document breaches copyrights. We will remove access to the work immediately and investigate your claim.



# **MESHLESS NUMERICAL METHODS APPLIED TO MULTIPHYSICS AND MULTISCALE PROBLEMS**

**ALEXANDER LUKYANOV**



# Propositions

belonging to the dissertation

## Meshless Numerical Methods Applied to Multiphysics and Multiscale Problems

by Alexander Lukyanov

1. Meshless methods can be considered as both truly physical modeling techniques and as mathematical interpolation methods.  
*Chapters 3, 4, 5 of this thesis.*
2. The thermodynamically consistent visco-elasto-plastic damage model for anisotropic constitutive equations are constructed which represent mathematical and physical generalizations of the conventional constitutive equations for isotropic materials and reduce to the conventional constitutive equations in the limit of isotropy.  
*Chapter 3 of this thesis.*
3. The optimum new discretization scheme presented in the thesis enhances the Laplace approximation (e.g., Brookshaw's scheme <sup>1</sup>). It also has a better properties than Schwaiger's scheme <sup>2</sup> used in the SPH community for thermal, viscous, and pressure projection problems with an isotropic elliptic operator.  
*Chapter 4 of this thesis.*
4. The sufficient monotonicity condition for the new SPH scheme is the strongest theoretical result for the SPH discretization schemes of this class.  
*Chapter 4 of this thesis.*
5. The multiscale, reduced order model, deflation and multigrid solver techniques are combined to build meshless multiscale solving techniques leading to a speed up of the solution strategies.  
*Chapter 5 of this thesis.*
6. Monotonicity and high order accuracy of the linear discretization schemes are two competitive mathematical properties and they converge to each other only at the continuum limit.
7. There is no "free lunch" in the numerical methods and, hence, researchers specializing in numerical analysis should look for drawbacks in the methods rather than CPU times.
8. The Dutch numerical scientists tend to avoid slow numerical algorithms - to them it's a waste of good canal hopping time.
9. Both the Dutch and the English share a vast love of the sea but, let's be frank, the English have a mild dislike to the raw herrings.
10. The current scientific progress is also driven by re-inventing a wheel and, hence, perydynamics <sup>3</sup> is a version of the SPH method.

These propositions are regarded as opposable and defendable, and have been approved as such by the supervisor prof. dr. ir. C. Vuik

---

<sup>1</sup> BROOKSHAW, L. "A method of calculating radiative heat diffusion in particle simulations". Proceedings of the Astronomical Society of Australia 6(2), 1985, 207-210.

<sup>2</sup>SCHWAIGER, H. "An implicit corrected SPH formulation for thermal diffusion with linear free surface boundary conditions". International Journal for Numerical Methods in Engineering 75, 2008, 647-671.

<sup>3</sup>SILLING, S. A. Reformulation of elasticity theory for discontinuities and long-range forces. J. Mech. Phys. Solids, 48(1), 2000, 175-209.

# **Meshless Numerical Methods Applied to Multiphysics and Multiscale Problems**

Dissertation

for the purpose of obtaining the degree of doctor  
at Delft University of Technology  
by the authority of the Rector Magnificus, prof.dr.ir. T.H.J.J. van der Hagen,  
Chair of the Board for Doctorates  
to be defended publicly on  
Monday 18 March 2019 at 12:30 o'clock

by

**Alexander LUKYANOV**

Master of Science in Mechanics and Applied Mathematics  
Lomonosov Moscow State University, Russia  
and  
Master of Science in Computer Science  
Lomonosov Moscow State University, Russia

born in Lipetsk, Russia

This dissertation has been approved by the promotor.

Composition of the doctoral committee:

Rector Magnificus  
Prof.dr.ir. C. Vuik

chairman  
Delft University of Technology, promotor

Independent members:

Prof.dr.ir. A. Heemink  
Prof.dr. J. Bruining  
Prof.ir. C.P.J.W. van Kruijsdijk  
Prof.dr. D. Tartakovsky  
Prof.dr. V. Druskin  
Prof.dr.ir. W. Schilders

Delft University of Technology  
Delft University of Technology  
Delft University of Technology  
Stanford University, USA  
Worcester Polytechnic Institute, USA  
Technical University Eindhoven, the Netherlands



The work described in this dissertation was carried out at the Department of Applied Mathematics, the Faculty of Electrical Engineering, Mathematics and Computer Science, Delft University of Technology, the Netherlands.

Keywords: meshless methods, shock waves, multiscale linear solver, high order discretization

Meshless Numerical Methods Applied to Multiphysics and Multiscale Problems.  
Dissertation at Delft University of Technology  
Copyright © 2019 by A. Lukyanov

To my mother, father, my son and my family.

---

---

# Contents

---

<b>SUMMARY</b>	<b>1</b>
<b>ACKNOWLEDGEMENT</b>	<b>3</b>
<b>INTRODUCTION</b>	<b>4</b>
I.    Background and Actuality of the thesis . . . . .	5
II.   Objectives and Scope . . . . .	9
III.  Organisation of the Thesis . . . . .	9
<b>1 PROBLEM FORMULATION AND SOLUTION METHODS</b>	<b>12</b>
§ 1.1 General Remarks . . . . .	12
1.1.1 Euler and Lagrangian Coordinates . . . . .	12
1.1.2 Conservation Laws . . . . .	13
1.1.3 Conservative Physical Quantities . . . . .	13
§ 1.2 Solid Mechanics Description . . . . .	14
1.2.1 Conservation Laws . . . . .	14
1.2.2 Mathematical Models of Failure. Damage Mechanics . . . . .	14
1.2.3 Damage Parameters. Effective Stresses . . . . .	15
1.2.4 Description of Existing Damage Models . . . . .	16
1.3.1 Conservation Laws . . . . .	16
§ 1.3 Fluid Mechanics Description . . . . .	17
1.3.2 Constitutive Relations . . . . .	18
§ 1.4 Boundary and Initial Conditions . . . . .	19
1.4.1 Solid Mechanics Boundary Conditions . . . . .	19
1.4.2 Fluid Mechanics Boundary Conditions . . . . .	19
§ 1.5 Numerical methods . . . . .	20
1.5.1 Smoothed Particle Hydrodynamic Method (SPH) . . . . .	20
1.5.2 Numerical Time Integration . . . . .	21
§ 1.6 Conclusion . . . . .	21
<b>2 SPH FORMULATION</b>	<b>22</b>
§ 2.1 Introduction . . . . .	22
2.1.1 SPH Method . . . . .	22
2.1.2 Various Forms of the Meshless Method . . . . .	23
2.1.3 Advantages of Meshless Methods . . . . .	24
§ 2.2 Concept of SPH Method . . . . .	24
2.2.1 Basic Relations . . . . .	25
2.2.2 Lagrangian SPH Method . . . . .	26

2.2.3	Spatial Derivative Approximation Using SPH Method . . . . .	26
§ 2.3	Corrected SPH Method . . . . .	27
2.3.1	Derivative Corrected SPH Method . . . . .	27
2.3.2	Normalized-Corrected SPH Method . . . . .	28
2.3.3	SPH symmetrization of smoothing length . . . . .	30
§ 2.4	SPH Approximation of Conservation Laws . . . . .	31
2.4.1	Conservation Law of Mass . . . . .	31
2.4.2	Conservation Law of Linear Momentum . . . . .	31
2.4.3	Conservation Law of Energy . . . . .	32
§ 2.5	SPH Approximation Kernel . . . . .	32
2.5.1	SPH Kernel . . . . .	32
2.5.2	Artificial Viscosity . . . . .	33
2.5.3	Smoothing and time selection strategies . . . . .	34
§ 2.6	Conclusion . . . . .	34
<b>3</b>	<b>SHOCK WAVE PROPAGATION IN COMPLEX MEDIA</b>	<b>35</b>
§ 3.1	Thermomechanical Model of Deformation and Continuum Fracture . . . . .	35
3.1.1	Basic Assumptions . . . . .	37
3.1.2	System of Constitutive Equations . . . . .	38
3.1.3	Criterion of Macrofracture . . . . .	41
§ 3.2	Numerical investigation of anisotropic plasticity . . . . .	42
3.2.1	The consistent tangent stiffness matrix . . . . .	42
3.2.2	Numerical algorithm for anisotropic incompressible plastic model . . . . .	43
3.2.3	Associated incompressible anisotropic plasticity . . . . .	44
3.3.4	Final procedure of numerical integration of anisotropic plasticity . . . . .	45
3.2.5	Verification of numerical implementation . . . . .	45
§ 3.3	Plate Impact Tests . . . . .	46
3.3.1	Definition of Material Properties . . . . .	46
3.3.2	Description of Experiment . . . . .	47
3.3.4	Shock wave propagation in aluminum alloy . . . . .	48
§ 3.4	Modeling of thermo-elastic-plastic damageable medium . . . . .	50
3.4.1	Uniaxial Plate Impact Test with Spall . . . . .	52
3.4.2	2D Plate Impact Simulation . . . . .	52
3.4.3	Irreversible Deformation Process During Impact Loading . . . . .	55
3.4.4	Failure of the Target and Flyer Plates . . . . .	56
§ 3.5	Conclusion . . . . .	57
<b>4</b>	<b>MESHLESS MULTI-POINT FLUX APPROXIMATION</b>	<b>61</b>
§ 4.1	Introduction . . . . .	61
4.1.1	Multi point flux approximation . . . . .	62
4.1.2	Two-point flux approximation . . . . .	63
4.1.3	Mimetic approximation . . . . .	63
§ 4.2	Fluid Flow Modelling Using SPH . . . . .	64
4.2.1	Brookshaw (1985) scheme . . . . .	65
4.2.2	Schwaiger (2008) scheme . . . . .	67
4.2.3	Meshless Transmissibilities . . . . .	71
4.2.4	New scheme . . . . .	72
§ 4.3	Meshless Multi-Point Flux Approximation (MMPFA) . . . . .	73
4.3.1	Scheme I and II for Anisotropic Media . . . . .	74
4.3.2	Scheme III for Anisotropic Media . . . . .	75
4.3.3	Discontinuous Mobility Case . . . . .	75
4.3.4	Scheme III . . . . .	76
§ 4.4	Monotonicity, Approximation, Stability and Convergence . . . . .	78
4.4.1	Approximation . . . . .	78
4.4.2	Isotropic Homogeneous Media . . . . .	79
4.4.3	Inhomogeneous Boundary Condition . . . . .	81



## Contents

---

4.4.4	Inhomogeneous Mixed Boundary Condition Test . . . . .	83
4.6.3	Fully Anisotropic Medium . . . . .	85
4.4.1	Monotonicity . . . . .	86
4.4.2	von Neumann stability analysis . . . . .	87
§ 4.5	SPE10 . . . . .	88
§ 4.7	Conclusion . . . . .	89
<b>5</b>	<b>MESHLESS RELAXED MULTISCALE METHODS</b>	<b>92</b>
§ 5.1	Introduction . . . . .	92
5.1.1	Commercial reservoir simulators . . . . .	93
5.1.2	Existing Solution Strategies . . . . .	94
5.1.3	Multiscale, Multilevel, Multigrid and Deflation Methods . . . . .	95
§ 5.2	Multiscale Restriction vs. Deflation . . . . .	96
5.2.1	Deflation Theory . . . . .	96
5.2.2	Multiscale Restriction Smoothed Basis and Deflation Vectors . . . . .	98
5.2.3	Meshless Deflation Vectors . . . . .	100
5.2.4	Meshless Deflation Method . . . . .	102
5.2.5	SPE10 simulation . . . . .	103
§ 5.3	Adaptive Deflated Meshless Multiscale Solver (ADMMS) . . . . .	104
5.3.1	Fully ADMMS (F-ADMMS) . . . . .	104
5.3.2	Decoupled ADMMS (D-ADMMS) . . . . .	105
5.3.3	Mixed ADMMS (M-ADMMS) . . . . .	105
5.3.4	Multiscale Meshless Based Method . . . . .	105
§ 5.4	Numerical Experiments . . . . .	106
5.4.1	"Islands" model problem . . . . .	106
5.4.2	FracturedReservoir . . . . .	108
5.4.3	Real Reservoir Simulation Test Cases . . . . .	110
§ 5.5	Conclusions . . . . .	112
	<b>Future research work</b>	<b>114</b>
§ 6.4	The Meshless Full Approximation Scheme . . . . .	114
6.4.1	The basics of meshless multilevel methods . . . . .	114
6.4.2	Nonlinear Multi-Level Meshless Method: FAS . . . . .	114
6.4.3	Nonlinear Meshless Coarse Level Method: FAS . . . . .	115
	<b>Notation</b>	<b>117</b>
	<b>Bibliography</b>	<b>132</b>

---



---

## List of Figures

---

2.1 Interactions of Kernels in SPH method. . . . .	24
2.2 SPH cubic spline. . . . .	33
3.1 Schematic diagram of the experimental target assembly. . . . .	47
3.2 Comparison between SPH and FEM of simulation results of uniaxial plate impact test using 450 m/s. . . . .	49
3.3 Comparison between SPH and FEM of simulation results of uniaxial plate impact test using 100 m/s. . . . .	50
3.4 Geometry of uniaxial plate impact test in the SPH method . . . . .	50
3.5 Back-surface gauge stress traces from plate-impact experiments versus numerical simulation of stress (PMMA) waves for plate impact test (impact velocity 450 m/s and 895 m/s) - aluminum alloy AA7010-T6 (Longitudinal Direction). . . . .	51
3.6 Back-surface gauge stress traces from plate-impact experiments versus numerical simulation of stress (PMMA) waves for plate impact test (impact velocity 450 m/s and 895 m/s) - aluminum alloy AA7010-T6 (Transverse Direction). . . . .	51
3.7 Distribution of total dissipation at $t = 2.472 \mu s$ during SPH simulations. The maxima of the dissipation are located at the positions of the impact and spallation. . . . .	52
3.8 Distribution of total dissipation at $t = 3.24 \mu s$ during SPH simulations. The target plate is separated into two parts demonstrating the effect of the macro-fracture criterion based on the specific internal entropy. . . . .	53
3.9 Distribution of temperature at $t = 2.472 \mu s$ during SPH simulations . . . . .	53
3.10 Distribution of damage at $t = 2.472 \mu s$ during SPH simulations . . . . .	54
3.11 Distribution of damage at $t = 3.24 \mu s$ during SPH simulations . . . . .	54
3.12 Geometry of normal impact . . . . .	55
3.13 Distribution of the effective plastic strain at $t = 64.015 \mu s$ . . . . .	56
3.14 Distribution of the hydrostatic pressure at $t = 17.026 \mu s$ . . . . .	57
3.15 Distribution of shear damage parameter at $t = 17.008 \mu s$ . . . . .	58
3.16 Distribution of volumetric damage parameter at $t = 17.008 \mu s$ . . . . .	58
3.17 Distribution of mechanical dissipation at $t = 17.008 \mu s$ . . . . .	59
3.18 Distribution of total dissipation at $t = 17.008 \mu s$ . . . . .	59
3.19 Distribution of temperature at $t = 17.008 \mu s$ . . . . .	60
4.1 Two dimensional $\mathcal{O}$ -method . . . . .	64
4.2 Values for $\nabla^2(x^2 + y^2)$ along $y = 0$ using Brookshaw's approximation with (a) conventional kernel $\nabla_\gamma W$ , (b) corrected kernel $\nabla_\gamma^* W$ and with the correction multiplier $[\mathbf{C}_{\alpha\alpha}]/n$ . The numerical domain is a unit square in $\mathbb{R}^2$ with the center at $a_i = 0, \forall i$ and side length $L = 1$ . The cubic spline (2.56) was used with $\tilde{h} = f \cdot h_p, h_p = 0.1, f = 1.0$ . . . . .	68

4.3	Values for $\nabla^2(x^2 + y^2)$ along $y = 0$ using Schwaiger's approximation with (a) conventional kernel $\nabla_\gamma W$ and (b) corrected kernel $\nabla_\gamma^* W$ . The numerical domain is a unit square in $\mathbb{R}^2$ with the center at $a_i = 0, \forall i$ . The cubic spline (2.56) was used with $\tilde{h} = f \cdot h_p, h_p = 0.1, f = 1.0$ . . . . .	71
4.4	Particles distribution in 2D for the numerical approximation analysis. . . . .	79
4.5	Cross-section of the test patch at $y = 2.5$ . Three SPH approximations of $\nabla^2(x^3 + y^3)$ with different kernel gradients are shown. Corrected Brookshaw's scheme (CB-SPH) is given by (4.28) with the correction multiplier, while Schwaiger's scheme (S-SPH) is given by (4.29)–(4.32). New approximation (M-SPH) considered here is the SPH form (4.44)–(4.46). In this case, the Schwaiger's scheme and new scheme have comparable accuracy at the boundaries and are accurate in the interior to the machine precision. Four different options of computing the kernel gradient (i.e., $\nabla_\gamma W, \nabla_\alpha \bar{W}$ , and corrected kernel gradients (i.e., $\nabla_\alpha^* W, \nabla_\alpha^* \bar{W}, \tilde{\nabla}_\alpha^* \bar{W}$ , and $\tilde{\nabla}_\alpha^* \bar{W}$ ) are shown. . . . .	80
4.6	Comparison of solutions of the Dirichlet problem for the Laplace equation. The method used are MPFA-O, Mimetic, TPFA, and Meshless methods (New Method: (4.44)–(4.46)). . . . .	82
4.7	Comparison of solutions of the inhomogeneous mixed boundary problems for the Laplace equations. The method used are MPFA-O, Mimetic, TPFA, and Meshless methods (New Method: (4.44)–(4.46)). . . . .	84
4.8	Comparison of solutions of the Dirichlet problem for the Laplace equation and permeability tensor (4.86) Case (c). The method used are MPFA-O, Mimetic, TPFA, and Meshless methods (New Method: (4.69)–(4.72)). Errors $\ E_R\ _\Omega^{L^2} = 0.000 \cdot 10^0$ (MPFA), $\ E_R\ _\Omega^{L^2} = 6.478 \cdot 10^{-5}$ (Mimetic), $\ E_R\ _\Omega^{L^2} = 8.458 \cdot 10^{-13}$ (TPFA), $\ E_R\ _\Omega^{L^2} = 5.945 \cdot 10^{-4}$ (Meshless Method) . . . . .	85
4.9	Comparison of solutions of the Dirichlet problem for the Laplace equations and permeability tensor (4.87). The method used are MPFA-O, Mimetic, TPFA, and Meshless methods (New Method: (4.69)–(4.72)). Errors $\ E_R\ _\Omega^{L^2} = 0.000 \cdot 10^0$ (MPFA), $\ E_R\ _\Omega^{L^2} = 4.060 \cdot 10^{-4}$ (Mimetic), $\ E_R\ _\Omega^{L^2} = 4.948 \cdot 10^{-3}$ (TPFA), $\ E_R\ _\Omega^{L^2} = 1.958 \cdot 10^{-2}$ (Meshless Method) . . . . .	86
4.10	(a) The mean value distribution of $\ \xi_I\ $ for 50 random configurations; (b) The dispersion $\sigma(\ \xi_I\ )$ of the $\ \xi_I\ $ distribution for 50 random configurations; . . . . .	88
4.11	von Neumann growth factor for different discretization schemes. Corrected Brookshaw's scheme (CB-SPH) is given by (4.28) with the correction multiplier, while Schwaiger's scheme (S-SPH) is given by (4.29)–(4.32). New approximation (M-SPH) considered here are the SPH form (4.44) – (4.46). Four different options of computing kernel gradients (i.e., $\nabla_\gamma W, \nabla_\alpha \bar{W}$ , and corrected kernel gradients (i.e., $\nabla_\alpha^* W, \nabla_\alpha^* \bar{W}, \tilde{\nabla}_\alpha^* \bar{W}$ , and $\tilde{\nabla}_\alpha^* \bar{W}$ ) are shown. . . . .	89
4.12	The lognormal permeability field in the SPE10 benchmark test. Case (a) $60 \times 60$ cells of 85 layer. Case (b) subsection of the SPE10 model defined by $60 \times 60 \times 60$ cells. . . . .	90
4.13	Numerical solution obtained with the new scheme for the SPE10 cases. The relative error distribution is also shown for 2D and 3D cases, where error is computed using (4.81) and numerical solution based on TPFA. The maximum relative errors in 2D and 3D are 0.07% and 0.4%, respectively . . . . .	90
4.14	Comparison of the convergence rate of the GMRES iterative method with and without preconditioner for different numerical discretization methods (TPFA, New Scheme (4.44)–(4.46), Schwaiger (4.29)–(4.32)). The linear system of equations is built using 2D case. . . . .	90
4.15	Comparison of the convergence rate of the GMRES iterative method with and without preconditioner for different numerical discretization methods (TPFA, New Scheme (4.44)–(4.46), Schwaiger (4.29)–(4.32)). The linear system of equations is built using 3D case. . . . .	91
5.1	Typical V-cycle scheme of five levels for (multilevel-) multiscale, multigrid, and multilevel deflated method. . . . .	95
5.2	Subdomain (a), levelset (b) and subdomain-levelset deflation (c). . . . .	98
5.3	X-direction permeability distribution in logarithmic scale and Darcy units for SPE10 case. . . . .	103
5.4	Numerical domain: 2D example with 64 high heterogeneities islands. . . . .	106
5.4	Application of the METIS-based grid partitioning: partitioning into 64 subdomains. . . . .	107
5.5	Numerical Domain: fractured reservoir. . . . .	108
5.6	Numerical domain with grid- and fracture-based partitioning: 57 fracture and 100 grid subdomains. . . . .	109

5.7	Total time of the linear solver stage for CPR-AMG-ILU(0) and MsMBM solution strategies. . .	112
5.8	Scalability of the total time of the simulation runs for CPR-AMG-ILU(0) and MsMBM solution strategies in the case 389557. . . . .	112

---



---

## List of Tables

---

3.1	Material properties for AA7010-T6 used in analysis. . . . .	41
3.2	EOS data for AA7010-T6 used in analysis. . . . .	41
3.3	Reference material properties I. . . . .	46
3.4	Reference material properties II. . . . .	46
3.5	Reference material properties III. . . . .	46
3.6	Verification of Numerical implementation. . . . .	47
3.7	Material Plasticity Properties. . . . .	48
3.8	Material EOS Properties. . . . .	48
4.1	The error of convergence for different schemes (uniform particle distribution) and $f = 0.5005$ . . . . .	81
4.2	The error of convergence for different schemes (uniformed particle distribution) and $f = 1.001$ . . . . .	81
4.3	The error of convergence for different schemes (random particle distribution) and $f = 0.6006$ . . . . .	82
4.4	The error of convergence for different schemes (random particle distribution) and $f = 1.2012$ . . . . .	82
4.5	The error of convergence for different schemes (uniform particle distribution) and $f = 0.5005$ . . . . .	83
4.6	The error of convergence for different schemes (uniform particle distribution) and $f = 1.001$ . . . . .	84
4.7	The error of convergence for different schemes (random particle distribution) and $f = 0.6006$ . . . . .	84
4.8	The error of convergence for different schemes (random particle distribution) and $f = 1.2012$ . . . . .	84
5.1	Comparison of $gMsMBM(3,8)$ (with AMG preconditioner), $gMsMBM(3,27)$ (with AMG preconditioner), $gMsMBM(3,64)$ (with AMG preconditioner) and CPR-AMG for the SPE10 case. . . . .	104
5.2	Numerical results: linear solver iterations using $\mathbf{Z}_t$ . . . . .	107
5.3	Linear solver iterations using $\mathbf{Z}_1$ , $\mathbf{Z}_{mms}$ , $\mathbf{Z}_{db}$ , $\mathbf{Z}_{mix}[\mathbf{Z}_1 \mathbf{Z}_{mms}]$ and $\mathbf{Z}_{mix}[\mathbf{Z}_1 \mathbf{Z}_{db}]$ . . . . .	107
5.4	Linear solver iterations using meshless multiscale operators. . . . .	108
5.5	Linear solver iterations of the decoupled ADMMS preconditioner. . . . .	108
5.6	Linear solver iterations using multiscale (grid- and fractures-based) deflation. Multiscale-based deflation ( $f$ and $g$ stand for the amount of fractures and grid subdomains respectively). . . . .	109
5.7	Linear solver iterations using mixed deflation matrix. . . . .	110
5.8	Linear solver iterations using meshless multiscale-based preconditioner. . . . .	110
5.9	Linear solver iterations of the ADMMS preconditioner with the GMRES solver. . . . .	110
5.10	Basic properties of the simulated test cases. . . . .	111

---

---

## List of Algorithms

---

1	Right-Preconditioned two stage CPR-GMRES . . . . .	94
2	Right-Preconditioned Meshless Deflation GMRES Based Method . . . . .	102
3	Multi-Level FAS-Newton-Raphson. . . . .	116



---

---

## SUMMARY

---

**I**N many fields of science and engineering, such as fluid or structural mechanics, and nanotechnology, dynamical systems at different scale need to be simulated, optimized or controlled. They are often described by discretizations of systems of nonlinear partial differential equations yielding high-dimensional discrete phase spaces. For this reason, in recent decades, research has mainly focused on the development of sophisticated analytical and numerical (linear and nonlinear) tools to help understand the overall multiscale system behavior. Various models and numerical methods have been developed to simulate different physical processes at different scales. The choice of these methods will depend largely on the problem, the available computational resources and constitutive equations.

Smoothed particle hydrodynamics (SPH) was developed a few decades ago to model inviscid fluid and gas flow dynamics in astrophysical problems. The SPH is an interpolation-based numerical technique that can be used to solve systems of partial differential equations (PDEs) using either Lagrangian or Eulerian descriptions. The nature of SPH method allows to incorporate different physical and chemical effects into the discretized governing equations with relatively small code-development effort. In addition, geometrically complex and/or dynamic boundaries, and interfaces can be handled without undue difficulty. The SPH numerical procedure of calculating state variables (i.e., density, velocity, and gradient of deformation) are computed as a weighted average of values in a local region.

The modelling of the dynamic irreversible behaviour of different materials is one of the most important and challenging aspects in the analysis of engineering problems. These problems require the identification of the stress-strain state of the solid body, which is bounded by the nature of the material (i.e. isotropic metals, anisotropic aluminium alloys, composite materials and energetic materials to name but a few). Typical applications include the civil aerospace industry, military applications, the construction of nuclear and chemical sectors and many other machinery production industries. In transient dynamic problems, it is essential to describe material behaviour under dynamic loading, such as shock wave propagation and damping, in order to predict the micro- and macro-damage initiation and propagation, as well as the origination of fracture surfaces (new boundary surfaces) within a material. In order to be able to achieve this, it is important to use a material model that can take into account fundamental mechanical characteristics that influence its response. A material model must be able to model the following principal stages of material behaviour: elastic behaviour, elastoplastic behaviour with hardening effects, strain rate dependency, damage nucleation and propagation, macro-fracture origination and thermal effects. This is further compounded by material models that show a degree of anisotropy with respect to some of the aforementioned characteristics. This thesis is addressed to the construction of a thermodynamically and mathematically consistent underlying theory of irreversible deformation, micro-and macro-fracture of anisotropic solids and structures coupled with the meshless (e.g., SPH) numerical technique. The objectives of this thesis are in line state of art and can be used as a foundation for further developments. A comparison of the thesis results with existing experimental data shows good agreement, and suggests that the constitutive equations perform satisfactorily.

The SPH method has been extensively used to model high and low Reynolds number flows, free surface flows and collapse of dams, study pore-scale flow and dispersion, elasticity, and thermal problems. In different



applications, it is required to have a stable and accurate discretization of the elliptic operator with homogeneous and heterogeneous coefficients. In this thesis, the stability and approximation analysis of different SPH discretization schemes (traditional and new) of the diagonal elliptic operator for homogeneous and heterogeneous media are presented. The new optimum (i.e., high order with monotonicity property) discretization scheme for the internal particles is also proposed. The new scheme enhances the Laplace approximation (Brookshaw's scheme (1985) and Schwaiger's scheme (2008) used in the SPH community for thermal, viscous, and pressure projection problems with an isotropic elliptic operator. The sufficient monotonicity condition is also formulated leading to the constraint on the kernel shape and particles distribution. The numerical results are illustrated by numerical examples, where the comparison between different versions of the meshless discretization methods are presented.

Accurate and efficient simulation of flow in highly heterogeneous oil reservoirs entails several challenges, one of which is due to the large scale ratios between the domain size and the resolution of the heterogeneous geological data. Traditionally, upscaling approaches have been used to obtain effective coarse-scale quantities so that the number of degrees of freedom (DOF) is reduced enough such that the problem lies within the range of state-of-the-art reservoir simulators capacity (typically in the order of  $10^6 - 10^7$  DOF). Similar to upscaling methods, multiscale methods have been developed over the past decade in order to construct an accurate coarse-scale system honoring the fine-scale heterogeneous data. Preconditioning can be used to damp slowly varying error modes in the linear solver residuals, corresponding to extreme eigenvalues. Existing multiscale solvers use a sequence of aggressive restriction, coarse-grid correction and prolongation operators to handle low-frequency modes on the coarse grid. High-frequency errors are then resolved by employing a smoother on fine grid. In reservoir simulations, the Jacobian system is usually solved by FGMRES method with two-level Constrained Pressure Residual (CPR) preconditioner. In this thesis, a parallel fully implicit SPH based multiscale method for solving pressure system is presented. The prolongation and restriction operators in this method are based on a SPH gradient approximation (instead of solving localized flow problems) commonly used in the meshless community for thermal, viscous, and pressure projection problems. This method has been prototyped in a commercially available simulator. This method does not require a coarse partition and can be applied to general unstructured topology of the fine scale. The SPH based multiscale method provides a reasonably good approximation to the pressure system and speeds up the convergence when used as a preconditioner for an iterative fine-scale solver. In addition, it exhibits expected good scalability during parallel simulations. Numerical results are presented and discussed.

---

---

## ACKNOWLEDGEMENT

---

**T**hat's it ! It is a time to write an acknowledgement part for the thesis which is both the easiest and the most difficult part to accomplish. After completing this thesis, it turns out that a writing up process is far from being an individual journey. I am happy to acknowledge here people who have been accompanied, inspired, supported, encouraged and stimulated me during my journey.

There are many people starting from undergraduate studies who helped, supported, encouraged and kept me in doing my research. This list could be very lengthy. Hence, I express my deep thankfulness to all my teachers for guidance and encouragement throughout my graduate studies. As usual, family plays an important role and I would like to express my sincere and deep gratitude to my parents, son and brother in general for their supports during all my graduate and research journeys.

Specifically, I would like to thank my promotor Professor Kees Vuik for the opportunity to do my research with him. This was an incredible experience and I truly hope to be able to continue my collaboration with him, throughout my academic and/or industrial journeys. Without Kees encouragements starting from the begging of this research journey, this work would not be completed. Our weekly discussions about the meshless modeling, including linear algebra, numerical methods, high performance computing, linear and nonlinear solvers and life in general, were the key elements in the completing of this research work.

Moreover, I would like to thank the independent members of the doctoral committee, Prof.dr.ir. A. Heemink, Prof.dr. J. Bruining, Prof.ir. C.P.J.W. van Kruijsdijk, Prof.dr. D. Tartakovsky, Prof.dr. V. Druskin, Prof.dr.ir. W. Schilders for accepting to be part of my defence and for their valuable feedback, enriching the end of my journey. I would also like to thank the Department of Applied Mathematics, the Faculty of Electrical Engineering, Mathematics and Computer Science, Delft University of Technology for the opportunity to perform this research work.

Many thanks to all my friends everywhere, you know who you are, for your support and understanding. Specially, I would like to thank my friend Lisa Wobbes for helping me to be my paranymp in Delft.

Last but not least, I should thank Nadezhda Kosintseva meeting with whom and discussing many subjects have helped me to make some final and important steps towards the finishing line. Nadya thank you for our inspiring conversations, your sharp positions with respect to some fundamental issues in the life, and for sharing with me some of my believes. Your introduction of me to the world of chess with pattern recognitions has taught me how to make one step back and to reflect before getting lost in details. This principal can be applied both for research and life.

2019, Harvard, Cambridge, MA, USA

---

---

## INTRODUCTION

---

**I**N many fields of science and engineering, such as fluid or structural mechanics, and nanotechnology, dynamical systems at different scale need to be simulated, optimized or controlled. They are often described by discretizations of systems of nonlinear partial differential equations yielding high-dimensional discrete phase spaces. For this reason, in recent decades, research has mainly focused on the development of sophisticated analytical and numerical (linear and nonlinear) tools to help understand the overall multiscale system behavior. Various models and numerical methods have been developed to simulate different physical processes at different scales. The choice of these methods will depend largely on the problem, the available computational resources and constitutive equations. A review of the most common of these formalisms used for modeling shock waves propagation, fluid flow in porous media is provided in this dissertation. During this time meshless methods have enjoyed significant interest in the research community and even appeared in some commercial simulators. This dissertation is dedicated to the investigation of meshless numerical methods applied to multi-physics and multiscale problems. In particular, the material behaviour (e.g., metal plate or bars) under transient intensive dynamic loading and multi-phase fluid flow in porous media are solved. The solid mechanics problems require the identification of the stress-strain state of the solid body, which is bounded by the nature of the material (i.e. isotropic metals). Typical applications include the civil aerospace industry, military applications, the construction of nuclear and chemical sectors and many other machinery production industries. On the other hand, the multi-phase fluid flow in porous media problems require the identification of pressure profiles, saturation distributions. Typical applications include oil recovery modellings, underground water flow simulations, radioactive waste migration modellings, blood flow simulations in the biological tissues.

The problems outlined above are described by the hyperbolic or almost hyperbolic (there is at least one parabolic/elliptic equations) partial differential governing equations. These equations are subject to the presence of either an initial or developed discontinuous fronts (e.g., elasto-plastic shock waves, fracture-waves, and discontinuity in the saturation) as a part of the global solution. Any numerical methods (linear or nonlinear) applicable to these problems should include specific procedures / formulations to treat the discontinuities.

In addition, the material behaviour under dynamic loading, such as shock wave propagation and damping, in order to predict the micro- and macro-damage initiation and propagation, as well as the origination of fracture surfaces (new boundary surfaces) within a material are required to have appropriate governing equations. In order to be able to achieve this, it is important to use a material model that can take into account fundamental mechanical characteristics that influence its response. A material model must be able to model the following principal stages of material behaviour: elastic behaviour, elastoplastic behaviour with hardening effects, strain rate dependency, damage nucleation and propagation, macro-fracture origination and thermal effects. This is further compounded by material models that show a degree of anisotropy with respect to some of the aforementioned characteristics.

The scope of this research does not cover all important aspects of material behaviour and fluid modelling. For example, the strain rate effects, the hardening effects, the relaxation aspects of a stress-strain state and many others have not been fully considered for description of the solid mechanics problems. On the other hand, the phase transition, miscibility and other processes were not taking into account during the fluid flow modelling in

---

the porous media.

The principal focus of this research is the usage of the meshless multi-scale technology for solving linear and non-linear discretized governing equations.

## I. Background and Actuality of the thesis

The *background and actuality* of this thesis is to construct a thermodynamically and mathematically consistent underlying theory and numerical implementation (explicit and implicit) including linear and nonlinear solvers of solid and fluid mechanics problems.

### Solid mechanics

Nowadays, there are a large variety of approaches for the description of failure processes when reviewing the large amount of published literature, such as L.M. Kachanov (1958, 1969, 1974, 1986) [126], [127], [128], [129], Yu.N. Rabotnov (1959, 1963) [225], [226], A.A. Il'ushin (1967) [114], V.I. Astafjev, Yu.N. Radayev, L.V. Stepanova (2001) [10], S. Murakami and Yu.N. Radayev (1994, 1996) [228], [227], G.P. Cherepanov (1974) [62], J.L. Chaboche (1984, 1988) [50], [51], [52], D. Krajcinovic (1996) [148], J. Lemaitre (1996) [159], J. Lemaitre and J.L. Chaboche (1990) [160], S. Murakami (1981, 1983, 1987, 1988) [219], [215], G. Maugin (1992) [198], G.Z. Voyiadjis and P.I. Kattan (1992) [266].

The approach developed by L.M. Kachanov (1958) [126] and Yu.N. Rabotnov (1959) [225], is accepted as a separate discipline of continuum mechanics and obtained the name "*Damage Mechanics*", or "*Mechanics of continual fracture*" (see Kachanov (1974) [128], Chaboche (1984, 1988) [50], [51], [52], Krajcinovic (1996) [148], Lemaitre (1996) [159], Lemaitre and Chaboche (1990) [160], Maugin (1992) [198]). *Damage Mechanics* (DM) allows the construction of physically and mathematically consistent models of a damageable medium, which describes the origination of the softening zones within a material, i.e. zones of micro- and macro-fracture. In the mechanics of continual fracture, evolution equations for damage parameters (microfracture) have the responsibility to describe the fracture process (origination of the new fracture surfaces), which are linked with other governing equations. Softening, or generally speaking failure, is based on the representation of failure as the loss of material ability to carry external loading due to damage concentration propagation (Astafjev *et al.* (2001) [10], Maugin (1992) [198]). Failure is described as an individual process and is characterized by damage parameters, which are linked to the other state variables (e.g., stress tensor, temperature), through the system of governing equations and initial-boundary conditions of thermomechanics.

The reduction of the stresses with in material is controlled by the damage parameters only via reduction of the stiffness matrix (elastic properties) with the growing of the damage parameters, which always remains positive. The positive definitive property of the elastic properties provides a necessary correction condition of the initial-boundary value problem according to Adamar's and Drucker's postulates. The decrease in material ability to carry external loading can be caused by non-thermal external loading (e.g., chemical, radiation), as well as thermal loading after the achievement of the realisation of the failure criterion. Further development of the damage mechanics has been done along the lines of generalisation of the principal assumption of damage mechanics onto a three dimensional anisotropic damage state by Kachanov (1986) [129], Lemaitre (1996) [159], Murakami (1983, 1987) [215], [216], Radayev (1994, 1996) [228], [227], Lubarda and Krajcinovic (1993) [179], Luccioni and Oller (2003) [180], Voyiadjis and Park (1997) [267], and Brunig (2003) [44], [45].

The criteria for macro-fracture can be formulated as the local limitation on the state parameters of the stress-strain state in the elementary physical volume  $V$  (see, Kachanov (1974) [128]), as integral-energetics relations for finite volumes (Cherepanov (1974) [62]), as criteria based on gradient of the stress-strain state parameters (non-local theory) Kukudzhnov (1999) [152], Jirasek (1998) [117].

In the fracture mechanics of a continuum medium, the macrofracture occurs instantaneously after realisation of the macrofracture criterion (without taking into account the damage nucleation and propagation of microfracture). In these models, the macrofracture is simulated by explicit extraction of the fracture surfaces as contact surfaces. Fracture mechanics has found wide applicability in engineering applications, but at the same time, current fracture mechanics cannot provide detailed physical description of the failure process. Therefore, this simple description of fracture in the framework of fracture mechanics is not suitable for problems that involve intensive dynamic loading.

A continual approach can be definitely considered as an extension of the fracture mechanics approach, which attempts to construct a theoretical model of continuum mechanics that is suitable for the description of failure, based upon a unified system of governing equations with damage parameters. This continual approach

implicitly (i.e. on the macrolevel) describes the microdamage zones and microcracks initiation and developing, which is very useful in numerical simulation. This fact has impact on simultaneous development of damage mechanics and the numerical methods for damage mechanics (for example, Aravas and McMeeking (1985) [8], [9], Gullerud (1999) [103], Bao *et al.* (2001) [19], Kim *et al.* (2003) [137], Kim and Gao (2005) [136], Kim *et al.* (2004) [138], Brunig (2003) [44], Belytschko and Lin (1987) [26]).

As it was mentioned before, the reduction of stresses within a material due to its decreasing load carrying capability of a material might occur due to nonthermal reasons at fixed deformation. This fact leads to the conclusion that in the continual description, the deformation and failure process should be treated independently (which does not exclude the fact of their influence on each other), and the failure process is necessary to characterise by using the damage parameter. This important step has been done by the following researchers: Kachanov (1958,1974) [128], [126]; Rabotnov (1959) [225]; Il'ushin (1967) [114]; Vakulenko (1971) [259]; Kukudzhanov (1999) [152]; Kiselev and Lukyanov (2002) [140]; Lukyanov (2007) [183]. Damage parameter can be described by a scalar or tensor (see, e.g. Kachanov [129], Lemaitre [159], Murakami (1983, 1987) [215], [216], Radayev (1994) [228], Lubarda and Krajcinovic [179], Luccioni *et al.* (2003) [180], Voyiadjis (1997) [267], Brunig [44], [45], Kukudzhanov [152], Kondaurov [145], [146], Kiselev and Lukyanov (2002) [140], Lukyanov [182], Betten [31]), which satisfies kinematic relations. With an increasing damage parameter, the resistance of the medium decreases, which is supported by experimental evidence of decreasing sound speed propagation by small perturbations.

Softening, or failure of the material is accompanied by localisation phenomenon of the plastic strain, damage, stress, temperature at the zones of weakest material resistance (Belytschko *et al.* [23]). In many cases of numerical simulation of continual fracture, calculated fracture zones appear unphysically large and localisation effects are expressed poorly. The analysis of such numerical models is difficult and sometimes even impossible. The appearance of a large zone of damage propagation can be observed in experimental studies with viscous materials, which have a relatively slow growth density of the microcracks (microdamage). Even greater, is the slow accumulation of damage parameters that is observed during creep failure. Decreasing influence of regulation terms during the simulation of strong localization of deformations leads in most cases, to the anomaly dependence solution from the size and form of the mesh cells, and finally, leads to the loss in convergence of the algorithm. Therefore, the construction of a constitutive relation (e.g., description of plasticity flow and shock wave propagation) and the numerical algorithms for accurate realisation of the continual models, represents one of the fundamental and important problems in predicting material behaviour. The construction of consistent approaches for the description of material behaviour (e.g., softening effects, the thermodynamic equation of state response, irreversible deformation) are not fully understood yet and therefore, it remains an active area of research.

The physical and numerical difficulties are further compound by materials that exhibit slow and fast stages during overall nonlinear material behaviour. Therefore, modelling requires significant efforts during numerical simulation of experimental measurements, making parametric investigations difficult. Therefore, real history matching of numerical simulation with experimental data should be performed quickly, especially for the real time applications (e.g., optimization of the hydrocarbons production).

In this thesis, the material (metal plate and nano-structure) behaviour under extensive dynamic loading (e.g., impact loading) is considered, whereby the material undergoes all the aforementioned stages of material response. This still remains a difficult and actual task of modern science, so this thesis mainly focuses on the modelling aspects of the problem.

### **Fluid Flow in Porous Media**

In modern reservoir simulation the geology of the reservoir, which includes faults and non-orthogonal grids, with a fully discontinuous permeability tensor in the discretization, and different physical and chemical effects (e.g., in-situ combustion, geochemistry, molecular diffusion, solubility etc.) is a major challenge. This results in a need to use more advanced and fast numerical techniques with a fully discontinuous permeability tensor in the discretization.

Several discretization methods have already been developed and tested within the reservoir simulation community (e.g., MPFA) (Aavatsmark, 2002 [2]; Aavatsmark *et al.*, 1996, 1998 [3], [4, 5]; Edwards and Rogers, 1998 [86]; Edwards 2002 [83, 84]; Chen *et al.*, 2007 [60]; Lee *et al.*, 1998 [155]). It has been noticed that some of the numerical methods for elliptic and parabolic equations may violate the maximum principle (i.e. lead to spurious oscillations). Therefore, proposed methods must satisfy a discrete maximum principle to avoid any spurious oscillations. The discrete maximum principle for MPFA methods was discussed, e.g., in Edwards and

---

Rogers (1994, 1998) [85, 86], Mlacnik and Durlafsky (2006) [207], Lee *et al.* (2002) [156]. However, non-physical oscillations can appear in some of the numerical methods when the anisotropy is particularly strong. It has been found that the oscillations are closely related to the poor approximation of the pressure gradient in the flux computation. In addition, the level of detail and range of property variability included in reservoir characterization models leads to a large number of grid cells describing the petro-physical properties with spatial information.

To account for the scale differences between geological model and flow simulation model, multiscale (e.g., multiscale finite-volume (MSFV) methodology) solution strategies was developed recently. The method bridges the scale differences by utilizing different grid systems and different physical scales. The fluid flow modeling is conducted in coarse scale level using basis functions with localization of domain and the transport phenomena in fine scale level are reconstructed. The strong benefit of multiscale simulation is a solution of the fluid flow PDEs in lower resolution scale or coarse scale model while it reconstructs the fine scale transport phenomena. In other words, ultimately the fluid flow PDEs are solved directly using geological model without upscaling or parameterization process. This removes the uncertainty of the upscaling process or parameterization process.

Note that, for example, the Multiscale Finite-Volume (MSFV) methodology (e.g., Hou and Wu, 1997 [110]; Jenny *et al.*, 2003 [115], 2006 [116]; Tchelepi *et al.*, 2005 [251]; Lee *et al.*, 2008 [157]; Hajibeygi *et al.*, 2008 [104]; Hajibeygi and Jenny, 2009 [107]; Lunati *et al.*, 2011 [193]) was developed to offer a computationally efficient alternative to the direct solution of large (fine-scale) problems. The method has been used to solve physically complex flows. The common step between related multiscale methods (e.g., Hou and Wu, 1997 [110]; Chen and Hou, 2003 [61]; Aarnes *et al.*, 2005 [1]; Hou and Wu, 1997 [110]; Jenny *et al.*, 2003, 2006 [115], [116]; Tchelepi *et al.*, 2005 [251]; Lee *et al.*, 2008 [157]; Hajibeygi and Jenny, 2008 [106]; Hajibeygi *et al.*, 2008 [104]; Lunati *et al.*, 2011 [193]) is to compute an approximate solution that models the system behavior with reasonable accuracy at different scales. This is achieved by solving a set of localized fine-scale problems, which are coupled by a global coarse-scale problem. Lunati *et al.* (2011) [193] constructed an iterative method based on the MSFV operator to improve the quality of the localization assumption, which can be stabilized by use of a Krylov-space accelerator.

Multiscale simulation involves numerical calculation of local boundary value problems. It is absolutely essential to have an appropriate formulation for local boundary value problems which incorporate fine scale physics. The construction of the basis functions and corrections functions for the sink/source terms are not fully understood yet and therefore, it remains an active area of research.

### **Non-linear solver**

The extreme-scale solvers (exascale computations) which are required for various problems in solid and fluid mechanics, which must be compatible with extensive use of parallel nonlinear solver technology. There are several solutions strategies for nonlinear implicit PDEs: e.g., Newton-based methods and Picard-type linearization or splitting operator (equations or coordinate), Nonlinear GMRES (NGMRES) (Washio and Oosterlee, 2000 [274]; de Sterck, 2013 [76]), Quasi-Newton (Dennis and More, 1977 [78]), Nonlinear additive Schwartz methods (NASM) (Cai *et al.* 2002 [46]), Nonlinear block-Jacobi methods, Nonlinear fieldsplit, Full approximation scheme (FAS), Newton-Krylov method.

The solution strategies such as mixing Newton-Raphson and Krylov methods (Kelley, 1995 [135]), the non-linear multigrid methods (Mavriplis, 2002 [200]; Brandt [39]) and Jacobian-Free Newton-Krylov methods (JFNK) (Brown and Saad, 1990 [42]; Chan and Jackson [53]; Kelley, 1995 [135]; Knoll and Keyes 2004 [144]; Mavriplis, 1998, 2002 [199, 200]) are commonly used in the scientific community for non-linear discretized governing PDEs. In addition, these strategies are very suitable for preconditioning strategy leading to a highly robust numerical tool. The JFNK methods are natural combinations of Newton-Raphson type methods for solving nonlinear equations and Krylov subspace methods for solving the Newton correction equations. In conventional JFNK methods (Brown and Saad, 1990 [42]; Chan and Jackson [53]; Kelley, 1995 [135]; Dembo *et al.*, 1982 [77]) the "inexact" nonlinear iterative method is on the outside loop, and a linear iterative method on the inside loop. A main advantage of JFNK is related to the approximation of matrix-vector multiplication (given a subroutine that evaluates the discrete residual on the numerical mesh). Furthermore, inexpensive linearized solvers can be applied as preconditioners. However, developing effective preconditioners require additional attention. The common nonlinear multigrid method, e.g., FAS method (Brandt, 1977 [39], Wesseling, 1992 [275]), is the solution method based on linearized equations on coarse grid levels. The nonlinear multigrid method performs solution on the full nonlinear problem on each coarsened grid level. The advantages of the non-linear multigrid method include low storage requirement and optimal convergence on some problems. However,

it has been acknowledged in the research community that conventional technologies (full Newton-Raphson linearization and multigrid-preconditioned linear solvers) are not fully appropriate for exascale computations due to high storage requirement and pure scalability for parallel computations. The disadvantages of these methods are complexity of forming hierarchical meshes, the skills required to develop coarse mesh representations of a nonlinear operators, and potentially a large number of complicated nonlinear function evaluations.

The nonlinear solver algorithm at the extreme scale will require additional development and analysis. Preconditioned nonlinear methods and compositions of nonlinear methods may be appropriately modified to suit a particular physical problem in conjunction with a particular computer architecture. In this thesis the particular interest will be paid to the hybrid compositions of non-linear solvers that include fast multiscale nonlinear algorithms, like multiscale FAS, and multi-scale preconditioned JFNK that are arithmetically intense and potentially asynchronous.

### Linear solver

In the framework of this thesis, the multiscale meshless computations involve the nonlinear simulation of a inhomogeneous media (solids, nano-tubes or reservoirs), where the difference in media properties leads to large differences in the entries of the resulting matrix (Jacobian) corresponding to the linear equations. It is important to stress that the nonlinear iterative methods have grown out of advances in linear iterative methods, multigrid methods, and preconditioned Krylov methods.

Modern iterative and direct solvers are capable of handling these large system of equations. Despite this and the enhancement in increasing power of CPUs and the introduction of multiple computing cores on one CPU, the demand for efficient, parallel computing algorithm is high. The common path for those developments is the combination of well-established techniques (i.e., Krylov subspace methods, multigrid, multi-scale and direct solution methods).

For relatively small and medium scale problems parallel direct solvers such as MUMPS, PARDISO, SuperLU or ILUPACK are choices in terms of cost and efficiency. For example, MUMPS a parallel (OpenMP) direct solver is hard to beat in robustness for small (3D) problems; SuperLU and MUMPS are parallel (MPI and OpenMP) direct solvers which are fast in the solution step and slow in set up; ILUPACK preconditioners are good ILU based solvers compatible with OpenMP technology.

In real life applications, the numerical domains are large and as a consequence a large number of degrees of freedom (i.e., unknowns) is required. The resulting matrix is usually sparse, but because of fill-in a direct method requires significant amounts of memory and time. Therefore, iterative methods are the preferred solution methods for solving the linear system of equations. Depending on the discretization method, the resulting matrix could be symmetric or non symmetric and positive definite or indefinite. For a symmetric positive definite matrix, the Conjugate Gradient method (CG) (Meijerink and Van der Vorst, 1977 [201]) is the solution method of choice, whereas for indefinite symmetric matrices the MINRES can be used. For nonsymmetric matrices, methods such as GMRES, Bi-CGSTAB (Van der Vorst, 1992 [79]), and TFQMR (Freund, 1993 [92]) can be used. However, the last two methods do not guarantee monotonically decreasing residuals. As a result, we tend to use GMRES (and its variants) exclusively in this paper. A common feature for most of existing iterative methods is the use of different projection method, arising from the Petrov-Galerkin conditions (Saad, 2003 [233]) where Krylov subspace is used. In our application, due to large contrasts in the permeability field, a large difference of the extreme eigenvalues is observable (Vuik *et al.*, 1999 [268]). This leads to slow convergence of aforementioned iterative methods (van der Sluis and van der Vorst, 1986 [261]).

A preconditioned Krylov subspace method can significantly improve convergence and robustness. Deflation based preconditioners were successfully applied within the field of computational biophysics (Barnard *et al.*, 1966), computational fluid dynamics (Nicolaidis, 1987 [221]) and with excellent results on problems with discontinuous jumps in coefficients (Frank and Vuik, 2001 [91]), (Tang *et al.*, 2009 [246]), (Tang *et al.*, 2010 [245]).

For the PDEs with coefficients considered in this thesis, there are several well established state-of-the-art (black box solvers) available. Direct solvers (e.g., SuperLU), the FETI solver, and Algebraic Multigrid (AMG) (Ruge and Stuben, 1987 [217]) are the most efficient solvers. Moreover, AMG is well known for its capability of handling large contrasts in the matrix. In recent years, in many applications there has been a shift from classical AMG to Smoothed Aggregation AMG (SA-AMG, Vanek, *et al.* 1996 [263]). SA-AMG has more aggressive coarsening and is well suited in capturing the near-null space components of the solution on the coarse grids. These components are related to the unfavorable eigenvalues of the matrix and hence responsible for the slow convergence of the iterative method. In this work we will compare our results with SA-AMG, as

---

it is the current-state-of-the-art preconditioner for the kind of problems considered in this research. The main drawback of this method for real applications is a large CPU overhead associated with the SA-AMG setting up step which has to be repeated in each iteration of the Newton process per each time step of the simulation time.

## II. Objectives and Scope

The objectives of this thesis are to address the improvement of the shortages of existing approaches and models. This thesis contains the theoretical and numerical investigation of the fundamental principals of material behaviour, such as elastoplastic behaviour, the nucleation, growth and coalescence of damage, macro-fracture propagation, shock wave formation and propagation. The main objectives of this thesis can be summarised as follows:

- Investigation of a damage model of an isotropic medium, that is capable of predicting brittle, ductile, and shear bands fracture, influence of thermal effects;
- Description of shock wave propagation (the thermodynamic equation of state response (EOS) in a damageable media;
- To construct stable meshless discretization schemes both for solid and fluid flow in porous media problems;
- To develop new optimum (i.e., high order with monotonicity property) discretization scheme for the internal particles. The new scheme should enhance the Laplace approximation (Brookshaw's and Schwaiger's schemes);
- Develop a meshless relaxed multiscale method for the solution of two-phase immiscible fluid flow modelling in the porous media;
- Investigation of meshless deflation and multi-scale preconditioners applicable for sparse linear equations with jump coefficients arising from dynamic fluid mechanics problems;

## III. Organisation of the Thesis

This thesis covers different topics related to numerical analysis of solid and fluid mechanics (material behaviour under dynamic loading, immiscible and incompressible fluid flow in porous media) and therefore, the structure of the thesis has been created in order to allow the reader without any difficulties to read each chapter independently. Such approach, of course, leads to some repetition of principle results, but in spite of that, there is confidence that the main results of the thesis will be understood. The remainder of the thesis is organized as follows.

### Chapter 1: Problem Formulation

In Chapter 1, a general formulation of boundary value problems including conservation laws of continuum mechanics with different types of boundary conditions and a critical review of the currently available approaches in damage/fracture mechanics and numerical methods are presented. In this regard, it should be noted that all prior micro- or macro- level models are decoupled described; the thermodynamical consistent links recovery of the composite micro fields is not considered. Consequently, most of the current models are constructed based on a stress-strain relation and different types of damage evolution equations. The review focuses on the implications of the damage mechanics concept to the description of material failure, the assumption of material homogeneity and thermodynamically consistent links between state variables, and the requirements imposed on the model construction. A general formulation of a thermodynamically consistent model is then constructed. In particular, the mechanics and thermodynamic aspects in the model formulation are examined within the confines of continuum mechanics.



### Chapter 2: Smoothed Particle Hydrodynamics (SPH)

A well-known Lagrangian particle method is called Smoothed Particle Hydrodynamics (SPH). It was originally developed for astrophysical problems and by now has been generalized to many other fluid and solid mechanics problems. A main focus of this thesis is to address the application of meshless method to multi-physics and multiscale problems. Since the particle positions are defined by the underlying physical problems, the data is given on a scattered point cloud. In this thesis we consider various aspects of meshless methods. Chapter 2 provides an overview of commonly used meshless methods to discretize governing equations. In addition, the aspects such as the connection between the meshless discretization and the graph of the system matrices, the aspect of positive stencils, as well as higher order discretizations are discussed in the following chapters.

### Chapter 3: Shock Wave Propagation in Complex Media

In Chapter 3, a new mathematically and thermodynamically consistent description of the irreversible deformation, micro- and macro-fracture of an anisotropic (including isotropic) medium is presented. The proposed model contains two damage parameters, which describe the evolution of volumetric damage and shear damage respectively and can be used to describe three main damage processes (brittle damage, ductile damage, and formation of adiabatic shear bands). The in-depth failure mechanism analysis provide the necessary guidelines for the formulation of a new constitutive equation that should be devoid of most of the inconsistencies inherent with existing models. The new model should be capable of obtaining accurate descriptions of material behaviour at different stages of material deformation (elastic, inelastic (e.g. plastic), damage initiation, and failure process).

### Chapter 4: Meshless Multi-Point Flux Approximation

Reservoir simulations of complex reservoirs with anisotropic permeability, include faults and non-orthogonal grids, and a fully discontinuous permeability tensor in the discretization are a major challenge. Several methods have already been developed and implemented within industry standard reservoir simulators for non-orthogonal grids (e.g., Multi-Point Flux Approximation (MPFA) "O" method). However, it has been noticed that some of the numerical methods for elliptic equations may violate the maximum principle (i.e., lead to spurious oscillations), especially when the anisotropy is particularly strong. It has been found that the oscillations are closely related to the poor approximation of the pressure gradient in the flux computation. Therefore, proposed methods must correctly approximate the underlying operator, satisfy a discrete maximum principle and have a coercivity property. Furthermore, the method must be robust and efficient. In this chapter some meshless discretizations are discussed and proposed. Special attention is paid to the meshless multi-point flux approximation. The method is based on a pressure gradient approximation commonly used in meshless method (or Smooth Particle Hydrodynamic method - SPH method). Advancing computer capabilities (i.e., transmissibilities compute) are linked with the reservoir simulation tools and discussed in the following chapters.

### Chapter 5: Meshless Relaxed Multiscale Methods

In this chapter we discuss the performance and limitations of the meshless relaxed multiscale and deflated meshless iterative (using Krylov accelerator) solvers applied to solid and fluid mechanics problems. We illustrate and explain these limitations by introduction of relatively small two-dimensional examples that involve the simulation of immiscible and incompressible two phase flow in homogeneous and highly heterogeneous porous media, resulting in small and large differences in the entries of the resulting matrix (Jacobian). We introduce the meshless restriction and prolongation including meshless deflation strategy and describe how to construct the meshless multiscale and deflation based preconditioner to improve the performance of the iterative (e.g., CG or GMRES) solvers. We show experimentally the convergence rates for different resulting matrices (Jacobians).

Nowadays the Krylov subspace iterative methods are widely used in the computational domains. The AMG and Incomplete LU factorization with various fill-in levels for convergence acceleration of these iterative methods are used in the reservoir simulation community. However, incomplete LU factorization and AMG has some HPC disadvantages. In particular, the robust black-box AMG solvers (e.g., SAMG, SA AMG, AMLI) are considered. We compare AMG methods with meshless multiscale preconditioned Krylov subspace solver. Furthermore, the computational effort (complexity) for solving linear systems arising from the different meshless discretization are considered.

---

The main purpose of the research in this chapter is to reduce the number of communications and maintain the good preconditioning quality applicable both for CPUs and GPUs.

## Chapter 6: Future Work

We discuss some ideas for future research. A brief overview on how we might improve existing multiscale meshless methods are described. We use the idea of the preconditioned non-linear meshless FAS method for nonlinear governing equations applicable to a real-life reservoir simulation cases.

This thesis is based on the following conference proceeding papers and journal papers:

### Peer Reviewed Journal Articles

- **Lukyanov, A. A.**, Vuik, C., *Meshless Multi-Point Flux Approximation*, In M. Griebel and M. A. Schweitzer, editors, *Meshfree Methods for Partial Differential Equations VII*, volume 100 of *Lecture Notes in Computational Science and Engineering*. Springer, 2016.
- van der Linden, J., Jonsthovel, T. B., **Lukyanov, A. A.**, and Vuik, C., *The Parallel Subdomain-Levelset Deflation Method in Reservoir Simulation*, *Journal Computational Physics*, Volume 304, Issue C, 2016, PP. 340-358.
- Cusini, M., **Lukyanov, A. A.**, Natvig, J. and Hajibeygi, H., *Constrained Pressure Residual Multiscale (CPR-MS) Method*, *Journal Computational Physics*, Volume 299, Issue C, 2015, PP. 472-486.
- **Lukyanov, A. A.**, *Shock Wave Structure in Anisotropic Carbon Fiber Composites*, *Mechanics of Solids*, 48(6), 2013, PP. 706-715.
- **Lukyanov, A. A.**, *Modeling the Effect of Orientation on the Shock Response of a Damageable Composite Material*, *J. Applied Physics*, 112, 2012, 084908.
- **Lukyanov, A. A.**, Segletes, S. B., *Frontiers in the Constitutive Modeling of Anisotropic Shock Waves*, *Applied Mechanics Reviews*, 64(4), 2012, 040802.

### Conference Publications

- **Lukyanov, A. A.**, Vuik, C., *Parallel Fully Implicit Smoothed Particle Hydrodynamics Based Multiscale Method*, *ECMOR XV - 15th European Conference on the Mathematics of Oil Recovery*, Amsterdam. Netherlands. 2016. 10.3997/2214-4609.201601748.
- **Lukyanov, A. A.**, van der Linden, J., Jonsthovel, T. B. and Vuik, C., *Meshless Subdomain Deflation Vectors in the Preconditioned Krylov Subspace Iterative Solvers*, *ECMOR XIV - 14th European Conference on the Mathematics of Oil Recovery*. 2014. 10.3997/2214-4609.20141773.  
**Lukyanov, A. A.**, Chugunov, N., Sadovskii, V. M. and Sadovskaya, O. V., *Modelling of Irreversible Deformation near the Tip of a Crack in a Porous Domain Containing Oil and Gas*, *ECMOR XIV - 14th European Conference on the Mathematics of Oil Recovery*. 2014. 10.3997/2214-4609.20141808.
- **Lukyanov, A. A.**, *Meshless Upscaling Method and Its application to a Fluid flow in Porous Media*, *ECMOR XIII*. Biarritz. France. 2012.
- **Lukyanov, A. A.**, *Meshless Multi-Point Flux Approximations*, *AIP Conf. Proc.* 1479. 2012. PP. 1607-1610.
- **Lukyanov, A. A.**, *Meshless Multi-Point Flux Approximation of Fluid Flow in Porous Media*. SPE 141617-PP. *SPE Reservoir Simulation Symposium*. Woodlands. USA. 2011.
- **Lukyanov, A. A.**, *Meshless Upscaling Method and Its application to a Fluid flow in Porous Media*, *ECMOR XII*. Oxford. UK. 2010.

## PROBLEM FORMULATION AND SOLUTION METHODS

---

**I**N this chapter, initial and boundary conditions of dynamic problems of the continuum mechanics at different scale are presented briefly. The conservation laws of continuum mechanics (e.g., solid and fluid mechanics) are derived from the physical balance and conservation principals for a given control volume and are usually written in integral form. In the part of the control volume where physical quantities are sufficiently smooth, those conservation laws can be written in form of partial differential equations (PDEs). In the following sections, the governing equation for solid mechanics, fluid mechanics, and interacting particles are briefly described.

### § 1.1 General Remarks

---

Let us consider a medium  $\Omega$  in the space  $\mathbb{R}^n$ ,  $n = 2, 3$  with the boundary  $\Gamma$  at some moment of time  $t$ . The image of the body and boundary in the initial configuration can be denoted as  $\Omega_0, \Gamma_0$ . The initial configuration can also be called the reference configuration. The motion of the medium is described by the law

$$\mathbf{x} = \phi(\mathbf{X}, t), \phi \in C^1(\mathbb{R}^n), J = \det \left[ (\nabla_{\mathbf{X}} \otimes \mathbf{x})^T \right] \neq 0 \forall \mathbf{X}, t \quad (1.1)$$

where  $\mathbf{X}$  are the Lagrangian coordinates associated with the coordinate system moving with the medium,  $\mathbf{x}$  are the Euler coordinates associated with the fixed in space and in time coordinate system,  $J$  is the Jacobian of actual configuration at time  $t$ .

#### 1.1.1 Euler and Lagrangian Coordinates

The displacement of the material points can be defined using both Euler and Lagrangian coordinates  $\mathbf{X}$  and  $\mathbf{x}$  in the following form:

$$\mathbf{u}(\mathbf{X}, t) = \mathbf{x} - \mathbf{X} = \phi(\mathbf{X}, t) - \mathbf{X}, \mathbf{u}(\mathbf{x}, t) = \mathbf{x} - \mathbf{X} = \mathbf{x} - \phi^{-1}(\mathbf{x}, t) \quad (1.2)$$

The displacement field is commonly used in the formulation of governing equations of the solid mechanics (as it will be shown in the upcoming sections). The kinematic relations are used to describe the relations between material point coordinates (or displacement) and their velocities. The velocity field  $\mathbf{v}$  can also be defined using both coordinates  $\mathbf{X}$  and  $\mathbf{x}$  in the following form:

$$\frac{\partial \mathbf{x}}{\partial t} = \mathbf{v}(\mathbf{X}, t), \frac{d\mathbf{x}}{dt} = \mathbf{v}(\mathbf{x}, t) \quad (1.3)$$

The velocity field is usually used to construct the governing equations of the fluid mechanics.

### 1.1.2 Conservation Laws

The conservation laws can be written using three approaches: (a) fully Euler method (Euler formalism and Euler coordinates); (b) arbitrary Lagrangian-Euler method (Lagrangian formalism and Euler coordinates); (c) fully Lagrangian method (Lagrangian formalism and Lagrangian coordinates). In this thesis, the primary focus is devoted to (a) and (b). Below, the general form of the conservation laws is outlined as per work of [97]. Let  $f(x, t)$  be a physical quantity on the domain  $\Omega$ . Then for every control volume  $V$  we investigate the evolution of the integral

$$I(t) = \int_V f dV, \quad \dot{I} = \frac{\delta I(t)}{\delta t} \quad (1.4)$$

where control volume  $V$  can be fixed in space and time or can move with the medium,  $I$  is the extensive variable,  $\delta$  is the variational derivative.

There are two mechanism of changing a physical extensive quantity in time

$$\frac{\partial I}{\partial t} = P[I] + F[I], \quad P[I] = \int_V p[I] dV, \quad F[I] = - \int_{\partial V} \mathbf{j}[I] \cdot \mathbf{n} d\Sigma \quad (1.5)$$

where  $P[I]$  is the production of  $I$ ,  $p[I]$  is the sink/source of  $I$ ,  $F[I]$  is the flux of  $I$  through the boundary of the control volume  $\partial V$ ,  $\mathbf{j}[I]$  is the density flux of  $I$ ,  $\mathbf{n}$  is the external normal to the boundary  $\partial V$  of the control volume  $V$ . In case of a moving control volume  $V$  with the medium velocity field, the flux term naturally reduces to zero. It is possible now to formulate fundamental axiom of classical mechanics:

**Axiom 1.1.** *For all conservative physical quantities, the production term equals zero:*

$$P[I] = 0 \quad (1.6)$$

In continuum mechanics there are five fundamentals laws (axioms) written in integral form (1.5) and (1.6): (1) conservation law of mass, (2) conservation law of linear momentum (or impulse), (3) conservation law of angular momentum, (4) conservation of energy (first law of thermodynamics) and (5) second laws of thermodynamics (entropy evolution law).

### 1.1.3 Conservative Physical Quantities

The mass, linear momentum, angular momentum, and total energy are conservative physical quantities in classical mechanics. They have the following definitions.

**Definition 1.2.** *The total mass of a volume  $V \in \Omega$  at time  $t$  is given by,*

$$m_V(t) = \int_V \rho(\mathbf{x}, t) dV \quad (1.7)$$

where  $\rho(\mathbf{x}, t)$  is the medium density at time  $t$ .

**Definition 1.3.** *The total linear momentum (impulse) of a volume  $V \in \Omega$  at time  $t$  is given by,*

$$\mathbf{P}_V(t) = \int_V \rho \mathbf{v}(\mathbf{x}, t) dV \quad (1.8)$$

where  $\mathbf{v}(\mathbf{x}, t)$  is the medium velocity field at time  $t$ .

**Definition 1.4.** *The total linear momentum (impulse) of a volume  $V \in \Omega$  at time  $t$  is given by,*

$$\mathbf{M}_V(t) = \int_V \rho \mathbf{v}(\mathbf{x}, t) \times \mathbf{x} dV \quad (1.9)$$

where  $\mathbf{v}(\mathbf{x}, t) \times \mathbf{x}$  is the specific angular momentum field at time  $t$ .

**Definition 1.5.** *The total energy of a volume  $V \in \Omega$  at time  $t$  is given by,*

$$\mathcal{E}_V(t) = \int_V \rho \left( e + \frac{\mathbf{v}^2}{2} \right) dV \quad (1.10)$$

where  $e$  is the specific internal energy at time  $t$ .

## § 1.2 Solid Mechanics Description

---

Let us consider a system  $\Upsilon$ , which consists of  $N$  bodies in  $\mathbb{R}^n$ ,  $n = 2, 3$  in the Cartesian coordinate system. Each of the bodies has volume  $V_i^0$ , mass  $m_i$  and initial velocity of the centre of mass  $U_i^0$ . In this work, high velocity impact problems are considered. From the mechanical point of view, impact is a process of elements interaction of this system as a consequence of presence of different velocities of the centre mass of bodies. At the same time, generally speaking at the macroscopic level, we can assume that any of the system bodies can be described as a deformable or as a rigid body. The coordinate system can be chosen connected with one of the bodies of system  $\Upsilon$ , so that this body lies upon this coordinate system, and this body will be called target and all others will be called flyers. Naturally, due to differences between relative flyers velocities, they can interact with each other and, therefore, for each case the aforementioned terminology can be applied. Governing equations (conservations laws) of the problem with the finite deformations will be presented in the Lagrangian formalism. We assume that there are no mass forces, internal moments (monopolar medium), and mass heat sources.

### 1.2.1 Conservation Laws

The conservation law of mass in the Lagrangian coordinates describes the fact that mass of a control volume stays the same from configuration to configuration, i.e.,  $m_{V_0}(t) = m_V(t)$ . Furthermore, the basic conservation laws can be formulated as the following theorem.

**Theorem 1.6.** *The conservation law of mass in Lagrangian coordinates is given by,*

$$\rho \cdot J = \rho_0 \cdot J_0 \quad (1.11)$$

where  $J_0$ ,  $J$  is the Jacobian of reference and actual configurations respectively.

**Theorem 1.7.** *The conservation law of linear momentum in Lagrangian coordinates is given by,*

$$\ddot{\mathbf{u}} = \frac{1}{\rho_0} \nabla_0 \cdot \mathbf{P} \quad (1.12)$$

where  $\mathbf{u}$  is the displacement vector,  $\rho_0$  is the density in the reference configuration,  $\mathbf{P}$  – Lagrangian stress tensor (or I-st Piola-Kirchhoff stress tensor).

In this research, the irreversible deformation process of the medium is considered under impact loading. In this case, the characteristic time of the process is about several  $\mu s$ . Therefore, the process can be considered as adiabatic:  $\nabla_0 \mathbf{q} = 0$ , where  $\mathbf{q}$  is the heat flux vector.

**Theorem 1.8.** *The conservation law of linear momentum in Lagrangian coordinates is given by,*

$$\dot{e} = \frac{1}{\rho_0} \dot{\mathbf{F}} : \mathbf{P}, \quad (1.13)$$

where  $\rho_0$  is the density in the reference configuration,  $\mathbf{P}$  is the Lagrangian stress tensor (or I-st Piola-Kirchhoff stress tensor),  $\mathbf{F}$  is the deformation gradient.

### 1.2.2 Mathematical Models of Failure. Damage Mechanics

For the description of the dynamic process of material fracture, the theory of continuum fracture (damage mechanics), which was developed in the researches of L. M. Kachanov (1958) [126], Yu. N. Rabotnov (1959) [225], is used in this thesis. During the past decades the constitutive modelling of damage materials in finite deformation ranges has received considerable attention, as can be seen from a large number of

bibliographies, reviews and discussions given, for example, by Kachanov (1958, 1969, 1974, 1986) [126], [127], [128] [129], Rabotnov (1959, 1963) [225], [226], Il'ushin (1967) [114], Murakami and Radayev (1994, 1996) [228], [227], Chaboche (1984, 1988) [50], [51], [52], Krajcinovic (1996) [148], Lemaitre (1996) [159], Lemaitre and Chaboche (1990) [160], Murakami (1983, 1987) [215], [216], Maugin (1992) [198], Voyiadjis and Kattan (1992) [266], Brunig (2003) [44], Baste and Audoin (1991) [22], Bamman and Aifantis (1987) [18], Betten (1983) [31], Chow and Wang (1987) [63], Tvergaard (1981, 1982, 1990) [254], [255], [256], Tvergaard and Needleman (1984) [258], Tvergaard and Hutchinson (2002) [257].

The development of damage mechanics was originated in the papers of Kachanov (1958) [126] and Rabotnov (1963) [226], dealing with theory of creep within materials, where one scalar damage parameter  $\omega$  and the concept of effective stress  $\tilde{\sigma}' = \frac{\tilde{\sigma}}{1-\omega}$  were introduced and developed. This has been the starting point of continuous damage mechanics and was developed further for dissipation and low cycle fatigue in metals Lemaitre (1996) [159], for coupling between damage and creep Leckie and Hayhurst (1977) [153], between damage and cycle creep Hult (1974) [159], for high cycle fatigue Chaboche (1974) [158], for creep fatigue interaction Lemaitre-Chaboche (1990) [160]. Later on, scalar valued damage variables have been proposed also by among many other authors. Krajcinovic and Fonseka (1981) [150], [149] and Krajcinovic (1983) [147] employed an axial vector representation that keeps to the concept of isotropic damage that its magnitude signifies the projected area density of planar microvoids onto a given cross-section defined by its normal which is defined as an average of the direction normal to the microcracks distributed over a representative volume element. Hence, vectors only seem to be adequate for a family of microcracks all with the same orientation.

To be able to take into account different damage mechanism, second order damage tensors have been proposed by Il'ushin (1967) [114] and later by Kachanov (1986) [129], Murakami and Ohno (1981) [219], Betten (1982, 1983) [30], [31], Krajcinovic (1983) [147], Chow and Wang (1987) [63], Murakami (1988) [218], Ju (1990) [124], Lu and Chow (1990) [178], Baste and Audoin (1991) [22], Voyiadjis and Kattan (1992) [266], Bruhns and Schiesse (1996) [43], and Steinmann and Carol (1998) [242], and fourth order rank damage tensors were already introduced, for example, in the anisotropic creep damage modelling by Chaboche (1984) [50]. Furthermore, various order damage tensors and their relationship to some typical two- and three-dimensional crack density distributions were analyzed by Lubarda and Krajcinovic (1993) [179].

In contrast to the concept of effective stress, there exists a wide range of damage theories proposed in literature, e.g. *the strain equivalence* used by Lemaitre (1996, 1990) [159], [158] and Ju (1989) [123], *the strain energy equivalence* proposed by Voyiadjis and Kattan (1992) [266], Steinmann and Carol (1998) [242] or *the stress working equivalence* introduced by Lu and Chow (1990) [178] to be able to couple damage and elasticity in their constitutive relation. An overview and classification of available models considering a local approach of fracture are given by Lemaitre (1996) [159]. Thermodynamics of irreversible processes provided the necessary scientific basis to justify continuous damage mechanics as a theory Chaboche (1978), Lemaitre-Chaboche (1978) (see, Lemaitre (1992) [158]), Murakami (1981) [219], Krajcinovic and Fonseka (1981) [149], [150], Lemaitre (1985) [158]. Several continuum damage models in terms of the framework of continuum thermodynamics have been proposed which are nowadays either phenomenological or micro-mechanically based, see Brunig (2003) [44] an overview.

### 1.2.3 Damage Parameters. Effective Stresses

Application of the "Kachanov – Rabotnov model" to the mathematical modelling of processes of damage accumulation can be simply demonstrated using one dimensional damage state of the uniaxial stretched specimen (see, [10], [128], [129], [148], [159]). In accordance with the classical Kachanov – Rabotnov theory, the current damage state of the stretched specimen can be described using a single scalar parameter (damage parameter)  $\omega$ , which represents a monotone increasing function (for some models, it will be shown later, this condition is not satisfied) of time  $0 \leq \omega \leq 1$ , at the same time, it is assumed that  $\omega = 0$  – for initial undamaged state and  $\omega = 1$  – for the final state of fracture (macrofracture). Usually, the damage parameter  $\omega$  is interpreted as a relative reduction of effective carried out loading cross section of a specimen due to damage initiation and propagation (see, [10], [128], [129], [150], [159]):

$$1 - \omega = \frac{\mathcal{S}^*}{\mathcal{S}}, \quad (1.14)$$

where  $\mathcal{S}$  is the original cross section,  $\mathcal{S}^*$  is the effective cross section. This leads to the introduction of the effective stress concept mentioned above

$$\sigma^* = \frac{\sigma}{1 - \omega}, \quad (1.15)$$

Equation(1.15) describes the effect of stress increasing within damaged material, where  $0 \leq \omega \leq 1$  (see, [128], [129]). Hence, the mechanical state of the virtual undamaged specimen's fully equivalent to the current state of the damaged specimen, and change of geometry's fully described by the damage parameters  $\omega$ .

At the same time, there is another interpretation of the damage parameter suggested, for example, by Kiselev (1998, 1992) [141], [139], Kiselev and Lukyanov (2002) [140], Lukyanov (2004) [182], Barder *et al.* (1972) [20], Carroll and Holt (2003) [49], Cocks (1989) [68], Cortes (1992) [70], Curran *et al.* (1987) [73], where it is assumed to consider the damage parameter as a characteristic of the volume fraction of the microvoids (pores within material)  $\omega$ , and the damage parameter represents monotone function of time  $0 \leq \omega \leq 1$ .

In this work, the damage model is considered where the damage parameter can increase and decrease, therefore, the effect of microvoids collapse (or microvoids treatment) is taken into account. Similar to the classical case it is assumed that  $\omega = 0$  – for the initial undamaged state and the damage parameter  $\omega$  is always less than 1. Besides, damage parameter  $\omega$ , according to its physical definition can be expressed in the following form:

$$\omega = \frac{V^*}{V}, \quad (1.16)$$

where  $V$  – a physical elementary volume (here it is assumed that an elementary volume should be interrelated in terms of conventional continuum mechanics approach),  $V^*$  – the volume of micropores in the physical elementary volume  $V$ . Three types of the damage process will be considered: (1) brittle, (2) ductile, (3) adiabatic shear bands [139], [182]. Therefore, the following invariants of the damage tensor (first and second damage parameters) are considered  $\omega_{ij}$ : first invariant  $\omega = \omega_{kk}/3$  – volumetric damage and  $\alpha = \sqrt{\omega'_{ij}\omega'_{ij}}$  – intensity of the deviatoric part of the damage tensor, where  $\omega'_{ij} = \omega_{ij} - (\omega_{kk}/3)\delta_{ij}$ . Besides, it is assumed that parameter  $\omega = \omega_{kk}/3$  describes the accumulation micropore type of damage, which can collapse during the compression, and  $\alpha$  describes the shear damage (fracture).

Exact analytical description of the damaged state of the medium is a difficult and complex problem due to the fact that during the solution of this problem, the following effects must be taking into account: microcrack orientation, microcrack interaction, etc. At this moment, there are many damage models including damage models for anisotropic materials, e.g. [10], [145], [216] [44], [45], [148], [159], [198], [179].

## 1.2.4 Description of Existing Damage Models

Fracture of many materials is a result of void nucleation, growth and coalescence. Due to sizable difference between the characteristic length scales involved in the material failure process and the dimensions of the actual structural component, it is impractical to model every void in detail in structure failure analysis, especially for situations involving extensive crack propagation. For this reason, various forms of porous material models have been developed to describe void growth and the associated macroscopic softening during the fracture process.

Many theoretical damage models, both empirical and micro-physical in nature, have been developed to describe and predict fracture. These include the *Cochran-Banner* (CB) model [67], the *void growth* (VG) model [120], the *DFRACT* model [73], the *Johnson-Cook* model [118], the *Davison-Stevens* model [75], the *Bai* model [15]. Some models are stress-threshold dependent, while others are strain-threshold dependent. These models usually compute the void volume in the region of fracture to quantify the damage level.

In conclusion, it is important to mention a straight-forward approach to simulate ductile failure processes based on the explicit introduction of individual voids by Aravas and McMeeking (1985) [8], [9], Tvergaard and Hutchinson (2002) [257], Kim *et al.* (2003) [137], and Gao *et al.* (2005) [95]. A distinct advantage of this approach is the ability for exact implementation of void growth behavior.

## 1.3.1 Conservation Laws

In this section let  $V$  be a control volume in  $\mathbb{R}^3$  ( $V \subset \Omega \subset \mathbb{R}^3$ ) and  $\partial V \subset \mathbb{R}^2$  a hyper-surface representing the boundary of  $V$ , and let the time  $t \in T \subset \mathbb{R}^+$ . The transition from the integral form to the differential form can be performed using Reynolds Transport Theorem.

**Theorem 1.9.** (*Reynolds Transport Theorem*). *Let  $f(\mathbf{x}, t)$  be a smooth quantity (scalar or vector) on the domain  $\Omega$ . Then for every control volume  $V(t) \in \Omega$  moving with the medium which have velocity field  $\mathbf{v}$ , we have*

$$\frac{d}{dt} \int_{V(t)} f d\mathbf{x} = \int_{V(t)} \left( \frac{\partial f}{\partial t} + \nabla \cdot (\mathbf{v}f) \right) d\mathbf{x} \quad (1.17)$$

*Proof.* This theorem can be derived using Leibniz integral rule applied to the integral with variable integration limits. The proof is given in [237].

The *conservation law of mass* is defined as per axiom (1.6) and (1.5) by

$$\frac{dm_V(t)}{dt} = \frac{d}{dt} \int_{V(t)} \rho d^3\mathbf{x} = 0 \quad (1.18)$$

where  $\rho$  is the mass density. Applying the Reynolds transport Theorem 1.9 to  $f = \rho$ , the continuity equation in integral form for Lagrangian formalism and Euler coordinates can be derived as:

$$\frac{d}{dt} \int_{V(t)} \rho d\mathbf{x} = \int_{V(t)} \left( \frac{\partial \rho}{\partial t} + \nabla \cdot (\mathbf{v}\rho) \right) d^3\mathbf{x} \quad (1.19)$$

On the other hand, due to the principle of conservation of mass, the mass in a control volume must be conserved, thus the left-hand side is zero. Since equation (1.19) holds for any control volume, one obtains the continuity equation in differential form:

$$\frac{\partial \rho}{\partial t} + \nabla \cdot (\rho\mathbf{v}) = 0 \quad (1.20)$$

In the case of ALE, the material derivative or substantial derivative is defined as

$$\frac{Df}{Dt} = \frac{\partial f}{\partial t} + \mathbf{v}(\mathbf{x}, t) \cdot \nabla f \quad (1.21)$$

Using definition (1.21) of the material derivative, the equation can be written as:

$$\frac{D\rho}{Dt} + \rho \nabla \cdot \mathbf{v} = 0 \quad (1.22)$$

The following corollary of the Reynolds Transport Theorem (1.9) can be formulated:

**Corollary 1.10.** *Let  $f(\mathbf{x}, t)$  be a smooth quantity (scalar or vector) on domain  $\Omega$ , and let  $\rho$  be a mass density satisfying the continuity equation. Then for every control volume  $V(t)$  we have*

$$\frac{d}{dt} \int_{V(t)} \rho f d\mathbf{x} = \int_{V(t)} \rho \frac{Df}{Dt} d\mathbf{x} \quad (1.23)$$

*Proof.* Due to conservation law of mass (1.18) for any control volume (including elementary control volume), the following steps can be performed:

$$\frac{d}{dt} \int_{V(t)} \rho f d\mathbf{x} = \frac{d}{dt} \int_{m_V(t)} f dm = \int_{m_V(t)} \frac{Df}{Dt} dm = \int_{V(t)} \rho \frac{Df}{Dt} d^3\mathbf{x} \quad (1.24)$$

where  $dm = \rho d^3\mathbf{x}$  is the element of  $m_V(t)$ .

The *conservation law of linear momentum* can be written as

$$\frac{d}{dt} \int_{V(t)} \rho \mathbf{u} d^3\mathbf{x} = \frac{D}{Dt} \int_{V(t)} \frac{D\mathbf{u}}{Dt} = \int_{V(t)} \rho \mathbf{b} d^3\mathbf{x} + \int_{\partial V(t)} \boldsymbol{\sigma} \cdot \mathbf{n} d^3\mathbf{x} \quad (1.25)$$

where  $\mathbf{b}$  contains the body forces,  $\boldsymbol{\sigma} = (\sigma_{ij})$  contains the surface forces, which act through the surface of the control volume  $V(t)$ , such as pressure and stress.

### § 1.3 Fluid Mechanics Description

Let us consider a domain  $\Omega$  in  $\mathbb{R}^n$ ,  $n = 2, 3$  with boundary  $\Gamma$  occupied with a fluid. The fluid velocity and density fields are denoted by  $\mathbf{v}(\mathbf{x}, t)$  and  $\rho(\mathbf{x}, t)$ . An important step is to formulate the governing equations in PDE form which is based on conservation laws which are described in the next section.



### 1.3.2 Constitutive Relations

The stress tensor  $\sigma_{ij}$  is typically decomposed into a pressure part and a viscous part. The important cases result from the specific assumptions on the viscous stress tensor and velocity field. The following cases will be considered in this work:

#### *Ideal fluid flow*

No viscous forces are acting between two layers of fluid. This leads to the following definition.

**Definition 1.11.** *The constitutive relation of an ideal fluid is defined by*

$$\tau_{ij} = 0 \quad (1.26)$$

This definition leads to the Euler equations using the ALE framework

$$\frac{d\rho}{dt} + \rho \nabla \cdot \mathbf{v} = 0 \quad (1.27)$$

$$\rho \frac{d\mathbf{v}}{dt} = -\nabla p + \rho \mathbf{b} \quad (1.28)$$

The Euler equations are typically closed by an equation of state.

#### *Navier-Stokes fluid flow*

In this case, there are viscous forces acting between two layers of fluid. This leads to the following definition.

**Definition 1.12.** *The constitutive relation of Navier-Stokes fluid is defined by*

$$\tau_{ij} = \lambda (\nabla \cdot \mathbf{v}) \delta_{ij} + 2\mu v_{ij} \quad (1.29)$$

where  $\lambda > 0$  and  $\mu > 0$  are viscous parameters,  $v_{ij}$  is the strain rate tensor.

This definition leads to the Navier-Stokes equations using ALE framework

$$\rho \frac{d\mathbf{v}}{dt} = -\nabla p + (\lambda + \mu) \nabla (\nabla \cdot \mathbf{v}) + \mu \Delta \mathbf{v} + \rho \mathbf{b} \quad (1.30)$$

The fluid flow is called to be incompressible if

$$\nabla \cdot \mathbf{v} = 0 \quad (1.31)$$

In the case of incompressible fluid flow, the governing equations (1.30) reduce to

$$\rho \frac{d\mathbf{v}}{dt} = -\nabla p + \mu \Delta \mathbf{v} + \rho \mathbf{b} \quad (1.32)$$

The incompressibility condition has closed the system of equations (1.31) leading to the differential algebraic equations:

$$\begin{aligned} \rho \frac{d\mathbf{v}}{dt} &= -\nabla p + \mu \Delta \mathbf{v} + \rho \mathbf{b}, \\ \nabla \cdot \mathbf{v} &= 0 \end{aligned} \quad (1.33)$$

The pressure  $p$  is the Lagrangian multiplier to satisfy the incompressibility condition.

#### *Darcy fluid flow*

**Definition 1.13.** *The constitutive relation of Darcy fluid flow is defined by*

$$\mathbf{v} = -\frac{\mathbf{K}}{\mu} \nabla p \quad (1.34)$$

where  $\mathbf{K}$  is the permeability tensor,  $\mu > 0$  is the viscosity.

## § 1.4 Boundary and Initial Conditions

The selection of appropriate boundary conditions is an important step to describe physical phenomena. In this work, the high velocity impact of different bodies and at different scales (e.g., plate impact test, shock wave propagation in nanotubes) and fluid flow in porous media are considered. Hence, the boundary conditions for these problems are described below.

### 1.4.1 Solid Mechanics Boundary Conditions

A system  $\Upsilon$ , which consists of  $N$  bodies in  $\mathbb{R}^n$ ,  $n = 2, 3$  in a Cartesian coordinate system is considered. Each of the bodies has volume  $V_\gamma^0$ , mass  $m_\gamma$  and initial velocity of the centre of mass  $U_\gamma^0$  and piecewise boundary  $\partial V_\gamma^0 = \Gamma_{\gamma 0}$ , where measure  $mes(\Gamma_{\gamma 0}) > 0$ . The boundary conditions are written in the following form for  $t \geq 0$ :

$$\begin{aligned}
 \mathbf{X} \in \Gamma_{\gamma 0}^{un} : \mathbf{u}(\mathbf{X}, t) \cdot \mathbf{n}^0(\mathbf{X}, t) &= \bar{u}_{\gamma n}(\mathbf{X}, t), \\
 \mathbf{X} \in \Gamma_{\gamma 0}^{tn} = \Gamma_{\gamma 0} \setminus \Gamma_{\gamma 0}^{un} : (\mathbf{P}(\mathbf{X}, t) \cdot \mathbf{n}^0(\mathbf{X}, t)) \cdot \mathbf{n}^0(\mathbf{X}, t) &= P_n^\gamma, \\
 \mathbf{X} \in \Gamma_{\gamma 0}^{u\tau} : \mathbf{u}(\mathbf{X}, t) \cdot \boldsymbol{\tau}(\mathbf{X}, t) &= \bar{u}_{\gamma \tau}(\mathbf{X}, t), \\
 \mathbf{X} \in \Gamma_{\gamma 0}^{t\tau} = \Gamma_{\gamma 0} \setminus \Gamma_{\gamma 0}^{u\tau} : (\mathbf{P}(\mathbf{X}, t) \cdot \mathbf{n}^0(\mathbf{X}, t)) \cdot \boldsymbol{\tau}(\mathbf{X}, t) &= P_\tau^\gamma, \\
 \mathbf{X} \in \Gamma_{\gamma 0}^T : T(\mathbf{X}, t) &= \bar{T}(\mathbf{X}, t), \\
 \mathbf{X} \in \Gamma_{\gamma 0}^q = \Gamma_{\gamma 0} \setminus \Gamma_{\gamma 0}^T : \mathbf{q}(\mathbf{X}, t) \cdot \mathbf{n}^0(\mathbf{X}, t) &= \bar{q}(\mathbf{X}, t)
 \end{aligned} \tag{1.35}$$

where  $\bar{u}_{\gamma n}(\mathbf{X}, t)$  – normal displacement at  $\Gamma_{\gamma 0}^{un}$ ,  $\bar{u}_{\gamma \tau}(\mathbf{X}, t)$  – tangent displacement at  $\Gamma_{\gamma 0}^{u\tau}$ ,  $P_n^\gamma$  – normal stress at  $\Gamma_{\gamma 0}^{tn}$ ,  $P_\tau^\gamma$  – tangent stress at  $\Gamma_{\gamma 0}^{t\tau}$ ,  $\bar{T}(\mathbf{X}, t)$  – given temperature at  $\Gamma_{\gamma 0}^T$ ,  $\bar{q}(\mathbf{X}, t)$  – given heat flux at  $\Gamma_{\gamma 0}^q$ , and  $\mathbf{n}^0(\mathbf{X}, t)$  – external normal to the boundary of an initial configuration,  $\boldsymbol{\tau}(\mathbf{X}, t)$  – tangent vector to the boundary of an initial configurations. The domain boundary  $\Gamma_{\gamma 0}$  is divided into no overlapping classes:

$$\begin{aligned}
 \bar{\Gamma}_{\gamma 0}^{tn} \cup \bar{\Gamma}_{\gamma 0}^{un} &= \Gamma_{\gamma 0}, \quad \Gamma_{\gamma 0}^{tn} \cap \Gamma_{\gamma 0}^{un} = \emptyset, \\
 \bar{\Gamma}_{\gamma 0}^{t\tau} \cup \bar{\Gamma}_{\gamma 0}^{u\tau} &= \Gamma_{\gamma 0}, \quad \Gamma_{\gamma 0}^{t\tau} \cap \Gamma_{\gamma 0}^{u\tau} = \emptyset
 \end{aligned} \tag{1.36}$$

where  $\gamma = 1, \dots, N$  – body index. Initial conditions at  $t = 0$  have a form:

$$\begin{aligned}
 \mathbf{X} \in \Omega_{\gamma 0} : \mathbf{x} = \mathbf{X}, \mathbf{v}(\mathbf{X}, t) &= \mathbf{v}_0(\mathbf{X}), \quad \tilde{\varepsilon}^e(\mathbf{x}, t) = \tilde{\varepsilon}_0^e(\mathbf{X}), \\
 \mathbf{X} \in \Omega_{\gamma 0} : \tilde{\varepsilon}^p(\mathbf{x}, t) &= \tilde{\varepsilon}_0^p(\mathbf{X}), \quad T(\mathbf{X}, t) = T_0(\mathbf{X}), \\
 \mathbf{X} \in \Omega_{\gamma 0} : \phi(\mathbf{X}, t) &= \phi_0(\mathbf{X}), \quad \psi(\mathbf{X}, t) = \psi_0(\mathbf{X})
 \end{aligned} \tag{1.37}$$

where  $\mathbf{v}_0(\mathbf{X})$  – initial velocity,  $\tilde{\varepsilon}_0^e(\mathbf{X})$  – initial elastic deformation,  $\tilde{\varepsilon}_0^p(\mathbf{X})$  – initial plastic deformation,  $T_0(\mathbf{X})$  – initial temperature,  $\phi_0(\mathbf{X})$  and  $\psi_0(\mathbf{X})$  – initial values for the internal state variables describing continual fracturing of the media.

### 1.4.2 Porous Media Fluid Mechanics Boundary Conditions

Let  $\Omega$  be a bounded domain in  $\mathbb{R}^n$ ,  $n = 1, 2, 3$  with a piecewise boundary  $\partial\Omega = \bar{\Gamma}_D \cup \bar{\Gamma}_N, \Gamma_D \cap \Gamma_N = \emptyset$ , where measure  $mes(\bar{\Gamma}_D \cup \bar{\Gamma}_N) > 0$ . The problem discussed in this work is related to fluid flow in porous media leading to the following Dirichlet and Neumann boundary conditions respectively:

$$p(\mathbf{x}) = p_0(\mathbf{x}) \text{ for } \mathbf{x} \in \Gamma_D \tag{1.38}$$

and

$$\mathbf{n}(\mathbf{x})^T \frac{\mathbf{K}(\mathbf{x})}{\mu(\mathbf{x})} \nabla p(\mathbf{x}) = q(\mathbf{x}) \text{ for } \mathbf{x} \in \Gamma_N \tag{1.39}$$

where  $p(\mathbf{x})$  is the pressure,  $\mathbf{K}(\mathbf{x})$  is the piecewise constant permeability tensor,  $\mu(\mathbf{x})$  is the fluid viscosity,  $\mathbf{n}(\mathbf{x})$  is the given outward unit normal on piecewise boundary  $\partial\Omega = \bar{\Gamma}_D \cup \bar{\Gamma}_N$ ,  $p_0(\mathbf{x})$  is the boundary pressure,  $q(\mathbf{x})$  is the boundary flux,  $n = 1, 2, 3$  is the spatial dimension.

## § 1.5 Numerical Methods

In many modern investigations, phenomenological models of, for example, continual fracture mechanics or fluid mechanics are coupled with numerical algorithms and its realizations into one mechanism. Numerical modelling of different physical processes can be realized by several numerical methods such as finite difference method (FDM), finite volume method (FVM), finite element method (FEM), and smoothed particle hydrodynamic method (SPH). In the current research, the smoothed particle hydrodynamic method (SPH) (see, e.g., [12], [14], [230], [27]) will be used. Special attention will be paid to the modelling of the fracture process which can be realized differently. In the current work, the macrofracture is modelled by the element erosion algorithm, where the criterion of macrofracture is realized. In the following subsection a brief description of the smoothed particle hydrodynamic method is presented.

### 1.5.1 Smoothed Particle Hydrodynamic Method

The objective of this section is to introduce basic steps governing the formalism of smoothed particle hydrodynamics SPH. The first basic idea behind the SPH method is that any physical variable field is smoothed over spatial domain by using appropriate smoothing kernels. Let  $V$  be a spatial domain in  $\mathbb{R}^n$ ,  $n = 1, 2, 3$  ( $V \subset \mathbb{R}^n$ ) and  $\partial V$  a hyper-surface (regular in all points) representing the boundary of  $S \subset \mathbb{R}^2$ , and let the time  $t \in T \subset \mathbb{R}^+$ . The smoothed value of any conservative physical field  $\rho(\mathbf{x}, t) \cdot \varphi(\mathbf{x}, t)$  according to the SPH methodology can be written as:

$$\langle \rho \cdot \varphi(\mathbf{x}, t) \rangle = \int_T \int_V \Gamma(t - t', \tau) W(\mathbf{x} - \mathbf{x}'(t'), h) \cdot \rho(\mathbf{x}', t') \cdot \varphi(\mathbf{x}', t') d^3 \mathbf{x}' dt', \quad (1.40)$$

where  $\rho(\mathbf{x}, t)$  represents the density,  $\varphi(\mathbf{x}, t)$  describes a physical quantity,  $\mathbf{x}$  and  $\mathbf{x}'$  are the position vectors in  $\mathbb{R}^n$ ,  $T > 0$  is spatial time domain,  $(t, t') \in [0, T] \times [0, T]$ , where  $[0, T]$  denotes time interval. Function  $W$  represents an appropriate positive radial kernel with a single maximum and compact support  $D_W^h \equiv \text{supp}(W)$ . The parameter  $h$  is a geometrical parameter that characterises  $D_W^h \equiv \text{supp}(W)$ .

The smoothing kernel should satisfied the following properties:

1. *Normalisation condition:*

$$\int_V W(\mathbf{x} - \mathbf{x}', h) d^3 \mathbf{x}' = 1 \quad (1.41)$$

2. *Dirac limit condition:*

$$\begin{aligned} \psi(\mathbf{x}, t) &= \lim_{h \rightarrow 0} \int_V \psi(\mathbf{x}', t) W(\mathbf{x} - \mathbf{x}', h) d^3 \mathbf{x}' = \\ &= \int_V \psi(\mathbf{x}', t) \delta(\mathbf{x} - \mathbf{x}') d^3 \mathbf{x}', \text{ for } \forall \psi(\mathbf{x}', t) \in \mathbf{L}_2, \end{aligned} \quad (1.42)$$

where  $\delta(\mathbf{x} - \mathbf{x}')$  is Dirac delta functional.

Function  $\Gamma(t)$  represents a temporal kernel having the same properties as  $W$  and introduces the smoothing with respect to time. In this work, a spatial discretisation is considered, therefore,  $\Gamma(t - t', \tau) \equiv \delta(t - t')$  is assumed. Thus, relation (1.40) transforms to a spatial convolution:

$$\langle \rho \cdot \varphi(\mathbf{x}, t) \rangle = \int_V W(\mathbf{x} - \mathbf{x}'(t), h) \cdot \rho(\mathbf{x}', t) \cdot \varphi(\mathbf{x}', t) d^3 \mathbf{x}' \quad (1.43)$$

The second important step in SPH formulation is that a continuum  $\Omega$  is introduced as a set of  $N$  discrete interacting particles with masses  $m_1, m_2, \dots, m_i, \dots, m_N$ . Let's introduce notations for the value of any non-conservative field of particle  $i$  located at discrete position  $(\mathbf{x}_i, t) \in V \times [0, T]$  as  $\varphi_i(t) = \varphi_i(\mathbf{x}_i, t)$ . Hence, for

any point  $((\mathbf{x}, t) \in V \times [0, T])$  the continuous form of the smoothed value is estimated by summation over all particles  $i \in M$ .

$$\langle \rho \cdot \varphi(\mathbf{x}, t) \rangle = \sum_{i \in M} m_i \cdot \varphi_i \cdot W(\mathbf{x} - \mathbf{x}_i, h), \quad (1.44)$$

where

$$m_i = \rho(\mathbf{x}_i, t) \cdot d^3 \mathbf{x}_i(t), \quad \forall t \in [0, T] \quad (1.45)$$

The particle mass  $m_i$  is defined by the introduction of the control volume (or Lumped volume) for each particle.

### 1.5.2 Numerical Time Integration

The governing equations after applying spatial SPH discretization can be written as

$$\frac{d\mathbf{U}}{dt} = \mathbf{L}(\mathbf{U}) \quad (1.46)$$

where  $\mathbf{U}$  is the state vectors containing all primary physical quantities,  $\mathbf{L}$  is the spatial SPH discretization. Equation (1.46) can be solved by the Runge-Kutta method of arbitrary order of accuracy (in the case of temporal explicit SPH discretization), which can be obtained by the formulae

$$\begin{aligned} \mathbf{U}^{(0)} &= \mathbf{U}^{(n)}, \\ \mathbf{U}^{(i)} &= \mathbf{U}^{(i-1)} + \frac{1}{2} dt \cdot \mathbf{L}(\mathbf{U}^{(i-1)}), \quad i = 1, \dots, m-1 \\ \mathbf{U}^{(m)} &= \sum_{k=0}^{m-2} \alpha_{m,k} \mathbf{U}^{(k)} + \alpha_{m,m-1} \left( \mathbf{U}^{(m-1)} + \frac{1}{2} dt \cdot \mathbf{L}(\mathbf{U}^{(i-1)}) \right), \\ \mathbf{U}^{(n+1)} &= \mathbf{U}^{(m)}, \end{aligned} \quad (1.47)$$

At the start of a time step  $t^n$  the following physical quantities  $\mathbf{U}^{(n)}$  are known. In most of the SPH simulations for fluid and solid mechanics problems  $m = 1$  (i.e., central difference method in time [27]). However, higher order time integration scheme can be used by setting  $m = 4$  and taking  $\alpha_{m,k}$  as  $\alpha_{4,0} = 0$ ,  $\alpha_{4,1} = \frac{2}{3}$ ,  $\alpha_{4,2} = 0$ ,  $\alpha_{4,3} = \frac{1}{3}$ .

## § 1.6 Conclusion

In this chapter, a general formulation of boundary value problems including conservation laws of continuum mechanics with different types of boundary conditions have been discussed. In addition, a critical review of the currently available approaches in damage mechanics have also been presented, including numerical methods. It was observed that all prior micro- or macro- level models are decoupled from the rest of physical processes. Consequently, most of the current models are constructed based on a stress-strain relation and different types of damage evolution equations. The review focuses on the implications of the damage mechanics concept to the description of material failure, the assumption of material homogeneity and thermodynamically consistent links between state variables, and the requirements imposed on the model construction. A general formulation of thermodynamically consistent models is then constructed. In particular, the mechanics and thermodynamic aspects in the model formulation are examined within the confines of continuum mechanics.

---

## SPH FORMULATION

---

A brief overview of particle method (SPH-method) concept, which is fundamental for all meshless method is given in this chapter. A more detailed overview of different meshless methods can be found in monographs: Li and Liu (2003) [164], Liu and Liu (2004) [173]. A comprehensive overview on meshless methods can be found in the papers of Belytschko *et al.* (1996) [25]. In the monograph on meshless methods by Liu (2002) [169], there is a large portion devoted to the history, theory, and applications of the existing meshless methods.

Various authors use different ways of constructing the same discretized governing equations applying SPH method. In this chapter, we will show only one way of constructing an approximation for our governing partial differential equations (PDEs) mainly related to solid and fluid dynamics. The SPH discretization for the fluid flow in porous media will be addressed in the following chapters.

### §2.1 Introduction

---

A strong interest has been shown in the last 30 years in the development of next generation numerical methods (e.g., meshless methods), which should, as expected, improve mesh dependent numerical methods (e.g., FEM, FDM, and FVM) for a large variety of applications. Smoothed particle hydrodynamics (SPH) as well as other meshless methods are developed a few decades ago to model inviscid fluid / gas dynamics in astrophysical problems (Lucy, 1977 [181]; Gingold and Monaghan, 1977 [96]); Monaghan, 1982 [208]; Monaghan, 1992 [209]) and later were adopted for solving continuum mechanics problems and fluid mechanics problems. The main idea of the meshless method consists of providing a stable and accurate solution of either integral or partial differential equations for any types of boundary conditions and particle distributions without using any type of mesh which provides connectivity between nodes or particles.

#### 2.1.1 SPH Method

The numerical technique known as SPH is a meshless method of Lagrangian nature for solving the governing equations of continuum media (e.g., fluid, gas and solids) dynamics in which the particles correspond to a small representative volume of fluid / solid. Hence, SPH is an interpolation-based numerical technique that can be used to solve systems of partial differential equations (PDEs). The Lagrangian particle nature of SPH allows physical and chemical effects to be incorporated into the modeling of flow / solid mechanics processes with

---

relatively little code-development effort. In addition, geometrically complex and / or dynamic boundaries and interfaces can be handled without undue difficulty. The term "smoothed" refers to the procedure for calculating state variables, such as density, velocity, and gradient of deformation, in which the function value at a point is determined as a weighted average of values in a local region. As a result, for example, the distribution of particles for conventional Lagrangian description is sparse in regions where density is low and dense in regions where density is high. Note that for fluids / gases or solids with non-trivial boundaries there is the incompleteness of the kernel support combined with the lack of consistency of the kernel interpolation in conventional meshless methods which results in fuzzy boundaries. In some cases this is presented as an automatic incorporation of the correct temperature and density boundary condition (Lucy, 1977 [181]). The completeness of mesh free particle methods was discussed by Belytschko *et al.* (1998) [24]. However, care must be taken to ensure that variables which values do not approach zero at boundaries are accurately represented.

Development of meshless methods is connected to the solution of the problems where traditional methods like FEM or FDM, or FVM are not applicable without losing of accuracy or complicated numerical computations. For example, it is difficult to solve problems with moving boundaries, free surfaces and interfaces, deformable boundaries using FDM or FVM, problems with large deformations using FEM, problems with complex geometries using both FEM and FDM or FVM, problems with mesh adaptivity and multi-scale resolution using both FEM and FDM.

Since its introduction, SPH has been successfully used to model a wide range of fluid flow processes and the behavior of solids subjected to large deformations. For example, the SPH method has been applied to simulate high energy explosions (Liu *et al.*, 2003 [175]) and impact (Lukyanov, 2007 [183]; Lukyanov and Pen'kov, 2007 [188]), most notably free surface flows and collapse of dams (Monaghan, 1994 [210]), elastoplasticity (Johnson *et al.*, 1996 [119]; Chen *et al.*, 1999, 2001 [56], [59]; Lukyanov and Penjkov, 2007 [188]), to model low Reynolds number flows (Morris *et al.*, 1997 [213] and dispersion (Zhu *et al.*, 1999 [283]); Zhu and Fox, 2001 [282]), and for thermal problems (Chen *et al.*, 1999 [56]; Chaniotis *et al.*, 2002 [54]; Schwaiger, 2008 [236]).

### 2.1.2 Various Forms of the Meshless Method

The SPH-method and its different variations are the basic type of a particle method. Liszka and Orkisz (1980) [167] proposed a generalization of the finite difference method, which can be used with arbitrary irregular meshes. Nayroles *et al.* (1992) [220] used a minimum least squares method to approximate integral equations in the Galerkin method and formulated so called diffuse element method (DEM). Based on the diffuse element method, Belytschko *et al.* (1994) [28] significantly improved the element free Galerkin method (EFG). Currently, the EFG method is the most popular meshless method, and it is applied to different problems of solid body mechanics (see, for example, Krysl and Belytschko, 1996 [151]). Atluri and Zhu (1998) [14] developed a meshless localized Petrov-Galerkin method, which requires only a local surrounding of the cells for integration purposes. The meshless localized Petrov-Galerkin method does not require a global surrounding of the cells for integration, and this has been used to analysis constructions made of beams and shells (Atluri *et al.*, 1999 [11]; Gu and Liu, 2001 [99], [162]), and for other mechanical problems. Detailed description of the meshless localized Petrov-Galerkin method can be found in the work of Atluri and Shen (2005) [13]. Liu *et al.* (1995, 1998, 2003) [177], Liu and Jun (1998) [176], Liu and Liu (2003) [174] considered the stability and reproducing conditions of SPH method and proposed reproducing Kernel particle method, which improves the accuracy of the approximation SPH-method, especially, near the boundary. Liu and his co-authors in a number of articles developed a method of point interpolation and some other variations, see Gu and Liu, (2001, 2002) [99], [101], [100], [102]; Liu and Gu (2001, 2003) [170], [171], [172]; Liu and Liu (2003) [174]. Other meshless methods include HP-cloud (Duarte and Oden, 1996 [82]), free meshless method (Yagawa and Yamada, 1996, 1996 [278]), [279], and the points assemble method (Liu, 1999 [168]).

Three types of meshless methods can be clearly distinguished: (1) meshless methods based on the strong form of PDEs; (2) meshless methods based on a weak form of PDEs; (3) particle methods. Methods based on the strong form such as collocation method have advantages in numerical implementation, efficiency and truly meshless nature (i.e., they do not require integration over some domain). However, they are often unstable and less accurate, particularly when they are used on irregularly distributed points within the problem domain described by the partial differential equations with the Neumann boundary conditions (Neumann problem), for problem of solid mechanics with boundary conditions expressed in stresses. On the other hand, methods using weak formulations such as Galerkin free element methods and others have advantages in stability and accuracy. The Neumann boundary conditions can be naturally (exactly) satisfied due to usage of the weak form which

includes smooth (integral) operators. However, methods of weak form do not have a truly meshless nature since the local or global mesh is required for the integration of the weak form. According to the work of Liu (2002) [169], approximation functions used in meshless methods can be classified into three main classes: methods of integral representation, sequential method representations, and differential representations. For the final cases (particle methods), these methods have a probabilistic nature. The main representative of the probabilistic meshless methods is a molecular dynamic method based on the Monte-Carlo method (Metropolis and Ulam, 1949 [202]).

### 2.1.3 Advantages of Meshless Methods

The main advantages of meshless methods over conventional methods are the following:

1. The numerical domain in meshless methods are discretized using particles without predefined particle connectivity,
2. The discretization of the complex geometry is cheap,
3. Particles property update is simpler to perform over the time,
4. For hyperbolic partial differential equations, it is simpler to update properties for the entire physical system via tracking each particle. Hence, it is simpler to identify free surfaces, moving interface-surfaces, and deformation of boundaries. The time history of the field variable at various points within materials can be easier extrapolated.

In this work, we use meshless methods which are a representation of smoothed particle methods (SPH-methods) using an integral representation for the approximation function field. The SPH method has common ground with the methods based on the weak form of PDEs. The main difference is that the operator of the weak form (integral operator) is used at the stage of function approximations in SPH method but not at the point of construction the final discretized governing equations as it is performed in the conventional methods based on a weak form. Using the integral function representation allows to move differential operator from the unknown function to the tested (weighted) function. This algorithm is similar to the construction of the generalized derivative (see, Vladimirov, 1979 [265]). This can be used to reduce requirements of the order of regularity of the approximation function. Therefore, the stability of SPH methods has been shown for the case of irregular particle distributions, and large deformations. The accuracy of the SPH method depends significantly on the selection of the interpolation functions. This will be discussed in more detail in the sections below.

## § 2.2 Concept of SPH Method

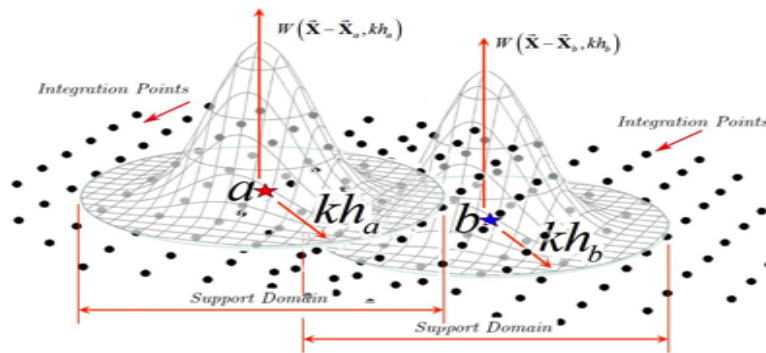


Figure 2.1: Interactions of Kernels in SPH method.

In the meshless method there is no need to use topological connectivity between particles. It is only required to have an initial particles distribution over the numerical domain. The initial particles distribution can

be done using different methods of grid generation within the numerical domain. There are a few algorithms of domain triangulation in 2D or 3D spaces. One approach consists of putting particles into barycentric or geometrical centres of the initially constructed grid. It is preferable to use Delaunay triangulation (tetrahedrization in 3D) or using quadrilateral meshes (hexahedron meshes in 3D) if possible. It is always possible to automatically generate the triangulation of domains with complex geometries. A good particle representation of the numerical domain would be placing the particles in the centres or vertices of the underlying grid.

## 2.2.1 Basic Relations

The basic relations of a particle method is based on the definition of the  $\delta$  functional (generalized  $\delta$  function), which has the following definition (see, Vladimirov, 1979 [265]):

$$\mathbf{F}(\mathbf{r}) = \langle \mathbf{F}(\mathbf{r}'), \delta(\mathbf{r} - \mathbf{r}') \rangle, \quad \delta : V^* \rightarrow \mathbb{R} \quad (2.1)$$

where  $V^*$  is a space of (vector or scalar) functions  $\mathbf{F}(\mathbf{r})$  (e.g.,  $\mathbf{F}(\mathbf{r}) \in V^* = C(\Omega)$ ). Using a weak convergence definition, the  $\delta$  functional can be approximated using a class of Kernel functions  $\{W(\mathbf{r} - \mathbf{r}', h), h \rightarrow 0\}$ , which satisfies

$$\int_{\Omega} W(\mathbf{r} - \mathbf{r}', h) d^n \mathbf{r}' = 1, \quad \forall \mathbf{r} \in \Omega \subset \mathbb{R}^n, h \in \mathbb{R}^1. \quad (2.2)$$

The limit in a weak sense from the function  $\{W(\mathbf{r} - \mathbf{r}', h)\}$  when  $h \rightarrow 0$ , equals to the value of delta functional for point  $\mathbf{r}$ , i.e.

$$\lim_{h \rightarrow 0} \int_{\Omega} \mathbf{F}(\mathbf{r}') W(\mathbf{r} - \mathbf{r}', h) d^n \mathbf{r}' = \langle \mathbf{F}(\mathbf{r}'), \delta(\mathbf{r} - \mathbf{r}') \rangle = \mathbf{F}(\mathbf{r}), \quad (2.3)$$

$$\mathbf{F}(\mathbf{r}) = \lim_{h \rightarrow 0} \int_{\Omega} \mathbf{F}(\mathbf{r}') W(\mathbf{r} - \mathbf{r}', h) d^n \mathbf{r}' \quad (2.4)$$

Additionally, it can be required the Kernels to be radially symmetric and compactly supported ( $\text{supp}W$ ):

$$\Omega_{r,h} = \text{supp}W = \{\mathbf{r} | W(\mathbf{r} - \mathbf{r}', h) = w(\|\mathbf{r} - \mathbf{r}'\|, h) \neq 0, w(s, h) = 0 \forall s > h\} \quad (2.5)$$

where  $h = f \cdot h_p$  is the radius of  $\Omega_{r,h} = \text{supp}W$ , and  $h_p$  is the inter-particle distance. Function  $W(\mathbf{r} - \mathbf{r}', h)$  is called the interpolation Kernel and it can be of different shapes always satisfying properties (2.2) and (2.3), which form the definition of the Kernel function. Under a certain selection of parameter  $h$ , which is called a Kernel radius, relation (2.4) can be rewritten in the form

$$\mathbf{F}(\mathbf{r}) = \int_{\Omega_{r,h}} \mathbf{F}(\mathbf{r}') W(\mathbf{r} - \mathbf{r}', h) d^n \mathbf{r}' + \mathcal{O}(h^2), \quad (2.6)$$

where the integral or smoothed approximation  $\mathbf{F}_h(\mathbf{r})$  of the original function  $\mathbf{F}(\mathbf{r})$  can be selected as:

$$\mathbf{F}_h(\mathbf{r}) = \int_{\Omega_{r,h}} \mathbf{F}(\mathbf{r}') W(\mathbf{r} - \mathbf{r}', h) d^n \mathbf{r}'. \quad (2.7)$$

Relation (2.7) is the fundamental aspect of the particle method concept (SPH-method). The final step in the particle method is to approximate integral relation (2.7) using Monte-Carlo expressions or any cubature rules (Fulk and Quinn, 1996 [94]; Chen *et al.*, 1999 [56], [57]; Belytschko *et al.*, 1998 [24]; Liu and Liu, 2003 [174]) and it is known as the particle approximation step:

$$\langle \mathbf{F}(\mathbf{r}) \rangle = \sum_{J \in S} \mathbf{F}(\mathbf{r}_J) \cdot W(\mathbf{r} - \mathbf{r}_J, h) \cdot V_J, \quad (2.8)$$

where  $V_J$  is the volume of an interpolation particle  $J$ . The subscript  $J$  in the above equations, including all capital Latin indices throughout this thesis, correspond to particle numbers while Greek indices correspond to spatial coordinates. In addition, the summation by the repeating Greek indices is assumed throughout this thesis. In relation (2.8), it is also possible to define a testing function as a multiplication of the particle volume with the weighted function:

$$\Phi_J(\mathbf{r}) = W(\mathbf{r} - \mathbf{r}_J, h) V_J, \quad (2.9)$$



A variable quantity  $\mathbf{F}(\mathbf{r})$  is defined in the particle of the medium  $J \in S$  with radius vector  $\mathbf{r}_J$  and it is approximated by relation (2.10) based on relation (2.9)

$$\mathbf{F}_h(\mathbf{r}) = \sum_{J \in S} \mathbf{F}(\mathbf{r}_J) \cdot \Phi_J(\mathbf{r}). \quad (2.10)$$

Using aforementioned relations, it is possible to define an expression for the approximation of the gradient of the variable quantity (function). It is important to assume that a Kernel of approximation satisfies all the necessary properties for existing different mathematical operations (i.e., differentiation and integration) of the required number of times. Let us also assume that

$$W(\mathbf{r} - \mathbf{r}_J, h)|_{\mathbf{r} \in \partial \text{supp} W_J} = 0 \quad (2.11)$$

for all particles  $J \in S$  which is not valid in general for boundary particles (in this case, the expression presented below have a more complex form), but it is fundamental for the concept of a particle approximation.

### 2.2.2 Lagrangian SPH Method

In the previous sections, the basic concepts of the SPH method have been described which can be applied both for the Eulerian and Lagrangian descriptions outlined in Chapter 1. In this section, some approximations will be described specific for the Lagrangian description, mainly used in solid mechanics. Note that in solid mechanics problems the interpolation particles move with the body, deform and, hence, change the volume and conserve mass. Therefore, let  $\rho$  be a density distribution function and  $d\mu_\rho = \rho d^n \mathbf{r}$ . Hence, equation (2.6) can be written by changing the integration variables as

$$\mathbf{F}(\mathbf{r}) = \int_{\Omega_{r,h}} \frac{\mathbf{F}(\mathbf{r}')}{\rho(\mathbf{r}')} W(\mathbf{r} - \mathbf{r}', h) d\mu_\rho(\mathbf{r}') + \mathcal{O}(h^2) \quad (2.12)$$

Introducing a set of Lagrangian particles  $P^N = \{P_1^N, \dots, P_N^N\}_{N \in \mathbb{N}}$  and associated radius vector  $(\mathbf{r}_1^N, \dots, \mathbf{r}_N^N)$  and masses  $(m_1^N, m_2^N, \dots, m_N^N)$  such that measure  $\mu_{P^N}(\mathbf{r}) = \sum_{k=1}^N m_k^N \delta(\mathbf{r} - \mathbf{r}_k)$  weakly converges to the measure  $\mu_\rho$  (where  $\mu_\rho = \int \rho d^n \mathbf{r}$ ) for any test functions  $\phi \in C(\Omega)$ :

$$\langle \phi(\mathbf{r}), \delta(\mathbf{r}) \rangle = \lim_{N \rightarrow \infty} \langle \phi(\mathbf{r}), \mu_{P^N} \rangle. \quad (2.13)$$

As a result, equation (2.12) can be written as

$$\langle \mathbf{F}(\mathbf{r}) \rangle = \sum_{J \in S} \mathbf{F}(\mathbf{r}_J) \cdot W(\mathbf{r} - \mathbf{r}_J, h) \cdot \frac{m_J}{\rho_J}, \quad (2.14)$$

which is also consistent with equation (2.8) by noting that  $V_J = \frac{m_J}{\rho_J}$  is the volume of particle  $J$ ,  $m_J$  is the mass of particle  $J$ ,  $\rho_J$  is the density of particle  $J$ , and  $S$  is the particle set located in  $\text{supp} W$ .

### 2.2.3 Spatial Derivative Approximation Using SPH Method

Using relations (2.7), (2.11) and integration by parts, it is possible to obtain the following approximation of the gradient of the variable quantity (function):

$$\begin{aligned} \nabla \mathbf{F}_h(\mathbf{r}) &= - \sum_{J \in S} \mathbf{F}(\mathbf{r}_J) \cdot \nabla W(\mathbf{r} - \mathbf{r}_J, h) \cdot \frac{m_J}{\rho_J}, \\ \nabla \otimes \nabla \mathbf{F}_h(\mathbf{r}) &= \sum_{J \in S} \mathbf{F}(\mathbf{r}_J) \cdot \nabla \otimes \nabla W(\mathbf{r} - \mathbf{r}_J, h) \cdot \frac{m_J}{\rho_J} \end{aligned} \quad (2.15)$$

where the symbol  $\nabla$  denotes partial differentiation with respect to spatial coordinates and  $\nabla \otimes \nabla$  denotes the second partial differentiation with respect to spatial coordinates.

In practice, more accurate approximations are used based on the following approach:

$$\nabla \mathbf{F}(\mathbf{r}) = \frac{1}{\rho} [\nabla(\rho \mathbf{F}) - \mathbf{F} \nabla \rho], \quad (2.16)$$

which leads to the expression for the gradient in the form:

$$\nabla \mathbf{F}_h(\mathbf{r}) = -\frac{1}{\rho(\mathbf{r})} \sum_{J \in S} m_J (\mathbf{F}(\mathbf{r}_J) - \mathbf{F}(\mathbf{r})) \cdot \nabla W(\mathbf{r} - \mathbf{r}_J, h). \quad (2.17)$$

To calculate the second derivatives of  $\mathbf{F}(\mathbf{r})$ , several methods were proposed (Chen *et al.*, 1999 [58], [57]; Bonet and Kulasegaram, 2000 [32]; Colin *et al.*, 2006 [69]). One of them is to assume that

$$\nabla \otimes \nabla \mathbf{F}_h(\mathbf{r}) = \frac{1}{\rho(\mathbf{r})} \sum_{J \in S} m_J (\mathbf{F}(\mathbf{r}_J) - \mathbf{F}(\mathbf{r})) \cdot \nabla \otimes \nabla W(\mathbf{r} - \mathbf{r}_J, h). \quad (2.18)$$

However, second-order derivatives can often be avoided entirely if the PDE is written in weak form. It is important to note that approximations using second-order derivatives of the kernel (see, relation (2.18)) are often noisy and sensitive to the particles distribution, particularly for spline kernels of lower order.

It follows from (2.17) that the expression for the gradient has a clear form and is less sensitive to the particles distribution. In the same way to (2.15), the divergence of the velocity can be written as

$$\nabla \mathbf{v}_h(\mathbf{r}) = -\sum_{J \in S} \mathbf{v}(\mathbf{r}_J) \cdot \nabla W(\mathbf{r} - \mathbf{r}_J, h) \cdot \frac{m_J}{\rho_J}, \quad (2.19)$$

or more accurate as:

$$\nabla \mathbf{v}_h(\mathbf{r}) = -\frac{1}{\rho(\mathbf{r})} \sum_{J \in S} m_J (\mathbf{v}(\mathbf{r}_J) - \mathbf{v}(\mathbf{r})) \cdot \nabla W(\mathbf{r} - \mathbf{r}_J, h). \quad (2.20)$$

Let us introduce the following commonly used notations:

$$W_{ab} = W(\mathbf{r}_a - \mathbf{r}_b, h), \quad \mathbf{v}_a - \mathbf{v}_b = \mathbf{v}_{ab}, \quad (2.21)$$

and to assume that  $\nabla_a W_{ab}$  corresponds to the gradient from  $W_{ab}$  with respect to the variable  $\mathbf{r}_a$  ( $\mathbf{r}_a$  - radius vector of particle  $a$ ). Hence, the relation (2.20), taking into account aforementioned notations (2.21), takes the following form:

$$\nabla \mathbf{v}_I^h = \frac{1}{\rho_I} \cdot \sum_{J \in S} m_J \cdot \mathbf{v}_{IJ} \cdot \nabla_J W_{IJ}(h). \quad (2.22)$$

The assumption that the boundary term from the integration by parts is zero in equations (2.17), (2.18) is valid only in regions where the kernel has full support or the function itself is zero. For particles near free surfaces or boundary, the neglect of these terms leads to significant errors for boundary value problems. Several techniques have been developed to address these errors through various correction methods, e.g., by calculating the boundary integrals (Campbell, 1989 [47]; Liu and Liu, 2003 [174]), by applying normalized corrected meshless methods in the derivative approximations (Belytschko *et al.*, 1998 [24]; Liu and Liu, 2003 [174]; Lukyanov, 2007 [183]; Lukyanov and Penjkov, 2007 [188]).

## § 2.3 Corrected SPH Method

Some approaches for improving approximation of the conventional SPH method have been proposed in the literature (Bonet and Kulasegaram, 2000 [32]; Bonet and Lok, 1999 [33]; Belytschko *et al.* 1998 [24], Liu and Liu, 2003 [174]).

### 2.3.1 Corrected SPH Method

Let us consider a vector or scalar function  $\mathbf{F}(\mathbf{r}')$ . In addition, it is assumed that function is at least, twice differentiable in the vicinity of the point  $\mathbf{r}$  (i.e.,  $\mathbf{F}(\mathbf{r}') = C^2(\Omega_{\mathbf{r},h})$ ). The Taylor series expansion for the function around the point  $\mathbf{r}$  has the form

$$\mathbf{F}(\mathbf{r}') = \mathbf{F}(\mathbf{r}) + (\mathbf{r}' - \mathbf{r}) \nabla \mathbf{F} + \frac{1}{2} (\mathbf{r}' - \mathbf{r}) \nabla \otimes \nabla \mathbf{F}(\mathbf{r}) (\mathbf{r}' - \mathbf{r}) + \mathcal{O}(\|\mathbf{r}' - \mathbf{r}\|^3) \quad (2.23)$$

Multiplying both sides of the equation (2.23) by the approximation Kernel function  $W(\mathbf{r} - \mathbf{r}', h)$  and integrating over entire definition domain  $\Omega_{\mathbf{r}, h}$  lead to the meshless approximation of the function  $\mathbf{F}(\mathbf{r})$ :

$$\begin{aligned} \mathbf{F}(\mathbf{r}) & \int_{\Omega_{\mathbf{r}, h}} W(\mathbf{r} - \mathbf{r}', h) d^n \mathbf{r}' = \\ & = \int_{\Omega_{\mathbf{r}, h}} \mathbf{F}(\mathbf{r}') W(\mathbf{r} - \mathbf{r}', h) d^n \mathbf{r}' - \int_{\Omega_{\mathbf{r}, h}} (\mathbf{r}' - \mathbf{r}) \nabla \mathbf{F} W(\mathbf{r} - \mathbf{r}', h) d^n \mathbf{r}' - \\ & - \int_{\Omega_{\mathbf{r}, h}} \frac{1}{2} (\mathbf{r}' - \mathbf{r})^2 \nabla \otimes \nabla \mathbf{F}(\mathbf{r}) W(\mathbf{r} - \mathbf{r}', h) d^n \mathbf{r}' + \mathcal{O}(\|\mathbf{r}' - \mathbf{r}\|^3) \end{aligned} \quad (2.24)$$

and

$$\langle \mathbf{F}(\mathbf{r}) \rangle = \frac{1}{V_W} \int_{\Omega_{\mathbf{r}, h}} \mathbf{F}(\mathbf{r}') W(\mathbf{r} - \mathbf{r}', h) d^n \mathbf{r}', \quad (2.25)$$

where  $V_W = \int_{\Omega_{\mathbf{r}, h}} W(\mathbf{r} - \mathbf{r}', h) d^n \mathbf{r}'$  is the kernel volume.

The meshless approximation of  $\nabla \mathbf{F}(\mathbf{r})$  can be derived by multiplying equation (2.23) with  $W(\mathbf{r} - \mathbf{r}', h)$  and integrating over the entire domain  $\Omega_{\mathbf{r}, h}$ :

$$\begin{aligned} \nabla \mathbf{F}(\mathbf{r}) & \int_{\Omega_{\mathbf{r}, h}} (\mathbf{r}' - \mathbf{r}) \nabla W(\mathbf{r} - \mathbf{r}', h) d^n \mathbf{r}' = \\ & = \int_{\Omega_{\mathbf{r}, h}} [\mathbf{F}(\mathbf{r}') - \mathbf{F}(\mathbf{r})] \nabla W(\mathbf{r} - \mathbf{r}', h) d^n \mathbf{r}' - \\ & - \int_{\Omega_{\mathbf{r}, h}} \frac{1}{2} (\mathbf{r}' - \mathbf{r})^2 \nabla \otimes \nabla \mathbf{F}(\mathbf{r}) \nabla W(\mathbf{r} - \mathbf{r}', h) d^n \mathbf{r}' + \mathcal{O}(\|\mathbf{r}' - \mathbf{r}\|^2) \end{aligned} \quad (2.26)$$

and

$$\langle \nabla \mathbf{F}(\mathbf{r}) \rangle = \int_{\Omega_{\mathbf{r}, h}} [\mathbf{F}(\mathbf{r}') - \mathbf{F}(\mathbf{r})] \nabla^* W(\mathbf{r} - \mathbf{r}', h) d^n \mathbf{r}', \quad (2.27)$$

$$\nabla^* W(\mathbf{r} - \mathbf{r}) = \mathbf{C} \cdot \nabla W(\mathbf{r} - \mathbf{r}', h) \quad (2.28)$$

where  $\mathbf{C} = \left[ \int_{\Omega_{\mathbf{r}, h}} (\mathbf{r}' - \mathbf{r}) \nabla W(\mathbf{r} - \mathbf{r}', h) d^n \mathbf{r}' \right]^{-1}$ . Expression (2.27) allows to achieve the zero and first order consistency (exact approximation for the constant and linear functions).

### 2.3.2 Normalized-Corrected SPH Method

A central point of the SPH formalism is the concept of the interpolating function (or kernel) and its derivatives through which the continuum properties of the medium are recovered from a discrete sample of  $N$  points (2.14) with prescribed mass  $m_I$  or volume  $V_I$  (for conventional Lagrangian methods) or volume  $V_I$  (for fully Eulerian methods), with finite characteristic width  $\tilde{h}_I$  around the particle  $I$ . The effective characteristic width  $\tilde{h}_I$  will be defined in the upcoming section using real smoothing particle length  $h_I$ . However, it is important to note that, in the case of the homogeneous particle distribution, it is common to use  $h_I = f \cdot h_p$ , where  $h_p$  is the inter-particles distance. Hence, it is important that  $h_I$  and  $h_p$  are not mixed up during the analysis. In general (e.g., for heterogeneous particle),  $h_I = f \cdot h_I^0$ , where  $h_I^0$  is the initial smoothing length. In the Lagrangian formulation, these points move according to the specified governing laws, whereas these points are fixed in space for the Eulerian formulation. A good interpolating kernel must satisfy a few basic requirements: it must weakly tend to the delta function in the continuum limit and has to be a continuous function with piece-wise first derivatives at least.

Although, the kernel is normalized in continuous sense, it is important to note that  $W(\mathbf{r}_J - \mathbf{r}_I, \tilde{h}_{IJ})$  does not satisfy the normalization condition in the discrete space

$$\sum_{\mathbf{r}_J \in \Omega_{\mathbf{r}_I, \tilde{h}_I}} W(\mathbf{r}_J - \mathbf{r}_I, \tilde{h}_{IJ}) V_{\mathbf{r}_J} \neq 1$$

due to particles distribution and incomplete kernel support near the boundary and, hence, the discretized-normalized kernel function can be considered:

$$\overline{W}(\mathbf{r}_J - \mathbf{r}_I, \tilde{h}_{IJ}) = \frac{W(\mathbf{r}_J - \mathbf{r}_I, \tilde{h}_{IJ})}{\sum_{\mathbf{r}_J \in \Omega_{\mathbf{r}_I, \tilde{h}_I}} W(\mathbf{r}_J - \mathbf{r}_I, \tilde{h}_{IJ}) V_{\mathbf{r}_J}} = \frac{W(\mathbf{r}_J - \mathbf{r}_I, \tilde{h}_{IJ})}{\nu(\mathbf{r}_I)} \quad (2.29)$$

where  $\nu(\mathbf{r}_I)$  is the specific volume of particle  $\mathbf{r}_I$  (i.e., it is approximately the inverse of the particle volume) which has a larger value in a dense particle region than in a dilute particle region. In regions of high particle density, the denominator in (2.29) is high, resulting in lower values of the kernel  $\overline{W}(\mathbf{r}_J - \mathbf{r}_I, \tilde{h}_{IJ})$ . Thus the denominator normalizes the kernel function to ensure that the kernel  $\overline{W}(\mathbf{r}_J - \mathbf{r}_I, \tilde{h}_{IJ})$  forms a local partitioning of unity

$$\sum_{\mathbf{r}_J \in \Omega_{\mathbf{r}_I, \tilde{h}_I}} \overline{W}(\mathbf{r}_J - \mathbf{r}_I, \tilde{h}_{IJ}) V_{\mathbf{r}_J} = 1 \quad (2.30)$$

regardless of the particle distribution within the  $\Omega_{\mathbf{r}_I, h_I} = \text{supp } W(\mathbf{r} - \mathbf{r}_I, h_I)$ . The discretized-normalized kernel function  $\overline{W}(\mathbf{r} - \mathbf{r}_I, h)$  will also be used in the discretization schemes below. At this point, all possible options of computing  $\overline{\nabla W}(\mathbf{r}_J - \mathbf{r}_I, \tilde{h}_{IJ})$  are listed:

**Definition 2.1.**

$$\overline{\nabla W}(\mathbf{r}_J - \mathbf{r}_I, \tilde{h}_{IJ}) = \nabla_{\mathbf{r}_I} W(\mathbf{r}_J - \mathbf{r}_I, \tilde{h}_{IJ}) = -\nabla_{\mathbf{r}_J} W(\mathbf{r}_J - \mathbf{r}_I, \tilde{h}_{IJ}), \quad (2.31)$$

**Definition 2.2.**

$$\begin{aligned} \overline{\nabla W}(\mathbf{r}_J - \mathbf{r}_I, \tilde{h}_{IJ}) &= \nabla_{\mathbf{r}_I} \overline{W}(\mathbf{r}_J - \mathbf{r}_I, \tilde{h}_{IJ}) = \\ &= \left[ \frac{\nabla_{\mathbf{r}_I} W(\mathbf{r}_J - \mathbf{r}_I, \tilde{h}_{IJ})}{\nu(\mathbf{r}_I)} - \frac{W(\mathbf{r}_J - \mathbf{r}_I, \tilde{h}_{IJ}) \nabla_{\mathbf{r}_I} \nu(\mathbf{r}_I)}{\nu^2(\mathbf{r}_I)} \right], \\ \nabla_{\mathbf{r}_I} \nu(\mathbf{r}_I) &= \sum_{\mathbf{r}_K \in \Omega_{\mathbf{r}_I, \tilde{h}_I}} \nabla_{\mathbf{r}_I} W(\mathbf{r}_K - \mathbf{r}_I, \tilde{h}_{IJ}) V_{\mathbf{r}_K}, \end{aligned} \quad (2.32)$$

where  $\nu(\mathbf{r}_I)$  is the specific volume of the particle located at the point  $\mathbf{r}_I$ .

Additionally, two options can be written as

**Definition 2.3.**

$$\overline{\nabla W}(\mathbf{r}_J - \mathbf{r}_I, \tilde{h}_{IJ}) = \tilde{\nabla}_{\mathbf{r}_I} \overline{W}(\mathbf{r}_J - \mathbf{r}_I, \tilde{h}_{IJ}) = -\frac{\nabla_{\mathbf{r}_J} W(\mathbf{r}_J - \mathbf{r}_I, \tilde{h}_{IJ})}{\nu(\mathbf{r}_I)}, \quad (2.33)$$

where  $\nu(\mathbf{r}_I)$  is assumed to be a constant during the differentiation with respect to  $\mathbf{r}_J$ .

The alternative case is when

$$\nu(\mathbf{r}_I, \mathbf{r}_J) = \sum_{\mathbf{r}_J \in \Omega_{\mathbf{r}_I, \tilde{h}_I}} W(\mathbf{r}_J - \mathbf{r}_I, \tilde{h}_{IJ}) V_{\mathbf{r}_J},$$

leading to the following relations

**Definition 2.4.**

$$\begin{aligned} \overline{\nabla W}(\mathbf{r}_J - \mathbf{r}_I, \tilde{h}_{IJ}) &= \overline{\nabla}_{\mathbf{r}_I} \overline{W}(\mathbf{r}_J - \mathbf{r}_I, \tilde{h}_{IJ}) = -\overline{\nabla}_{\mathbf{r}_J} \overline{W}(\mathbf{r}_J - \mathbf{r}_I, \tilde{h}_{IJ}) \\ &= -\left[ \frac{\nabla_{\mathbf{r}_J} W(\mathbf{r}_J - \mathbf{r}_I, \tilde{h}_{IJ})}{\nu(\mathbf{r}_I, \mathbf{r}_J)} - \frac{W(\mathbf{r}_J - \mathbf{r}_I, \tilde{h}_{IJ}) \nabla_{\mathbf{r}_J} \nu(\mathbf{r}_I, \mathbf{r}_J)}{\nu^2(\mathbf{r}_I, \mathbf{r}_J)} \right], \\ \nabla_{\mathbf{r}_J} \nu(\mathbf{r}_I, \mathbf{r}_J) &= \nabla_{\mathbf{r}_J} W(\mathbf{r}_J - \mathbf{r}_I, \tilde{h}_{IJ}) V_{\mathbf{r}_J} \end{aligned} \quad (2.34)$$

Where  $\overline{\nabla W}(\mathbf{r}_J - \mathbf{r}_I, \tilde{h}_{IJ})$  and  $\nabla_{\mathbf{r}_I}$  in all definitions above represent the nabla operator with respect to  $\mathbf{r}_I$ . Assuming this for the rest of the thesis, the  $\mathbf{r}_I$  index is omitted throughout this paper starting from here. Similar to the MLS method [40], equations (2.32) and (2.34) are two different forms of "full derivatives". At the same time, equations (2.31) and (2.33) are two different forms of "diffuse derivatives". From these options, it follows that "full derivatives" are connected with the differentiation of a discrete function and "diffuse derivatives" are connected with the differentiation of an exact function. Both types of derivatives have some advantages and disadvantages and the choice depends on the application. The impact of different options on numerical results will be shown below. Finally, it is important to note the following relation for the kernel gradients (2.31), (2.33), and (2.34):

$$\overline{\nabla_{\alpha} W}(\mathbf{r}_J - \mathbf{r}_I, \tilde{h}_{IJ}) = -\frac{1}{\tilde{h}_{IJ}} G(z_J, \mathbf{r}_I) \frac{[\mathbf{r}_J^{\alpha} - \mathbf{r}_I^{\alpha}]}{\|\mathbf{r}_J - \mathbf{r}_I\|}, \quad (2.35)$$

where function  $G(z_J, \mathbf{r}_I)$  has a different shape depending on the definitions (2.31), (2.33) and (2.34). The SPH method shows good approximation properties in regions where the kernel has full support. For particles near free surfaces or boundaries, the SPH method shows a poor approximation. Several techniques have been developed to address these errors through various correction methods, e.g., by applying normalized corrected meshless methods in the derivative approximations (Belytschko *et al.*, 1998 [24]; Liu and Liu, 2003 [174]; Lukyanov, 2007 [183]; Lukyanov and Penjkov, 2007 [188]), which requires normalized corrected definitions of the kernel gradient as follows:

$$\overline{\nabla_{\alpha}^* W} = \mathbf{C}_{\alpha\beta} \overline{\nabla_{\beta} W}, \quad (2.36)$$

$$\mathbf{C}_{\alpha\beta} = \left[ \sum_{\mathbf{r}_J \in \Omega_{\mathbf{r}_I, \tilde{h}_{IJ}}} V_{\mathbf{r}_J} [\mathbf{r}_J^{\alpha} - \mathbf{r}_I^{\alpha}] \overline{\nabla_{\beta} W}(\mathbf{r}_J - \mathbf{r}_I) \right]^{-1}, \quad (2.37)$$

$$\sum_{\Omega_{\mathbf{r}_I, h}} V_{\mathbf{r}_J} [\mathbf{r}_J^{\gamma} - \mathbf{r}_I^{\gamma}] \overline{\nabla_{\alpha}^* W}(\mathbf{r}_J - \mathbf{r}_I, h) = \delta_{\gamma\alpha}, \quad \forall \gamma, \alpha; \quad (2.38)$$

where summation by repeating indexes is assumed throughout this paper,  $\overline{\nabla_{\alpha}^* W}$  is the normalized corrected gradient of kernel, and  $\mathbf{C}_{\alpha\beta}$  is the correction tensor (Randles and Libersky, 1996 [231]). It was shown that the value of the minimum eigenvalue  $\lambda^C(\mathbf{r}_I)$  of the matrix  $\mathbf{C}^{-1}$  based on discretized-normalized kernel function depends on the particle distribution within the domain  $\Omega_{\mathbf{r}_I, \tilde{h}_{IJ}} = \text{supp}W(\mathbf{r} - \mathbf{r}_I, \tilde{h}_{IJ})$ . When going away from the  $\Omega_{\mathbf{r}_I, \tilde{h}_{IJ}}$  domain this eigenvalue tends theoretically to zero, while inside this domain the eigenvalue tends theoretically to one. This important information allows determining regions of the continuum media where free-surfaces are located (Marrone *et al.*, 2010 [196]).

### 2.3.3 SPH symmetrization of smoothing length

The true particle smoothing length  $h_I$  may vary both in space and time in general. Therefore, in general case, each particle has its own smoothing length  $h_I$ . Considering the case where  $h_I \neq h_J$  for two different interacting particles  $I$  and  $J$  and the kernel support based on  $\tilde{h}_I$  and located in  $I$  which covers the particle  $J$  but the kernel support located in  $J$  does not cover the particle  $I$ . In this case, the particle  $I$  acting on particle  $J$  (produces, e.g., a flux or a force) without particle  $J$  acting on the particle  $I$ , which leads to a violation of fundamental laws (e.g., mass conservation or Newton's third law) for a closed system of particles. This problem has been resolved by introducing the symmetrization of the smoothing length. In this study, the following symmetrization option is used:

$$\tilde{h}_{IJ} = \frac{h_I + h_J}{2}. \quad (2.39)$$

In addition, it is clear that  $\tilde{h}_I$  has to be defined as

$$\tilde{h}_I = \sup_{J: \mathbf{r}_J \in \Omega_{\mathbf{r}_I, \tilde{h}_I}} \tilde{h}_{IJ}. \quad (2.40)$$

This completes the description of basic properties of SPH method allowing to construct all necessary building elements of SPH discretization such as list of neighbors, kernel values, and kernel gradients. The following sections describe the traditional and newly proposed discretization schemes for different governing equations.

In this thesis, the discretizations of the Laplace operator are based on the gradient of the kernel. However, several methods of Laplace discretizations were proposed (Chen *et al.*, 1999 [56], [57]; Bonet and Kulasegaram,

2000 [32]; Colin *et al.*, 2006 [69]) using second derivatives of the variable  $\mathbf{u}$ . However, second-order derivatives can often be avoided entirely if the PDE is written in weak form. It is important to note that approximations using second-order derivatives of the kernel are often noisy and sensitive to the particles distribution, particularly for spline kernels of lower orders.

## § 2.4 SPH Approximation of Conservation Laws

In this subsection, the SPH approximation of the basic conservation laws in both Euler and Lagrangian coordinates is considered. There are many ways to construct these approximations in different forms; therefore the selection procedure of the approximation is discussed here.

### 2.4.1 Conservation Law of Mass

Let us consider firstly the fundamental law of physics – conservation law of mass. In the Euler coordinates, the continuity equation (conservation law of mass) has the following form:

$$\frac{d\rho}{dt} + \rho \nabla \mathbf{v} = 0, \quad (2.41)$$

using relation (2.20), it is straightforward to obtain the expression for the approximation of the derivative from the density with respect to time:

$$\langle \dot{\rho}_I \rangle = -\rho_I \sum_{J \in S} \frac{m_J}{\rho_J} (\mathbf{v}_I - \mathbf{v}_J) \cdot \overline{\nabla W}_{IJ}. \quad (2.42)$$

In the case of Lagrangian coordinates, the conservation law of mass has the following simpler form and can be expressed as

$$\rho \cdot J = \rho_0 \cdot J_0, \quad (2.43)$$

which, at the same time, can be written in the following form:

$$\rho \cdot \det \mathbf{F} = \rho_0 \cdot \det \mathbf{F}_0, \quad (2.44)$$

where the  $\mathbf{F}$  is the gradient of deformation (in the initial configuration it is assumed  $\mathbf{F}_0 = \mathbf{I}$ ,  $\mathbf{I}$  – unity tensor). Hence, for the approximation of the conservation law of mass, it is enough to have an approximation of gradient of deformation:

$$\langle \mathbf{F} \rangle = \sum_{J \in S} \frac{m_J}{\rho_J} \cdot (\mathbf{u}_I - \mathbf{u}_J) \otimes \overline{\nabla W}_{IJ} + \mathbf{I}. \quad (2.45)$$

Therefore, based on relations (2.44) and (2.45) the density of the medium can be calculated at any moment of time.

### 2.4.2 Conservation Law of Linear Momentum

The particle motion "a" is described by the following kinematic relations:

$$\frac{d\mathbf{r}_a}{dt} = \mathbf{v}_a, \quad (2.46)$$

and the conservation law of impulse (taking into account the conservation law of mass) in a full Lagrangian description has the following form:

$$\dot{\mathbf{v}} = \frac{1}{\rho_0} \nabla_0 \cdot \mathbf{P} + \mathbf{b}, \quad \mathbf{b} = 0 \quad (2.47)$$

Using relations (2.20), the divergence of the stress tensor (the nominal stress tensor or the transpose of the first Piola-Kirchoff stress) is written in the form:

$$(\nabla_0 \cdot \mathbf{P})_I \cong -\frac{1}{\rho_I} \sum_{J \in S} m_J (\mathbf{P}_J - \mathbf{P}_I) \cdot \overline{\nabla W}_{IJ}. \quad (2.48)$$

From expression (2.48), it follows that the force between particles is zero; for the stability point of view this expression has advantages while the impulse and energy are not exactly conserved. If one uses the relation

$$\frac{\nabla_0 \cdot \mathbf{P}}{\rho_0} = \nabla_0 \left( \frac{\mathbf{P}}{\rho_0} \right) + \left( \frac{\mathbf{P}}{\rho_0^2} \right) \nabla_0 \rho_0, \quad (2.49)$$

then taking into account relation (2.19) and (2.49) for the velocity approximation, following expression can be obtained:

$$\left( \frac{d\mathbf{v}}{dt} \right)_I = - \sum_{J \in S} m_J \left( \frac{\mathbf{P}_I}{(\rho_0^2)_I} + \frac{\mathbf{P}_J}{(\rho_0^2)_J} \right) \cdot \overline{\nabla_I W}_{IJ}, \quad (2.50)$$

and, in this case, the impulse and angular momentum are conserved in accordance with Newton's third law.

### 2.4.3 Conservation Law of Energy

The energy evolution equation (or conservation law of energy taking into account the conservation of kinetic energy) in the full Lagrangian form has the following form:

$$\dot{e} = \frac{1}{\rho_0} \dot{\mathbf{F}} : \mathbf{P}. \quad (2.51)$$

Using (2.45), the following approximate relation can be derived

$$\langle \dot{e}_I \rangle = \left( \sum_{J \in S} m_J (\mathbf{v}_I - \mathbf{v}_J) \otimes \overline{\nabla W}_{IJ} \right) : \frac{\mathbf{P}_I}{(\rho_0^2)_I}. \quad (2.52)$$

It is easy to verify that using relations (2.49) and (2.52) the conservation law of total energy is fulfilled:

$$\frac{d(E_k + e)}{dt} = \frac{dE_k}{dt} + \frac{de}{dt} = 0, \quad (2.53)$$

where

$$\frac{dE_k}{dt} = -\frac{1}{2} \sum_{I \in \Omega} \sum_{J \in \Omega} m_I m_J (\mathbf{v}_I - \mathbf{v}_J) \left( \frac{\mathbf{P}_I}{(\rho_0^2)_I} + \frac{\mathbf{P}_J}{(\rho_0^2)_J} \right) \overline{\nabla_I W}_{IJ}, \quad (2.54)$$

therefore, full energy is conserved.

## §2.5 SPH Additional Components

---

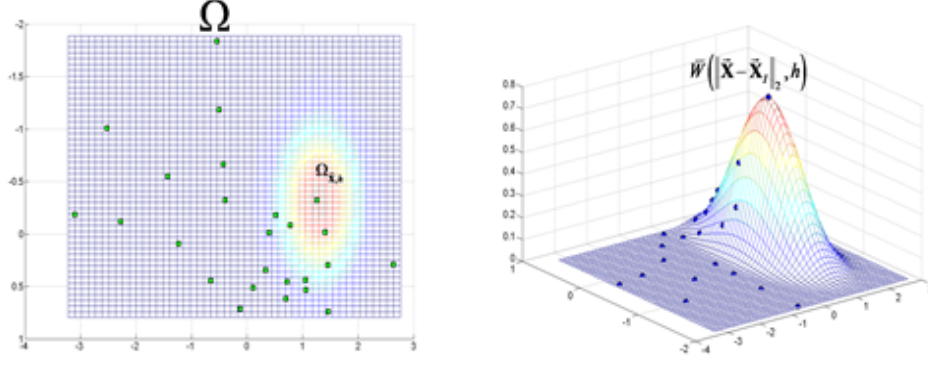
The main aim of this subsection is to consider fundamental properties and form of Kernel functions of the approximation of governing equations. An explicit form of the most popular (used) Kernel functions will be discussed.

### 2.5.1 SPH Kernel

Theoretically, the Kernel function must satisfy only the relations (2.2) and (2.3). Let us consider a Kernel of the form:

$$W(r, h) = \frac{1}{h^D} f\left(\frac{r}{h}\right), \quad (2.55)$$

where  $D$  – dimension of the considered numerical problem and  $r = \|\mathbf{r} - \mathbf{r}_0\|$ . There are many factors influencing the selection of the Kernel function for the approximation of governing equations. The most important factors are the order of the resulting approximation, the number of neighboring domains, symmetry of Kernel, and stability properties. Initially, the Gaussian Kernel was used for the approximation of governing equations. However, this function is not finite (it does not have compact support), and, therefore, in the SPH discretization with the Gaussian Kernel each particle will influence any other particle in the numerical domain (it follows from the discretized set of governing equations). From a more practical point of view it is also advisable to deal with symmetric finite range kernels, the latter to avoid  $N^2$  calculations. Cubic and quintic splines are the commonly used kernels in SPH formulations Li and Liu (2002), (2003) [163, 174]. The cubic spline is firstly used in the work by Monaghan and Lattanzio (1985) [211]. However, the work of Morris (1996) [212], it was



**Figure 2.2:** SPH cubic spline.

shown that dispersion relation for linear waves in the structure of SPH method has some undesirable properties affecting the stability of the method. These problems can have negligible impact onto a solution depending on the application of the approximation Kernel function. The cubic spline is used:

$$W(z, \tilde{h}) = \frac{\Xi}{\tilde{h}^D} \begin{cases} 1 - \frac{3}{2}z^2 + \frac{3}{4}z^3, & 0 \leq z \leq 1 \\ \frac{1}{4}(2-z)^3, & 1 \leq z \leq 2 \\ 0, & z > 2 \end{cases} \quad (2.56)$$

where  $z = \|\mathbf{r}_J - \mathbf{r}_I\|_2 / \tilde{h}$  is the dimensionless variable,  $\tilde{h} = \tilde{h}_{IJ}$  is the effective smoothing length between particles  $I$  and  $J$ , and  $\Xi$  is the normalization factor equal to  $3/2$ ,  $10/(7\pi)$ , and  $1/\pi$  in 1D, 2D and 3D, respectively. The different choices of computing the effective smoothing length between particles used in this paper will be discussed in the upcoming subsection. The quintic spline kernel is given by:

$$W(z, \tilde{h}) = \frac{\Xi}{\tilde{h}^D} \begin{cases} (3-z)^5 - 6(2-z)^5 + 15(1-z)^5, & \text{if } 0 \leq z < 1 \\ (3-z)^5 - 6(2-z)^5, & \text{if } 1 \leq z < 2 \\ (3-z)^5, & \text{if } 2 \leq z < 3 \\ 0, & \text{if } z \geq 3 \end{cases} \quad (2.57)$$

$\Xi$  where the normalization factor equal to  $1/120$ ,  $7/478\pi$ , and  $1/120\pi$  in 1D, 2D and 3D, respectively. The different choices of computing the effective smoothing length between particles used in this paper will be discussed in the upcoming subsection. There are other kernels (Liu and Liu, 2003 [174]; Li and Liu, 2002 [163]) which have superior stability properties compared to the cubic and quintic splines, at no extra computational expense. However, it is not clear, if these kernels represent a significant improvement over the cubic or quintic splines for the applications discussed in this paper.

## 2.5.2 Artificial Viscosity

In many numerical methods with finite approximation, the artificial viscosity is used (or low order diffusion, or Riemann's method) for describing shock wave propagation. In the case of a particle method it is enough to use artificial viscosity. The most popular form of an artificial viscosity is based on the viscous stresses (tensor Navier-Stokes viscosity):

$$(\Pi_I)_{kl} = -q_I \mathbb{I}_{kl} + (\Pi'_I)_{kl}, \quad (2.58)$$



where

$$q_I = \begin{cases} \alpha_q h_I \rho_I c_I^v |\nabla \mathbf{v}_I| + \beta_q h_I^2 \rho_I |\nabla \mathbf{v}_I|^2, & \nabla \mathbf{v}_I < 0, \\ 0, & \nabla \mathbf{v}_I \geq 0, \end{cases} \quad (2.59)$$

$$(\Pi'_I)_{kl} = 2 \cdot \alpha_{\Pi'} \cdot c_I^s \cdot \rho_I \cdot h_I \cdot \left( \dot{\epsilon}_{kl} - \frac{1}{3} \dot{\epsilon}_{rr} \delta_{kl} \right)_I, \quad (2.60)$$

where  $\rho_I$  – density in the particle  $I$ ,  $c_I^v$  – speed of sound in the particle  $I$  (volumetric speed of sound  $c_I = \sqrt{\frac{K_I}{\rho_I}}$ ),  $c_I^s$  – speed of shear perturbations, and  $h_I$  – radius of approximation Kernel function. The parameters of the artificial viscosity  $\alpha_q$ ,  $\beta_q$ ,  $\alpha_{\Pi'}$  are defined from numerical experiments and usually take a value around unity.

By introducing an artificial viscosity, it is required to make a correction of our equation of motion and energy respectively. For this reason, the stress tensor correction is used:

$$\tilde{\sigma}_I = \tilde{\sigma}_I + (\Pi_I)_{kl}. \quad (2.61)$$

Introducing artificial viscosity in this way one does not violate the first and second law of thermodynamics.

### 2.5.3 Smoothing and time selection strategies

The smoothing length can be selected as a constant for all particles which significantly simplifies the searching algorithms for the neighboring particles. However, this approach is not suitable for large deformation and ALE discretization approach (the support domain could be significantly deformed and some of particles could be outside of the original undeformed support). This problem for ALE discretization approach is solved using a smoothing length adaptivity approach where the smoothing length is changing with time. One possible approach is based on the constant number of particles in the Kernel support. However, practically, the half smoothing length equals to the maximum distance between host and neighboring particles.

In case of using an artificial viscosity, the stability condition is defined as (Monaghan, 1992 [209])

$$\delta_{ta} = \min \left( \frac{h}{\sqrt{|\mathbf{F}_a|}}, \frac{h}{c_a + 0.6(\alpha_q c_a + \beta_q \max_b \mu_{ab})} \right) \quad (2.62)$$

where  $\mathbf{F}_i$  is the magnitude of force per unit of mass (acceleration),  $\mu_{ab} = \frac{h \mathbf{v}_{ab} \mathbf{r}_{ab}}{\|\mathbf{r}_{ab}\|^2 + 0.01 h^2}$ ,  $c_a$  is the speed of sound in particle  $a$ ,  $\alpha_q$  and  $\beta_q$  are defined in 2.60.

Hence, the time step is selected as

$$\tau = \min_a \delta_{ta} \quad (2.63)$$

## § 2.6 Conclusion

---

In this chapter, the history of the method development is presented where the key results during this development are highlighted. In addition, different ways of developing of SPH methods are given. A special attention is paid to the strategy of deriving an SPH discretization scheme. All main SPH relations are presented. The justification of the accuracy and correctness is outlined.

---

## SHOCK WAVE PROPAGATION IN COMPLEX MEDIA

---

Investigation of anisotropic materials behaviour (such as aluminium alloys, composite materials) has found significant interest in the research community due to the widespread application of anisotropic materials in aerospace and civil engineering problems. For example, aluminium alloys are one of the main materials in the construction of modern aircraft and rockets. The strain rate dependent mechanical behavior of anisotropic material (e.g. aluminium alloys) in air and space vehicles is important for applications involving impact. These applications cover a wide range of situations such as crashworthiness and protective armours in air and space vehicles and other applications. <sup>1</sup>

### § 3.1 Thermomechanical Model of Deformation and Continuum Fracture

Let us consider a thermoelastoplastic continuum medium with a possible initial distribution of microvoids (microfractures). The damage model of solids body is constructed based on fundamental principles of thermodynamics (Lukyanov, 2004 [182]) and is, therefore, thermodynamically consistent, see Kiselev and Lukyanov (2002) [140]. All processes (irreversible deformation, thermal effect, microfracture) are coupled. The following set of state variables will be considered (Kiselev, 1998 [139]; Kiselev and Lukyanov, 2002 [140]; Lukyanov, 2004 [182]):  $\sigma_{ij}$ ,  $\varepsilon_{ij}^e$  and  $\varepsilon_{ij}^p$ ,  $\omega_{ij}$  is the stress tensor, elastic and inelastic (plastic) parts of strain tensor and the damage tensor, respectively; at the same time, the decomposition of the strain rate tensor into an elastic rate and a plastic rate parts is assumed:  $\dot{\varepsilon}_{ij} = \dot{\varepsilon}_{ij}^e + \dot{\varepsilon}_{ij}^p$ .

---

<sup>1</sup>This chapter is based on the following publications:

1. **Lukyanov, A. A.**, Shock Wave Structure in Anisotropic Carbon Fiber Composites, *Mechanics of Solids*, 48(6), 2013, PP. 706-715.
2. **Lukyanov, A. A.**, Modeling the Effect of Orientation on the Shock Response of a Damageable Composite Material, *J. Applied Physics*, 112, 2012, 084908.
3. **Lukyanov, A. A.**, Segletes, S. B., Frontiers in the Constitutive Modeling of Anisotropic Shock Waves, *Applied Mechanics Reviews*, 64(4), 2012, 040802. **Lukyanov, A. A.**, Chugunov, N., Sadvskii, V. M. and Sadovskaya, O. V., *Modelling of Irreversible Deformation near the Tip of a Crack in a Porous Domain Containing Oil and Gas*, ECMOR XIV - 14th European Conference on the Mathematics of Oil Recovery. 2014. 10.3997/2214-4609.20141808.

The first law of thermodynamics can be written in the following form (change of internal energy)

$$\dot{e} = \frac{1}{\rho} \sigma_{ij} \dot{\varepsilon}_{ij} - \frac{1}{\rho} \operatorname{div} \mathbf{q}. \quad (3.1)$$

Where the dot above the symbol represents the material derivative with respect to time. The second law of thermodynamics can be written in the form of the Clausius-Duhem inequality:

$$\dot{S} \geq -\frac{1}{\rho} \operatorname{div} \left( \frac{\mathbf{q}}{T} \right). \quad (3.2)$$

Here  $e$  and  $S$  is the internal energy and entropy respectively;  $T$  is the absolute temperature;  $\mathbf{q}$  is the heat flux vector;  $\rho$  is the density.

Using the Legendre transformation for the physical quantities  $e$  and  $S$ , the expression for the specific free energy can be written as follows,  $F = e - TS$ . Combing inequality (3.2), together with (3.1) can now be rewritten as

$$\frac{1}{\rho} \sigma_{ij} \dot{\varepsilon}_{ij} - \frac{1}{\rho} \frac{\mathbf{q} \cdot \operatorname{grad} T}{T} - \dot{T} S - \dot{F} \geq 0. \quad (3.3)$$

Taking into account that the free energy is a function of the following set of state variables:  $\varepsilon_{ij}^e, \varepsilon_{ij}^p, \omega_{ij}, T$ , i.e.  $F = F(\varepsilon_{ij}^e, \varepsilon_{ij}^p, \omega_{ij}, T)$ , inequality (3.3) yields the following condition, which is valid for all processes taking place within the continuum:

$$\begin{aligned} & \left( \frac{1}{\rho} \sigma_{ij} - \frac{\partial F}{\partial \varepsilon_{ij}^e} \right) \dot{\varepsilon}_{ij}^e - \left( \frac{\partial F}{\partial T} + S \right) \dot{T} + \frac{1}{\rho} \sigma_{ij} \dot{\varepsilon}_{ij}^p - \\ & - \frac{\partial F}{\partial \varepsilon_{ij}^p} \dot{\varepsilon}_{ij}^p - \frac{\partial F}{\partial \omega_{ij}} \dot{\omega}_{ij} - \frac{1}{\rho} \frac{\mathbf{q} \cdot \operatorname{grad} T}{T} \geq 0. \end{aligned} \quad (3.4)$$

Using inequality (3.4), the following qualities are required to guarantee positive definite form in (3.4) for all physical processes:

$$\sigma_{ij} = \rho \frac{\partial F}{\partial \varepsilon_{ij}^e}, \quad S = -\frac{\partial F}{\partial T}. \quad (3.5)$$

Furthermore, (3.5) and (3.4) yield an expression for the total dissipation function to be obtained

$$d = d_M + d_F + d_T \geq 0, \quad (3.6)$$

where  $d = \rho \gamma$  is the dissipation; ( $\gamma = T \dot{S}_i$  is the entropy production) and the following notations and relations are assumed:

$$d_M = \left( \sigma_{ij} - \rho \frac{\partial F}{\partial \varepsilon_{ij}^p} \right) \dot{\varepsilon}_{ij}^p, \quad d_F = -\rho \frac{\partial F}{\partial \omega_{ij}} \dot{\omega}_{ij}, \quad d_T = -\frac{\mathbf{q} \cdot \operatorname{grad} T}{T}. \quad (3.7)$$

Here  $d_M$  is the mechanical dissipation;  $d_F$  is the dissipation of continuum fracture;  $d_T$  is the thermal dissipation;

$\tau_{ij} = \left( \sigma_{ij} - \rho \frac{\partial F}{\partial \varepsilon_{ij}^p} \right)$  is the effective stress tensor. It can be seen from (3.7) that the free energy  $F$  depends upon the plastic deformations, which in turn means that the dissipation process is defined by the effective stress  $\tau_{ij}$  (Kiselev, 1998 [139]) and not the real Cauchy stress  $\sigma_{ij}$ . The introduction of plastic deformation  $\varepsilon_{ij}^p$  into  $F$  is the free energy, allows to take into account deformative anisotropy of the material during plastic deformation (Kiselev, 1998 [139]).

In addition, expression (3.1) can be expressed in the following form by using  $F = e - TS$

$$\dot{F} + \dot{S}T + S\dot{T} = \frac{1}{\rho} \sigma_{ij} \dot{\varepsilon}_{ij}^e + \frac{1}{\rho} \sigma_{ij} \dot{\varepsilon}_{ij}^p - \frac{1}{\rho} \operatorname{div} \mathbf{q}.$$

Using (3.5), the final expression for entropy production can now be obtained

$$T\dot{S} = \frac{1}{\rho} \tau_{ij} \dot{\varepsilon}_{ij}^p - \frac{\partial F}{\partial \omega_{ij}} \dot{\omega}_{ij} - \frac{1}{\rho} \operatorname{div} \mathbf{q}. \quad (3.8)$$

In conclusion, the entropy in the heat conduction equation can be characterised by a set of independent state variables:  $\varepsilon_{ij}^e, \varepsilon_{ij}^p, \omega_{ij}, T$ .

### 3.1.1 Basic Assumptions

The following set of assumptions can be applied in order to simplify the formulation of a final set of constitutive equations. Let us assume:

1. Rate of elastic deformations are small:  $\dot{\varepsilon}_{ij}^e \dot{\varepsilon}_{ij}^e \ll 1$ ;
2. Dissipation function (3.6), is a sum of the three positive terms defined in (3.7):

$$d_M \geq 0, \quad d_F \geq 0, \quad d_T \geq 0. \quad (3.9)$$

Note, that in a case of classical Fourier laws,  $\mathbf{q} = -\kappa \text{grad } T$ , where the thermal dissipation is always taken to be positive using:

$$d_T = \frac{\tilde{\kappa}(\text{grad}T)^2}{T} \geq 0,$$

where  $\tilde{\kappa} \geq 0$  is the conductivity tensor. The hypothesis  $d_M \geq 0$  is the well-known Planck inequality. This assumption (3.9) will be used in order to choose the kinematic relations for the internal state variables  $\varepsilon_{ij}^p, \omega_{ij}$ .

3. The free energy,  $F$ , includes several parts, namely:

$$F = F_1(\varepsilon_{ij}^e, \omega_{ij}, T) + F_2(\varepsilon_{ij}^p, \omega_{ij}, T) + F_0(T) \quad (3.10)$$

$$\widehat{F}(\varepsilon_{ij}^e, \varepsilon_{ij}^p, \omega_{ij}, T) = F_1(\varepsilon_{ij}^e, \omega_{ij}, T) + F_2(\varepsilon_{ij}^p, \omega_{ij}, T) \quad (3.11)$$

The first relation of (3.5), together with (3.10) supports the assumption that the accumulation of plastic deformation does not change the elastic properties of the materials. Let us assume also that

$$-\rho \frac{\partial F}{\partial \varepsilon_{ij}^p} = \Gamma \varepsilon_{ij}^p,$$

$\Gamma \geq 0$  is the parameter for material strain anisotropy. In this research, the parameter for material strain anisotropy is equal zero, so  $\Gamma = 0$  is assumed.

5. For the Free energy, the following relation is assumed (Duhamel-Neumann's law – the generalized Hooke's law of the thermo-elasticity)

$$\frac{\partial F}{\partial T} = -\bar{\alpha}_{ij}^v \mathbb{C}_{ijkl} \varepsilon_{kl}^e, \quad \bar{\alpha}_{ij}^v = \frac{\alpha_{ij}^v}{\rho}, \quad (3.12)$$

where  $\alpha_{ij}^v$  is the tensor of volume expansion coefficients.

6. For dissipation of continuum fracture  $d_M$ , the Onsager theory is applied which can be written for isotropic media as:

$$-\rho \frac{\partial F}{\partial \omega_{ij}} = \Lambda_{ijkl} \dot{\omega}_{kl}, \quad (3.13)$$

where  $\Lambda_{ijkl} \geq 0$  is the Onsager's tensor. Relations (3.13) state that the linear link between the thermodynamic forces and thermodynamic flows are in accordance with Onsager's theory (Sedov, 1972 [237]; Glansdorff and Prigogine, 1971 [98]).

The specific heat capacity at constant volume (it approaches the classical Dulong and Petit constant after Debye's temperature (Poirier, 2002 [224])) is defined as

$$c_v = -T \left. \frac{\partial^2 F_0}{\partial T^2} \right|_v, \quad S_0 = -\frac{\partial F_0}{\partial T}, \quad (3.14)$$

where  $S_0$  is the reference entropy. It follows that

$$S_0 = c_v \ln \left( \frac{T}{T_0} \right), \quad S = S_0 - \frac{\partial \widehat{F}}{\partial T}. \quad (3.15)$$

Using Duhamel-Neumann's law (3.12) and differentiating relation (3.15) with respect to time leads to the following form:

$$\dot{S}(\tilde{\varepsilon}, T) = \dot{S}_0(T) + [\bar{\alpha}_{ij}^v \mathbb{C}_{ijkl} \varepsilon_{kl}^e]^\bullet = c_v \frac{\dot{T}}{T} + [\bar{\alpha}_{ij}^v \mathbb{C}_{ijkl} \varepsilon_{kl}^e]^\bullet. \quad (3.16)$$

Using relation (3.16) and the Onsager's theory (3.13), equation (3.8) can be rewritten in the form:

$$\rho \left( c_v \dot{T} + T \cdot [\bar{\alpha}_{ij}^v \mathbb{C}_{ijkl} \epsilon_{kl}^e]^\bullet \right) = \tau_{ij} \dot{\epsilon}_{ij}^p + \dot{\omega}_{ij} \Lambda_{ijkl} \dot{\omega}_{kl} - \nabla \cdot \mathbf{q}. \quad (3.17)$$

where  $[\cdot]^\bullet$  represents the material time derivative.

In summary, it has been possible to derive an equation describing the change of temperature, by taken into account all dissipative processes and finite deformation which can occur within a material (plastic deformation, damage evolution, mechanical dissipation). In order to complete our description, the system of constitutive equations are now required.

### 3.1.2 System of Constitutive Equations

Thermodynamically consistent modeling approach should allow for the damage formation and accumulation of different shapes (described by the damage tensor  $\omega_{ij}$ ) in regions of pronounced tension, their disappearance under compression as well as the heating effects and the accumulation of damage in the domains of intensive tension. The deformation, damage development and heating processes are mutually dependent.

The damage parameters in this work are two invariants of the damage tensor  $\omega_{ij}$ : the first invariant  $\omega = \alpha_{ij} \omega_{ij} / 3$  is the volumetric damage (concentration of microvoids) and  $\alpha = \sqrt{\omega'_{ij} \omega'_{ij}}$  is the intensity of deviatoric part of the damage tensor, where  $\omega'_{ij} = \omega_{ij} - (\omega_{kk} / 3) \alpha_{ij}$  is the shear damage. A general form of the constitutive equations proposed for the investigation of damage processes in anisotropic media with the associated and generalised incompressible plasticity flow model can be written as (the contraction by repeating indices is assumed throughout this model):

$$\sigma'_{ij} = -p'_* \alpha_{ij} + \tilde{\mathbf{S}}'_{ij}, \quad p'_* = p'_{eos} + \frac{\beta_{ij} \tilde{\mathbf{S}}'_{ij}}{\beta_{kl} \alpha_{kl}}, \quad \tilde{\mathbf{S}}'_{ij} = \sigma_{ij} - \alpha_{ij} \cdot \frac{\sigma_{kl} \alpha_{kl}}{\|\alpha\|^2}, \quad (3.18)$$

$$\mathbb{C}_{ijkl}^\alpha \dot{\epsilon}_{kl} = \left( \tilde{\mathbf{S}}'_{ij} \right)^\nabla + \lambda \mathbb{C}_{ijkl}^\alpha \frac{\partial \Pi(\tilde{\mathbf{S}}'_{ij}, p'_*)}{\partial \tilde{\mathbf{S}}_{kl}} + \mathbb{C}_{ijkl}^\alpha \Lambda_\omega \dot{\omega} \frac{\partial \psi}{\partial \tilde{\mathbf{S}}_{kl}}, \quad (3.19)$$

$$\hat{\mathbf{F}}(\tilde{\mathbf{S}}'_{kl}, p'_*) = 0, \quad \tilde{\mathbf{S}}'_{ij} = \frac{\tilde{\mathbf{S}}_{ij}}{(1-\omega)(1-\alpha)}, \quad p'_* = \frac{p_*}{(1-\omega)(1-\alpha)}, \quad (3.20)$$

$$\mathbb{C}_{ijkl}^\alpha = \left( \mathbb{C}_{ijkl} - \frac{\alpha_{ij} \alpha_{pq} \mathbb{C}_{pqkl}}{\|\alpha\|^2} \right), \quad p'_{eos} = \frac{p_{eos}}{(1-\omega)(1-\alpha)}, \quad (3.21)$$

$$p'_{eos} = K_C(\rho, T) \left( \dot{\epsilon}_{kk} - \alpha'_{ij} \alpha_{ij} \dot{T} + \Lambda_{\tilde{\omega}} \frac{\partial \chi}{\partial p'_*} \dot{\omega} \right), \quad (3.22)$$

$$\rho c_v \dot{T} + \rho T [\bar{\alpha}_{ij}^v \mathbb{C}_{ijkl} \epsilon_{kl}^e]^\bullet = \tau_{ij} \dot{\epsilon}_{ij}^p + \Lambda_\omega \dot{\omega}^2 + \Lambda_\alpha \dot{\alpha}^2 - \frac{\partial \mathbf{q}_i}{\partial \mathbf{x}_i}, \quad (3.23)$$

where  $p_* \alpha_{ij}$  is the generalized spherical part of the stress tensor (Lukyanov, 2008 [184]; Lukyanov and Segletes, 2012 [189]; Lukyanov, 2012 [187]),  $p_{eos}$  is the thermodynamic (equation of state) response pressure,  $\tilde{\mathbf{S}}_{ij}$  is the generalized deviatoric stress tensor ( $\alpha_{ij} \tilde{\mathbf{S}}_{ij} = 0$ ),  $\alpha_{ij}$  and  $\beta_{ij}$  are the first and second generalizations of the Kronecker delta,  $\mathbb{C}_{ijkl}$  is the elastic stiffness matrix of the undamaged material,  $\mathbb{C}_{ijkl}^\alpha$  is the generalized shear elastic stiffness matrix of the undamaged material,  $K_C$  is the first generalized bulk modulus,  $\|\alpha\| = \sqrt{\alpha_{ij} \alpha_{ij}}$  is the Frobenius norm,  $\Pi(\tilde{\mathbf{S}}'_{ij}, p'_*)$  is the plastic potential for associated anisotropic generalized incompressible plasticity,  $\lambda$  is the Lagrangian plasticity multiplier,  $\hat{\mathbf{F}}$  is the yield function,  $\Lambda_\omega$  and  $\Lambda_\alpha$  are the Onsager's parameters,  $\epsilon_{kl}$  is the deviatoric part of the strain tensor,  $\mathbf{q}_i = -\kappa_{ij} \frac{\partial T}{\partial \mathbf{x}_j}$  is the heat flux vector,  $\kappa_{ij}$  is the heat conductivity tensor. The dot above symbols indicate the total (substantial) derivative with respect to time. The procedure of construction for the tensor functions  $\alpha_{kl}$  and  $\beta_{kl}$  have been defined in (Lukyanov, 2008 [184]; Lukyanov and Segletes, 2012 [189]; Lukyanov, 2012 [187]):

$$\begin{aligned} \alpha_{11} &= \left( \sum_{k=1}^3 \mathbf{C}_{k1} \right) \cdot 3\bar{K}_C, \quad \alpha_{22} = \left( \sum_{k=1}^3 \mathbf{C}_{k2} \right) \cdot 3\bar{K}_C, \\ \alpha_{33} &= \left( \sum_{k=1}^3 \mathbf{C}_{k3} \right) \cdot 3\bar{K}_C, \quad \alpha_{ij} \alpha_{ij} = 3, \end{aligned} \quad (3.24)$$

$$K_C = \frac{1}{3\sqrt{3}} \sqrt{\left(\sum_{k=1}^3 \mathbf{C}_{k1}\right)^2 + \left(\sum_{k=1}^3 \mathbf{C}_{k2}\right)^2 + \left(\sum_{k=1}^3 \mathbf{C}_{k3}\right)^2}, \quad (3.25)$$

$$K_C = \frac{1}{9\bar{K}_C},$$

where  $\mathbf{C}_{ij}$  is the elastic stiffness matrix  $\mathbb{C}_{ijkl}^\alpha$  (written in Voigt notation). The elements of the tensor  $\beta_{kl}$  are

$$\beta_{11} = \left(\sum_{k=1}^3 \mathbf{J}_{k1}\right) \cdot 3K_S, \quad \beta_{22} = \left(\sum_{k=1}^3 \mathbf{J}_{k2}\right) \cdot 3K_S, \quad (3.26)$$

$$\beta_{33} = \left(\sum_{k=1}^3 \mathbf{J}_{k3}\right) \cdot 3K_S, \quad \beta_{ij}\beta_{ij} = 3,$$

$$\frac{1}{K_S} = \sqrt{3} \sqrt{\left(\sum_{k=1}^3 \mathbf{J}_{k1}\right)^2 + \left(\sum_{k=1}^3 \mathbf{J}_{k2}\right)^2 + \left(\sum_{k=1}^3 \mathbf{J}_{k3}\right)^2}, \quad (3.27)$$

where  $\mathbf{J}_{ij}$  are elements of the compliance matrix  $\left(\mathbb{C}_{ijkl}^\alpha\right)^{-1}$  (written in Voigt notation). In the limit of isotropy, the proposed generalisation returns to the traditional classical case where tensors  $\alpha_{ij}$  and  $\beta_{ij}$  equal  $\delta_{ij}$ .

Problems of impact loading are characterised by shock formation and propagation within the material. Therefore, for these types of problems it is necessary to consider integral conservation laws at the front of shock wave propagation. According to the classical theory of continuum mechanics, the satisfaction of conservation laws for the physical variables with discontinuous leads to the Rankine - Hugoniot condition (or equation of state). Introduction of an equation of state into the system of constitutive equations allows the compression shock wave distribution to be correctly defined.

The Mie-Grüneisen equation of state with cubic shock velocity as a function of particle velocity can be used which defines pressure as

$$p^{EOS} = \begin{cases} \frac{\rho_0 c^2 \mu \left[1 + \left(1 - \frac{\Gamma}{2}\right) \mu - \frac{\Gamma}{2} \mu^2\right]}{\left[1 - (S_1 - 1) \mu - S_2 \frac{\mu^2}{\mu + 1} - S_3 \frac{\mu^3}{(\mu + 1)^2}\right]^2} + (1 + \mu) \cdot \Gamma \cdot E, & \mu > 0; \\ \rho_0 c^2 \mu + (1 + \mu) \cdot \Gamma \cdot E, & \mu < 0; \end{cases}, \quad (3.28)$$

$$K_C(\rho, T) = \rho \left(\frac{\partial p^{EOS}}{\partial \rho}\right), \quad \Gamma = \frac{\gamma_0 + a\mu}{1 + \mu}, \quad \rho \frac{\partial E}{\partial \rho} = \frac{p_{eos}}{\rho_0}, \quad (3.29)$$

where  $\mu = \frac{\rho}{\rho_0} - 1$ ,  $\rho$  is the current density,  $\rho_0$  is the initial density,  $E$  is the internal energy per initial density  $\left(E = \frac{e}{\rho_0}\right)$ ,  $S_1, S_2, S_3$  is the intercept of the  $U-u_p$  curve. Parameters  $c, S_1, S_2, S_3, \gamma_0, a$  represent material properties which define its EOS. Parameters have been defined to cover a large number of isotropic materials (Steinberg, 1991 [241]).

In a case of isotropic media, a system of constitutive equations for the damageable thermo-visco-elasto-plastic medium 3.18-3.20 reduces to the following form:

$$\sigma'_{ij} = -p'_{EOS} \delta_{ij} + \mathbf{S}'_{ij}, \quad (3.30)$$

$$(\mathbf{S}'_{ij})^\nabla + \tilde{\lambda} \mathbf{S}'_{ij} = 2\mu \left(e_{ij}^e - \Lambda_\alpha \frac{\partial \psi}{\partial \sigma_{ij}} \dot{\alpha}\right), \quad \dot{e}_{ij} = \dot{e}_{ij}^p + \dot{e}_{ij}^e - \Lambda_\alpha \frac{\partial \psi}{\partial \sigma_{ij}} \dot{\alpha}, \quad (3.31)$$

$$\dot{e}_{ij}^p = \dot{e}_{ij}^p = 2\tilde{\lambda} \cdot \mathbf{S}'_{ij}, \quad \mathbf{S}'_{ij} = \frac{\mathbf{S}_{ij}}{(1 - \omega)(1 - \alpha)}, \quad \mathbf{S}'_{ij} \mathbf{S}'_{ij} \leq \frac{2}{3} Y_0^2, \quad (3.32)$$

where  $\mu$  is the shear modulus, symbol  $\nabla$  is the Jaumann derivative with respect to time for the tensor component:

$$(\mathbf{S}_{ij})^\nabla = \dot{\mathbf{S}}_{ij} - \mathbf{S}_{ik} \mathbf{W}_{jk} - \mathbf{S}_{jk} \mathbf{W}_{ik}. \quad (3.33)$$

where  $\mathbf{W}_{ij}$  is the skew symmetric part of the velocity gradient.

It should be noted that a part of the classical model of an elastoplastic medium, the expression for the total deviatoric part of the strain tensor consists of three parts. An additional term, conditioned by the developing shear damage, is incorporated to take into account the growth of the damage. The decomposition of the strain tensor into three similar parts can be found also in papers (Bamman, 1989 [16]; Bamman *et al.* [17]; Kiselev and Lukyanov, 2002 [140]; Lukyanov, 2004 [182]).

In order to describe the evolution of volumetric damage (spherical type of damage), the following expression can be used:

$$\begin{aligned} \dot{\omega} = \varphi(\omega, \sigma) = & B \left( \frac{\sigma}{1-\omega} - \sigma^* \right)^\beta H \left( \frac{\sigma}{1-\omega} - \sigma^* \right) + \\ & + \omega \frac{\sigma - \sigma^+}{4\eta} H(\sigma - \sigma^+) + \omega \frac{\sigma - \sigma^-}{4\eta} H(\sigma^- - \sigma), \\ \sigma^+ = & -\frac{2}{3}Y \ln \omega, \quad \sigma^- = \frac{2}{3}Y \ln \omega, \end{aligned} \quad (3.34)$$

which consists of three terms, the first one describes the initiation of the spherical damage (Kiselev and Lukyanov, 2002 [140]). The next two terms describe expansion and collapse of micropores and are obtained from the solution of the dynamic behaviour of a single spherical pore (see previous section). In order to obtain the description of shear damage, the phenomenological model is used, which is based upon the assumption that shear damage is initiated when the effective plastic strain (intensity of plastic deformation) achieves a critical value:

$$\begin{aligned} \dot{\alpha} = & C \cdot \dot{\varepsilon}_u^p \cdot H(\varepsilon_u^p - \varepsilon_{u*}^p), \\ \eta = & \eta_0(1-\omega)(1-\alpha), \quad Y = Y_0(1-\omega)(1-\alpha), \\ \rho c_v \dot{T} + \alpha_v K \dot{\varepsilon}^e T = & S_{ij} \dot{\varepsilon}_{ij}^p + \Lambda_\omega \dot{\omega}^2 + \Lambda_\alpha \dot{\alpha}^2 - \text{div} \mathbf{q}, \\ \mathbf{q} = & -\varkappa \text{grad} T, \quad \varepsilon_u^p = \sqrt{\varepsilon_{ij}^p \varepsilon_{ij}^p}, \quad S_u = \sqrt{S_{ij} S_{ij}}. \end{aligned}$$

Here  $\sigma_{ij}$ ,  $\varepsilon_{ij}^e$ ,  $\varepsilon_{ij}^p$  represent the components of stress tensor, elastic and inelastic strain (viscoplastic deformation) respectively. ( $\varepsilon_{ij} = \varepsilon_{ij}^e + \varepsilon_{ij}^p$ ;  $\varepsilon_{kk}^p = 0$ );  $T$  is the absolute temperature;  $\mathbf{q}$  is the heat flux;  $\rho$  is the density,  $\varepsilon_u^p$  is the intensity of plastic deformation;  $B$ ,  $C$ ,  $\Lambda_\omega$ ,  $\Lambda_\alpha$ ,  $\sigma_*$ ,  $\varepsilon_{u*}^p$  is the material parameters;  $\eta_0$ ,  $Y_0$  is the dynamic viscosity, yield limit for undamaged (virgin) materials;  $c_v$  is the heat capacity at constant stress;  $\alpha_v$  is the volume expansion coefficient;  $\varkappa$  is the conductivity coefficient;  $H(x)$  is the Heaviside function; the dot above the symbol means material derivative with respect to time.

The main aspects of a phenomenological strength model can be characterized by a yield criterion representing a surface that separates the elastic and plastic regions of the stress space, a flow potential gradient that represents the direction of plastic strain rate, a strain hardening rule and that plastic flow is incompressible. Following work by Lukyanov (2008) [184], the mathematically consistent yield function of a fully anisotropic material based on generalized decomposition of the stress tensor is developed:

$$\begin{aligned} \hat{F}(\tilde{S}_{ij}) = \Psi(\tilde{S}_{ij}) (1 + \chi p^*) \leq & Y(\bar{\varepsilon}_p), \\ p^* = \frac{1}{\|\alpha\|^2} \sigma_{ij} \alpha_{ij}, \end{aligned} \quad (3.35)$$

where  $\Psi(\tilde{S}_{ij})$  is described by generalized Hill's yield functions:

$$\begin{aligned} \Psi^2(\tilde{S}_{ij}) = & F(\alpha_3 \tilde{S}_2 - \alpha_2 \tilde{S}_3)^2 + G(\alpha_1 \tilde{S}_3 - \alpha_3 \tilde{S}_1)^2 + \\ & + H(\alpha_{22} \tilde{S}_{11} - \alpha_{11} \tilde{S}_{22})^2 + 2N \tilde{S}_{12}^2 + 2L \tilde{S}_{23}^2 + 2M \tilde{S}_{13}^2, \end{aligned} \quad (3.36)$$

where  $\tilde{S}_{ij}$  is the generalized deviatoric stress tensor ( $\tilde{S}_i = \tilde{S}_{ii}$ ,  $i = 1, 2, 3$ );  $\alpha_{ij}$  is the generalized Kronecker's symbol (Lukyanov, 2008 [184]) ( $\alpha_i = \alpha_{ii}$ ,  $i = 1, 2, 3$ ). The material constants  $\chi$ ,  $F$ ,  $G$ ,  $H$ ,  $N$ ,  $L$ ,  $M$  are specified in terms of selected initial yield stresses in uniaxial tension, compression, and equibiaxial tension. It is important to note that plasticity model (3.36) is naturally independent from the generalized hydrostatic pressure and therefore, the following equality can be written:

$$\Psi(\tilde{S}_{ij}) \equiv \Psi(\sigma_{ij}), \quad \sigma_{ij} = p^* \alpha_{ij} + \tilde{S}_{ij}, \quad p^* \neq 0, \quad (3.37)$$

where  $\sigma_{ij}$  is the stress tensor. In this paper, a uniaxial strain state (one-dimensional reduced mathematical formulation in strain space) and the adiabatic approximation assumptions are considered for modelling shock waves propagation in anisotropic solids. Therefore, material parameters and their numerical values for AA7010-T6 are taken as presented in Table 3.1. Parameters  $c \in [c_{II}, c_I]$ ,  $S_1, S_2, S_3, \gamma_0, a$  represent material properties

**Table 3.1:** *Material properties for AA7010-T6 used in analysis.*

Parameter	Description	AA7010-T6
$F$	Anisotropy coefficient	0.6898
$G$	Anisotropy coefficient	0.2873
$H$	Anisotropy coefficient	0.6824
$Y$ [MPa]	Yield stress	500.0
$\chi$ [MPa <sup>-1</sup> ]	Pressure dependency factor	0.0
$\alpha_{11}$	Tensor $\alpha_{ij}$ (11 direction)	0.9976
$\alpha_{22}$	Tensor $\alpha_{ij}$ (22 direction)	1.0029
$\alpha_{33}$	Tensor $\alpha_{ij}$ (33 direction)	0.9994

which define its EOS (3.28). A description of their numerical values for AA7010-T6 is shown in Table 3.2.

**Table 3.2:** *EOS data for AA7010-T6 used in analysis.*

Parameter	Description	AA7010-T6
$c$ [m/s]	Velocity curve intercept	5154
$S_1$	First slope coefficient	1.4
$S_2$	Second slope coefficient	0.0
$S_3$	Third slope coefficient	0.0
$\gamma_0$	Grüneisen gamma	2.0
$a$	First-order volume correction	0.48
$\rho_0$ [kg/m <sup>3</sup> ]	Initial density	2810
$K_C$ [GPa]	Generalized bulk modulus	74.65

### 3.1.3 Criterion of Macrofracture

It has been shown that the development of intensive plastic flow and the accumulation of microvoids within a material, represents the pre-damage stage of the material. The criterion based on specific internal part of entropy (3.38) was chosen to describe the initiation of new free surfaces (macrofracture of the material). For the case of an impact test with spallation, where there are regions of high tensile stresses (Kiselev, 1998 [139]; Kiselev and Lukyanov, 2002 [140]), the main contribution to dissipation (3.38) will come from the terms  $d_M$  and  $d_F$ . When criterion (3.38) is realized in some point of the material, a crack will occur, or in mathematical language, a new free surface occurs which will propagate within the material. The problem of numerical simulation of crack propagation is a self-independent problem and requires additional investigations.

The development of intensive plastic flow and the accumulation of microdamage is the pre-damage stage of a macrofracture (fracture of material). The criterion used to mark the beginning of a macrofracture (new free surface origination) is based upon an entropy criterion expressed in terms of the dissipative processes within the material (Kiselev and Yumashev, 1992 [141]; Kiselev, 1998 [139]; Kiselev and Lukyanov, 2002 [140]):

$$D = \int_0^{t_*} \frac{1}{\rho} (d_M + d_F + d_T) dt = D_*, \quad (3.38)$$

where  $t_*$  is the time of macrofracture process,  $D_*$  is the material parameter (internal part of total specific entropy).



### § 3.2 Numerical Integration of Anisotropic Plasticity Model

The newly developed plasticity model takes into account isotropic material as a special case (associated anisotropic plasticity model reduces to the classical associated von Misses plasticity model, i.e. yield function (3.36) equals to von Misses yield function, therefore, associated plastic flow takes a place). Therefore, the new numerical technique being developed must take into account the numerical aspect of the isotropic plasticity as a special case.

#### 3.2.1 Numerical Aspects of Isotropic Case

Firstly, the isotropic case is considered as a special case of anisotropy. This well-studied case is used in the verification process of the anisotropic material model. In the limit of isotropy (i.e., mechanical properties are independent from the material orientation), generalised deviatoric stress coincides with the classical deviatoric stress tensor and satisfies to:

$$\mathbf{S}_{ij}^{\nabla} = (\mathbf{S}_{ij}^*)^{\nabla} - 4 \cdot \mu \cdot \dot{\lambda} \cdot \mathbf{S}_{ij} = 2 \cdot \mu \cdot \dot{\mathbf{e}}_{ij} - 4 \cdot \mu \cdot \dot{\lambda} \cdot \mathbf{S}_{ij}, \quad (3.39)$$

where  $\mathbf{S}_{ij}^*$  is a trial deviatoric stress tensor,  $\mathbf{S}_{ij}$  is a true deviatoric stress tensor,  $\mu$  is a shear modulus,  $\mathbf{e}_{ij}$  is a deviatoric strain tensor. Finite difference scheme of the first order approximation can be written in the form:

$$\frac{\mathbf{S}_{ij}^{n+1} - \hat{\mathbf{S}}_{ij}^n}{\Delta t} = \frac{(\mathbf{S}_{ij}^*)^{n+1} - \hat{\mathbf{S}}_{ij}^n}{\Delta t} - 4 \cdot \mu^{n+1} \cdot \dot{\lambda}^{n+1} \cdot \mathbf{S}_{ij}^{n+1}, \quad (3.40)$$

where  $\hat{\mathbf{S}}_{ij}^n = \mathbf{S}_{ij}^n + (\mathbf{S}_{ik}^n \mathbf{W}_{jk}^n + \mathbf{S}_{jk}^n \mathbf{W}_{ik}^n) \cdot \Delta t$ . Therefore, (3.40) leads to the relation

$$\mathbf{S}_{ij}^{n+1} = (\mathbf{S}_{ij}^*)^{n+1} - 4 \cdot \mu^{n+1} \cdot \dot{\lambda}^{n+1} \cdot \mathbf{S}_{ij}^{n+1} \cdot \Delta t, \quad (3.41)$$

which can be rewritten as

$$\mathbf{S}_{ij}^{n+1} = \frac{(\mathbf{S}_{ij}^*)^{n+1}}{1 + 4 \cdot \mu^{n+1} \cdot \dot{\lambda}^{n+1} \cdot \Delta t} \quad (3.42)$$

In the case of isotropic material, the anisotropic yield function (3.36) reduces to the von Misses yield function. Thus, substituting (3.42) into von Misses yield function, the parameter  $\dot{\lambda}^{n+1}$  (or  $d\dot{\lambda}^{n+1}$ ) can be rewritten as

$$\dot{\lambda}^{n+1} = \frac{1}{4 \cdot \mu^{n+1} \cdot \Delta t} \cdot \left( \frac{\sqrt{(S_{ij}^*)^{n+1} (S_{ij}^*)^{n+1}}}{k^{n+1}} - 1 \right) \cdot H \left( \frac{\sqrt{(S_{ij}^*)^{n+1} (S_{ij}^*)^{n+1}}}{k^{n+1}} - 1 \right), \quad (3.43)$$

$$d\dot{\lambda}^{n+1} = \frac{1}{4 \cdot \mu^{n+1}} \cdot \left( \frac{\sqrt{(S_{ij}^*)^{n+1} (S_{ij}^*)^{n+1}}}{k^{n+1}} - 1 \right) \cdot H \left( \frac{\sqrt{(S_{ij}^*)^{n+1} (S_{ij}^*)^{n+1}}}{k^{n+1}} - 1 \right), \quad (3.44)$$

where  $S_{ij}^*$  is the trial value of the deviatoric stress tensor at  $n + 1$  moment of time,  $\mu^{n+1}$  is the shear modulus at  $n + 1$  moment of time,  $k^{n+1} = \sqrt{\frac{2}{3}} Y^{n+1}$  is the effective yield stress,  $H(\bullet)$  is the Heaviside function.

The true deviatoric stress tensor at the von Misses yield surface can be derived by using (3.44):

$$S_{ij}^{n+1} = \frac{k^{n+1} (S_{ij}^*)^{n+1}}{\sqrt{(S_{ij}^*)^{n+1} (S_{ij}^*)^{n+1}}}. \quad (3.45)$$

It is very important to investigate the finite difference scheme of second order. In this case (3.39) can be written in the following form:

$$\frac{S_{ij}^{n+1} - \hat{S}_{ij}^n}{\Delta t} = (\mu^{n+1} + \mu^n) \cdot \dot{\mathbf{e}}_{ij}^{n+\frac{1}{2}} - 4 \cdot \frac{1}{2} \cdot (\mu^{n+1} + \mu^n) \cdot \frac{1}{2} \left( \dot{\lambda}^{n+1} \cdot S_{ij}^{n+1} + \dot{\lambda}^n \cdot S_{ij}^n \right) \quad (3.46)$$

where  $\hat{S}_{ij}^n = S_{ij}^n + (S_{ik}^n \mathbf{W}_{jk}^n + S_{jk}^n \mathbf{W}_{ik}^n) \cdot \Delta t$ . Finally, (3.46) can be rewritten

$$(S_{ij}^*)^{n+1} = \hat{S}_{ij}^n + \mu^{n+\frac{1}{2}} \cdot \dot{\mathbf{e}}_{ij}^{n+\frac{1}{2}} \cdot \Delta t - 4 \cdot \mu^{n+\frac{1}{2}} \cdot \frac{\Delta t}{2} \dot{\lambda}^n \cdot S_{ij}^n. \quad (3.47)$$

Furthermore, substituting (3.47) into von Misses yield function, the parameter  $\dot{\lambda}^{n+1}$  (or  $d\dot{\lambda}^{n+1}$ ) and true deviatoric stress tensor at the yield surface can be rewritten as

$$\dot{\lambda}^{n+1} = \frac{1}{4 \cdot \mu^{n+\frac{1}{2}} \cdot \frac{\Delta t}{2}} \cdot \left( \frac{\sqrt{(S_{ij}^*)^{n+1} (S_{ij}^*)^{n+1}}}{k^{n+1}} - 1 \right) H \left( \frac{\sqrt{(S_{ij}^*)^{n+1} (S_{ij}^*)^{n+1}}}{k^{n+1}} - 1 \right), \quad (3.48)$$

$$S_{ij}^{n+1} = \frac{k^{n+1} (S_{ij}^*)^{n+1}}{\sqrt{(S_{ij}^*)^{n+1} (S_{ij}^*)^{n+1}}}. \quad (3.49)$$

In conclusion, the equations (3.48) and (3.49) provides the numerical integration with prediction-correction type of scheme-algorithm for isotropic elasto-plastic constitutive equations. The equation (3.49) will be used in the next section for the verification and validation of the numerical algorithm for anisotropic incompressible plasticity model.

### 3.2.2 Numerical Algorithm for Anisotropic Incompressible Plastic Model

The differential equation for the generalised deviatoric stress tensor in a case of full decomposition of the stress tensor can be written as follows:

$$\left( \tilde{\mathbf{S}}_{ij} \right)^\nabla = \mathbf{C}_{ijkl} (\dot{\epsilon}_{kl} - \dot{\epsilon}_{kl}^p) - \frac{\alpha_{ij} \cdot [\alpha_{pq} \cdot \mathbf{C}_{pqkl} (\dot{\epsilon}_{kl} - \dot{\epsilon}_{kl}^p)]}{\|\alpha\|}, \quad (3.50)$$

or

$$\left( \tilde{\mathbf{S}}_{ij} \right)^\nabla = \mathbf{C}_{ijkl} \dot{\epsilon}_{kl} - \frac{\alpha_{ij} \cdot \alpha_{pq} \cdot \mathbf{C}_{pqkl} \dot{\epsilon}_{kl}}{\|\alpha\|} - \left[ \mathbf{C}_{ijkl} \dot{\epsilon}_{kl}^p - \frac{\alpha_{ij} \alpha_{pq} \cdot \mathbf{C}_{pqkl} \dot{\epsilon}_{kl}^p}{\|\alpha\|} \right], \quad (3.51)$$

Based on (3.51), the trial deviatoric part of stress tensor is calculated as follows:

$$\left( \tilde{\mathbf{S}}_{ij}^* \right) = \hat{\mathbf{S}}_{ij}^n + \left( \mathbf{C}_{ijkl} \dot{\epsilon}_{kl} - \frac{\alpha_{ij} \cdot \alpha_{pq} \cdot \mathbf{C}_{pqkl} \dot{\epsilon}_{kl}}{\|\alpha\|} \right) \cdot \Delta t, \quad (3.52)$$

where  $\hat{\mathbf{S}}_{ij}^n = \tilde{\mathbf{S}}_{ij}^n + \left( \tilde{\mathbf{S}}_{ik}^n \mathbf{W}_{jk}^n + \tilde{\mathbf{S}}_{jk}^n \mathbf{W}_{ik}^n \right) \cdot \Delta t$ , and  $\tilde{\mathbf{S}}_{ij}^n$  is the generalised deviatoric stress tensor.

The plasticity flow is described by

$$\dot{\epsilon}_{kl}^p = 2 \cdot \dot{\lambda} \cdot \mathbb{V}_{klpq} \cdot \tilde{\mathbf{S}}_{pq}, \quad (3.53)$$

where  $\mathbb{V}_{klpq}$  is the plastic flow matrix. In matrix notation, (3.52) will be rewritten as

$$\left\{ \tilde{\mathbf{S}}^{n+1} \right\} = \left\{ \tilde{\mathbf{S}}^* \right\} - 2 \cdot d\lambda^{n+1} \cdot \left[ \mathbf{C}^{n+1} \cdot \mathbb{V}^{n+1} - \frac{\{\alpha\} \cdot \{\alpha\}^T}{\|\alpha\|} \cdot \mathbf{C}^{n+1} \cdot \mathbb{V}^{n+1} \right] \left\{ \tilde{\mathbf{S}}^{n+1} \right\} \quad (3.54)$$

or

$$\left\{ \tilde{\mathbf{S}}^{n+1} \right\} = \left\{ \tilde{\mathbf{S}}^* \right\} - 2 \cdot d\lambda^{n+1} \cdot \left[ \mathbf{E} - \frac{\{\alpha\} \cdot \{\alpha\}^T}{\|\alpha\|} \right] \cdot \mathbf{C}^{n+1} \cdot \mathbf{A}^{n+1} \cdot \left\{ \tilde{\mathbf{S}}^{n+1} \right\}, \quad (3.55)$$

where  $\{\alpha\}^T = \{\alpha_{11}, \alpha_{22}, \alpha_{33}, 0, 0, 0\}$ , and  $\mathbf{E}_{(6 \times 6)}$  is the unit matrix. Therefore, (3.55) represents the numerical approximation of the true generalised deviatoric part of stress tensor with first order of approximation. From (3.55), the correction matrix  $\mathbf{E}_\alpha$  due to generalized decomposition of the stress tensor can be introduced and has the expression:

$$\mathbf{E}_\alpha = \left[ \mathbf{E} - \frac{\{\alpha\} \cdot \{\alpha\}^T}{\|\alpha\|} \right] \quad (3.56)$$

and as a result (3.55) takes the final form

$$\left\{ \tilde{\mathbf{S}}^{n+1} \right\} = \left\{ \tilde{\mathbf{S}}^* \right\} - 2 \cdot d\lambda^{n+1} \cdot \mathbf{E}_\alpha \cdot \mathbf{C}^{n+1} \cdot \mathbf{V}^{n+1} \cdot \left\{ \tilde{\mathbf{S}}^{n+1} \right\}. \quad (3.57)$$

Using expression (3.57) and yield function (3.36)  $\hat{\mathbf{F}} = f(\tilde{S}_{ij}) - k^2 = 0$  (in the case of an isotropic material  $k^2 = \frac{2}{3}Y^2$ ) the following equation to respect  $d\lambda$  (at  $n + 1$  moment of time) can be obtained

$$\Delta k^2 = 4 \cdot d\lambda^2 \cdot \left\{ \tilde{\mathbf{S}}^{n+1} \right\}^T \mathbf{V} \cdot \mathbf{C} \cdot \mathbf{E}_\alpha \cdot \mathbf{U} \cdot \mathbf{E}_\alpha \cdot \mathbf{C} \cdot \mathbf{V} \left\{ \tilde{\mathbf{S}}^{n+1} \right\} - 4 \cdot d\lambda \cdot \left\{ \tilde{\mathbf{S}}^{n+1} \right\}^T \mathbf{V} \cdot \mathbf{C} \cdot \mathbf{E}_\alpha \cdot \mathbf{U} \left\{ \tilde{\mathbf{S}}^* \right\}, \quad (3.58)$$

where  $\Delta k^2 = (k^*)^2 - (k^{n+1})^2$ . Besides, the following notation in this thesis will be assumed:

$$b_1 = \left\{ \tilde{\mathbf{S}}^{n+1} \right\}^T \mathbf{V} \cdot \mathbf{C} \cdot \mathbf{E}_\alpha \cdot \mathbf{U} \left\{ \tilde{\mathbf{S}}^* \right\}, \quad (3.59)$$

$$b_2 = \left\{ \tilde{\mathbf{S}}^{n+1} \right\}^T \mathbf{V} \cdot \mathbf{C} \cdot \mathbf{E}_\alpha \cdot \mathbf{U} \cdot \mathbf{E}_\alpha \cdot \mathbf{C} \cdot \mathbf{V} \left\{ \tilde{\mathbf{S}}^{n+1} \right\}, \quad (3.60)$$

where  $b_1 > 0$ ,  $b_2 > 0$  are positive coefficients due to the fact that matrixes  $\mathbf{U}$ ,  $\mathbf{V}$ ,  $\mathbf{C}$ ,  $\mathbf{E}$ , and  $\mathbf{E}_\alpha$  are positive definitive. According to the notation presented in (3.59), (3.60), the equation for parameter  $d\lambda$  can be written in the form:

$$0 = \Delta k^2 - 4 \cdot b_1 \cdot d\lambda + 4 \cdot b_2 \cdot d\lambda^2. \quad (3.61)$$

In the case when anisotropic materials undergoes plastic deformation, parameters  $\Delta k^2 > 0$ ,  $b_1 > 0$ ,  $b_2 > 0$ ,  $4 \cdot b_1^2 - 4 \cdot b_2 \cdot \Delta k^2 > 0$ , therefore, (3.61) has two positive roots which are defined as follows:

$$d\lambda_1 = \frac{2 \cdot b_1 + \sqrt{4 \cdot b_1^2 - 4 \cdot b_2 \cdot \Delta k^2}}{4 \cdot b_2}, \quad d\lambda_2 = \frac{2 \cdot b_1 - \sqrt{4 \cdot b_1^2 - 4 \cdot b_2 \cdot \Delta k^2}}{4 \cdot b_2}, \quad (3.62)$$

where  $d\lambda_1 > 1$ ,  $d\lambda_2 < 1$  and, thus, based on the fundamental property of the compression transformation (function), it follows that in the case of choosing  $d\lambda_2$ , the convergence of the numerical algorithm exists but in the case of choosing  $d\lambda_1$ , the convergence does not exist.

### 3.2.3 Associated Incompressible Anisotropic Plasticity

In case of associated plasticity flow, the yield surface coincides with plastic potential, i.e.  $\mathbf{U} = \mathbf{V}$ . Note again that general non-associated thermodynamically and mathematically consistent incompressible anisotropic plasticity model presented in this thesis reduces to the associated plasticity model in the limit of isotropy. The final set of equations for anisotropic associated plasticity model takes the form:

$$\left\{ \tilde{\mathbf{S}}^{n+1} \right\} = \left\{ \tilde{\mathbf{S}}^* \right\} - 2 \cdot d\lambda^{n+1} \cdot \mathbf{E}_\alpha \cdot \mathbf{C}^{n+1} \cdot \mathbf{U}^{n+1} \cdot \left\{ \tilde{\mathbf{S}}^{n+1} \right\}, \quad (3.63)$$

where  $d\lambda$  (at  $n + 1$  moment of time) satisfies relations<sup>2</sup>

$$0 = \Delta k^2 - 4 \cdot b_1^a \cdot d\lambda + 4 \cdot b_2^a \cdot d\lambda^2. \quad (3.64)$$

Where

$$\Delta k^2 = (k^*)^2 - (k^{n+1})^2,$$

$$b_1^a = \left\{ \tilde{\mathbf{S}}^{n+1} \right\}^T \mathbf{U} \cdot \mathbf{C} \cdot \mathbf{E}_\alpha \cdot \mathbf{U} \left\{ \tilde{\mathbf{S}}^* \right\}, \quad (3.65)$$

$$b_2^a = \left\{ \tilde{\mathbf{S}}^{n+1} \right\}^T \mathbf{U} \cdot \mathbf{C} \cdot \mathbf{E}_\alpha \cdot \mathbf{U} \cdot \mathbf{E}_\alpha \cdot \mathbf{C} \cdot \mathbf{U} \left\{ \tilde{\mathbf{S}}^{n+1} \right\}. \quad (3.66)$$

Therefore, (3.64) has two positive roots which are defined as follows:

$$d\lambda_1^a = \frac{2 \cdot b_1^a + \sqrt{4 \cdot (b_1^a)^2 - 4 \cdot b_2^a \cdot \Delta k^2}}{4 \cdot b_2^a}, \quad d\lambda_2^a = \frac{2 \cdot b_1^a - \sqrt{4 \cdot (b_1^a)^2 - 4 \cdot b_2^a \cdot \Delta k^2}}{4 \cdot b_2^a}, \quad (3.67)$$

where  $d\lambda_1^a > 1$  — no convergence,  $d\lambda_2^a < 1$  — convergence.

<sup>2</sup>The index "a" corresponds to the associated flow plasticity.

### 3.3.4 Final Procedure of Numerical Integration of Incompressible Anisotropic Plasticity

In this section, the final relations are presented, which describe the numerical integration algorithm for the anisotropic incompressible plasticity model presented in the previous section. The presented algorithm is based on classical prediction-correction type of scheme. First step is based on the trial value of generalised deviatoric stress, which is calculated based on generalised Hook's law. Based on the trial value of the generalised deviatoric stress tensor, the plasticity status can be checked. In case when plasticity criterion is realised the correction step is performed. Mathematically, the aforementioned steps can be written as follows

**Prediction (Elastic Behaviour):**

1.

$$a) \left( \tilde{S}_{ij}^* \right) = \hat{S}_{ij}^n + \left( C_{ijkl} \dot{\epsilon}_{kl} - \frac{\alpha_{ij} \cdot \alpha_{pq} \cdot C_{pqkl} \dot{\epsilon}_{kl}}{\|\alpha\|} \right) \cdot \Delta t,$$

$$\hat{S}_{ij}^n = S_{ij}^n + \left( S_{ik}^n \mathbf{W}_{jk}^n + S_{jk}^n \mathbf{W}_{ik}^n \right) \cdot \Delta t,$$

$$b) \Delta k^2 = (k^*)^2 - (k^{n+1})^2.$$

**Correction if  $\Delta k^2 > 0$  (Elastoplastic behaviour):**

2.

$$d\lambda_i = 1.0,$$

$$d\lambda_{i+1} = 0.0,$$

$$\varepsilon = \text{required accuracy},$$

$$\mathbf{do\ while\ } \text{abs} (d\lambda_{i+1} - d\lambda_i) > \varepsilon$$

$$d\lambda_i = d\lambda_{i+1},$$

$$\left\{ \tilde{S}^{n+1} \right\}_{i+1} = (\mathbf{E} - 2 \cdot d\lambda_i \cdot \mathbf{C} \cdot \mathbf{U})^{-1} \cdot \left\{ \tilde{S}^* \right\} = \mathbf{B} (d\lambda_i) \cdot \left\{ \tilde{S}^* \right\},$$

$$\mathbf{B} (d\lambda_i) = (\mathbf{E} - 2 \cdot d\lambda_i \cdot \mathbf{C} \cdot \mathbf{U})^{-1},$$

$$b_1 = \left\{ \tilde{S}^{n+1} \right\}_{i+1}^T \mathbf{V} \cdot \mathbf{C} \cdot \mathbf{E}_\alpha \cdot \mathbf{U} \left\{ \tilde{S}^* \right\},$$

$$b_2 = \left\{ \tilde{S}^{n+1} \right\}_{i+1}^T \mathbf{V} \cdot \mathbf{C} \cdot \mathbf{A} \cdot \mathbf{C} \cdot \mathbf{V} \left\{ \tilde{S}^{n+1} \right\}_{i+1},$$

$$d\lambda_{i+1} = \frac{2 \cdot b_1 - \sqrt{4 \cdot b_1^2 - 4 \cdot b_2 \cdot \Delta k^2}}{4 \cdot b_2},$$

**end do**

where  $\mathbf{E}$  is the unit matrix ( $6 \times 6$ ),  $\mathbf{C}$  is the stiffness matrix,  $\mathbf{U}$  is the matrix of yield surface,  $\mathbf{V}$  is the plastic flow.

### 3.2.5 Verification of Numerical Implementation

The process of verification is required to provide confidence in numerical modelling. Note that in the limit of isotropy, the aforementioned models reduce to the conventional constitutive equations suitable for isotropic materials. Therefore, in order to be confident that the implementation of the constitutive equation into the meshless code has been done correctly, a special case of anisotropy (i.e. isotropy of the materials) is considered.

Analysis of an isotropic case shows that parameter  $d\lambda$  can be calculated analytically by using (3.44). For the isotropic model the following set of parameters presented in Tables 3.3, 3.4, 3.5 have been used to validate the procedure of numerical integration of anisotropic associated plastic flow.

The isotropy of materials applies restriction to the elastic moduli of materials and identifies the relation

**Table 3.3:** Reference material properties I.

Parameter	Description	value
$E$	Young's modulus ("a" direction)	28.0 GPa
$\nu$	Poisson's ratio	0.4
$\mu$	Shear modulus	10 GPa

**Table 3.4:** Reference material properties II.

Parameter	Description	value
$E$	Young's modulus ("a" direction)	48.0 GPa
$\nu$	Poisson's ratio	0.2
$\mu$	Shear modulus	20 GPa

between them  $\mu = \frac{E}{2 \cdot (1 + \nu)}$ . Let us recall  $d\lambda$  expression for isotropic materials

$$d\lambda = \frac{1}{4 \cdot \mu} \cdot \left( \frac{k^*}{k^{n+1}} - 1 \right), \quad k^* = \sqrt{\left( \tilde{S}_{ij}^* \right)^{n+1} \left( \tilde{S}_{ij}^* \right)^{n+1}}. \quad (3.68)$$

Using (3.68) and different trial values of the yield limit  $k^*$ , the  $d\lambda_{Analytical}$ ,  $d\lambda_{Numerical}$ , and number of iterations of the numerical algorithm had been calculated and presented in Table 3.6.

### § 3.3 Plate Impact Tests

---

In the previous sections, the thermoviscoplastic model with two damage parameters are defined to explain damage initiation and propagation and origination of new free surfaces (Kiselev, 1998 [139]; Lukyanov, 2004 [182]). This model depends upon several nonstandard parameters, which are related to damage initialization and propagation and to the criterion of macrofracture of the material. These parameters have to be identified for different types of materials.

#### 3.3.1 Definition of Material Properties

The plane shock-wave technique provides a powerful tool for experimental studying material properties at different strain rates (Steinberg, 1991 [241]; Meyers, 1994 [203]; Bourne and Gray, 2003 [36]; Millett *et al.*, 2002 [206]). The characteristics as spall pressure, shock velocity, particle velocity, Hugoniot elastic limit, thickness of the spall section, time to spall, and free surface velocity of the spall section can be measured and used for the characterization of material dynamic response (Bourne and Gray, 2003 [36]; Millett *et al.*, 2002 [206], Stoffel, 2005 [243], Meziere *et al.*, 2006 [204]).

In order to identify the non-standard materials parameters, the method based on the comparison of numerical simulation with the plate impact test with spallation (Kiselev, 1998 [139]; Kiselev and Lukyanov, 2002 [140]) is used. It should be noted that experiments with spallation are nowadays the most informative approach to

**Table 3.5:** Reference material properties III.

Parameter	Description	value
$E$	Young's modulus ("a" direction)	55.0 GPa
$\nu$	Poisson's ratio	0.1
$\mu$	Shear modulus	25 GPa

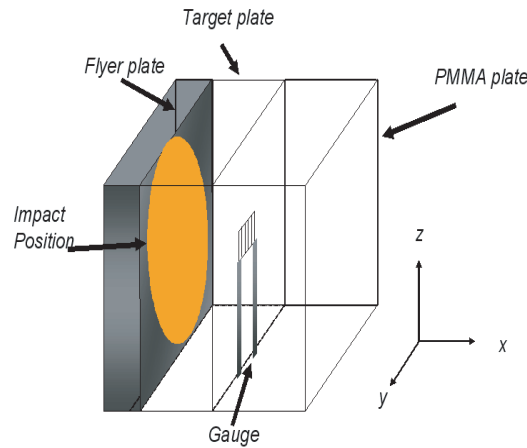
**Table 3.6:** *Verification of Numerical implementation.*

Parameter	Description	Material I.	Material II.	Material III.
$k^*$	Trial value of yield limit	351.738 MPa	567.798 MPa	605.907 MPa
$k$	Real value of yield limit	350.0 MPa	350.0 MPa	350.0 MPa
$d\lambda_{Analytical}$	Analytical Calculation	$1.2414 \cdot 10^{-2}$	$77.7849 \cdot 10^{-2}$	$73.1163 \cdot 10^{-2}$
$d\lambda_{Numerical}$	Numerical Calculation	$1.2414 \cdot 10^{-2}$	$77.7849 \cdot 10^{-2}$	$73.1163 \cdot 10^{-2}$
Iterations	Number of Iterations	5	27	30

characterise the dynamical behaviour of materials and to construct a set of constitutive equations (Kanel *et al.*, 1987 [133]). The model with two damage parameters for isotropic media (Kiselev, 1998 [139]; Kiselev and Lukyanov, 2002 [140]) contains seven unknown variables:  $B$ ,  $C$ ,  $\Lambda_\omega$ ,  $\Lambda_\alpha$ ,  $\sigma_*$ ,  $\varepsilon_{u*}^p$ ,  $D_*$ .

### 3.3.2 Description of the Experiment

The flyer plates were launched using a 75 mm bore, 1 m long and 50 mm bore, and 1 m long single stage gas gun the Royal Military College of Science (Bourne and Stevens, 2001 [37]). The shock propagation in the target is monitored using manganin stress gauges, placed between target plate and PMMA (poly methylmethacrylate) plate within the target assembly. The target assembly is shown in Figure 3.1. The results from the stress gauges



**Figure 3.1:** *Schematic diagram of the experimental target assembly.*

were converted to in material (Target) values  $\sigma_M$ , using the shock impedances of the target  $A_T$  and PMMA  $A_P$ , via the well-known relation

$$\sigma_M = \frac{A_T + A_P}{2A_P} \sigma_P, \quad (3.69)$$

where  $\sigma_P$  is the stress gauges values. The 2.5mm thick flyer plates of 6082-T6 (dural) were impacted onto the targets (test material AA 7010-T6) over the velocity range 234 to 895, inducing stresses in the range 2.7 to 7.2 GPa. The aluminium alloy 6082-T6 was chosen as the flyer due to the close similarity in density and wave speeds, so that the impact experiments were near symmetrical (Lukyanov, 2008 [184]). The elastic material properties of 7010-T6 can be found in Lukyanov, 2008 [184]). Material properties of plates 6082-T6 and PMMA can be found in Steinberg (1991) [241].

### 3.3.3 Verification of the model

The process of verification is intended to provide, and quantify, confidence in numerical modelling and the results from the corresponding simulations. Note that in the limit of isotropy, the aforementioned models re-

duce to the conventional constitutive equations suitable for the shock wave propagation in isotropic materials described by Steinberg (1991) [241] and Meyers (1994) [203]. Therefore, in order to be confident that the implementation of the constitutive equation into the SPH code has been done correctly, a special case of anisotropy (i.e. isotropy of the materials) is considered. Plate impact tests of isotropic aluminum are considered; the data for the aluminum was taken from the report (Steinberg, 1991 [241]). The material properties (density  $\rho_0$ , shear modulus  $\mu_0$ , yield strength  $Y_0$ , isotropic hardening parameter  $E_p$ ) of the flyer (aluminum – Al 2024-T4) and the target (copper – Cu OFHC  $\frac{1}{2}$  Hard) are presented in Table 3.7. The target parameters have been used in the

**Table 3.7: Material Plasticity Properties.**

Plate	$\rho_0, kg/m^3$	$\mu_0, GPa$	$Y_0, MPa$	$E_p, MPa$
Flyer Al 2024-T4	2785	28.6	260	700
Flyer Al 6082-T6	2700	26.8	250	130
Target Cu OFHC $\frac{1}{2}$ Hard	8930	47.7	120	0.0
PMMA	1180	2.68	200	300

proposed anisotropic elasto-plasticity model (without kinematic or isotropic hardening), in order to represent an isotropic material, which is a special case of anisotropy. Parameters for the Mie-Grüneisen equation of state (3.28) in isotropic case for the flyer Al 2024-T4 and for the target Cu OFHC  $\frac{1}{2}$  Hard are presented in Table 3.8. The back plate PMMA has been modelled as an isotropic material with the properties presented in Table 3.7 and 3.8. Accuracy of the SPH scheme used to approximate the governing equation were evaluated by comparing

**Table 3.8: Material EOS Properties.**

Plate	$c, m/s$	$S_1$	$S_2$	$S_3$	$\gamma_0$	a
Flyer Al 2024-T4	5328	1.338	0	0	2.0	0.48
Flyer Al 6082-T6	5240	1.4	0	0	1.97	0.48
Target Cu OFHC $\frac{1}{2}$ Hard	3940	1.489	0	0	2.02	0.47
PMMA	2600	1.52	0	0	1.0	0.0

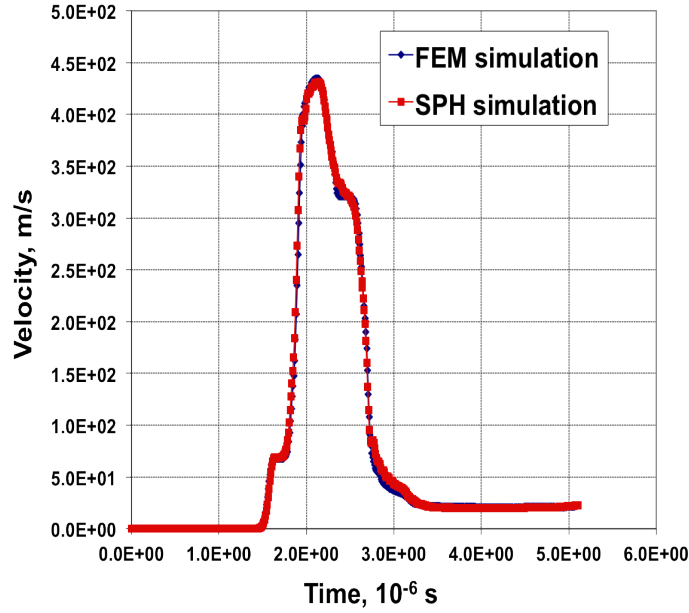
the reference simulation results of uniaxial plate impact. A numerical simulation was performed using meshless discretization equations described in the previous section. Below, the comparison of SPH and FEM simulation results for different impact velocities using isotropic constitutive equations is presented.

In figures 3.2 and 3.3, the comparison between LS-DYNA results and the SPH results is presented for the impact velocity 450  $m/s$  and 100  $m/s$  respectively. It shows the time history of back surface velocity of the target plate (Cu OFHC  $\frac{1}{2}$  Hard). It is clear from these figures that simulation results diverge at low impact velocities (over-smoothing effect). This effect is strain rate dependent since at higher impact velocities the divergence between simulations results less compare to low impact velocities.

The above simulations were run again starting with a random distribution of internal particles (the boundary particles were fixed) to understand its effect of the order of accuracy. The random distribution of particles was generated by perturbing the regularly distributed particles using a uniform random variable varying between +10% and -10% of the smoothing length. The perturbation of the particles did not change the order of accuracy significantly. All the above results were obtained using the cubic spline kernel (2.56) in the simulations. Replacing the cubic spline kernel with the quintic spline kernel (2.57) did not result in any significant change in the simulation results.

### 3.3.4 Shock wave propagation in aluminum alloy

Plate impact experiments on aluminum alloy 7010-T6 have been performed to determine the effect of orientation of the loading axis to the longitudinal and transverse directions for the shock induced mechanical properties (Lukyanov, 2008 [184]). In this experiment, the flyer plate of 6082-T6 was impacted onto the target plate of 7010-T6 over the velocity range 450  $m/s$  to 895  $m/s$ . Material parameters and parameters for the



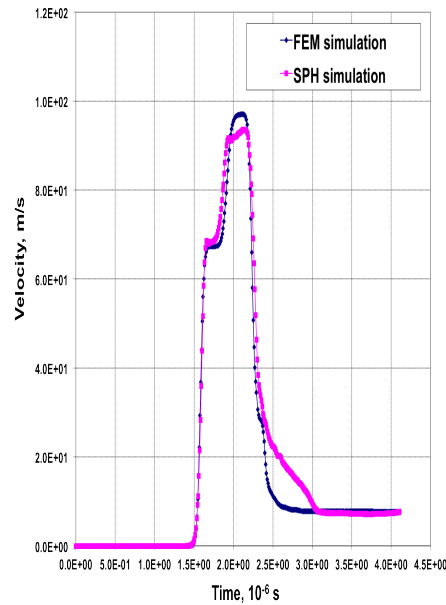
**Figure 3.2:** Comparison between SPH and FEM of simulation results of uniaxial plate impact test using 450 m/s.

Mie-Grüneisen equation of state (3.28) of the flyer Al 6082-T6 are presented in Table 3.7 and 3.8 (Steinberg, 1991 [241]).

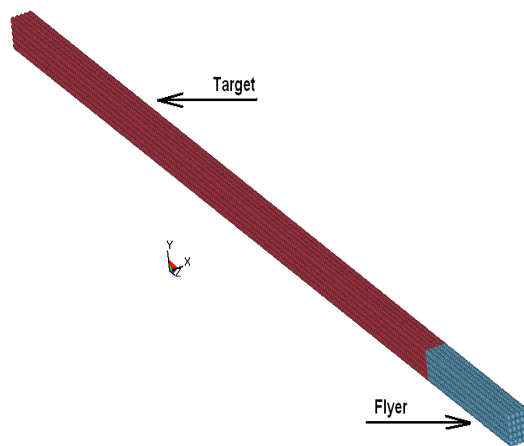
Based upon the characteristics of the thin plate impact test, the numerical domains (target and flyer plates) can be modelled as rectangular bars (flyer plate - 0.02cm × 0.02cm × 0.2cm, target plate - 0.02cm × 0.02cm × 1.0cm) (see fig. 3.4). Symmetry conditions were applied on all sides to ensure one-dimensional waves will travel along the length of the bar which is a basic requirement of a plate impact test. Free surface boundary conditions were applied to the back and front surfaces of the bar (see fig. 3.4). The flyer-plate was modelled using 1250 particles (5 particles through thickness and 5 in height) and the target-plate was modelled using 6250 particles (5 particles through thickness and 5 in height). With this resolution, all the characteristic features of the stress pulse can be resolved, for the smallest computational cost, as further increases in resolution brings no advantage in accuracy. Figures 3.5 and 3.6 show the comparison between experimental data and the numerical simulation resulting from the new anisotropic equation of state and non-associated anisotropic plasticity model for the longitudinal and transverse cases.

The experimental values, 0.39 GPa and 0.33 GPa for elastic response from the longitudinal and short transverse directions, respectively figures 3.5 and 3.6, are in good correlation with the modelled values of the HEL longitudinal - 0.395 GPa and short transverse - 0.333 GPa. The errors with respect to the experimental values are 1.4 % and 0.9 %, respectively to the longitudinal and short transverse directions. Further comparison shows that the stress pulse width (approximately, 0.81  $\mu s$ ) and release trace are in good agreement with the experiment as well (see fig. 3.5 and 3.6). Besides, another important characteristic, the arrival time to the HEL and the plastic wave velocity are in good correlation with experimental data. The main conclusion obtained from these results is that the non-associated anisotropic plasticity model, as it stands, is suitable for simulating elastoplastic shock wave propagation in anisotropic solids. Different HELs are obtained when the material is impacted in different directions; their excellent agreement with the experiment demonstrates adequateness of the proposed anisotropic plasticity model. However, further work is required both in the experimental and constitutive modelling areas to find a better description of anisotropic material behavior and, particularly, Hugoniot stress level.





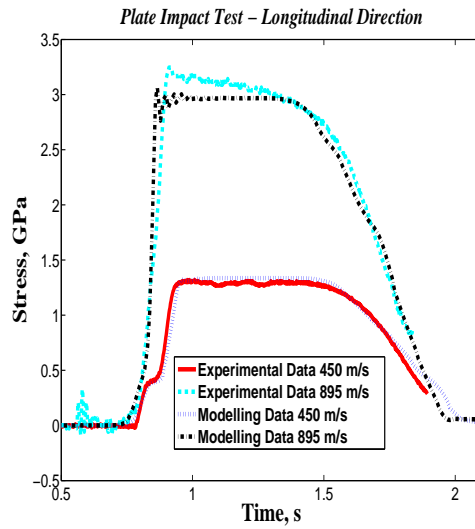
**Figure 3.3:** Comparison between SPH and FEM of simulation results of uniaxial plate impact test using 100 m/s.



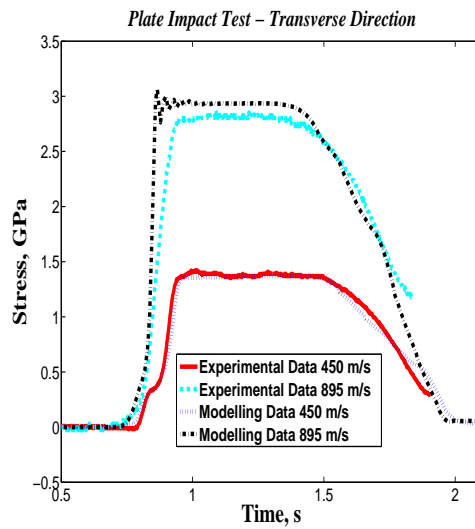
**Figure 3.4:** Geometry of uniaxial plate impact test in the SPH method

### § 3.4 Modeling of thermo-elastic-plastic damageable medium

On the topic of dynamic loading of materials, there are many publications related to the planar plate impact test with spallation (Mayers, 1994 [203]), which allows the determination of dynamic materials properties, including damage (Kiselev and Lukyanov, 2002 [140]). Shock wave experiments have certain potential advantages associated with the level of strain rate which can be induced. It has frequently provided the motivation for the construction of material constitutive relations and has been the principal means for determining material parameters for some of these relations (Steinberg, 1991 [241]; Meyers, 1994 [203]), therefore, the numerical simulation of the planar plate impact test is considered. The planar plate impact test is considered where the diameters of the flyer and the target are much greater than their thicknesses and the characteristic time of the process is the time of several runs of elastic waves across the thickness of the target plate. Based on these



**Figure 3.5:** Back-surface gauge stress traces from plate-impact experiments versus numerical simulation of stress (PMMA) waves for plate impact test (impact velocity 450 m/s and 895 m/s) - aluminum alloy AA7010-T6 (Longitudinal Direction).

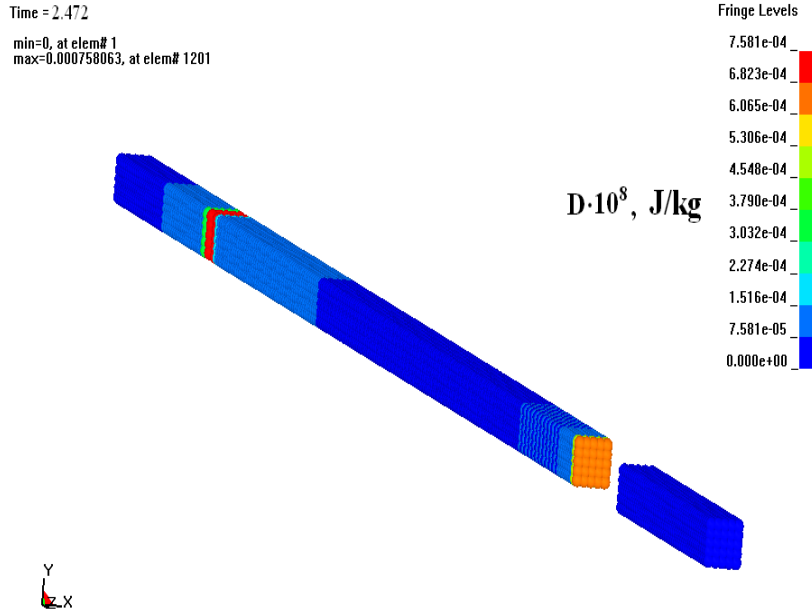


**Figure 3.6:** Back-surface gauge stress traces from plate-impact experiments versus numerical simulation of stress (PMMA) waves for plate impact test (impact velocity 450 m/s and 895 m/s) - aluminum alloy AA7010-T6 (Transverse Direction).

properties, the plate impact problem may be solved using a uniaxial strain state (one-dimensional mathematical formulation in strain space) and the adiabatic approximation ( $\text{div} \mathbf{q} = 0$ ).

### 3.4.1 Uniaxial Plate Impact Test with Spall

The flyer and target were assigned aluminium and titanium properties respectively. Figures 3.7 – 3.11 depict the distribution of damage parameter, total internal dissipation and temperature at different moments in time using the SPH method for the impact velocity  $V_0 = 660$  m/s. Material parameters  $B, C, \Lambda_\omega, \Lambda_\alpha, \sigma_*, \varepsilon_{u*}^p, D_*$



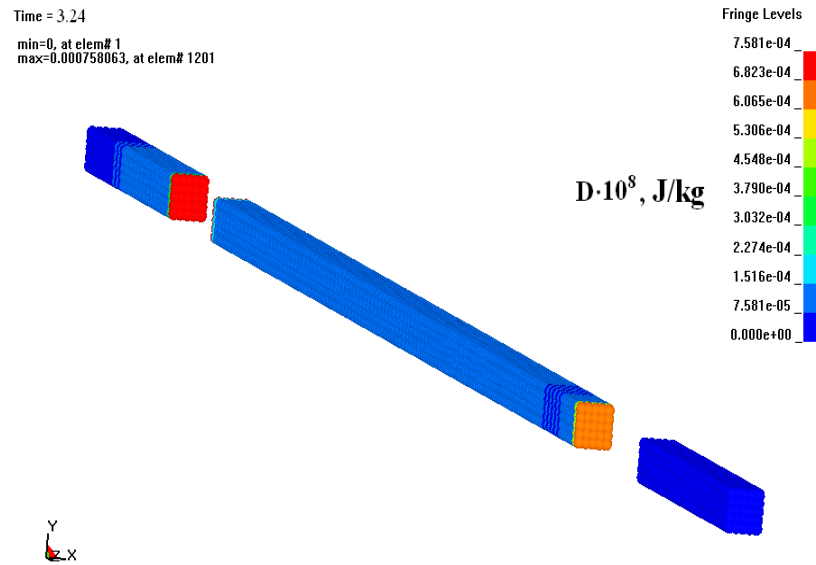
**Figure 3.7:** Distribution of total dissipation at  $t = 2.472 \mu\text{s}$  during SPH simulations. The maxima of the dissipation are located at the positions of the impact and spallation.

were chosen from the condition of the best comparison between numerical simulation and experimental data (Kanel *et al.*, 1987 [133]): For titanium:  $\rho = 4530 \text{ kg/m}^3$ ,  $K_0 = 123.4 \text{ GPa}$ ,  $\mu_0 = 43.4 \text{ GPa}$ ,  $\Lambda_\alpha = 750 \text{ (Pa} \cdot \text{s)}$ ,  $\eta_{00} = 75 \text{ (Pa} \cdot \text{s)}$ ,  $B = 507 \cdot 10^{-5} \text{ (Pa} \cdot \text{s})^{-1}$ ,  $C = 0.8$ ,  $\Lambda_\omega = 49.31 \text{ (Pa} \cdot \text{s)}$ ,  $\varepsilon_{u*}^p = 0.35$ ,  $\sigma_* = 4.0 \text{ GPa}$ ,  $D_* = 75 \text{ kJ/kg}$ ,  $c_\sigma = 520.7 \text{ J/(kg} \cdot \text{K)}$ ,  $\alpha_v = 2.52 \cdot 10^{-5} \text{ K}^{-1}$ ,  $\kappa_T = 20 \text{ W/(m} \cdot \text{K)}$ .

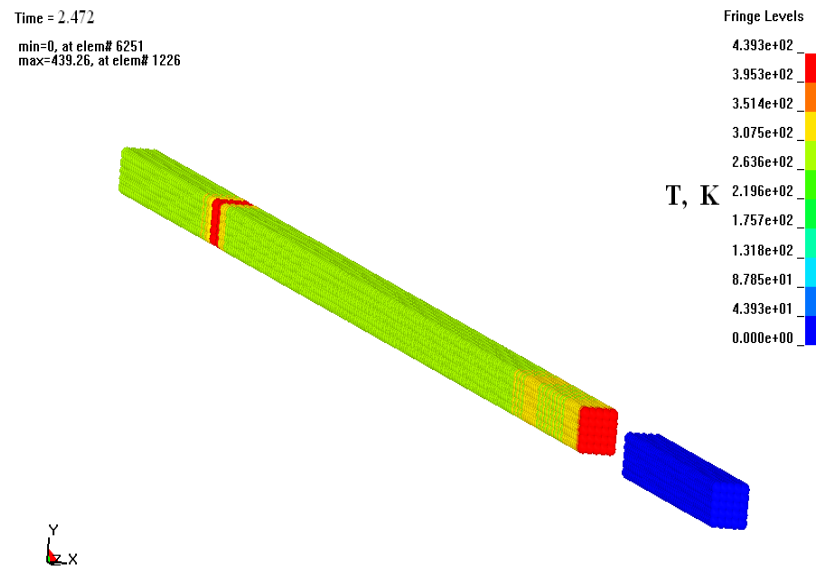
Figures 3.10, 3.11 show the damage evolution due to presented in this thesis thermoviscoelastoplastic model with internal state variable (damage parameters) subject to the criterion of fracture based on critical value of specific internal entropy. The solution corresponds to the existing observations (Meyers, 1994 [203]). The temperature distribution presented in Fig. 3.9 shows that it has maxima at the point of impact and at the cross section of the spall origination (see also, the dissipation distribution 3.7, 3.8). Hence, based on uniaxial plate impact test, it is shown that model allows to adequately describe the basic special features of fracture process and the criterion of fracture can be used to describe the spall problems. Using the uniaxial planar plates impact test and numerical forward model, it is possible to identify the nonstandard parameters of the model.

### 3.4.2 2D Plate Impact Simulation

Interaction between target and flyer with finite dimensions is a difficult problem for numerical simulation, as, it is necessary to take into account the development of large deformation in both bodies (target and flyer), and their associated failure processes. This makes the correlation to experiments difficult. Significant attention had been applied to investigate and numerical simulate one dimension spall problem (see, for example, Kanel *et al.* (1987) [133]; Kanel, 1998 [130]; Kanel *et al.* (1995) [131]; Kanel *et al.*, (1996) [132], [134]; Kiselev and Lukyanov (2002) [140]; Meyers (1994) [203]; Steinberg (1991) [241]; Gray *et al.* (2000, 2002) [112], [113];



**Figure 3.8:** Distribution of total dissipation at  $t = 3.24 \mu\text{s}$  during SPH simulations. The target plate is separated into two parts demonstrating the effect of the macro-fracture criterion based on the specific internal entropy.



**Figure 3.9:** Distribution of temperature at  $t = 2.472 \mu\text{s}$  during SPH simulations

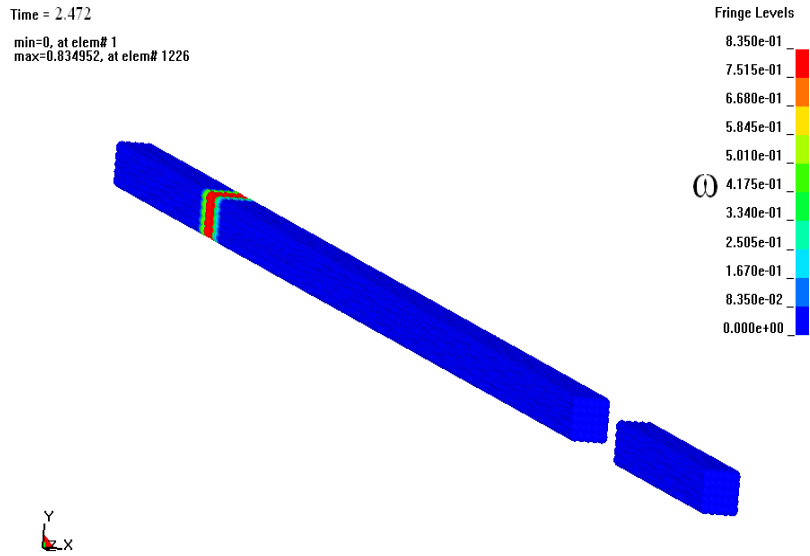


Figure 3.10: Distribution of damage at  $t = 2.472 \mu s$  during SPH simulations

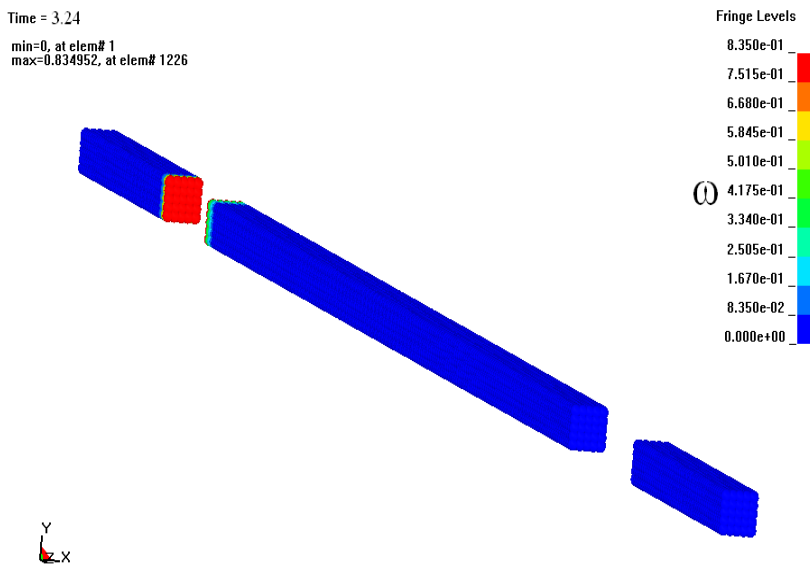
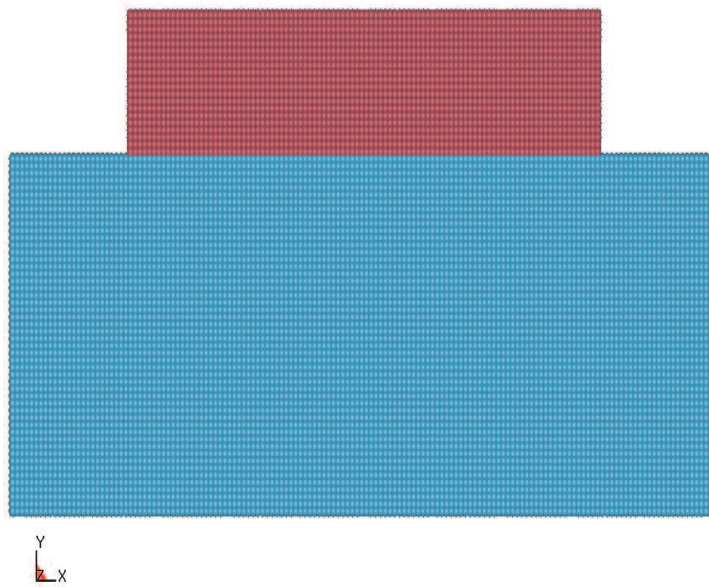


Figure 3.11: Distribution of damage at  $t = 3.24 \mu s$  during SPH simulations

Millett and Bourne (2001) [205]). The plane shock-wave technique provides a powerful tool for studying material properties at different strain rates. Such characteristics as spall pressure, shock velocity, particle velocity, Hugoniot elastic limit (HEL), thickness of the spall, time to spall, and free-surface velocity of the spall can be measured and used for the characterization of material dynamic response.

### 3.4.3 Irreversible Deformation Process During Impact Loading

For understanding of the fracture process under impact loading, the deformation process is investigated in detail. Significant investigation had been done on the uniaxial strain state, which started from the work of Taylor. Problems of plate impact loading are very important in understanding the mechanism of fracture origination and propagation, and also, this problem can be considered as benchmark in validating a proposed damage model. As mentioned early, the uniaxial plate impact test raised the importance of material characterisation (specification of mechanical and chemical properties of the material) Kanel *et al.* (1987) [133], Kiselev and Lukyanov (2002) [140], Meyers (1994) [203], Steinberg (1991) [241]. The deformation processes within the target and flyer during low velocity impact (when no fracture occurs) are considered. The wave distribution during low velocity impact is used to understand the possible regions of macrocrack formation and propagation. Taking in account



**Figure 3.12:** *Geometry of normal impact*

the finite thickness and radius of the plates was characterised by the existence of free boundary surfaces. As a result of that, the wave distribution picture is changed drastically. Existence of the free boundary surfaces leads to wave reflection and formation of the compressive release wave. This fact significantly complicates the wave distribution picture within interacting bodies and leads to non-uniaxial strain state, which in turn will affect the initial shape of the interacting bodies. Let us consider a problem of the interaction of two copper plates with the following mechanical properties: density  $\rho = 8900 \text{ kg/m}^3$ , Young modulus  $E = 110 \text{ GPa}$ , and Poisson's ratio  $\nu = 0.3$ , yield limit  $Y_0 = 120 \text{ MPa}$ .

Let us consider a normal impact of flyer-plate onto target-plate. Flyer-plate (radius 1.0 cm, thickness 0.4 cm) is propelled by the product of an explosion onto a copper target-plate (radius 1.5 cm, thickness 1 cm). Figure 3.12 shows the position of the plates at the beginning of impact loading, where the velocity of the flyer was  $V_0 = 100 \text{ m/s}$ . From the contact surface, the compressive wave propagates inside the flyer and target plates. From the free surface after reflection of the initial compressive wave, the release wave forms. Since the flyer and target are made from the same material then the mass velocity after the compressive wave front is equal to half of the initial flyer velocity. After arrival of the compressive wave at the back surface of the target plate, formation of the release wave fan occurs, where in the uniaxial strain state, full breaking of the material

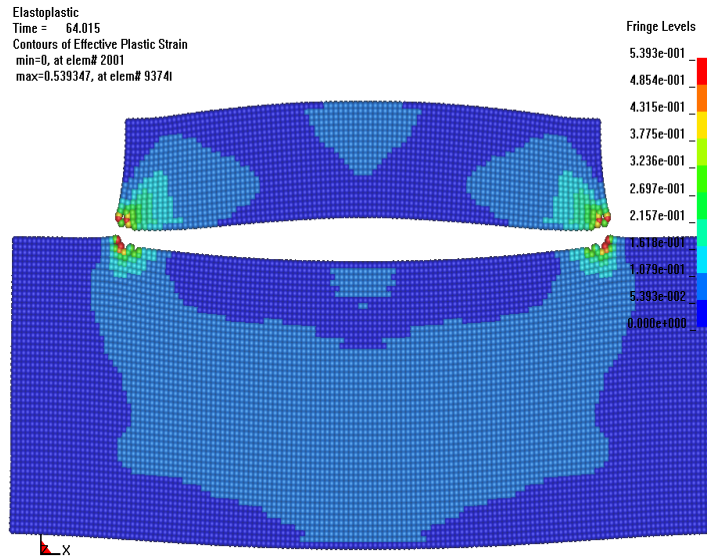


Figure 3.13: Distribution of the effective plastic strain at  $t = 64.015 \mu s$

occurs. Since the amount of deformation reduces due to the release loading, as a result of breaking the target material and radial target material flow, it follows that in this region there is no full breaking of the flyer–plate and, therefore, the motion of the flyer plate continues even after arriving release waves from the back surface of the target plate. After the compressive wave reaches the back surface of the target plate, the compressive wave transforms into a release wave fan, where material accelerates to the initial impact velocity. However, there exist a region of uniaxial strain state, which has smaller dimensions when compared with the thin plate impact problem, due to the presence of a free surface and the existence of release waves. Arrival of the release wave from the flyer side and interaction of these waves in the target plate leads to the formation of tensile stresses, which accelerates the material near the contact surface, resulting in the formation of a gap between flyer and target in the central part of the contact surface (see 3.13 – 3.14). Since the central part of the flyer-plate has been brought to rest, the outer fringe region continues to move, causing the flyer to adopt the following shape presented in figure 3.14. Figures 3.13 – 3.14 show the position of the plates at different moments in time, together with the distribution of effective plastic strain. In order to understand the initiation and propagation of microfracture, an investigation into the distribution of hydrostatic pressure allows the zone of initiation and propagation of the damage to be defined.

### 3.4.4 Failure of the Target and Flyer Plates

Let us consider the problem of an elastoplastic damageable material behaviour (target plate) under impact loading of an elastoplastic flyer plate, where flyer–plate (density -  $\rho = 4530 \text{ kg/m}^3$  (titanium), radius – 1.0 cm, thickness – 0.2 cm) has normal impact velocity 700 m/s into the direction of target plate (density -  $\rho = 4530 \text{ kg/m}^3$  (titanium), radius - 3.0 cm, thickness - 1.0 cm). The relative positions of target and flyer are shown at the moment of impact on figure 3.12.

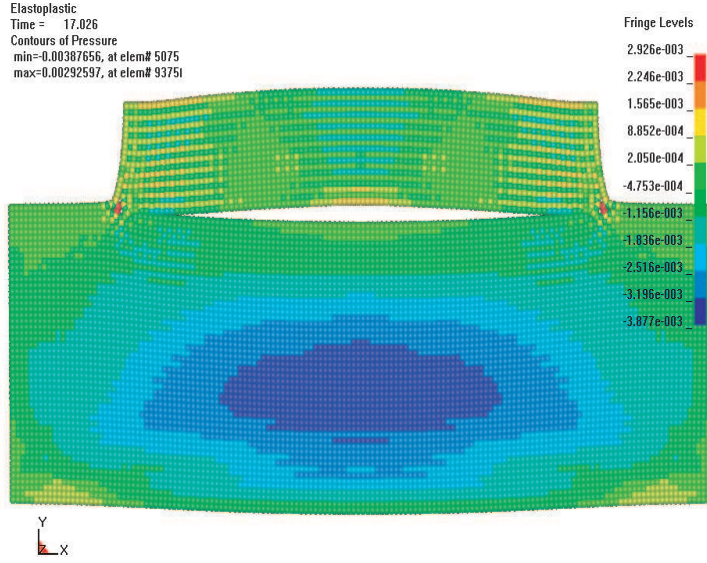
Problem formulation: at any moment in time  $t > 0$ , in the region of the location of target and flyer plates, requires to find the following unknown functions  $\mathbf{x}$ ,  $\mathbf{u}$ ,  $\rho$ ,  $\sigma_{ij}$ , which are described by damageable thermoelastoviscoplastic constitutive equations, criterion of macrofracture (3.38) and initial data

$$\rho(\mathbf{x}, 0) = \rho(\mathbf{x}), \quad \mathbf{u}(\mathbf{x}, 0), \quad \sigma_{ij} = 0 \quad (3.70)$$

At the boundary of the target plate, the following conditions are realised:

- At the free surface boundary conditions are:

$$\sigma_n = 0, \quad \sigma_\tau = 0, \quad (3.71)$$



**Figure 3.14:** Distribution of the hydrostatic pressure at  $t = 17.026 \mu s$

- At the contact surface of target and flyer, the slip conditions without friction, which allows the possibility of separation are realised. Thus, we have the following algorithm: for compressive stresses:

$$u(\mathbf{x}, t) = u(t) \quad \mathbf{x} \in \partial\Omega, \quad \sigma_\tau = 0, \quad \sigma_n < 0. \quad (3.72)$$

If at some point along the boundary, the stresses become positive (region of tension), then for these points, boundary conditions take the form (3.71).

Figures 3.15 - 3.16 show distribution of the different solution variables inside the plates at time  $t = 17.008 \mu s$ , and zones of future and current macrofracture. Figures 3.15 and 3.16 show the distribution of the shear and volumetric damage parameters. Figures 3.17 and 3.18 show distribution of mechanical and total dissipations. Figure 3.19 shows distribution of temperature. Numerical results of fracture initiation and propagation within the target plate under impact loading of damageable elastoplastic plate are also presented and discussed. It has been shown that fracture occurs at the zone of interaction of three release-compressive waves.

### § 3.5 Conclusion

This chapter presents thermoviscoelastoplastic model for isotropic and anisotropic materials with internal state variable (damage parameters) subject to the criterion of fracture based on critical value of specific internal entropy. Furthermore, the generalized decomposition has allowed the formulation and investigation of a generalized incompressibility constraint,  $\alpha_{ij}\varepsilon_{ij}^p = 0$ , on the plastic potential, where  $\varepsilon_{ij}^p$  is the plastic strain rate, and is the generalized Kronecker delta symbol (Lukyanov, 2012 [187]). Using the generalized deviatoric stress tensor and generalized incompressibility constraint,  $\alpha_{ij}\varepsilon_{ij}^p = 0$ , the plastic potential was proposed.

The numerical aspects of newly developed mathematically and thermodynamically consistent incompressible anisotropic plasticity model has been discussed in this chapter. The development of an iterative numerical algorithm for solving the anisotropic incompressible plasticity model is based on the generalisation of the available iterative numerical algorithm for isotropic materials. The algorithm reduces to the classical numerical algorithm in the limit of isotropy. In this chapter, the comparison of numerical iterative process of one step in time of newly developed numerical algorithm in the case of an isotropic material with analytical expression for returning scale factor for isotropic algorithm is performed.

Numerical simulations based on the proposed non-associated anisotropic plasticity model were performed, in order to describe the behavior of the aluminum alloy AA7010-T6 under shock loading conditions. A comparison of the experimental HELs with numerical simulation shows excellent agreement (maximum error is 1.4%).



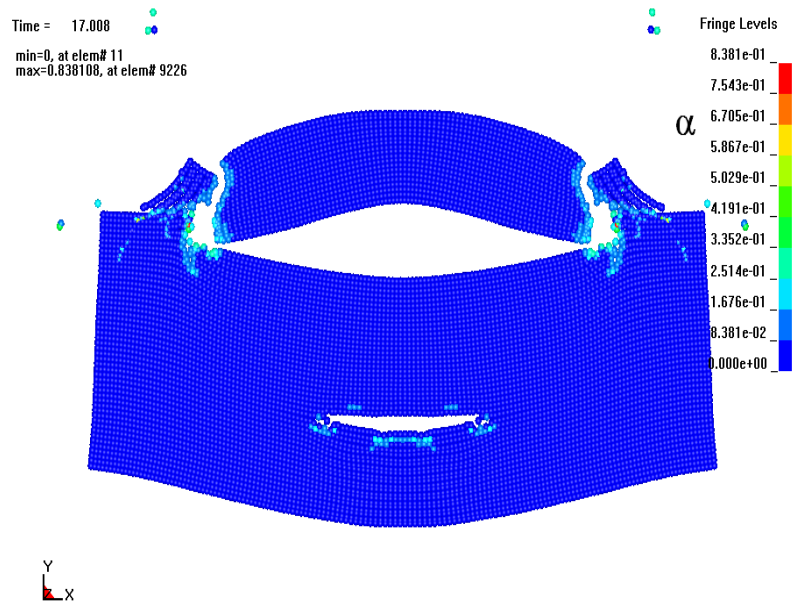


Figure 3.15: Distribution of shear damage parameter at  $t = 17.008 \mu s$

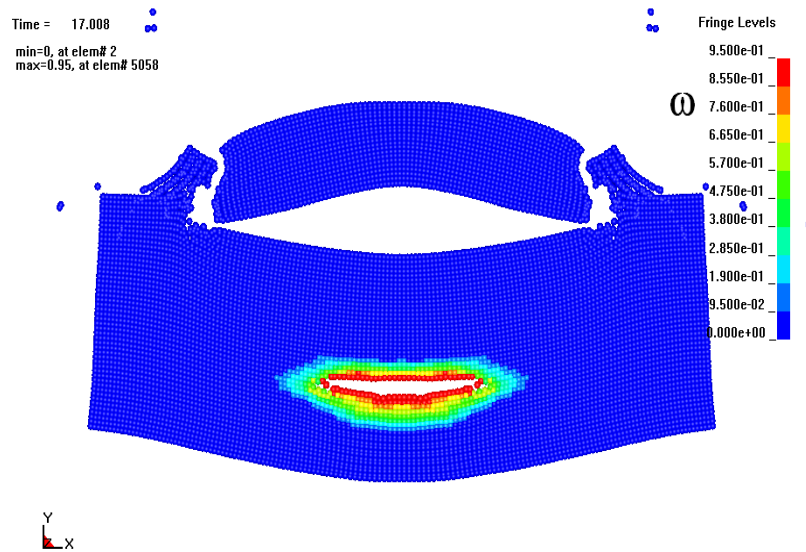


Figure 3.16: Distribution of volumetric damage parameter at  $t = 17.008 \mu s$

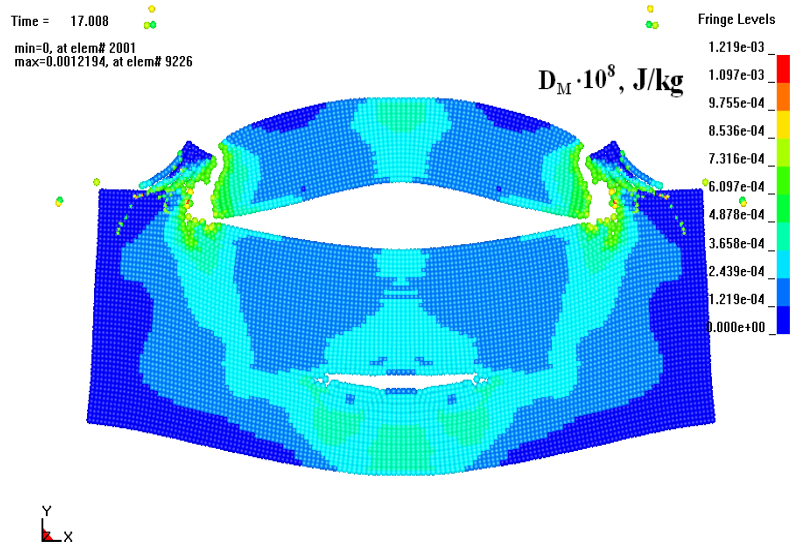


Figure 3.17: Distribution of mechanical dissipation at  $t = 17.008 \mu\text{s}$

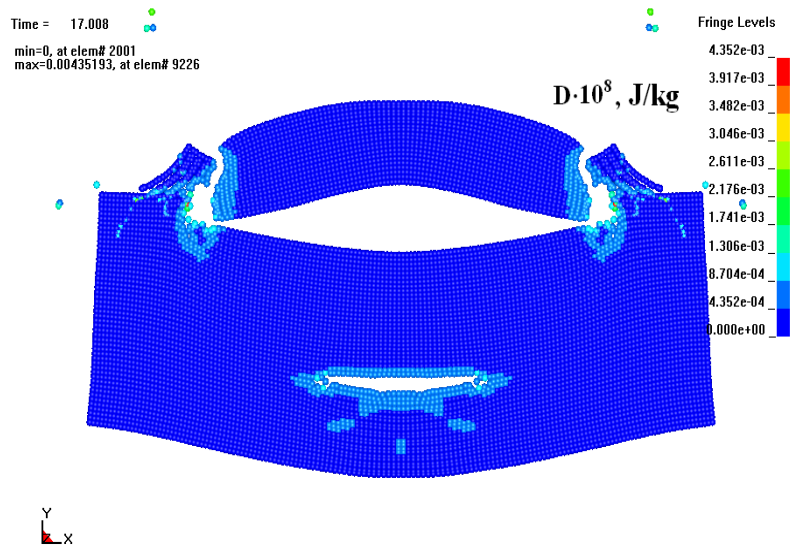
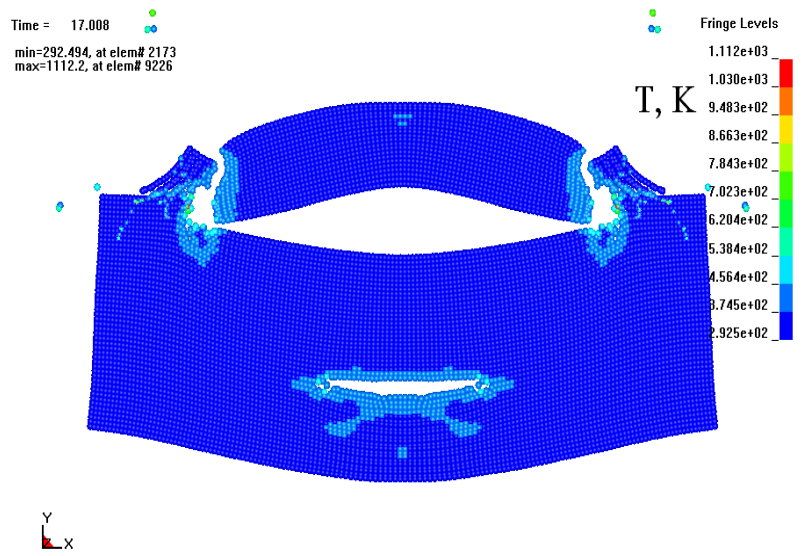


Figure 3.18: Distribution of total dissipation at  $t = 17.008 \mu\text{s}$



**Figure 3.19:** *Distribution of temperature at  $t = 17.008 \mu s$*

Furthermore, the good agreement of the general pulse shape and Hugoniot stress level suggests that the non-associated anisotropic plasticity model is performing satisfactorily. However, further numerical simulations of the proposed constitutive equations, taking into account more precise anisotropic SDE, are required (Stoughton and Yoon, 2004 [244]).

---

## MESHLESS MULTI-POINT FLUX APPROXIMATION

---

**S**MOOTHED particle hydrodynamics (SPH) has been extensively used to model high and low Reynolds number flows, free surface flows and collapse of dams, study pore-scale flow and dispersion, elasticity, and thermal problems. In different applications, it is required to have a stable and accurate discretization of the elliptic operator with homogeneous and heterogeneous coefficients. In this paper, the stability and approximation analysis of different SPH discretization schemes (traditional and new) of the diagonal elliptic operator for homogeneous and heterogeneous media are presented. The optimum and new discretization scheme is also proposed. The new scheme enhances the Laplace approximation (Brookshaw's scheme [41] and Schwaiger's scheme [236]) used in the SPH community for thermal, viscous, and pressure projection problems with an isotropic elliptic operator. The sufficient monotonicity condition is also formulated leading to the constraint on the kernel shape and particles distribution. The numerical results are illustrated by numerical examples, where the comparison between different versions of the meshless discretization methods are presented<sup>1</sup>

### §4.1 Introduction

---

In different applications including, but not limited to, fluid flow related problems, it is required to have the stable and accurate discretization of the following operator (diagonal elliptic operator), which is the research

---

<sup>1</sup>This chapter is based on the following publications:

1. **Lukyanov, A. A.**, Vuik, C., *Meshless Multi-Point Flux Approximation*, In M. Griebel and M. A. Schweitzer, editors, Meshfree Methods for Partial Differential Equations VII, volume 100 of Lecture Notes in Computational Science and Engineering. Springer, 2016.
2. **Lukyanov, A. A.**, *Meshless Upscaling Method and Its application to a Fluid flow in Porous Media*, ECMOR XIII, Biarritz, France. 2012;
3. **Lukyanov, A. A.**, *Meshless Multi-Point Flux Approximations*, AIP Conf. Proc. 1479, 2012. PP. 1607-1610;
4. **Lukyanov, A. A.**, *Meshless Multi-Point Flux Approximation of Fluid Flow in Porous Media*, SPE 141617-PP, SPE Reservoir Simulation Symposium, Woodlands, USA, 2011;
5. **Lukyanov, A. A.**, *Meshless Upscaling Method and Its application to a Fluid flow in Porous Media*, ECMOR XII. Oxford. UK. 2010;

subject of this paper:

$$\begin{aligned} \mathbf{L}(\mathbf{u}) &= -\nabla(\mathbf{M}(\mathbf{r}) \nabla \mathbf{u}(\mathbf{r})) - g(\mathbf{r}), \quad \forall \mathbf{r} \in \Omega \subset \mathbb{R}^n, \\ \mathbf{M}(\mathbf{r}) &\in \{\text{diag}[m(\mathbf{r})] : m(\mathbf{r}) \in \mathbb{R}_+^n, m(\mathbf{r}) \in L_2(\Omega)\}, \quad \text{diag} : \mathbb{R}^n \rightarrow \mathbb{R}^{n \times n}, \end{aligned} \quad (4.1)$$

where  $\mathbf{u}(\mathbf{r})$  is the unknown scalar or vector variable field,  $\mathbf{M}^{\alpha\beta}(\mathbf{r})$  is the diagonal matrix of the mobility field, e.g., one example includes  $\mathbf{M}^{\alpha\beta}(\mathbf{r}) = m(\mathbf{r}) \delta_{\alpha\beta}$ ,  $\alpha, \beta = 1, \dots, n$ ; where  $m(\mathbf{r})$  is the mobility scalar field,  $\delta_{\alpha\beta}$  is the Kronecker symbol,  $n = 1, 2, 3$  is the spatial dimension. The sink/source term  $g(\mathbf{r})$  is assumed to be zero in this chapter. Consider the operator in the expression (4.1) with piecewise continuous coefficients  $\mathbf{M}(\mathbf{r})$  in  $\Omega$ . It has been noticed that some of the numerical methods for elliptic equations may violate the maximum principle (i.e. lead to spurious oscillations). Therefore, proposed methods must satisfy a discrete maximum principle to avoid any spurious oscillations. This is also applicable to meshless discretizations. Usually, the oscillations are closely related to the poor approximation of the variable gradient  $\nabla \mathbf{u}$  in the flux computation. In this paper, different numerical discretizations of the elliptic isotropic operator are analyzed. The objective of this paper is to develop numerical scheme satisfying the two-point flux approximation nature in the form

$$\mathbf{L}(\mathbf{u}) \approx \sum_J V_{r_J} \Psi([\mathbf{u}(\mathbf{r}_J) - \mathbf{u}(\mathbf{r}_I)], \mathbf{r}_J - \mathbf{r}_I) - g(\mathbf{r}_I), \quad (4.2)$$

where  $J$  is the neighboring particle of the particle  $I$ ,  $V_{r_J}$  is the  $J$ -particle volume,  $\Psi$  is the special kernel. This structure (4.2) allows to have a better analysis of the stability and monotonicity. Furthermore, this will allow to apply upwinding strategy during the solution of nonlinear PDEs. The optimum discretization scheme of the shape (4.2) is proposed in this paper. This scheme is based both on the Laplace approximation (Brookshaw's scheme [41]) and on a gradient approximation commonly used in the SPH community for thermal, viscous, and pressure projection problems. The proposed discretization scheme is combined with mixed corrections, which ensure linear completeness. The mixed correction utilizes Shepard Functions in combination with a correction to derivative approximations. In corrected meshless methods, the domain boundaries and field variables at the boundaries are approximated with the improved accuracy comparing to the conventional SPH method. The resulting new scheme improves the particle deficiency (kernel support incompleteness) problem.

The reservoir simulation of the complex reservoirs with anisotropic permeability, which includes faults and non-orthogonal grids, with a fully discontinuous permeability tensor in the discretization is a major challenge. Several methods have already been developed and implemented within industry standard reservoir simulators for non-orthogonal grids. The multi point flux approximation, MPFA, is a discretization method developed by the oil industry to be the next generation method in reservoir simulation and it can be applied to different types of mesh, for example using quadrilateral meshes as in Aavatsmark *et al.* (1998) [6], [4], [5], Aavatsmark (2002) [2], Edwards and Rogers (1998) [86], Klausen and Russell (2004) [142] or unstructured grids as in Edwards (2002) [84], [83] to approximate the following operator:

$$\mathbf{L}p = -\nabla(\mathbf{M}(p) \nabla p(\mathbf{r})), \quad \forall \mathbf{r} \in \Omega \subset \mathbb{R}^n, \quad (4.3)$$

where  $p(\mathbf{r})$  is the pressure,  $\mathbf{M}(p) = (m_{\alpha\beta})$  is the mobility tensor,  $g(\mathbf{r})$  is the known sink/source term,  $n = 1, 2, 3$  is the spatial dimension. Consider operator in equation (4.3) with piecewise constant mobility  $\mathbf{M}(p)$  in  $\Omega$ .

### 4.1.1 Multi point flux approximation

Several MPFA methods have already been developed and implemented within an industry standard reservoir simulator for non-orthogonal grids. The methods are known as the O-method, U-method and the L-method for quadrilateral meshes in two and three dimensions (see, Edwards and Rogers, 1998 [86]; Aavatsmark, 2002 [2]; Chen *et al.*, 2007 [60]; Lee *et al.*, 1998, 2002 [155], [156]; Oian, 2006 [222]). The MPFA methods are not restricted to quadrilateral meshes and have been investigated in Aavatsmark *et al.* (1996) [3], Aavatsmark *et al.* (1998) [4], [5], Edwards (2002) [84], [83]. It has been noticed that some of the numerical methods for elliptic equations may violate the maximum principle (i.e. lead to spurious oscillations). Therefore, proposed methods must satisfy a discrete maximum principle to avoid any spurious oscillations. The discrete maximum principle for MPFA methods was discussed, e.g., in Edwards and Rogers (1998) [86], Mlacnik and Durlofsky (2006) [207], Lee *et al.* (2002) [156]. However, non-physical oscillations can appear in the developed multi-point flux approximations when the anisotropy is particularly strong. It has been found that the oscillations

are closely related to the poor approximation of the pressure gradient in the flux computation. Therefore, proposed methods must correctly approximate underlying operators, satisfy a discrete maximum principle and have coercivity properties. Furthermore, the method must be robust and efficient.

### 4.1.2 Two-point flux approximation

The well-known two-point flux approximation (TPFA) is a mesh dependent numerical scheme used in solving elliptic equation (4.1):  $\mathbf{L}(\mathbf{u}) = 0$  with the diagonal matrix of coefficients  $\mathbf{M}$ . The net flow rate from a cell  $I$  into neighboring cells in this scheme is obtained by summing fluxes over the neighboring cells  $J$ :

$$\mathbf{q} = \sum_J \tilde{T}_{JI} [\mathbf{u}(\mathbf{r}_J) - \mathbf{u}(\mathbf{r}_I)], \quad \tilde{T}_{JI} \geq 0, \quad (4.4)$$

where  $\tilde{T}_{JI}$  is the transmissibility between cells  $J$  and  $I$ ,  $\mathbf{q}$  is the total flux through the boundary of the control volume located at the point  $\mathbf{r}_I$ . The transmissibility  $\tilde{T}_{JI}$  defined at an interior face  $f$  between cells  $J$  and  $I$  is calculated as

$$\tilde{T}_{JI} = \frac{1}{\left[ \frac{\|\mathbf{r}_{f,J}\|^2}{\mathbf{S}_f \mathbf{M} \mathbf{r}_{f,J}} + \frac{\|\mathbf{r}_{f,I}\|^2}{\mathbf{S}_f \mathbf{M} \mathbf{r}_{f,I}} \right]}, \quad (4.5)$$

where  $\mathbf{r}_{f,J}$  and  $\mathbf{r}_{f,I}$  are the vectors from centers of cells  $J$  and  $I$  to the face  $f$  respectively,  $\mathbf{S}_f$  is the area vector of the face  $f$ . In the case of  $\mathbf{M}$ -orthogonal mesh, when  $\mathbf{M} \mathbf{S}_f$  and  $[\mathbf{r}_J - \mathbf{r}_I]$  are collinear, the expression (4.4) reduces to the form of the central finite difference scheme and approximates the flux with  $\mathcal{O}(h^2)$  order of accuracy for any mobility tensor field  $\mathbf{M}$ . The expression (4.5) ensures that the flux into the adjoining region is continuous (Clearly and Monaghan, 1999 [66]). The TPFA scheme (4.4) is the unconditionally monotone scheme.

### 4.1.3 Mimetic approximation

Consider the elliptic equation for pressure,

$$\mathbf{v} + \mathbf{K} \nabla p = 0, \quad (4.6)$$

$$\nabla \cdot \mathbf{v} = q, \quad (4.7)$$

where  $\mathbf{K}$  is the permeability tensor,  $p$  is the fluid pressure and  $\mathbf{v} \in \mathbb{R}^n$  is the fluid velocity. To discretize (4.6) using a local-flux mimetic method, the mass matrix  $\mathbf{B}$  is introduced. If  $\mathbf{B}$  is exact for linear pressures, one can expect to get a consistent discretisation of (4.6). Thus, for any linear pressure  $p = p_o + \mathbf{a} \cdot \mathbf{x}$ , the following relation can be written

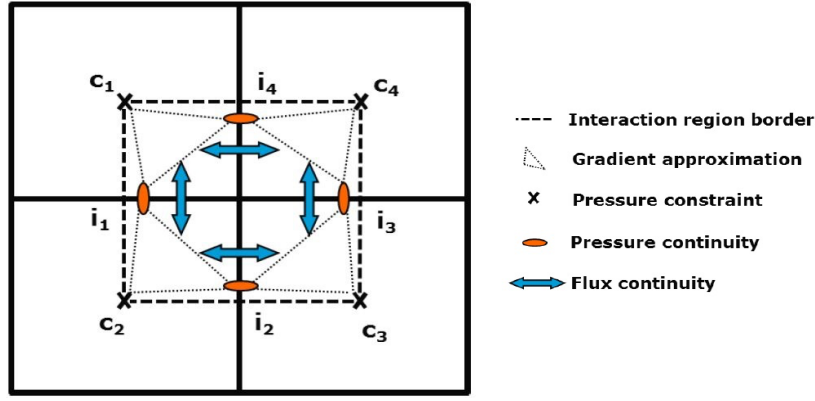
$$\mathbf{N} \mathbf{a} = -\mathbf{N} \mathbf{R}^{-1} \{\Delta p\}, \quad (4.8)$$

where  $\mathbf{N}$  is the  $d \times n$  matrix of face normals and  $\mathbf{R}$  is the corresponding matrix of vectors from the cell center to the face centers (e.g., from  $C_4$  to  $i_4$ ) (see interaction region border, gradient pressure approximation contour and location of cell centers (cell pressure) on Fig.4.1),  $\{\Delta p\}$  is the corresponding pressure difference between cell center pressure (e.g., pressure at the point  $C_4$ ) and face centers pressure (e.g., pressure at the point  $i_4$ ). The local expression for the face flux are computed by splitting each  $k$ -orthogonal face into  $k$  sub-faces, each with one corner belonging to the face. Let us denote  $\mathbf{N}_i$  and  $\mathbf{R}_i$  as normal and distance for each sub-face of face  $i$ , respectively. It is required that  $\mathbf{B}$  is the block-diagonal matrix with one block for each corner in the cell. For a regular grid, each such corner will be the intersection of  $d$  sub-faces and, hence, will be unique. Note that this matrix is not symmetric and does not form an inner-product but does form a bilinear form on sub-face-fluxes.

To derive a cell-centered scheme from the definition of  $\mathbf{B}$ , the conventional mimetic mixed hybrid formulation is used [166]

$$\begin{bmatrix} \mathbf{B} & \mathbf{C} & \mathbf{D} \\ \mathbf{C}^T & \mathbf{0} & \mathbf{0} \\ \mathbf{D}^T & \mathbf{0} & \mathbf{0} \end{bmatrix} \begin{bmatrix} \mathbf{v}_H \\ -\mathbf{p} \\ \boldsymbol{\pi} \end{bmatrix} = \begin{bmatrix} \mathbf{0} \\ \mathbf{q} \\ \mathbf{0} \end{bmatrix} \quad (4.9)$$

where the vectors  $\mathbf{v}_H$ ,  $\mathbf{p}$ , and  $\boldsymbol{\pi}$  collect the degrees-of-freedom associated with fluxes across the cell interfaces, face pressures, and cell pressures, respectively. The  $\mathbf{C}$  is block-diagonal with blocks  $\mathbf{e} = (1, 1, \dots, 1)$ , that


 Figure 4.1: Two dimensional  $\mathcal{O}$ -method

adds up sub-faces, and  $\mathbf{D}$  maps from cell-wise ordering to global ordering of sub-faces. A number of methods for solving such systems have been proposed in the literature, but these are generally not as efficient as solving a symmetric, positive-definite system. Hence, a so-called Schur-complement method (the Schur complement for the face pressure) can be used to reduce the mixed hybrid system to a positive-definite system [165]:

$$(\mathbf{D}^T \mathbf{B}^{-1} \mathbf{D} - \mathbf{F}^T \mathbf{V}^{-1} \mathbf{F}) \boldsymbol{\pi} = \mathbf{F}^T \mathbf{V}^{-1} \mathbf{q}, \quad (4.10)$$

where  $\mathbf{F} = \mathbf{C}^T \mathbf{B}^{-1} \mathbf{D}$  and  $\mathbf{V} = \mathbf{C}^T \mathbf{B}^{-1} \mathbf{C}$ . Given the face pressure, the cell pressures and fluxes can be reconstructed by back-substitution, i.e., by solving

$$\mathbf{V} \mathbf{p} = \mathbf{q} + \mathbf{F} \boldsymbol{\pi}, \quad \mathbf{B} \mathbf{v}_H = \mathbf{C} \boldsymbol{\pi} - \mathbf{D} \boldsymbol{\pi}. \quad (4.11)$$

The mimetic method has a so-called property of explicit flux representation, which allows to express the inter-cell fluxes as a linear combination of neighboring values for the pressure. This property is particularly useful in fully implicit discretizations of time-dependent problems

The choice of the discretization scheme (e.g., either a mimetic method or a multi-point flux scheme) puts certain limitations on its use. In the case of MPFA, the schemes are quite computationally demanding to assemble, store and handle, while in the mimetic case, the inclusion of gravity and forcing boundary condition, wells is not yet adequately solved problem.

## § 4.2 Fluid Flow Modelling Using SPH

Let  $\Omega$  be a bounded domain in  $\mathbb{R}^n$  (a compact) with a piecewise boundary  $\partial\Omega = \bar{\Gamma}_D \cup \bar{\Gamma}_N$ ,  $\bar{\Gamma}_D \cap \bar{\Gamma}_N = \emptyset$ , where measure  $\mu(\Gamma_D) \neq 0$ ,  $\Gamma_D$  is the part of the boundary corresponding to the Dirichlet boundary condition,  $\Gamma_N$  is the part of the boundary corresponding to the Neumann boundary condition. In the following sections this question will be analyzed in details for some modified schemes by stating that the solution of the equation for  $\mathbf{M}(\mathbf{r}) = m(\mathbf{r}) \cdot \mathbf{I}$ ,  $m(\mathbf{r}) \geq 0$ ,  $\forall \mathbf{r} \in \Omega \subset \mathbb{R}^n$ , where  $\mathbf{I}$  is the unit tensor:

$$\mathbf{L}(\mathbf{u}(\mathbf{r}_I)) = -\nabla(\mathbf{M}(\mathbf{r}) \nabla \mathbf{u}(\mathbf{r})) = -m(\mathbf{r}_I) \mathbf{u}_{,\alpha\alpha}(\mathbf{r}_I) - m_{,\alpha}(\mathbf{r}_I) \mathbf{u}_{,\alpha}(\mathbf{r}_I) = g(\mathbf{r}), \quad (4.12)$$

From (4.12), it follows that second order derivatives need to be approximated.

To calculate the second derivatives of  $\mathbf{F}$ , several methods were proposed (Chen *et al.* (1999, 2000) [57], [56], [55]; Bonet and Kulasegaram (2000) [32]; Colin *et al.* (2006) [69]) in SPH community. However, second-order derivatives can often be avoided entirely if the PDE is written in weak form. It is important to note that approximations using second-order derivatives of the kernel are often noisy and sensitive to particle distribution, particularly for spline kernels of lower order. This section presents the meshless multi-point flux approximation (MMPFA) of second order elliptic operators containing scalar inhomogeneous coefficient. The method is based on a pressure gradient approximation commonly used in meshless methods (or Smoothed Particle Hydrodynamics method - SPH method). The standard SPH spatial discretization of the Laplace operator (4.1) arises from

the following relations with  $g(\mathbf{r}) = 0$ ,  $\forall \mathbf{r} \in \tilde{\Omega}_{\mathbf{r}_I, \tilde{h}_I}$  and  $W \in C_0(\Omega_{\mathbf{r}_I, \tilde{h}_I})$ :

$$\begin{aligned} \mathbf{L}(\mathbf{u}(\mathbf{r}_I)) &= \lim_{\tilde{h}_I \rightarrow 0} \int_{\Omega_{\mathbf{r}_I, \tilde{h}_I}} \mathbf{L}(\mathbf{u}(\mathbf{r})) W(\mathbf{r} - \mathbf{r}_I, \tilde{h}_I) dV_{\mathbf{r}} \approx \\ &\approx \left[ \int_{\Omega_{\mathbf{r}_I, \tilde{h}_I}} \mathbf{M}(\mathbf{r}) \nabla \mathbf{u}(\mathbf{r}) \cdot \nabla W(\mathbf{r} - \mathbf{r}_I, \tilde{h}_I) dV_{\mathbf{r}} \right], \end{aligned} \quad (4.13)$$

where  $W(\mathbf{r} - \mathbf{r}_I, \tilde{h}_I)$  is the kernel that weakly approximates the Dirac delta function  $\delta(\mathbf{r} - \mathbf{r}_I)$  but with finite characteristic width  $\tilde{h}_I$  around the particle  $I$ . The proposed discretization schemes should be compatible with a discontinuous  $m(\mathbf{r})$  (or piecewise function) coefficient of the operator (4.1) since this coefficient cannot be differentiable in the classical sense.

Without loss of generality, the discretization schemes below are build for  $-\langle \mathbf{L}(\mathbf{u}(\mathbf{r}_I)) \rangle$ . Hence, there are two sources of the discretization error: (a) the error associated with the weak approximation of the Dirac delta function  $\delta(\mathbf{r} - \mathbf{r}_I)$ , which is related to the smoothing particle length  $\tilde{h}_I$  and (b) the error associated with Monte-Carlo expressions or any cubature rules, which is related to the number of particles and particles distribution within the control volume  $\Omega_{\mathbf{r}_I, \tilde{h}_I}$ .

#### 4.2.1 Brookshaw (1985) scheme

Brookshaw (1985) [41] proposed an approximation of the Laplacian for an inhomogeneous scalar field  $m(\mathbf{r})$  that only includes first order derivatives:

$$\begin{aligned} \langle \nabla(m(\mathbf{r}_I) \nabla \mathbf{u}(\mathbf{r}_I)) \rangle &= \\ \sum_{\Omega_{\mathbf{r}_I, \tilde{h}_I}} V_{\mathbf{r}_J} [\mathbf{u}(\mathbf{r}_J) - \mathbf{u}(\mathbf{r}_I)] &\frac{(\mathbf{r}_J - \mathbf{r}_I) \cdot (m_J + m_I) \overline{\nabla W}(\mathbf{r}_J - \mathbf{r}_I, \tilde{h}_{IJ})}{\|\mathbf{r}_J - \mathbf{r}_I\|^2}, \end{aligned} \quad (4.14)$$

where  $V_{\mathbf{r}_J}$  is the volume of a particle  $J$ ,  $\|\bullet\|$  is the Euclidean norm throughout this paper,  $\mathbf{F}(\mathbf{r})$  is the unknown scalar or vector field (e.g., pressure  $p$ )  $\forall \mathbf{r} \in \Omega \subset \mathbb{R}^n$ ,  $m_I = m(\mathbf{r}_I)$ ,  $\mathbf{r}_I \in \Omega \subset \mathbb{R}^n$  and  $m_J = m(\mathbf{r}_J)$ ,  $\mathbf{r}_J \in \Omega \subset \mathbb{R}^n$  are the field coefficients,  $W(\mathbf{r}_J - \mathbf{r}_I, h)$  is the Kernel. This scheme can be derived by applying the particle approximation step to the right-hand side of (4.13) with the following assumptions

$$\nabla \mathbf{u}(\mathbf{r}_J) \approx [\mathbf{u}(\mathbf{r}_J) - \mathbf{u}(\mathbf{r}_I)] \frac{(\mathbf{r}_J - \mathbf{r}_I)}{\|\mathbf{r}_J - \mathbf{r}_I\|^2}. \quad (4.15)$$

Some special words need to be said about the mobility approximation, which comes in the form

$$2m(\mathbf{r}_J) \approx m_J + m_I. \quad (4.16)$$

The factor 2 is introduced to compensate the factor of 1/2 in the second leading term of the Taylor expansion of the relation (4.15). Furthermore, the relation (4.16) allows to capture a heterogeneous mobility field distribution.

**Theorem 4.1.** *The discretization scheme (4.14) at a given point  $\mathbf{r}_I \in \Omega \subset \mathbb{R}^n$  sufficiently far away from the boundary  $\partial\Omega$  (i.e., where the kernel  $W$  has a full support) has an error bounded by  $C(\tilde{h}_{I,m}) \cdot \left(\frac{h_{I,p}^\omega}{\tilde{h}_{I,m}}\right)$ ,*

$$0 \leq \omega < 2, \lim_{\tilde{h}_{I,m} \rightarrow 0} \frac{C(\tilde{h}_{I,m})}{\tilde{h}_{I,m}} = 0, h_{I,p} = \sup_{J: \mathbf{r}_J \in \Omega} \|\mathbf{r}_J - \mathbf{r}_I\|, \tilde{h}_{I,m} = \inf_{J: \mathbf{r}_J \in \Omega_{\mathbf{r}_I, \tilde{h}_I}} \tilde{h}_{IJ} \text{ for any scalar mobility field } m(\mathbf{r}) \in C^1(\Omega), m(\mathbf{r}) \geq 0.$$

*Proof.* Using Taylor series expansions about a point  $\mathbf{r}_I$ , the following relations can be written:

$$\mathbf{u}(\mathbf{r}_J) = \mathbf{u}(\mathbf{r}_I) + \mathbf{u}_{,\alpha}(\mathbf{r}_I) [\mathbf{r}_J^\alpha - \mathbf{r}_I^\alpha] + \frac{1}{2} \mathbf{u}_{,\alpha\gamma}(\mathbf{r}_I) [\mathbf{r}_J^\alpha - \mathbf{r}_I^\alpha] [\mathbf{r}_J^\gamma - \mathbf{r}_I^\gamma] + \mathcal{O}(\|\mathbf{r}_J - \mathbf{r}_I\|^3), \quad (4.17)$$



$$m(\mathbf{r}_J) = m(\mathbf{r}_I) + m_{,\alpha}(\mathbf{r}_I) [\mathbf{r}_J^\alpha - \mathbf{r}_I^\alpha] + \mathcal{O}(\|\mathbf{r}_J - \mathbf{r}_I\|^2). \quad (4.18)$$

Substituting relations (4.17)-(4.18) into the scheme (4.14), it leads to the following relations:

$$\begin{aligned} & \sum_{\Omega_{\mathbf{r}_I, \tilde{h}_I}} V_{\mathbf{r}_J} [\mathbf{u}(\mathbf{r}_J) - \mathbf{u}(\mathbf{r}_I)] \frac{(\mathbf{r}_J - \mathbf{r}_I) \cdot (m_J + m_I) \cdot \overline{\nabla W}(\mathbf{r}_J - \mathbf{r}_I, \tilde{h}_{IJ})}{\|\mathbf{r}_J - \mathbf{r}_I\|^2} = \\ & = 2m(\mathbf{r}_I) \mathbf{u}_{,\alpha}(\mathbf{r}_I) \sum_{\Omega_{\mathbf{r}_I, \tilde{h}_I}} V_{\mathbf{r}_J} \overline{\nabla_\alpha W}(\mathbf{r}_J - \mathbf{r}_I, \tilde{h}_{IJ}) + \\ & + m(\mathbf{r}_I) \mathbf{u}_{,\alpha\gamma}(\mathbf{r}_I) \sum_{\Omega_{\mathbf{r}_I, \tilde{h}_I}} V_{\mathbf{r}_J} [\mathbf{r}_J^\alpha - \mathbf{r}_I^\alpha] \overline{\nabla_\gamma W}(\mathbf{r}_J - \mathbf{r}_I, \tilde{h}_{IJ}) + \\ & + m_{,\alpha}(\mathbf{r}_I) \mathbf{u}_{,\gamma}(\mathbf{r}_I) \sum_{\Omega_{\mathbf{r}_I, \tilde{h}_I}} V_{\mathbf{r}_J} [\mathbf{r}_J^\alpha - \mathbf{r}_I^\alpha] \overline{\nabla_\gamma W}(\mathbf{r}_J - \mathbf{r}_I, \tilde{h}_{IJ}) + \mathcal{E}, \end{aligned} \quad (4.19)$$

where the leading term is bounded as follows

$$\left\| 2m(\mathbf{r}_I) \mathbf{u}_{,\alpha}(\mathbf{r}_I) \sum_{\Omega_{\mathbf{r}_I, \tilde{h}_I}} V_{\mathbf{r}_J} \overline{\nabla_\alpha W}(\mathbf{r}_J - \mathbf{r}_I, \tilde{h}_{IJ}) \right\| \leq 2 \cdot C(\tilde{h}_{I,m}) \cdot m(\mathbf{r}_I) \left( \frac{1}{\tilde{h}_{I,m}} \right) \quad (4.20)$$

where  $C(\tilde{h}_{I,m}) = \left( \sum_{\Omega_{\mathbf{r}_I, h}} V_{\mathbf{r}_J} |G(z_J, \mathbf{r}_I)| \right)$  and  $\lim_{\tilde{h}_{I,m} \rightarrow 0} \frac{C(\tilde{h}_{I,m})}{\tilde{h}_{I,m}} = 0$ . The leading term of the error function  $\mathcal{E}$  is defined by the following expression

$$\begin{aligned} \mathcal{E} & = \frac{1}{6} m(\mathbf{r}_I) \mathbf{u}_{,\alpha\omega\gamma}(\mathbf{r}_I) \sum_{\Omega_{\mathbf{r}_I, h}} V_{\mathbf{r}_J} [\mathbf{r}_J^\alpha - \mathbf{r}_I^\alpha] [\mathbf{r}_J^\omega - \mathbf{r}_I^\omega] \overline{\nabla_\gamma W}(\mathbf{r}_J - \mathbf{r}_I, \tilde{h}_{IJ}) + \\ & + \frac{1}{2} \mathbf{u}_{,\alpha\gamma}(\mathbf{r}_I) m_{,\omega}(\mathbf{r}_I) \sum_{\Omega_{\mathbf{r}_I, h}} V_{\mathbf{r}_J} [\mathbf{r}_J^\alpha - \mathbf{r}_I^\alpha] [\mathbf{r}_J^\omega - \mathbf{r}_I^\omega] \overline{\nabla_\gamma W}(\mathbf{r}_J - \mathbf{r}_I, \tilde{h}_{IJ}) \end{aligned} \quad (4.21)$$

and error bound can be found by applying several times triangle inequality

$$\|\mathcal{E}\| \leq C(\tilde{h}_{I,m}) \cdot \left( \frac{1}{6} m(\mathbf{r}_I) \|\mathbf{u}_{,\alpha\omega\gamma}(\mathbf{r}_I)\| + \frac{1}{2} \|\mathbf{u}_{,\alpha\gamma}(\mathbf{r}_I)\| \|m_{,\omega}(\mathbf{r}_I)\| \right) \left( \frac{h_{I,p}^2}{\tilde{h}_{I,m}} \right), \quad (4.22)$$

While obtaining (4.19), the following relation has been used

$$[\mathbf{r}_J^\alpha - \mathbf{r}_I^\alpha] \frac{(\mathbf{r}_J^\gamma - \mathbf{r}_I^\gamma) \overline{\nabla_\gamma W}(\mathbf{r}_J - \mathbf{r}_I, \tilde{h}_{IJ})}{\|\mathbf{r}_J - \mathbf{r}_I\|^2} = \overline{\nabla_\alpha W}(\mathbf{r}_J - \mathbf{r}_I, \tilde{h}_{IJ}), \quad \forall \alpha. \quad (4.23)$$

As noted in [236], since matrix  $H = (\mathbf{u}_{,\alpha\gamma}(\mathbf{r}_I))$  is coupled with the tensor

$$\Gamma_{\alpha\gamma} = \left( \sum_{\Omega_{\mathbf{r}_I, h}} V_{\mathbf{r}_J} [\mathbf{r}_J^\alpha - \mathbf{r}_I^\alpha] \overline{\nabla_\gamma W}(\mathbf{r}_J - \mathbf{r}_I, \tilde{h}_{IJ}) \right)$$

via inner product, it is difficult to separate them. However, using the identity  $[H : \Gamma] = \text{tr}[H\Gamma^T]$ , along with the fact that both  $H$  and  $\Gamma$  are symmetric, one can write the relation as in [236]

$$\mathbf{u}_{,\omega\gamma} = (\mathbf{u}_{,\alpha\beta} \Gamma_{\alpha\beta}) \frac{\Gamma_{\omega\gamma}^{-1}}{n} + \Gamma_{\omega\alpha}^{-1} \mathbf{W}_{\alpha\gamma}. \quad (4.24)$$

The  $\mathbf{W}_{\alpha\beta}$  is a tensor with zero trace:

$$\mathbf{W}_{\alpha\beta} = (\mathbf{u}_{,\alpha\omega} \Gamma_{\omega\beta}) - \delta_{\alpha\beta} (\mathbf{u}_{,\omega\gamma} \Gamma_{\omega\gamma}) / n. \quad (4.25)$$

Hence, the maximum accuracy is achieved when

$$\begin{aligned}
(a) \quad & \sum_{\Omega_{\mathbf{r}_I, \tilde{h}_I}} V_{\mathbf{r}_J} \overline{\nabla_\alpha W}(\mathbf{r}_J - \mathbf{r}_I, \tilde{h}_{IJ}) = 0, \quad \forall \alpha; \\
(b) \quad & \sum_{\Omega_{\mathbf{r}_I, \tilde{h}_I}} V_{\mathbf{r}_J} [\mathbf{r}_J^\alpha - \mathbf{r}_I^\alpha] \overline{\nabla_\gamma W}(\mathbf{r}_J - \mathbf{r}_I, \tilde{h}_{IJ}) = \Gamma_{\alpha\beta} = \delta_{\alpha\gamma}, \quad \forall \alpha, \gamma;
\end{aligned} \tag{4.26}$$

which is difficult to fulfill simultaneously for different kernel gradients. Therefore, the overall error is bounded by  $C\left(\tilde{h}_{I,m}\right) \cdot \left(\frac{h_{I,p}^\omega}{\tilde{h}_{I,m}}\right)$ ,  $0 \leq \omega < 2$  for any scalar mobility field  $m(\mathbf{r}) \in C^1(\Omega)$ ,  $m(\mathbf{r}) \geq 0$  covering the worse and best cases.  $\square$

In the chapter 2, several options of computing kernel gradients  $\overline{\nabla W}(\mathbf{r}_J - \mathbf{r}_I, \tilde{h}_{IJ})$  (i.e.,  $\nabla_\alpha W$ ,  $\nabla_\alpha \overline{W}$ ,  $\overline{\nabla_\alpha W}$ , and  $\tilde{\nabla}_\alpha \overline{W}$ ) are proposed (2.31), (2.32), (2.33), and (2.34), respectively. Different kernel gradients have different accuracy with respect to the condition (4.23) and (4.26)(a)-(b). For example, the kernel gradient (2.32) satisfies for any particles distribution condition (4.26)(a) but not the condition (4.23) and (4.26)(b). Kernel gradients (2.31), (2.33), and (2.34) do satisfy (4.23) for any particles distribution but not the conditions (4.26)(a)-(b). At the same time, all corrected options  $\overline{\nabla^* W}(\mathbf{r}_J - \mathbf{r}_I, \tilde{h}_{IJ})$  (i.e.,  $\nabla_\gamma^* W$ ,  $\nabla_\alpha^* \overline{W}$ ,  $\overline{\nabla_\alpha^* W}$ , and  $\tilde{\nabla}_\alpha^* \overline{W}$ ) satisfy the condition (4.26)(b) for any particles distribution but not the conditions (4.23) and (4.26)(a). One may decide to use  $\overline{\nabla^* W}(\mathbf{r}_J - \mathbf{r}_I, \tilde{h}_{IJ})$  in the discretization scheme (4.14) which leads to the error with the leading term

$$2m(\mathbf{r}_I) \mathbf{u}_{,\alpha}(\mathbf{r}_I) \sum_{\mathbf{r}_J \in \Omega_{\mathbf{r}_I, \tilde{h}_I}} V_{\mathbf{r}_J} [\mathbf{r}_J - \mathbf{r}_I] \frac{(\mathbf{r}_J - \mathbf{r}_I) \cdot \overline{\nabla^* W}(\mathbf{r}_J - \mathbf{r}_I, \tilde{h}_{IJ})}{\|\mathbf{r}_J - \mathbf{r}_I\|^2}. \tag{4.27}$$

This leads to the incorporation of the correction factor into Brookshaw's approximation. A different correction factor has been introduced and investigated in [236]. Alternatively, as was discussed in [236], the correction multiplier can be introduced in (4.14) defined as  $[\mathbf{C}_{\alpha\alpha}]/n$  leading to:

$$\langle \nabla(m(\mathbf{r}_I) \nabla \mathbf{u}(\mathbf{r}_I)) \rangle^* = \frac{\mathbf{C}_{\alpha\alpha}}{n} \cdot \langle \nabla(m(\mathbf{r}_I) \nabla \mathbf{u}(\mathbf{r}_I)) \rangle. \tag{4.28}$$

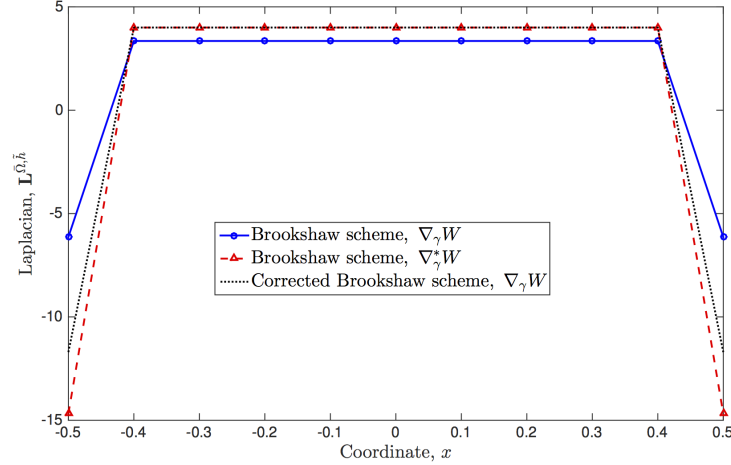
Figure 4.2 shows Laplacian values for the function  $\nabla^2(x^2 + y^2)$  using original Brookshaw's approximation (4.14) with (a) conventional kernel  $\nabla_\gamma W$ , (b) corrected kernel  $\nabla_\gamma^* W$  and corrected Brookshaw's approximation (4.28) with the conventional kernel  $\nabla_\gamma W$ . In addition, Figure 4.2 shows that the discretization scheme (4.14) with the  $\overline{\nabla^* W}(\mathbf{r}_J - \mathbf{r}_I, \tilde{h}_{IJ})$  kernel gradient is less accurate near the boundary due to the magnitude of the (4.27) which is related to the associated leading term of the error.

The scheme (4.14) is widely (almost unconditionally) used in the SPH modeling community. For example, it was used for a thermal conduction [41, 66, 125], for modeling a viscous diffusion [213], for a vortex spin-down [72] and Rayleigh-Taylor instability, for simulating Newtonian and non-Newtonian flows with a free surface [154] for the comparison of weakly compressible and truly incompressible algorithms, for macroscopic and mesoscopic flows [111], for a simulation of a solid-fluid mixture flow [280]. Recently, it has been used to model electrokinetic flows [223].

There are different numerical SPH schemes used in numerical simulations. High order accuracy approximations can also be derived by using the SPH discretization on the higher order Taylor series expansion [90, 94, 174, 236]. However, it is usually required that the discrete numerical schemes can reproduce linear fields [33, 183, 188, 231] or polynomials up to a given order [176].

## 4.2.2 Schwaiger (2008) scheme

The correction terms to the Brookshaw formulation which improve the accuracy of the Laplacian operator



**Figure 4.2:** Values for  $\nabla^2(x^2 + y^2)$  along  $y = 0$  using Brookshaw's approximation with (a) conventional kernel  $\nabla_\gamma W$ , (b) corrected kernel  $\nabla_\gamma^* W$  and with the correction multiplier  $[\mathbf{C}_{\alpha\alpha}]/n$ . The numerical domain is a unit square in  $\mathbb{R}^2$  with the center at  $a_i = 0$ ,  $\forall i$  and side length  $L = 1$ . The cubic spline (2.56) was used with  $\tilde{h} = f \cdot h_p$ ,  $h_p = 0.1$ ,  $f = 1.0$ .

near boundaries were proposed by Schwaiger in [236]:

$$\begin{aligned} \frac{n}{\Gamma_{kk}^{-1}} \langle \nabla (m(\mathbf{r}_I) \nabla \mathbf{u}(\mathbf{r}_I)) \rangle = & \\ \left\{ \sum_{\Omega_{\mathbf{r}_I, \tilde{h}_I}} V_{\mathbf{r}_J} [\mathbf{u}(\mathbf{r}_J) - \mathbf{u}(\mathbf{r}_I)] \frac{(\mathbf{r}_J - \mathbf{r}_I) \cdot (m_J + m_I) \overline{\nabla W}(\mathbf{r}_J - \mathbf{r}_I, \tilde{h}_{IJ})}{\|\mathbf{r}_J - \mathbf{r}_I\|^2} \right\} - & \quad (4.29) \\ - \{ \langle \nabla_\alpha (m(\mathbf{r}_I) \mathbf{u}(\mathbf{r}_I)) \rangle - \mathbf{u}(\mathbf{r}_I) \langle \nabla_\alpha m(\mathbf{r}_I) \rangle + m(\mathbf{r}_I) \langle \nabla_\alpha \mathbf{u}(\mathbf{r}_I) \rangle \} \mathbf{N}^\alpha, & \end{aligned}$$

$$\mathbf{N}^\alpha(\mathbf{r}_I) = \left[ \sum_{\Omega_{\mathbf{r}_I, \tilde{h}_I}} V_{\mathbf{r}_J} \overline{\nabla_\alpha W}(\mathbf{r}_I - \mathbf{r}_J, \tilde{h}_{IJ}) \right], \quad (4.30)$$

$$\langle \nabla_\alpha \mathbf{u}(\mathbf{r}_I) \rangle = \sum_{\Omega_{\mathbf{r}_I, \tilde{h}_I}} V_{\mathbf{r}_J} [\mathbf{u}(\mathbf{r}_J) - \mathbf{u}(\mathbf{r}_I)] \overline{\nabla_\alpha^* W}(\mathbf{r}_I - \mathbf{r}_J, \tilde{h}_{IJ}), \quad (4.31)$$

where  $n = 1, 2, 3$  is the spatial dimension and the tensor  $\Gamma_{\alpha\beta}$  is defined by

$$\Gamma_{\alpha\beta}(\mathbf{r}_I) = \sum_{\Omega_{\mathbf{r}_I, \tilde{h}_I}} V_{\mathbf{r}_J} \frac{(\mathbf{r}_J^\gamma - \mathbf{r}_I^\gamma) \overline{\nabla_\gamma W}(\mathbf{r}_J - \mathbf{r}_I, \tilde{h}_{IJ})}{\|\mathbf{r}_J - \mathbf{r}_I\|^2} (\mathbf{r}_J^\alpha - \mathbf{r}_I^\alpha) (\mathbf{r}_J^\beta - \mathbf{r}_I^\beta). \quad (4.32)$$

The gradient  $\langle \nabla_\alpha \mathbf{u}(\mathbf{r}_I) \rangle$  is the corrected gradient which can reproduce linear fields [33, 231]. For multi-dimensional problems, the correction tensor  $\Gamma_{\alpha\beta}(\mathbf{r}_I)$  is a matrix. If the particle  $\mathbf{r}_I$  has entire stencil support (i.e., the domain support for all kernels  $W(\mathbf{r}_J - \mathbf{r}_I, \tilde{h}_{IJ})$  is entire and symmetric) then  $\Gamma_{\alpha\beta}(\mathbf{r}_I) \approx \delta_{\alpha\beta}$ .

**Lemma 4.2.** The following identities are valid for  $\overline{\nabla_\gamma W}(\mathbf{r}_J - \mathbf{r}_I, \tilde{h}_{IJ})$  described by (2.31), (2.33) and (2.34):

$$\begin{aligned} [\mathbf{r}_J^\alpha - \mathbf{r}_I^\alpha] \frac{(\mathbf{r}_J^\gamma - \mathbf{r}_I^\gamma) \overline{\nabla_\gamma W}(\mathbf{r}_J - \mathbf{r}_I, \tilde{h}_{IJ})}{\|\mathbf{r}_J - \mathbf{r}_I\|^2} = & \\ = -\frac{1}{\tilde{h}_{IJ}} G(z_J, \mathbf{r}_I) \frac{[\mathbf{r}_J^\alpha - \mathbf{r}_I^\alpha]}{\|\mathbf{r}_J - \mathbf{r}_I\|} = \overline{\nabla_\alpha W}(\mathbf{r}_J - \mathbf{r}_I, \tilde{h}_{IJ}), & \quad (4.33) \end{aligned}$$

where  $z_J = \|\mathbf{r}_J - \mathbf{r}_I\| / \tilde{h}_{IJ}$ ,  $\forall \mathbf{r}_J, \mathbf{r}_I \in \Omega \subset \mathbb{R}^n$ .

*Proof.* These identities can be established by applying chain rule differentiation.  $\square$

**Proposition 4.3.** *The correction tensors  $\Gamma$  (described by (4.32)) and  $\mathbf{C}^{-1}$  (where  $\mathbf{C}$  is defined by (2.37)) are the symmetrical and identical tensors for  $\overline{\nabla_\gamma \overline{W}}$  described by (2.31), (2.33) and (2.34).*

*Proof.* The following relation can be established (using Lemma 4.2):

$$\begin{aligned} \Gamma_{\alpha\beta}(\mathbf{r}_I) &= \sum_{\Omega_{\mathbf{r}_I, \tilde{h}_{IJ}}} V_{\mathbf{r}_J} \frac{(\mathbf{r}_J^\gamma - \mathbf{r}_I^\gamma) \overline{\nabla_\gamma \overline{W}}(\mathbf{r}_J - \mathbf{r}_I, \tilde{h}_{IJ})}{\|\mathbf{r}_J - \mathbf{r}_I\|^2} (\mathbf{r}_J^\alpha - \mathbf{r}_I^\alpha) (\mathbf{r}_J^\beta - \mathbf{r}_I^\beta) = \\ &= - \sum_{\Omega_{\mathbf{r}_I, \tilde{h}_{IJ}}} V_{\mathbf{r}_J} \frac{G(z_J, \mathbf{r}_I)}{\tilde{h}_{IJ}} \frac{(\mathbf{r}_J^\alpha - \mathbf{r}_I^\alpha) (\mathbf{r}_J^\beta - \mathbf{r}_I^\beta)}{\|\mathbf{r}_J - \mathbf{r}_I\|} = - \sum_{\Omega_{\mathbf{r}_I, \tilde{h}_{IJ}}} V_{\mathbf{r}_J} \frac{G(z_J, \mathbf{r}_I)}{\tilde{h}_{IJ}} \frac{(\mathbf{r}_J^\beta - \mathbf{r}_I^\beta) (\mathbf{r}_J^\alpha - \mathbf{r}_I^\alpha)}{\|\mathbf{r}_J - \mathbf{r}_I\|} \quad (4.34) \\ &= \Gamma_{\beta\alpha}(\mathbf{r}_I) = \sum_{\Omega_{\mathbf{r}_I, \tilde{h}_{IJ}}} V_{\mathbf{r}_J} [\mathbf{r}_J^\alpha - \mathbf{r}_I^\alpha] \overline{\nabla_\beta \overline{W}}(\mathbf{r}_J - \mathbf{r}_I, \tilde{h}_{IJ}), \quad \Gamma(\mathbf{r}_I) = \mathbf{C}^{-1}(\mathbf{r}_I). \end{aligned}$$

$\square$

It follows that the scheme (4.29)-(4.31) requires to use the trace of  $\Gamma_{\alpha\beta}^{-1}(\mathbf{r}_I)$  or  $\mathbf{C}_{\alpha\beta}(\mathbf{r}_I)$ . The trace of  $\Gamma_{\alpha\beta}(\mathbf{r}_I)$  provides to us the sum of all eigenvalues. It does not give us any range for the eigenvalues which is necessary to estimates  $\mathbf{C}_{\alpha\alpha}(\mathbf{r}_I)$ . Even if we have a positive trace we can still theoretically have several small and large eigenvalues with an opposite sign. Before we get to the analysis of the eigenvalues, it is convenient to introduce a condition for matrices known as strictly diagonally dominant (SDD).

**Definition 4.4.** *A square matrix  $\mathbf{A} = (a_{ij})_{1 \leq i \leq n, 1 \leq j \leq n} \in \mathbb{R}^{n \times n}$  is called strictly diagonally non-dominant matrix if  $|a_{ii}| > \sum_{j \neq i} |a_{ij}| \forall i$ .*

Hence, the following Lemma can be formulated.

**Lemma 4.5.** *The diagonal elements of the matrix  $\Gamma_{ij}(\mathbf{r}_I)$  are positive and the tracer of the  $\Gamma_{ij}(\mathbf{r}_I)$  is bounded, i.e.  $\Gamma_{ii}(\mathbf{r}_I) \geq 0 \forall \beta$  for all kernel  $\overline{\nabla_\gamma \overline{W}}(\mathbf{r}_J - \mathbf{r}_I, \tilde{h}_{IJ})$  defined by (2.31), (2.33) and (2.34) with  $G(z_J, \mathbf{r}_I) \leq 0 \forall z_J$  and  $\Gamma_{\beta\beta}(\mathbf{r}_I) \leq \sum_{\Omega_{\mathbf{r}_I, \tilde{h}_{IJ}}} V_{\mathbf{r}_J} |G(z_J, \mathbf{r}_I)|$ . Furthermore, if matrix  $\Gamma_{ij}(\mathbf{r}_I)$  is strictly diagonally dominant matrix then all eigenvalues  $\lambda(\Gamma_{ij}(\mathbf{r}_I)) > 0$ .*

*Proof.* It follows from the fact that:

$$\Gamma_{ii}(\mathbf{r}_I) = - \sum_{\Omega_{\mathbf{r}_I, \tilde{h}_{IJ}}} V_{\mathbf{r}_J} \frac{(\mathbf{r}_J^i - \mathbf{r}_I^i)^2}{\tilde{h}_{IJ} \|\mathbf{r}_J - \mathbf{r}_I\|} G(z_J, \mathbf{r}_I) \geq 0, \quad G(z_J, \mathbf{r}_I) \leq 0 \forall z_J; \quad (4.35)$$

$$\Gamma_{\beta\beta}(\mathbf{r}_I) = - \sum_{\Omega_{\mathbf{r}_I, \tilde{h}_{IJ}}} V_{\mathbf{r}_J} \|\mathbf{r}_J - \mathbf{r}_I\| \frac{1}{\tilde{h}_{IJ}} G(z_J, \mathbf{r}_I) \geq 0, \quad \frac{\|\mathbf{r}_J - \mathbf{r}_I\|}{\tilde{h}_{IJ}} \leq 1, \quad G(z_J, \mathbf{r}_I) \leq 0 \forall z_J; \quad (4.36)$$

where the summation by repeating indices is only assumed throughout this paper. In order to figure out what range the eigenvalues of the strictly diagonally dominant matrix  $\Gamma_{\alpha\beta}(\mathbf{r}_I)$  (i.e.,  $-\sum_{j \neq i} |\Gamma_{ij}(\mathbf{r}_I)| + \Gamma_{ii}(\mathbf{r}_I) > 0$ ,  $\Gamma_{ii}(\mathbf{r}_I) > 0$ ) would be in, we use Gershgorin's theorem:

$$0 < - \sum_{j \neq i} |\Gamma_{ij}(\mathbf{r}_I)| + \Gamma_{ii}(\mathbf{r}_I) \leq \lambda \leq \sum_{j \neq i} |\Gamma_{ij}(\mathbf{r}_I)| + \Gamma_{ii}(\mathbf{r}_I), \quad i \in \{1, \dots, n\} \quad (4.37)$$

$\square$

**Remark 4.6.** Since strictly diagonally dominant matrices are always nonsingular, the correction matrix  $\mathbf{C}_{\alpha\beta}(\mathbf{r}_I)$  can be defined and  $\mathbf{C}_{\alpha\alpha}(\mathbf{r}_I) = \sum_{\alpha=1}^n \frac{1}{\lambda_\alpha(\Gamma_{ij}(\mathbf{r}_I))} > 0$ .

In addition, it is important to note that

$$\Gamma_{\alpha\beta} = \sum_{\Omega_{\mathbf{r}_I, \tilde{h}_I}} V_{\mathbf{r}_J} (\mathbf{r}_J^\gamma - \mathbf{r}_I^\gamma) \cdot \overline{\nabla_\gamma^* W}(\mathbf{r}_J - \mathbf{r}_I, \tilde{h}_{IJ}) = \delta_{\alpha\beta} \quad (4.38)$$

in the case of using only the corrected gradient  $\overline{\nabla_\gamma^* W}$  and, hence,  $\frac{\Gamma_{kk}^{-1}}{n} = 1$ . However,  $\overline{\nabla_\gamma^* W}$  does not satisfy relation (4.33). For multi-dimensional problems, the correction tensor  $\Gamma_{\alpha\beta}(\mathbf{r}_I)$  is a matrix. If the particle  $\mathbf{r}_I$  has entire stencil support (i.e., the domain support for all kernels  $W(\mathbf{r}_J - \mathbf{r}_I, \tilde{h}_{IJ})$  is entire and symmetric) then  $\Gamma_{\alpha\beta}(\mathbf{r}_I) \approx \delta_{\alpha\beta}$ . Unfortunately,  $\Gamma_{\alpha\beta}(\mathbf{r}_I)$  deviates from  $\delta_{\alpha\beta}$  for the provided algorithm and, hence, it is important to minimize this deviation from  $\delta_{\alpha\beta}$  in the new methods.

To calculate coefficients in the scheme (4.29)–(4.32) is a trivial task. However, in general, it should be performed at each Newton-Raphson iteration in the non-linear case (i.e.,  $m = m(\mathbf{u}(\mathbf{r}_I))$ ). It also requires additional efforts to compute the correction matrices  $\mathbf{C}_{\alpha\beta}$  and  $\Gamma_{\alpha\beta}$  (inversion of  $n \times n$  matrices per each particle, where  $n = 1, 2, 3$  is the spatial dimension) and storage cost of  $\overline{\nabla_\alpha W}(\mathbf{r}_J - \mathbf{r}_I, h)$ ,  $\overline{\nabla_\alpha^* W}(\mathbf{r}_J - \mathbf{r}_I, h)$ , and corresponding  $\Gamma_{\alpha\alpha}^{-1}$  per each particle.

**Theorem 4.7.** The discretization scheme (4.29)–(4.32) at a given point  $\mathbf{r}_I \in \Omega \subset \mathbb{R}^n$  sufficiently far away from the boundary  $\partial\Omega$  (i.e., where the kernel  $W$  has a full support) has an error bounded by  $C(\tilde{h}_{I,m}) \cdot \left(\frac{h_{I,p}^\omega}{\tilde{h}_{I,m}}\right)$ ,

$$1 \leq \omega < 2, \quad \lim_{\tilde{h}_{I,m} \rightarrow 0} \frac{C(\tilde{h}_{I,m})}{\tilde{h}_{I,m}} = 0, \quad h_{I,p} = \sup_{J: \mathbf{r}_J \in \Omega} \|\mathbf{r}_J - \mathbf{r}_I\|, \quad \tilde{h}_{I,m} = \inf_{J: \mathbf{r}_J \in \Omega_{\mathbf{r}_I, \tilde{h}_I}} \tilde{h}_{IJ} \text{ for any scalar mobility field } m(\mathbf{r}) \in C^1(\Omega), \quad m(\mathbf{r}) \geq 0.$$

*Proof.* Using Lemmas 4.2 and 4.3, additional terms proposed by Schwaiger [236] reduce to

$$\begin{aligned} & [(\nabla_\alpha m(\mathbf{r}_I) \mathbf{u}(\mathbf{r}_I)) - \mathbf{u}(\mathbf{r}_I) \langle \nabla_\alpha m(\mathbf{r}_I) \rangle + m(\mathbf{r}_I) \langle \nabla_\alpha \mathbf{u}(\mathbf{r}_I) \rangle] \mathbf{N}^\alpha = \\ & = 2m(\mathbf{r}_I) \mathbf{u}_\alpha(\mathbf{r}_I) \cdot \mathbf{N}^\alpha + \\ & m_{,\beta}(\mathbf{r}_I) \mathbf{u}_{,\omega}(\mathbf{r}_I) \left( \sum_{\Omega_{\mathbf{r}_I, \tilde{h}_I}} V_{\mathbf{r}_J} [\mathbf{r}_J^\omega - \mathbf{r}_I^\omega] [\mathbf{r}_J^\beta - \mathbf{r}_I^\beta] \overline{\nabla_\alpha^* W}(\mathbf{r}_J - \mathbf{r}_I, \tilde{h}_{IJ}) \right) \cdot \mathbf{N}^\alpha + \\ & m(\mathbf{r}_I) \mathbf{u}_{,\beta\omega}(\mathbf{r}_I) \left( \sum_{\Omega_{\mathbf{r}_I, \tilde{h}_I}} V_{\mathbf{r}_J} [\mathbf{r}_J^\omega - \mathbf{r}_I^\omega] [\mathbf{r}_J^\beta - \mathbf{r}_I^\beta] \overline{\nabla_\alpha W}(\mathbf{r}_J - \mathbf{r}_I, \tilde{h}_{IJ}) \right) \cdot \mathbf{N}^\alpha + \tilde{\mathcal{E}} \end{aligned} \quad (4.39)$$

in the vicinity of the point  $\mathbf{r}_I$  with the error  $\tilde{\mathcal{E}}$ . The expression (4.39) has the leading term outlined in (4.19). Subtraction of these terms from (4.19) leads to

$$\langle \nabla(m(\mathbf{r}_I) \nabla \mathbf{u}(\mathbf{r}_I)) \rangle = m(\mathbf{r}_I) \mathbf{u}_{,\alpha\gamma}(\mathbf{r}_I) \Gamma_{\alpha\gamma}^* + m_{,\alpha}(\mathbf{r}_I) \mathbf{u}_{,\gamma}(\mathbf{r}_I) \Gamma_{\alpha\gamma}^* + \tilde{\mathcal{E}} + \mathcal{E}, \quad (4.40)$$

where

$$\Gamma_{\alpha\beta}^* = \Gamma_{\alpha\beta} - \left( \sum_{\Omega_{\mathbf{r}_I, \tilde{h}_I}} V_{\mathbf{r}_J} [\mathbf{r}_J^\omega - \mathbf{r}_I^\omega] [\mathbf{r}_J^\beta - \mathbf{r}_I^\beta] \overline{\nabla_\alpha^* W}(\mathbf{r}_J - \mathbf{r}_I, \tilde{h}_{IJ}) \right) \cdot \mathbf{N}^\alpha \quad (4.41)$$

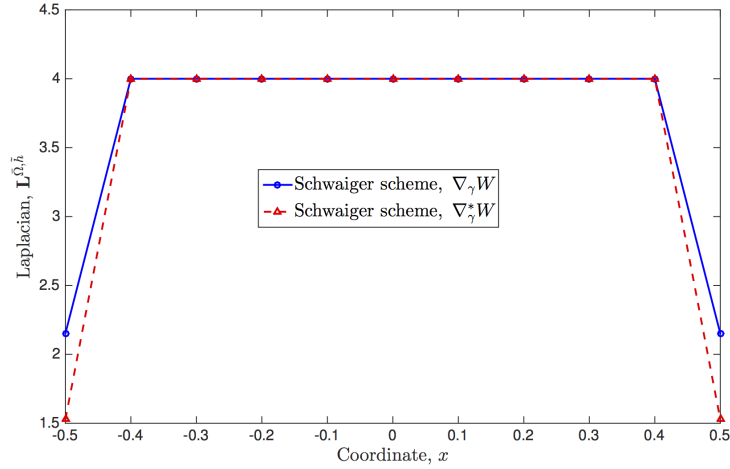
and performing the normalization lead to the announced in the theorem result.  $\square$

It follows that the usage of  $\Gamma_{\alpha\beta}^*$  instead of  $\Gamma_{\alpha\beta}$  in (4.29) will improve the accuracy of the scheme (4.29)–(4.32). Furthermore, if one uses  $\overline{\nabla W}(\mathbf{r}_J - \mathbf{r}_I, \tilde{h}_{IJ}) = \overline{\nabla^* W}(\mathbf{r}_J - \mathbf{r}_I, \tilde{h}_{IJ})$  in the first term of the discretization

scheme (4.29) then the definition for  $\mathbf{N}^\alpha$  has to be modified in accordance of (4.27) to maintain the higher order discretization accuracy, for example, as:

$$\tilde{\mathbf{N}}^\alpha = \sum_{\Omega_{\mathbf{r}_I, \tilde{h}_I}} V_{\mathbf{r}_J} [\mathbf{r}_J^\alpha - \mathbf{r}_I^\alpha] \frac{(\mathbf{r}_J - \mathbf{r}_I) \cdot \overline{\nabla W}(\mathbf{r}_J - \mathbf{r}_I, \tilde{h}_{IJ})}{\|\mathbf{r}_J - \mathbf{r}_I\|^2}, \quad \forall \alpha \quad (4.42)$$

which reduces to the conventional  $\mathbf{N}^\alpha$  in the case of  $\overline{\nabla W}(\mathbf{r}_J - \mathbf{r}_I, \tilde{h}_{IJ}) \neq \overline{\nabla^* W}(\mathbf{r}_J - \mathbf{r}_I, \tilde{h}_{IJ})$  due to (4.33). Figure 4.3 shows the Laplacian for the function  $\nabla^2(x^2 + y^2)$  using Schwaiger's approximation (4.29)–(4.32) with (a) conventional kernel  $\nabla_\gamma W$  and (b) corrected kernel  $\nabla_\gamma^* W$ .



**Figure 4.3:** Values for  $\nabla^2(x^2 + y^2)$  along  $y = 0$  using Schwaiger's approximation with (a) conventional kernel  $\nabla_\gamma W$  and (b) corrected kernel  $\nabla_\gamma^* W$ . The numerical domain is a unit square in  $\mathbb{R}^2$  with the center at  $a_i = 0, \forall i$ . The cubic spline (2.56) was used with  $\tilde{h} = f \cdot h_p, h_p = 0.1, f = 1.0$ .

### 4.2.3 Meshless Transmissibilities

It is clear that the expression (4.29) cannot be written in the form (4.4) due to terms  $\langle \nabla_\alpha (m(\mathbf{r}_I) \mathbf{u}(\mathbf{r}_I)) \rangle \mathbf{N}^\alpha$  and  $\mathbf{u}(\mathbf{r}_I) \langle \nabla_\alpha m(\mathbf{r}_I) \rangle \mathbf{N}^\alpha$ . Hence, it is only possible in this case to introduce a definition of a partial meshless transmissibility between particles  $\mathbf{r}_J$  and  $\mathbf{r}_I$  as follows:

$$T^P(\mathbf{r}_J, \mathbf{r}_I) = T_{JI}^P = \frac{\Gamma_{\beta\beta}^{-1}}{n} \times V_{\mathbf{r}_J} \left\{ \frac{(\mathbf{r}_J - \mathbf{r}_I) \cdot (m_J + m_I) \cdot \overline{\nabla W}(\mathbf{r}_J - \mathbf{r}_I, \tilde{h}_{IJ})}{\|\mathbf{r}_J - \mathbf{r}_I\|^2} - m_I \overline{\nabla W}(\mathbf{r}_J - \mathbf{r}_I, \tilde{h}_{IJ}) \mathbf{N}^\alpha \right\}. \quad (4.43)$$

It is important to note that transmissibilities  $T_{JI}^P$  and  $\tilde{T}_{JI}^P$  have different physical units. Furthermore, it raises the question wherever the scheme (4.29)–(4.32) is monotone.

Hence, there is an additional term that has not been taken into account in (4.29)–(4.32). The following section describes an alternative numerical scheme for the heterogeneous Laplace operator. Some initial attempts were also made in [191].

## 4.2.4 New scheme

The correction terms to the Brookshaw [41] and Schwaiger [236] formulations which improve the accuracy of the Laplacian operator near boundaries can be done as follows:

$$\begin{aligned} & \frac{n}{\bar{\Gamma}_{\beta\beta}^{-1}} \langle \nabla (\mathbf{M}(\mathbf{r}_I) \nabla \mathbf{u}(\mathbf{r}_I)) \rangle = \\ & \left\{ \sum_{\Omega_{\mathbf{r}_I, \tilde{h}_I}} V_{\mathbf{r}_J} [\mathbf{u}(\mathbf{r}_J) - \mathbf{u}(\mathbf{r}_I)] \frac{(\mathbf{r}_J - \mathbf{r}_I) \cdot (\mathbf{M}_J + \mathbf{M}_I) \cdot \overline{\nabla W}(\mathbf{r}_J - \mathbf{r}_I, \tilde{h}_{IJ})}{\|\mathbf{r}_J - \mathbf{r}_I\|^2} \right\} - \\ & - \left\{ \tilde{\mathbf{N}} \cdot \left( \sum_{\Omega_{\mathbf{r}_I, \tilde{h}_I}} V_{\mathbf{r}_J} \cdot (\mathbf{M}_J + \mathbf{M}_I) \cdot [\mathbf{u}(\mathbf{r}_J) - \mathbf{u}(\mathbf{r}_I)] \overline{\nabla^* W}(\mathbf{r}_J - \mathbf{r}_I, \tilde{h}_{IJ}) \right) \right\}, \end{aligned} \quad (4.44)$$

where  $n = 1, 2, 3$  is the spatial dimension. The tensor  $\bar{\Gamma}_{\alpha\beta}$  can be defined by the relation (4.32). However, the higher accuracy can be achieved by taking into account higher order corrections in  $\Gamma_{\alpha\beta}(\mathbf{r}_I)$  as per relation (4.41). Hence, the following definition can be used

$$\bar{\Gamma}_{\alpha\beta}(\mathbf{r}_I), \tilde{\mathbf{N}} = \begin{cases} \Gamma_{\alpha\beta}^*(\mathbf{r}_I), \tilde{\mathbf{N}} \neq 0, & \text{if } \Gamma_{\alpha\beta}^*(\mathbf{r}_I) \neq 0, \\ \Gamma_{\alpha\beta}(\mathbf{r}_I), \tilde{\mathbf{N}} = 0, & \text{if } \Gamma_{\alpha\beta}^*(\mathbf{r}_I) = 0 \end{cases} \quad (4.45)$$

where

$$\begin{aligned} \Gamma_{\alpha\beta}^*(\mathbf{r}_I) &= \sum_{\Omega_{\mathbf{r}_I, \tilde{h}_I}} V_{\mathbf{r}_J} [\mathbf{r}_J^\beta - \mathbf{r}_I^\beta] \overline{\nabla_\alpha W}(\mathbf{r}_J - \mathbf{r}_I, \tilde{h}_{IJ}) - \\ & - \tilde{\mathbf{N}}^\gamma \sum_{\Omega_{\mathbf{r}_I, \tilde{h}_I}} V_{\mathbf{r}_J} [\mathbf{r}_J^\alpha - \mathbf{r}_I^\alpha] [\mathbf{r}_J^\beta - \mathbf{r}_I^\beta] \overline{\nabla_\gamma^* W}(\mathbf{r}_J - \mathbf{r}_I, \tilde{h}_{IJ}) \end{aligned} \quad (4.46)$$

and

$$\Gamma_{ii}^*(\mathbf{r}_I) = - \sum_{\Omega_{\mathbf{r}_I, \tilde{h}_I}} V_{\mathbf{r}_J} \frac{(\mathbf{r}_J^i - \mathbf{r}_I^i)^2}{\tilde{h}_{IJ} \|\mathbf{r}_J - \mathbf{r}_I\|} G(z_J, \mathbf{r}_I) \left[ 1 - \tilde{\mathbf{N}}^\gamma(\mathbf{r}_I) \mathbf{C}_{\gamma\omega}(\mathbf{r}_I) (\mathbf{r}_J^\omega - \mathbf{r}_I^\omega) \right], \quad (4.47)$$

$$\Gamma_{\beta\beta}^*(\mathbf{r}_I) = - \sum_{\Omega_{\mathbf{r}_I, \tilde{h}_I}} V_{\mathbf{r}_J} \|\mathbf{r}_J - \mathbf{r}_I\| \frac{1}{\tilde{h}_{IJ}} G(z_J, \mathbf{r}_I) \left[ 1 - \tilde{\mathbf{N}}^\gamma(\mathbf{r}_I) \mathbf{C}_{\gamma\omega}(\mathbf{r}_I) (\mathbf{r}_J^\omega - \mathbf{r}_I^\omega) \right]. \quad (4.48)$$

Following (4.44), we only need to compute the trace of the matrix  $\bar{\Gamma}_{\alpha\beta}^{-1}(\mathbf{r}_I)$ . Furthermore, it is clear that one can apply results of the Lemma 4.5 to  $\Gamma_{\beta\beta}^*(\mathbf{r}_I)$  with following function

$$G^*(z_J, \mathbf{r}_I) = G(z_J, \mathbf{r}_I) \left[ 1 - \tilde{\mathbf{N}}^\gamma(\mathbf{r}_I) \mathbf{C}_{\gamma\omega}(\mathbf{r}_I) (\mathbf{r}_J^\omega - \mathbf{r}_I^\omega) \right] \text{ if } G^*(z_J, \mathbf{r}_I) \leq 0, \quad (4.49)$$

where

$$\tilde{\mathbf{N}}(\mathbf{r}_I) \mathbf{C}(\mathbf{r}_I) (\mathbf{r}_J - \mathbf{r}_I) = \tilde{\mathbf{N}}(\mathbf{r}_I) \left[ \sum_{\Omega_{\mathbf{r}_I, \tilde{h}_I}} V_{\mathbf{r}_J} [\mathbf{r}_J - \mathbf{r}_I] \overline{\nabla W} \right]^{-1} (\mathbf{r}_J - \mathbf{r}_I). \quad (4.50)$$

The function  $G^*(z_J, \mathbf{r}_I)$  is negative if

$$\left[ 1 - \tilde{\mathbf{N}}^\gamma(\mathbf{r}_I) \mathbf{C}_{\gamma\omega}(\mathbf{r}_I) (\mathbf{r}_J^\omega - \mathbf{r}_I^\omega) \right] > 0 \quad \forall \mathbf{r}_J, \mathbf{r}_I. \quad (4.51)$$

The reason for having the correction factor in the form (4.45)–(4.46) is that  $\Gamma_{\alpha\beta}^*(\mathbf{r}_I) = 0$  in some cases, where particles have the incomplete kernel support (e.g., at the corners and boundaries of the numerical domain). For multi-dimensional problems, the correction tensor  $\bar{\Gamma}_{\alpha\beta}(\mathbf{r}_I)$  is also a matrix. If the particle  $\mathbf{r}_I$  has entire stencil support (i.e., the domain support for all kernels  $W(\mathbf{r}_J - \mathbf{r}_I, \tilde{h}_{IJ})$  is completed and symmetric) then  $\bar{\Gamma}_{\alpha\beta}(\mathbf{r}_I) \approx \delta_{\alpha\beta}$ . The proposed correction matrix deviates less from the unit matrix compare to (4.32).

**Theorem 4.8.** *The discretization scheme (4.44)–(4.46) at a given point  $\mathbf{r}_I \in \Omega \subset \mathbb{R}^n$  sufficiently far away from the boundary  $\partial\Omega$  (i.e., where the kernel  $W$  has a full support) has an error bounded by  $C \left( \tilde{h}_{I,m} \right) \cdot \left( \frac{h_{I,p}^\omega}{\tilde{h}_{I,m}} \right)$ ,*

$$1 \leq \omega < 2, \lim_{\tilde{h}_{I,m} \rightarrow 0} \frac{C \left( \tilde{h}_{I,m} \right)}{\tilde{h}_{I,m}} = 0, h_{I,p} = \sup_{J: \mathbf{r}_J \in \Omega} \|\mathbf{r}_J - \mathbf{r}_I\|, \tilde{h}_{I,m} = \inf_{J: \mathbf{r}_J \in \Omega_{\mathbf{r}_I, \tilde{h}_I}} \tilde{h}_{IJ} \text{ for any scalar mobility field } m(\mathbf{r}) \in C^1(\Omega), m(\mathbf{r}) \geq 0.$$

*Proof.* Using Lemmas 4.2 and 4.3, additional term proposed by new scheme (4.44) subject to the diagonal mobility tensor  $\mathbf{M}^{\alpha\beta}(\mathbf{r}) = m(\mathbf{r}) \delta_{\alpha\beta}$  reduces to

$$\begin{aligned} & \left\{ \tilde{\mathbf{N}} \cdot \left( \sum_{\Omega_{\mathbf{r}_I, \tilde{h}_I}} V_{\mathbf{r}_J} \cdot (m_J + m_I) \cdot [\mathbf{u}(\mathbf{r}_J) - \mathbf{u}(\mathbf{r}_I)] \nabla^* \overline{W}(\mathbf{r}_J - \mathbf{r}_I, \tilde{h}_{IJ}) \right) \right\} = \\ & = 2m(\mathbf{r}_I) \mathbf{u}_\alpha(\mathbf{r}_I) \cdot \tilde{\mathbf{N}}^\alpha + \\ & m_{,\beta}(\mathbf{r}_I) \mathbf{u}_{,\omega}(\mathbf{r}_I) \left( \sum_{\Omega_{\mathbf{r}_I, \tilde{h}_I}} V_{\mathbf{r}_J} [\mathbf{r}_J^\omega - \mathbf{r}_I^\omega] [\mathbf{r}_J^\beta - \mathbf{r}_I^\beta] \nabla_\alpha^* \overline{W}(\mathbf{r}_J - \mathbf{r}_I, \tilde{h}_{IJ}) \right) \cdot \tilde{\mathbf{N}}^\alpha + \\ & m(\mathbf{r}_I) \mathbf{u}_{,\beta\omega}(\mathbf{r}_I) \left( \sum_{\Omega_{\mathbf{r}_I, \tilde{h}_I}} V_{\mathbf{r}_J} [\mathbf{r}_J^\omega - \mathbf{r}_I^\omega] [\mathbf{r}_J^\beta - \mathbf{r}_I^\beta] \nabla_\alpha^* \overline{W}(\mathbf{r}_J - \mathbf{r}_I, \tilde{h}_{IJ}) \right) \cdot \tilde{\mathbf{N}}^\alpha + \hat{\mathcal{E}} \end{aligned} \quad (4.52)$$

in the vicinity of the point  $\mathbf{r}_I$  with the error  $\hat{\mathcal{E}}$  which has the leading term outlined in (4.19). Subtraction of this terms from (4.19) and performing the normalization lead to the announced in the theorem result.  $\square$

The scheme has the two-point flux approximation nature and can be written in the form of (4.2), which can be proved using the arguments above. The scheme (4.44)–(4.46) is in line with an alternative formulation for continuum mechanics called the peridynamic model [240], which was proposed several years ago.

All presented schemes in this paper do not require exact expressions for the gradient (i.e., spatial derivatives) of the mobility field  $\nabla_\gamma m(\mathbf{r})$  to keep a higher order of accuracy for any mobility field. Hence, this scheme can be used with the discontinuous (or piecewise continuous) mobility field  $m(\mathbf{r}) \in L_2(\Omega)$ . It is important to note that Brookshaw [41] and Schwaiger [236] schemes can also be written for the diagonal mobility matrix  $\mathbf{M}^{\alpha\beta}(\mathbf{r})$  by substituting  $\mathbf{M}^{\alpha\beta}$  into (4.14) and (4.29) instead of  $m(\mathbf{r})$  and performing summation by repeating indices.

### § 4.3 Meshless Multi-Point Flux Approximation (MMPFA)

In this section, the meshless multi-point flux approximation to the operator  $\mathbf{L}$  (4.3) is considered. The mobility  $\mathbf{M}(\mathbf{r})$  is a symmetric tensor which is uniformly positive definite in  $\Omega \subset \mathbb{R}^n$ . In addition, it is an important feature of reservoir simulation that  $\mathbf{M}(\mathbf{r})$  is allowed to be a discontinuous (or piece-wise function), and meshless multi-point approximation must be adapted to this case since the mobility field  $\mathbf{M}(\mathbf{r})$  cannot be differentiable in the classical sense.

The control volumes in the meshless multi-point flux approximation method (see, Lukyanov, 2010 [185]) are the patches which are interior to the support of the Kernels  $\overline{W}(\mathbf{r} - \mathbf{r}_I, h)$ ,  $\Omega_{\mathbf{r},h} = \text{supp} \overline{W}(\mathbf{r} - \mathbf{r}_I, h)$  (Fig.2.1),  $h$  is the diameter,  $\mathbf{r} = (\mathbf{r}^\alpha) \in \mathbb{R}^n$ ,  $\mathbf{r}_I = (\mathbf{r}_I^\alpha) \in \mathbb{R}^n$  are points in Euclidean space (see, Figure 2.2). Hence, it follows that there is an infinite cover of our domain  $\Omega$ :

$$\Omega = \bigcup_{\mathbf{r} \in \Omega} \Omega_{\mathbf{r},h} \quad (4.53)$$

According to the *Heine-Borel theorem*, there is a finite subcover, that is

$$\Omega = \text{span}\{\Omega_{\mathbf{r}_I,h}/I = 1, \dots, N\}; \quad (4.54)$$

where  $N$  is the number of particles in the numerical discretization. The mass is conserved on each control volume, i.e. we can integrate the equation (1) on control volumes  $\Omega_{\mathbf{r}_I,h}$  to obtain the final set of discretized



equations. Therefore, let  $L_2(\Omega)$  denote the square Lebesgue-integrable function on the domain  $\Omega \subset \mathbb{R}^n$  with inner product  $(\cdot, \cdot)_\Omega$  and norm  $\|\cdot\| = (\cdot, \cdot)_\Omega^{1/2}$ . Also, let

$$H(\nabla^h; \mathbf{r} \in \Omega) = \{\mathbf{u} \in L_2(\Omega) : \nabla^h \mathbf{u}(\mathbf{r}) \in L_2(\Omega)\} \quad (4.55)$$

denote the Sobolev space of first order generalized differentiable functions in  $L_2(\Omega)$  with norm

$$\|\mathbf{u}(\mathbf{r})\|_{\nabla^h, \Omega} = \left( \|\mathbf{u}(\mathbf{r})\|_\Omega^2 + \|\nabla^h \mathbf{u}(\mathbf{r})\|_\Omega^2 \right) \quad (4.56)$$

where  $\nabla^h$  is the generalized Nabla operator which has the following definition:

$$(a) \nabla^h \mathbf{u}(\mathbf{r}) = \int_{\Omega_{\mathbf{r}, h}} [\mathbf{u}(\mathbf{r}') - \mathbf{u}(\mathbf{r})] \nabla_{\mathbf{r}'} W^*(\mathbf{r} - \mathbf{r}', h) d^n \mathbf{r}' \forall \mathbf{r}(\mathbf{r}), \mathbf{r} \in \Omega, \quad (4.57)$$

$$(b) \nabla \mathbf{u}(\mathbf{r}) = \stackrel{def}{\lim_{h \rightarrow 0}} \nabla^h \mathbf{u}(\mathbf{r}) \quad \forall \mathbf{u}(\mathbf{r}), \mathbf{r} \in \Omega, \quad (4.58)$$

where  $\nabla_{\mathbf{r}'} W^*(\mathbf{r} - \mathbf{r}', h)$  is the corrected gradient of the Kernel (2.27), (2.28). It is important to note that the correct sign of the gradient (4.58) is hidden in  $\nabla_{\mathbf{r}'} W^*(\mathbf{r} - \mathbf{r}', h)$ . In this paper, the Darcy velocity 4.59 is assumed to satisfy  $\mathbf{v}(\mathbf{r}) \in H(\nabla^h; \mathbf{r} \in \Omega)$ :

$$\mathbf{v}(\mathbf{r}) = -\mathbf{M}(\mathbf{r}) \nabla \mathbf{u}(\mathbf{r}), \quad (4.59)$$

where  $\mathbf{v}$  is the Darcy velocity.

### 4.3.1 Scheme I and II for Anisotropic Media

Although expression (4.28) was derived for an inhomogeneous scalar field  $m(\mathbf{r})$ , an attempt can be made to generalize this scheme for fully anisotropic heterogeneous media with the tensor characteristic  $\mathbf{M}(\mathbf{r}) = \{m^{\alpha\gamma}(\mathbf{r})\}$  by assuming (Scheme I), for example,

$$\begin{aligned} \langle \nabla(\mathbf{M}(\mathbf{r}_I) \nabla \mathbf{u}(\mathbf{r}_I)) \rangle &= n \cdot [\mathbf{C}_{\alpha\alpha}]^{-1} \times \\ &= \sum_{\Omega_{\mathbf{r}_I, h}} V_{\mathbf{r}_J} [\mathbf{u}(\mathbf{r}_J) - \mathbf{u}(\mathbf{r}_I)] \frac{(\mathbf{r}_J^\alpha - \mathbf{r}_I^\alpha) \cdot (m_{\alpha\cdot}^{\cdot\gamma}(\mathbf{r}_J) + m_{\alpha\cdot}^{\cdot\gamma}(\mathbf{r}_I)) \overline{\nabla_\gamma W}(\mathbf{r}_J - \mathbf{r}_I, h)}{\|\mathbf{r}_J - \mathbf{r}_I\|^2}. \end{aligned} \quad (4.60)$$

Analogously, the following modification to Schwaiger (2008) [236] expression (4.29)–(4.32) is proposed (Scheme II) for anisotropic permeability case (similar to isotropic case) which reduces to the scheme (4.29)–(4.32) in the limit of spherical tensor  $m^{\alpha\beta} = m\delta^{\alpha\beta}$ :

$$\begin{aligned} \frac{n}{\Gamma_{kk}^{-1}} \langle \nabla_\alpha (m^{\alpha\beta}(\mathbf{r}_I) \nabla_\beta \mathbf{u}(\mathbf{r}_I)) \rangle &= \\ \left\{ \sum_{\Omega_{\mathbf{r}, h}} V_{\mathbf{r}_J} [\mathbf{u}(\mathbf{r}_J) - \mathbf{u}(\mathbf{r}_I)] \frac{(\mathbf{r}_J^\alpha - \mathbf{r}_I^\alpha) \cdot [m_{\alpha\cdot}^{\cdot\beta}]_{IJ} \cdot \nabla_\beta W(\mathbf{r}_J - \mathbf{r}_I, h)}{\|\mathbf{r}' - \mathbf{r}\|^2} \right\} &- \\ - \{ \langle \nabla_\alpha (m^{\alpha\beta}(\mathbf{r}_I) \mathbf{u}(\mathbf{r}_I)) \rangle - \mathbf{u}(\mathbf{r}_I) \langle \nabla_\alpha m^{\alpha\beta}(\mathbf{r}_I) \rangle + & \\ + m^{\alpha\beta}(\mathbf{r}_I) \langle \nabla_\alpha \mathbf{u}(\mathbf{r}_I) \rangle \} \mathbf{N}^\beta \}, & \end{aligned} \quad (4.61)$$

where  $[m_{\alpha\cdot}^{\cdot\beta}]_{IJ} = (m_{\alpha\cdot}^{\cdot\beta}(\mathbf{r}_J) + m_{\alpha\cdot}^{\cdot\beta}(\mathbf{r}_I))$ ,  $\mathbf{N}^\alpha$  is defined by (4.30).

### 4.3.2 Scheme III for Anisotropic Media

Alternative to the *Scheme I* and *II*, it is possible to formulate the scheme in the form:

$$\begin{aligned} & \frac{n}{\Gamma_{kk}^{-1}} \langle \nabla_\alpha (m^{\alpha\beta}(\mathbf{r}_I) \nabla_\beta \mathbf{u}(\mathbf{r}_I)) \rangle = \\ & \left\{ \sum_{\Omega_{\mathbf{r}_I, h}} V_{\mathbf{r}_J} [\mathbf{u}(\mathbf{r}_J) - \mathbf{u}(\mathbf{r}_I)] \frac{(\mathbf{r}_J^\alpha - \mathbf{r}_I^\alpha) \cdot [m_{\alpha\cdot}^{\cdot\beta}]_{IJ} \cdot \overline{\nabla_\beta W}(\mathbf{r}_J - \mathbf{r}_I, h)}{\|\mathbf{r}' - \mathbf{r}\|^2} \right\} - \\ & - \left\{ \left( \sum_{\Omega_{\mathbf{r}_I, h}} V_{\mathbf{r}_J} \cdot m_{IJ}^{\omega\gamma} \cdot [\mathbf{u}(\mathbf{r}_J) - \mathbf{u}(\mathbf{r}_I)] \overline{\nabla_\gamma^* W}(\mathbf{r}_J - \mathbf{r}_I, h) \right) \mathbf{N}^\omega \right\}, \end{aligned} \quad (4.62)$$

which reduces to the scheme (4.44) in the limit of spherical tensor  $m^{\alpha\beta} = m\delta^{\alpha\beta}$ . This scheme has a more desirable structure since it can be written in the form of (4.4). Hence, it is more suitable for monotonicity analysis. A full meshless transmissibility between particle  $\mathbf{r}_J$  and  $\mathbf{r}_I$  in this case can be defined as:

$$\begin{aligned} T^M(\mathbf{r}_J, \mathbf{r}_I) &= T_{JI}^M = \\ & \frac{\Gamma_{kk}^{-1}}{n} \left\{ \sum_{\Omega_{\mathbf{r}_I, h}} V_{\mathbf{r}_J} \frac{(\mathbf{r}_J^\alpha - \mathbf{r}_I^\alpha) \cdot [m_{\alpha\cdot}^{\cdot\beta}]_{IJ} \cdot \overline{\nabla_\beta W}(\mathbf{r}_J - \mathbf{r}_I, h)}{\|\mathbf{r}' - \mathbf{r}\|^2} \right\} - \\ & - \frac{\Gamma_{kk}^{-1}}{n} \left\{ \left( \sum_{\Omega_{\mathbf{r}_I, h}} V_{\mathbf{r}_J} \cdot [m_{\omega\cdot}^{\cdot\gamma}]_{IJ} \cdot \overline{\nabla_\gamma^* W}(\mathbf{r}_J - \mathbf{r}_I, h) \right) \mathbf{N}^\omega \right\}. \end{aligned} \quad (4.63)$$

It is desirable to have positive meshless transmissibility  $T^M(\mathbf{r}_J, \mathbf{r}_I) \geq 0$  in (4.63). This is directly related to the monotonicity property. Note that in the limit of homogeneous isotropic media (e.g.,  $\mathbf{M}(\mathbf{r}) = m(\mathbf{r}) \cdot \mathbf{I}$ ), the aforementioned *schemes I* and *II* reduce to the discretization of the generalized Laplace equation with at least  $\mathcal{O}(h^\omega)$ ,  $1 \leq \omega < 2$ . The analysis above has been performed for differentiable scalar mobility field  $\mathbf{M}(\mathbf{r}) \in C^1(\Omega)$ . It has been noted that an important feature of reservoir simulation that  $\mathbf{M}(\mathbf{r})$  is allowed to be a discontinuous (or piece-wise function). Hence, the discretization schemes should take this effect into account.

The accuracy of the above *Schemes* (4.60), (4.61) will be investigated for two separate cases: (a) for diagonal homogeneous anisotropic mobility tensor field  $m^{\omega\gamma} \in L_2(\Omega) \geq 0$ ,  $m^{\omega\gamma} = 0, \omega \neq \gamma$  and (b) fully homogeneous anisotropic mobility tensor field  $m^{\omega\gamma} \in L_2(\Omega) \geq 0$ . Both cases are considered everywhere within the numerical domain  $\Omega$ . Note that there is no difference between following tensors  $m_{\omega\cdot}^{\cdot\gamma}$ ,  $m_{\cdot\gamma}^{\omega\cdot}$ ,  $m_{\omega\gamma}$  and  $m^{\omega\gamma}$  in Cartesian coordinate system.

### 4.3.3 Discontinuous Mobility Case

Using the same idea behind the expression (4.5) and heterogeneous discontinues mobility field  $m(\mathbf{r})$ , it can be shown that the effect of requiring the flux into the adjoining region to be continuous leads to the equivalent to the (4.5) expression in terms of effective mobility between particle  $\mathbf{r}_I$  and  $\mathbf{r}_J$  (Clearly and Monaghan, 1999 [66]):

$$\tilde{m} = \left( \frac{m(\mathbf{r}_J) \cdot m(\mathbf{r}_I)}{m(\mathbf{r}_J) + m(\mathbf{r}_I)} \right). \quad (4.64)$$

If we examine the discretization *Scheme II* then it can be seen that the effective mobility ( $m(\mathbf{r}_J) + m(\mathbf{r}_I)$ ) has been applied which does not guarantee the continuity of flux between the particles with discontinuous mobilities. Taking this into account and applying (4.64), the final discretization scheme for discontinuous scalar mobility

field can be written as

$$\begin{aligned} & \frac{n}{\Gamma_{kk}^{-1}} \langle \nabla_\alpha (m(\mathbf{r}_I) \nabla_\alpha \mathbf{u}(\mathbf{r}_I)) \rangle = \\ & \left\{ \sum_{\Omega_{\mathbf{r}_I, h}} V_{\mathbf{r}_J} \cdot \tilde{m} \cdot [\mathbf{u}(\mathbf{r}_J) - \mathbf{u}(\mathbf{r}_I)] \frac{(\mathbf{r}_J^\alpha - \mathbf{r}_I^\alpha) \cdot \overline{\nabla_\alpha W}(\mathbf{r}_J - \mathbf{r}_I, h)}{\|\mathbf{r}' - \mathbf{r}\|^2} \right\} - \\ & - \left\{ \left( \sum_{\Omega_{\mathbf{r}_I, h}} V_{\mathbf{r}_J} \cdot \tilde{m} \cdot [\mathbf{u}(\mathbf{r}_J) - \mathbf{u}(\mathbf{r}_I)] \overline{\nabla_\alpha^* W}(\mathbf{r}_J - \mathbf{r}_I, h) \right) \mathbf{N}^\alpha \right\}. \end{aligned} \quad (4.65)$$

This numerical scheme is the additional alternative for heterogeneous discontinuous isotropic scalar mobility field which is used for numerical tests throughout this thesis. It ensures that flux is automatically continuous between particles with the reasonable accuracy. Multiple PVT regions with substantially different fluid properties and specific mobilities can then be simulated.

The analytical analysis of the *schemes I, II* for a fully anisotropic mobility tensor field is complicated. However, the numerical analysis reveals that these schemes do not produce a reasonable approximation for a linear pressure field for anisotropic mobility tensor field. The following section describes a scheme applicable the fully anisotropic mobility tensor field.

### 4.3.4 Scheme III

Generally speaking, any second order tensor can be decomposed into the spherical part and the deviatorical part. In the case of continuum mechanics, the decomposition of the second order tensor (e.g., stress tensor or the strain tensor) into their volumetric and deviatoric components has certain physical justification. This step is done in order to distinguish between volumetric and shear responses. However, any mobility field  $\mathbf{M}(\mathbf{r})$  for fluid flow in porous media is better to split as (based on the numerical experiments):

$$\mathbf{M}(\mathbf{r}) = \mathbf{M}_d(\mathbf{r}) + \mathbf{M}_o(\mathbf{r}), \quad (4.66)$$

where  $\mathbf{M}_d(\mathbf{r})$  is the diagonal part of the mobility tensor,  $\mathbf{M}_o(\mathbf{r})$  is the off-diagonal part of the mobility tensor. In addition, the Darcy velocity (4.59) can be written as

$$\begin{aligned} \mathbf{v}(\mathbf{r}) &= \mathbf{v}_d(\mathbf{r}) + \mathbf{v}_o(\mathbf{r}), \\ \mathbf{v}_d(\mathbf{r}) &= -\mathbf{M}_d(\mathbf{r}) \nabla \mathbf{u}(\mathbf{r}), \\ \mathbf{v}_o(\mathbf{r}) &= -\mathbf{M}_o(\mathbf{r}) \nabla \mathbf{u}(\mathbf{r}), \end{aligned} \quad (4.67)$$

where  $\mathbf{v}_d(\mathbf{r})$  is the diagonal velocity,  $\mathbf{v}_o(\mathbf{r})$  is the off-diagonal velocity. The problem discussed in this thesis is the elliptic equation (4.3):

$$\nabla \mathbf{v}(\mathbf{r}) = \nabla \mathbf{v}_d(\mathbf{r}) + \nabla \mathbf{v}_o(\mathbf{r}) = g(\mathbf{r}), \quad \forall \mathbf{r} \in \Omega \subset \mathbb{R}^n. \quad (4.68)$$

However, the discretization scheme can be constructed in two steps. The first step is to discretize diagonal term  $\nabla \mathbf{v}_d(\mathbf{r})$  following either (4.61) or (4.65), e.g., the scheme (4.65) is used below:

$$\begin{aligned} -\langle \nabla \mathbf{v}_d(\mathbf{r}) \rangle &= \\ & \frac{\Gamma_{kk}^{-1}}{n} \left\{ \sum_{\Omega_{\mathbf{r}_I, h}} V_{\mathbf{r}_J} \cdot \tilde{\mathbf{M}}_d \cdot [\mathbf{u}(\mathbf{r}_J) - \mathbf{u}(\mathbf{r}_I)] \frac{(\mathbf{r}_J^\alpha - \mathbf{r}_I^\alpha) \cdot \overline{\nabla_\alpha W}(\mathbf{r}_J - \mathbf{r}_I, h)}{\|\mathbf{r}' - \mathbf{r}\|^2} \right\} - \\ & - \frac{\Gamma_{kk}^{-1}}{n} \left\{ \left( \sum_{\Omega_{\mathbf{r}_I, h}} V_{\mathbf{r}_J} \cdot \tilde{\mathbf{M}}_d \cdot [\mathbf{u}(\mathbf{r}_J) - \mathbf{u}(\mathbf{r}_I)] \overline{\nabla_\alpha^* W}(\mathbf{r}_J - \mathbf{r}_I, h) \right) \mathbf{N}^\alpha \right\}, \end{aligned} \quad (4.69)$$

where  $\tilde{\mathbf{M}}_d$  is defined as

$$(a) \quad \tilde{\mathbf{M}}_d = \left[ (\mathbf{M}_d(\mathbf{r}_J))^{-1} + (\mathbf{M}_d(\mathbf{r}_I))^{-1} \right]^{-1} \quad \text{or} \quad (b) \quad \tilde{\mathbf{M}}_d = \mathbf{M}_d(\mathbf{r}_J) + \mathbf{M}_d(\mathbf{r}_I). \quad (4.70)$$

The second step is to discretize off-diagonal term  $\nabla \mathbf{v}_o(\mathbf{r})$  as follows:

$$\langle \nabla_\gamma \mathbf{v}_o^\gamma(\mathbf{r}) \rangle = \sum_{\Omega_{\mathbf{r}_I, h}} V_{\mathbf{r}_J} [\langle \mathbf{v}_o^\gamma(\mathbf{r}_J) \rangle - \langle \mathbf{v}_o^\gamma(\mathbf{r}_I) \rangle] \overline{\nabla_\gamma^* W}(\mathbf{r}_J - \mathbf{r}_I, h), \quad (4.71)$$

$$\langle \mathbf{v}_d^\gamma(\mathbf{r}_I) \rangle = -\mathbf{M}_d^{\gamma\alpha} \langle \nabla_\alpha \mathbf{u}(\mathbf{r}_I) \rangle,$$

$$\langle \nabla_\alpha \mathbf{u}(\mathbf{r}_I) \rangle = \sum_{\Omega_{\mathbf{r}_I, h}} V_{\mathbf{r}_J} [\mathbf{u}(\mathbf{r}_J) - \mathbf{u}(\mathbf{r}_I)] \overline{\nabla_\alpha^* W}(\mathbf{r}_J - \mathbf{r}_I, h). \quad (4.72)$$

It is important to make here a few remarks.

**Remark 4.9.** *The aforementioned schemes I, II can be written in the form:*

$$\langle \nabla_\alpha (m^{\alpha\beta}(\mathbf{r}_I) \nabla_\beta \mathbf{u}(\mathbf{r}_I)) \rangle = \sum_S \bar{T}_{SI}^M p_S, \quad \sum_S \bar{T}_{SI}^M = 0. \quad (4.73)$$

*In the case of approximation conventional Laplacian  $\nabla^2 p$  (i.e.,  $m(\mathbf{r}_I) \equiv 1$ ), it can be derived  $\forall \mathbf{r}_I$  and general particles distribution:*

$$\begin{aligned} (a) \quad & \sum_S \bar{T}_{SI}^M = 0, \\ (b) \quad & \sum_S \bar{T}_{SI}^M [\mathbf{r}_S - \mathbf{r}_I] = \mathbf{0}, \\ (c) \quad & \sum_S \bar{T}_{SI}^M [\mathbf{r}_S - \mathbf{r}_I] \cdot [\mathbf{r}_S - \mathbf{r}_I]^T \neq \mathbf{I}. \end{aligned} \quad (4.74)$$

*The condition (4.74)(c) does hold in some cases far away from the boundary, e.g., for homogeneous particles distribution. This follows from the fact that Taylor expansion of pressure around the point  $\mathbf{r}_I$  can be written*

$$\begin{aligned} \mathbf{u}(\mathbf{r}_J) &= \mathbf{u}(\mathbf{r}_I) + \nabla \mathbf{u}(\mathbf{r}_I) \cdot [\mathbf{r}_S - \mathbf{r}_I] + \\ &+ \frac{1}{2} [\mathbf{r}_S - \mathbf{r}_I]^T \cdot \nabla \otimes \nabla \mathbf{u}(\mathbf{r}_I) \cdot [\mathbf{r}_S - \mathbf{r}_I] + \mathcal{O}(h^3) \end{aligned} \quad (4.75)$$

*The constraints (4.74) lead to significant differences between multi-point flux approximation schemes and mesh-free finite difference approximation schemes (see, Seibold, 2006 [238]). It is important to recall here that meshfree finite difference approximation schemes, which satisfy the constraints (a)-(c), are based on the following steps: (1) to define the neighbors list for each point (it is important to choose more neighbors than constraints); (2) to select unique stencil which can be satisfied addition requirements (e.g., monotonicity Seibold (2006) [238])*

**Remark 4.10.** *The scheme (4.71) and (4.72) can be applied directly to the Darcy's velocity (4.59) with the full mobility tensor. Furthermore, the following theorem is valid for the full mobility tensor:*

**Theorem 4.11.** *The discretization scheme (4.71), (4.72) is at least of  $\mathcal{O}(h^\omega)$ ,  $0 \leq \omega < 2$  order of accuracy for any differentiable heterogeneous full mobility tensor field everywhere within the numerical domain  $\Omega$  and sufficiently far away from the boundary.*

*The proof of Theorem 4.11 can be seen from the construction. However, the scheme (4.71), (4.72) is not unconditionally monotone but as was shown by Seibold (2006) [238] in case of meshfree finite difference methods, it is possible to have positive stencils, i.e. all neighbor entries are of the same sign.*

**Remark 4.12.** *The presented schemes in the thesis do not require exact expressions for special gradient of the mobility field  $\nabla_\gamma \mathbf{M}^{\alpha\beta}(\mathbf{r}) = \mathbf{M}^{\alpha,\beta}_\gamma(\mathbf{r})$  to keep first order consistent scheme for any mobility field  $\mathbf{M}(\mathbf{r}) \in L_2(\Omega)$ . Hence, an important feature of reservoir simulation that mobility field  $\mathbf{M}(\mathbf{r})$  is to be a discontinuous (or piece-wise function) is allowed in this scheme.*

**Remark 4.13.** *Applying aforementioned meshless discretization schemes to the elliptic problem (4.3) results in formulating a general non-linear system which can be solved by iterative Newton-Raphson method leading in the sequence of linear systems with matrix  $\mathbf{A} (a_{ij})_{1 \leq i \leq n, 1 \leq j \leq n} \in \mathbb{R}^{n \times n}$*

$$\mathbf{A} \mathbf{f} = \mathbf{b}, \quad (4.76)$$

where the vector  $\mathbf{f}$  of unknowns contains approximations to the function  $\mathbf{F}(\mathbf{r})$ . It is assumed that (4.3) admits a unique solution with discontinuity permeability tensor. The  $I$ -th row of the matrix  $\mathbf{A}$  consists of the stencil corresponding to the point  $\mathbf{r}_I$ . Let the unknowns be labeled by an index set  $N$  same as particles labels. We consider square matrices  $\mathbf{A} \in \mathbb{R}^{n \times n}$ .

**Definition 4.14.** A matrix  $\mathbf{A}$  is called essentially irreducible if every point is connected to a Dirichlet boundary point.

The matrix  $\mathbf{A}$  resulting from the meshless discretization is an essentially irreducible which is guaranteed by the Heine-Borel theorem.

**Remark 4.15.** Meshless multi-point flux approximation matrices are in general non-symmetric. Consider two points  $\mathbf{r}_I$  and  $\mathbf{r}_J$  with the corresponding smoothing lengths  $h_I$  and  $h_J$ . Since each stencil entry depends on the smoothing length, the point  $\mathbf{r}_J$  influences the matrix entry  $a_{ij}$  if  $\|\mathbf{r}_J - \mathbf{r}_I\| \leq f \cdot h_I$  whereas  $\mathbf{r}_I$  does not influence the matrix entry  $a_{ij}$  if  $\|\mathbf{r}_J - \mathbf{r}_I\| > f \cdot h_I$ , where  $f$  is the scaling factor defined by the shape of the Kernel function.

This ends the derivation of a first-order meshless multi-point flux approximation method that can be used to solve different boundary value problems.

## §4.4 Approximation, Stability, Monotonicity and Convergence

The approximation, stability and monotonicity are important properties of numerical schemes which provide and quantify the confidence in the numerical modeling and results from corresponding simulations. Therefore, in order to be confident that the proposed numerical schemes provide the adequate accuracy of the elliptic operator (4.1), several numerical analyses to identify the order of approximation, stability and monotonicity have been performed.

The proof of the convergence of linear meshless multi-point flux approximation schemes applied to a linear elliptic boundary value problem can be found in the following references (see, Bouchon (2007) [34], Bouchon and Peichl (2007) [35], Matsunaga and Yamamoto (2000) [197], Thomée (2001) [252]: if it is shown that the truncation error  $\varepsilon$  tends to 0 as the maximum smoothing length  $\max_{I \in N} h_I$  goes to 0, and then the linear system  $\mathbf{A}\delta\mathbf{f} = \varepsilon$  coupling the local variable error  $\delta\mathbf{f}$  with  $\varepsilon$  proves the convergence of the schemes, given that the matrix  $\mathbf{A} \in \mathbb{R}^{n \times n}$  of the discretized meshless operator is monotone. Note that a weaker condition (i.e., the norm of the inverse matrix is bounded by the constant independent of the mesh size) can be assumed to guarantee the convergence.

### 4.4.1 Approximation

It is important to recall that all numerical schemes are characterized by two length scales:  $\tilde{h} = f \cdot h_p$  is the radius of  $\Omega_{\mathbf{r}, \tilde{h}} = \text{supp}W$ , and  $h_p$  is the inter-particle distance. Hence, while investigating the approximation of the meshless discretization scheme, it is important to distinguish two cases: (a) the neighborhood number of particles is fixed  $f = \text{const}$  with varying the inter-particle distance, (b) the inter-particle distance is fixed  $h_p = \text{const}$  with varying the neighborhood number of particles. The first case will be analyzed by looking at the error defined by

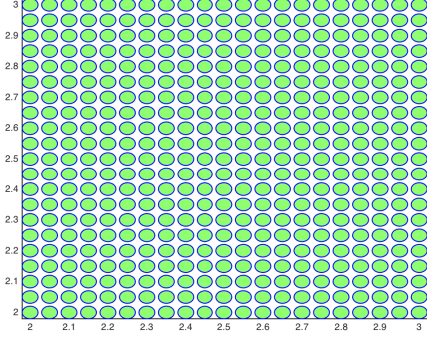
$$\|E\|_{\Omega}^{L_2} = \left[ \frac{1}{\sum_J V_{\mathbf{r}_J}} \sum_J V_{\mathbf{r}_J} (\mathbf{L}[\mathbf{u}(\mathbf{r}_J)] - \langle \mathbf{L} \rangle[\mathbf{u}(\mathbf{r}_J)])^2 \right]^{1/2}, \quad (4.77)$$

where  $\mathbf{L}[\cdot]$  is the analytical Laplacian at the particle  $\mathbf{r}_J$  and  $\langle \mathbf{L} \rangle[\cdot]$  is the approximation of the Laplacian at the particle  $\mathbf{r}_J$ ,  $\|E\|_{\Omega}^{L_2}$  is the averaged error over the entire domain. In the following paragraph, the numerical analysis is performed for various functions, particle distributions, and media properties.

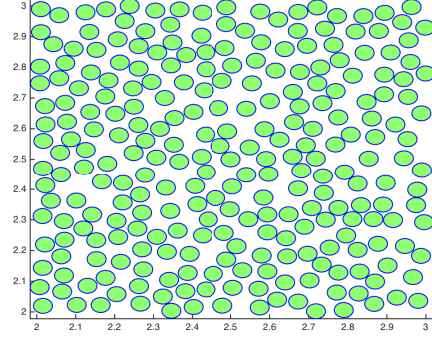
Let us consider a rectangular in  $\mathbb{R}^n$ ,  $n = 1, 2, 3$ :

$$\Omega = \{\mathbf{r} = \{x_i\} \in \mathbb{R}^n \mid 0 < |x_i - a_i| < l_i, l_i \in \mathbb{R}^+, \forall i = 1, \dots, n\} \quad (4.78)$$

as the numerical domain. Here,  $a_i$  are the center coordinates of the rectangular and  $l_i$  are the side lengths. Figures 4.4 show the uniform and random particle distribution 2D. The approximation analysis was also run with



Uniform particles distribution



Random particle distribution

**Figure 4.4:** Particles distribution in 2D for the numerical approximation analysis.

a random distribution of particles to understand its effect on the order of approximation. The random distribution of particles was generated by generated  $N$  random 2D dimensional points  $x_i, y_i$ , where ( $i = 1, \dots, n; j = 1, \dots, n$ ) points in a box of size  $l_i$  with  $a_i$  center, so that each point has at least one neighbour. All the above results were obtained using the cubic spline kernel in the simulations.

Following the work [236], the ability of the discretization to reproduce the Laplacian was tested for several functions in  $\mathbb{R}^n$ ,  $n = 1, 2, 3$ :

$$(a) \mathbf{u}^s(\mathbf{x}) = \sum_{i=1}^n x_i^s, \quad (b) \mathbf{u}_m^s(\mathbf{x}) = \prod_{i=1}^n x_i^{m_i}, \quad |m| = s \quad (4.79)$$

where  $m = (m_1, \dots, m_n)$ ,  $\forall i : m_i \geq 0$  is the  $n$ -dimensional multi-index with the property  $|m| = \sum_{i=1}^n m_i$ .

The reason for selecting these testing polynomials is as follows. Since the functional space  $L_p(\Omega)$  is separable, the above polynomials form the everywhere dense subset of the  $L_p(\Omega)$ . Hence, any function  $\mathbf{u} \in L_p$  can be approximated in  $L_p$  using linear combination of the above polynomials leading to the following relations:

$$\mathbf{u}(\mathbf{r}) \approx \sum_{k=1}^{\infty} \sum_{|m| \leq k} a_m \left( \prod_{i=1}^n x_i^{m_i} \right), \quad \mathbf{M}(\mathbf{r}) \approx \sum_{k=1}^{\infty} \sum_{|m| \leq k} b_m \left( \prod_{i=1}^n x_i^{m_i} \right). \quad (4.80)$$

The approximation error produced by the discretization schemes and considered in this paper for the polynomials  $\mathbf{u}^s(\mathbf{x})$  and  $\mathbf{u}_m^s(\mathbf{x})$  gives the information about the error growth for the arbitrary function  $\mathbf{u}(\mathbf{r})$ . In each test, the homogenous and heterogeneous particle distribution varying the smoothing length  $\tilde{h}$  and inter-particle distance  $h_p$  are used to study the approximation properties of the proposed discretization scheme.

#### 4.4.2 Isotropic Homogeneous Media

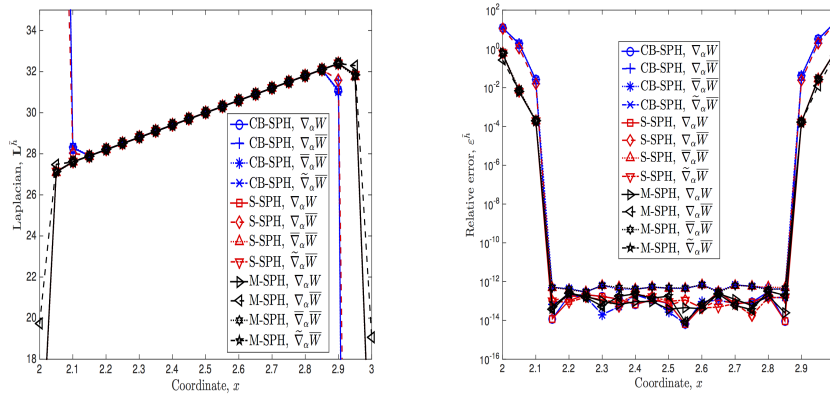
Note that in the limit of the homogeneous isotropic media (i.e.,  $\mathbf{M}^{\alpha\beta}(\mathbf{r}) = m(\mathbf{r}) \delta_{\alpha\beta}$ ,  $m(\mathbf{r}) = 1$ ) and without the source term, the aforementioned operator  $\mathbf{L}(\mathbf{u})$  in (4.1) reduces to the conventional Laplacian operator (i.e.,  $\mathbf{L}(\mathbf{u}) \equiv \nabla^2 \mathbf{u}$ ). The domain for the patch test is a unit square similar to [236] for  $n = 2$ :

$$\Omega = \left\{ \mathbf{r} = \{x_i\} \in \mathbb{R}^n \mid |x_i - 2.5| \leq \frac{1}{2} \quad \forall i \right\}$$

with  $N = 21$  particles in each direction characterized by two length spacings:  $\tilde{h} = f \cdot h_p$ ,  $h_p = 0.05$ ,  $f = 1.2$ .

In all of the following tests, the results are displayed along the cross-section  $y = 2.5$  in  $\mathbb{R}^n$ ,  $n = 2$  (similar to [236] for  $n = 2$ ). In each test, the following discretizations are compared: corrected Brookshaw's scheme (CB-SPH) (4.28), Schwaiger's scheme (S-SPH) (4.29)–(4.32), and new proposed scheme (M-SPH)

(4.44)–(4.46). Note that the Schwaiger’s scheme was tested against several schemes published in [56], [54] and show better accuracy; hence, schemes in [56], [54] are not considered in this paper. The comparison of different schemes starts with test functions of the form  $\mathbf{u}^s(\mathbf{x})$  described by (4.79)(a) in  $\mathbb{R}^n$ ,  $n = 2$ . Plots of the Laplacian approximations and the relative errors defined by (4.77) for the case  $m = 3$  are shown in Figure 4.5.



**Figure 4.5:** Cross-section of the test patch at  $y = 2.5$ . Three SPH approximations of  $\nabla^2(x^3 + y^3)$  with different kernel gradients are shown. Corrected Brookshaw’s scheme (CB-SPH) is given by (4.28) with the correction multiplier, while Schwaiger’s scheme (S-SPH) is given by (4.29)–(4.32). New approximation (M-SPH) considered here is the SPH form (4.44)–(4.46). In this case, the Schwaiger’s scheme and new scheme have comparable accuracy at the boundaries and are accurate in the interior to the machine precision. Four different options of computing the kernel gradient (i.e.,  $\nabla_\gamma W$ ,  $\nabla_\alpha W$ ,  $\nabla_\alpha^* W$ , and corrected kernel gradients (i.e.,  $\nabla_\alpha^* W$ ,  $\nabla_\alpha^* W$ ,  $\nabla_\alpha^* W$ , and  $\nabla_\alpha^* W$ ) are shown.

The new scheme (M-SPH) has the greatest accuracy at the boundary and is accurate to machine precision  $\varepsilon$  in the interior. The same behavior is observed in 3D where the M-SPH scheme with the  $\nabla_\alpha W$  is the most accurate scheme. Furthermore, the new scheme should be tested for the functions requiring cross-derivatives as was reported in [236]. To examine the effect of the cross-derivative terms, the same suite of tests was run with the function  $\mathbf{u}_m^s(\mathbf{x})$  described by (4.79)(b) in  $\mathbb{R}^n$ ,  $n = 2, 3$ . Relative errors for  $(xy)^m$  on a same array as in Figure 4.5 along  $y = 2.5$  were computed and again the proposed scheme (4.44)–(4.46) was uniformly more accurate for the various experiments. The behavior of each discretization is similar to that shown in Figure 4.5. The proposed new scheme (M-SPH) performed nearly as well as the Schwaiger’s scheme at the boundary. The CB-SPH and S-SPH forms also perform with greater accuracy than all other forms in the interior except in the case with the highest exponent.

An additional concern is that although it deviates from the exact solution near boundaries, it acquires no off-diagonal terms due to the alignment of the array of particles and the boundaries with the coordinate axes. To test the accuracy of the new approximations when there are off-diagonal terms, an array with particles rotated  $45^\circ$  was used with the test function  $(xy)^m$  (similar to [236]). The new proposed scheme formulation performs consistently well for lower exponents.

Following the work by [236], the numerical tests for inhomogeneous Dirichlet, Neumann and mixed boundary conditions are considered for homogeneous and heterogeneous media with the characteristics  $\mathbf{M}(\mathbf{r})$ . To illustrate the performance of the proposed scheme, a modelling of a single phase steady-state fluid flow in fully anisotropic porous media with different type of boundary conditions is also presented in this section. The square 2D and 3D domains (4.78) are considered. The relative error used to quantify the accuracy of the proposed schemes during numerical simulation in this section is given by:

$$\|E_R\|_{\Omega}^{L_2} = \left[ \frac{1}{\sum_{\Omega} V_{r_j}} \sum_{\Omega} V_{r_K} \left( \frac{\mathbf{u}(\mathbf{r}_K) - \langle \mathbf{u}(\mathbf{r}_K) \rangle}{\mathbf{u}(\mathbf{r}_K)} \right)^2 \right]^{1/2} \quad (4.81)$$

where  $\mathbf{u}(\mathbf{r})$  is the analytical or reference solution field and  $\langle \mathbf{u}(\mathbf{r}_K) \rangle$  is the approximated solution field. Several numerical results using considered in this paper schemes for uniform and pseudo random particle distributions are shown in the following sections that confirm the theoretical results from the previous sections.

### 4.4.3 Inhomogeneous Boundary Condition

Firstly, the homogeneous properties of the porous media  $\mathbf{M}(\mathbf{r}) = \mathbf{I}$  are assumed for simplicity of the derivation. The analytical solution of (4.1) subject to the assumption that  $g(\mathbf{r}) \equiv 0$  for  $\mathbf{r} \in \Omega \subset \mathbb{R}^2$  and constant boundary conditions is the following:

$$\begin{aligned}
\mathbf{u}(x, y) = & \sum_{n=odd} \left[ \frac{4\psi_1}{n\pi \sinh\left(\frac{n\pi H}{L}\right)} \right] \sin\left(\frac{n\pi}{L}x\right) \sinh\left(\frac{n\pi}{L}(H-y)\right) + \\
& + \sum_{n=odd} \left[ \frac{4\psi_2}{n\pi \sinh\left(\frac{n\pi L}{H}\right)} \right] \sin\left(\frac{n\pi}{H}y\right) \sinh\left(\frac{n\pi}{H}x\right) + \\
& + \sum_{n=odd} \left[ \frac{4\psi_3}{n\pi \sinh\left(\frac{n\pi L}{H}\right)} \right] \sin\left(\frac{n\pi}{H}y\right) \sinh\left(\frac{n\pi}{H}x\right) + \\
& + \sum_{n=odd} \left[ \frac{4\psi_4}{n\pi \sinh\left(\frac{n\pi L}{H}\right)} \right] \sin\left(\frac{n\pi}{H}y\right) \sinh\left(\frac{n\pi}{H}(L-x)\right),
\end{aligned} \tag{4.82}$$

where  $\psi_1$  is the boundary at  $y = 0$ ,  $\psi_2$  at  $x = L$ ,  $\psi_3$  at  $y = H$ , and  $\psi_4$  at  $x = 0$ .

Tables 4.1, 4.2 shows the convergence rate of different schemes for uniform particle distribution. The solutions with MPFA and Mimetic schemes were obtained using MATLAB Reservoir Simulation Toolbox (MRST) [165]. It is clear from the convergence results that schemes (4.29)–(4.32) and (4.44)–(4.46) are identical and they overperform the scheme (4.28). The convergence rate as was predicted theoretically is at least  $\mathcal{O}(h^\omega)$ ,  $1 \leq \omega \leq 2$ . Tables 4.3, 4.4 shows the convergence rate for different schemes and pseudo random dis-

**Table 4.1:** *The error of convergence for different schemes (uniform particle distribution) and  $f = 0.5005$ .*

DoF	MPFA	Mimetic	Brookshaw (4.28)	Schwaiger (4.29)–(4.32)	New Scheme (4.44)–(4.46)
25	$1.318 \cdot 10^{-1}$	$1.240 \cdot 10^{-1}$	$1.314 \cdot 10^0$	$6.608 \cdot 10^{-2}$	$6.608 \cdot 10^{-2}$
100	$3.296 \cdot 10^{-2}$	$3.078 \cdot 10^{-2}$	$3.925 \cdot 10^{-1}$	$1.865 \cdot 10^{-2}$	$1.865 \cdot 10^{-2}$
400	$8.233 \cdot 10^{-3}$	$7.685 \cdot 10^{-3}$	$1.105 \cdot 10^{-1}$	$4.714 \cdot 10^{-3}$	$4.714 \cdot 10^{-3}$
1600	$2.058 \cdot 10^{-3}$	$1.920 \cdot 10^{-3}$	$3.025 \cdot 10^{-2}$	$1.179 \cdot 10^{-3}$	$1.179 \cdot 10^{-3}$
6400	$5.318 \cdot 10^{-4}$	$4.968 \cdot 10^{-4}$	$8.152 \cdot 10^{-3}$	$3.213 \cdot 10^{-4}$	$3.213 \cdot 10^{-4}$
25600	$3.007 \cdot 10^{-4}$	$2.955 \cdot 10^{-4}$	$2.193 \cdot 10^{-3}$	$2.807 \cdot 10^{-4}$	$2.807 \cdot 10^{-4}$

**Table 4.2:** *The error of convergence for different schemes (uniformed particle distribution) and  $f = 1.001$ .*

DoF	Brookshaw (4.28)	Schwaiger (4.29)–(4.32)	New Scheme (4.44)–(4.46)
25	$2.312 \cdot 10^{-1}$	$1.091 \cdot 10^{-1}$	$1.091 \cdot 10^{-1}$
100	$1.120 \cdot 10^{-1}$	$2.698 \cdot 10^{-2}$	$2.698 \cdot 10^{-2}$
400	$3.998 \cdot 10^{-2}$	$6.737 \cdot 10^{-3}$	$6.737 \cdot 10^{-3}$
1600	$1.262 \cdot 10^{-2}$	$1.684 \cdot 10^{-3}$	$1.684 \cdot 10^{-3}$
6400	$3.737 \cdot 10^{-3}$	$4.418 \cdot 10^{-4}$	$4.418 \cdot 10^{-4}$
25600	$1.097 \cdot 10^{-3}$	$2.919 \cdot 10^{-4}$	$2.919 \cdot 10^{-4}$

tribution. The reason for starting from  $f = 0.5005$  is that we want to force the same number of non-zero entries in the matrix as for MPFA or Memetic methods. This procedure may lead to a badly conditioned matrix since  $\nabla \bar{W}(\mathbf{r}_J - \mathbf{r}_I, h) \ll 1$ . This distribution of particles was generated by perturbing the regularly distributed particles using a uniform random variable varying between +10% and -10% of the maximum smoothing length  $h_{max} = 1.001$ . Since random realizations are used to compute errors, the statistical data about 30 realizations are used to compute mean values and standard deviations. This data is presented in Tables 4.3, 4.4. The positive



trends of the scheme remain the same as for the case of uniform particle distributions. The scheme (4.28) has higher error compare to schemes (4.29)–(4.32) and (4.44)–(4.46). However, the dispersion of the approximation error is higher in the scheme (4.44)–(4.46). Figure 4.6 shows the numerical solution of the boundary value

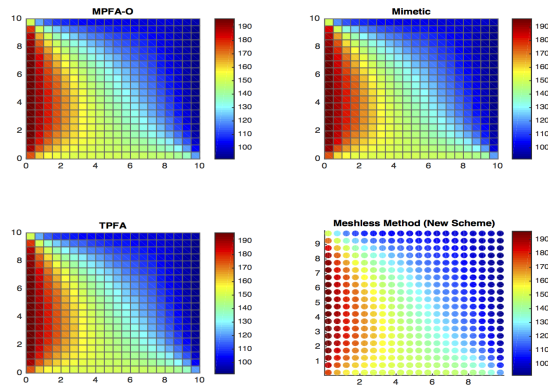
**Table 4.3:** The error of convergence for different schemes (random particle distribution) and  $f = 0.6006$ .

DoF	Brookshaw (4.28)	Schwaiger (4.29)–(4.32)	New Scheme (4.44)–(4.46)
25	$1.102 \cdot 10^{+0} \pm 1.966 \cdot 10^{-2}$	$1.940 \cdot 10^{-1} \pm 3.954 \cdot 10^{-2}$	$3.707 \cdot 10^{-1} \pm 1.319 \cdot 10^{-1}$
100	$3.361 \cdot 10^{-1} \pm 4.923 \cdot 10^{-3}$	$5.511 \cdot 10^{-2} \pm 1.205 \cdot 10^{-2}$	$9.074 \cdot 10^{-2} \pm 2.668 \cdot 10^{-2}$
400	$9.576 \cdot 10^{-2} \pm 8.705 \cdot 10^{-4}$	$1.376 \cdot 10^{-2} \pm 2.440 \cdot 10^{-3}$	$2.299 \cdot 10^{-2} \pm 6.972 \cdot 10^{-3}$
1600	$2.640 \cdot 10^{-2} \pm 2.551 \cdot 10^{-4}$	$4.157 \cdot 10^{-3} \pm 7.485 \cdot 10^{-4}$	$5.912 \cdot 10^{-3} \pm 1.289 \cdot 10^{-3}$
6400	$7.185 \cdot 10^{-3} \pm 5.982 \cdot 10^{-5}$	$1.044 \cdot 10^{-3} \pm 1.465 \cdot 10^{-4}$	$1.406 \cdot 10^{-3} \pm 3.090 \cdot 10^{-4}$
25600	$1.944 \cdot 10^{-3} \pm 1.451 \cdot 10^{-5}$	$3.858 \cdot 10^{-4} \pm 5.887 \cdot 10^{-5}$	$4.960 \cdot 10^{-4} \pm 8.425 \cdot 10^{-5}$

**Table 4.4:** The error of convergence for different schemes (random particle distribution) and  $f = 1.2012$ .

DoF	Brookshaw (4.28)	Schwaiger (4.29)–(4.32)	New Scheme (4.44)–(4.46)
25	$3.578 \cdot 10^{-1} \pm 2.879 \cdot 10^{-2}$	$2.162 \cdot 10^{-1} \pm 2.800 \cdot 10^{-2}$	$1.842 \cdot 10^{-1} \pm 8.871 \cdot 10^{-3}$
100	$1.261 \cdot 10^{-1} \pm 4.859 \cdot 10^{-3}$	$5.696 \cdot 10^{-2} \pm 5.518 \cdot 10^{-3}$	$4.596 \cdot 10^{-2} \pm 1.999 \cdot 10^{-3}$
400	$4.224 \cdot 10^{-2} \pm 1.092 \cdot 10^{-3}$	$1.493 \cdot 10^{-2} \pm 1.546 \cdot 10^{-3}$	$1.157 \cdot 10^{-2} \pm 5.691 \cdot 10^{-4}$
1600	$1.299 \cdot 10^{-2} \pm 2.031 \cdot 10^{-4}$	$3.934 \cdot 10^{-3} \pm 3.969 \cdot 10^{-4}$	$2.889 \cdot 10^{-3} \pm 1.451 \cdot 10^{-4}$
6400	$3.862 \cdot 10^{-3} \pm 3.452 \cdot 10^{-5}$	$1.037 \cdot 10^{-3} \pm 8.443 \cdot 10^{-5}$	$7.507 \cdot 10^{-4} \pm 4.060 \cdot 10^{-5}$
25600	$1.133 \cdot 10^{-3} \pm 2.125 \cdot 10^{-5}$	$4.087 \cdot 10^{-4} \pm 5.405 \cdot 10^{-5}$	$3.475 \cdot 10^{-4} \pm 3.814 \cdot 10^{-5}$

problem obtained using different discretization methods. The solution was obtained using 40 particles/cells in each direction.



**Figure 4.6:** Comparison of solutions of the Dirichlet problem for the Laplace equation. The method used are MPFA-O, Mimetic, TPFA, and Meshless methods (New Method: (4.44)–(4.46)).

#### 4.4.4 Inhomogeneous Mixed Boundary Condition Test

The general steady-state solution for a Dirichlet condition along the base of the plate and Neumann conditions elsewhere is given in [236] by

$$\mathbf{u}(x, y) = \psi_1 + \psi_3 y + \sum_{n=1}^{\infty} \frac{2\psi_2 \cosh(\lambda_n x) + 2\psi_4 \cosh(\lambda_n (L - x))}{H \lambda_n^2 \sinh(\lambda_n L)} \sinh(\lambda_n y), \quad (4.83)$$

where  $\psi_1$  is the boundary value of  $\mathbf{u}$  at  $y = 0$ ,  $\psi_2$  is the flux at  $x = L$ ,  $\psi_3$  is the flux at  $y = H$ , and  $\psi_4$  is the flux at  $x = 0$ , and  $\lambda_n = \frac{(2n-1)\pi}{2H}$ . The following parameters (dimensionless) were chosen:  $\psi_1 = 150$ ,  $\psi_3 = 150$ ,  $\psi_4 = 200$ ,  $\psi_2 = 90$ . Again, for uniform and regular particles distribution, MPFA method reduces to the TPFA. Similar to the previous section, the regular and pseudo random particle distribution are considered to access the convergence properties of the proposed schemes.

**Remark 4.16.** Let  $\Gamma_N = \emptyset$  and  $\Gamma_D = \emptyset$ ,  $g(\mathbf{r}) \geq 0$ ,  $\mathbf{r} \in \Omega$ ,  $g_N(\mathbf{r}) \geq 0$ ,  $\mathbf{r} \in \Gamma_N$ ,  $g_D(\mathbf{r}) \geq 0$ ,  $\mathbf{r} \in \Gamma_D$  and the solution of

$$\mathbf{L}(\mathbf{u}) = 0, \text{ or } \nabla(\mathbf{M}(\mathbf{r}) \nabla \mathbf{u}(\mathbf{r})) = g(\mathbf{r}), \forall \mathbf{r} \in \Omega \subset \mathbb{R}^n, \quad (4.84)$$

exists then it can be discretized in all internal particles by the following schemes Brookshaw (4.28), Schwaiger (4.29)–(4.32), and New Scheme (4.44)–(4.46) and compounded with the following condition for all  $\mathbf{r} \in \Gamma_N$ :

$$\langle \mathbf{v}^\alpha \mathbf{n}_\alpha \rangle = \mathbf{n}_\alpha \mathbf{M}^{\alpha\beta}(\mathbf{r}) \sum_{\Omega_{\mathbf{r},h}} V_{\mathbf{r}_J} [\mathbf{u}(\mathbf{r}_J) - \mathbf{u}(\mathbf{r}_I)] \overline{\nabla_\beta^* W}(\mathbf{r}_J - \mathbf{r}_I, h) \quad (4.85)$$

where  $\mathbf{n}_\alpha$  are the component of the external normal to the boundary  $\mathbf{r} \in \Gamma_N$ .

The following smoothing multiplication factors  $f = 0.5005$ ,  $f = 1.001$ , and  $f = 2.002$  are considered. Tables 4.5, 4.6 show the convergence rate for different schemes using the uniform and pseudo random particle distribution. The convergence rate as was predicted theoretically is at least  $\mathcal{O}(h^\omega)$ ,  $1 \leq \omega < 2$ . Interestingly, the scheme (4.28) shows a very bad convergence rate for  $f = 0.5005$ . This explains by the fact that we have one particle from each side in the kernel support almost next to the boundary of the kernel support leading to  $\overline{\nabla W}(\mathbf{r}_J - \mathbf{r}_I, h) \ll 1$  and, hence, to a badly conditioned matrix. This does not observed for other schemes due to the normalization coefficient. As a result, the scheme (4.28) should be used with more than one particle in the compact support in each direction leading to a larger bandwidth in the matrix.

**Table 4.5:** The error of convergence for different schemes (uniform particle distribution) and  $f = 0.5005$ .

DoF	MPFA	Mimetic	Brookshaw (4.28)	Schwaiger (4.29)–(4.32)	New Scheme (4.44)–(4.46)
25	$1.489 \cdot 10^{-1}$	$2.651 \cdot 10^{-2}$	$1.489 \cdot 10^6$	$8.244 \cdot 10^{-1}$	$8.244 \cdot 10^{-1}$
100	$2.015 \cdot 10^{-2}$	$4.424 \cdot 10^{-3}$	$9.471 \cdot 10^5$	$2.178 \cdot 10^{-1}$	$2.178 \cdot 10^{-1}$
400	$2.727 \cdot 10^{-3}$	$6.889 \cdot 10^{-4}$	$5.378 \cdot 10^5$	$5.550 \cdot 10^{-2}$	$5.550 \cdot 10^{-2}$
1600	$3.666 \cdot 10^{-4}$	$1.024 \cdot 10^{-4}$	$2.859 \cdot 10^5$	$1.398 \cdot 10^{-2}$	$1.398 \cdot 10^{-2}$
6400	$4.951 \cdot 10^{-5}$	$1.522 \cdot 10^{-5}$	$1.473 \cdot 10^5$	$3.504 \cdot 10^{-3}$	$3.504 \cdot 10^{-3}$
25600	$7.309 \cdot 10^{-6}$	$2.920 \cdot 10^{-6}$	$7.474 \cdot 10^4$	$8.770 \cdot 10^{-4}$	$8.770 \cdot 10^{-4}$

Tables 4.7, 4.8 show the convergence rate for different schemes with pseudo random particle distribution. The pseudo random distribution of particles was again generated by perturbing the regularly distributed particles using the uniform random variable varying between +10% and –10% of the maximum smoothing length  $h_{max} = 1.001$ . Similar to the above case, the statistical data about 30 realizations are used to compute mean values and standard deviations. These data are presented in Tables 4.7, 4.8. The general trends of the scheme prosperities remain the same as for uniform particle distributions. The scheme (4.28) has higher error compared to schemes (4.29)–(4.32) and (4.44)–(4.46). However, the dispersion of the approximation error is higher in the scheme (4.44)–(4.46). Results of the numerical solution are compared with the series solution in Figure 11.

**Table 4.6:** The error of convergence for different schemes (uniform particle distribution) and  $f = 1.001$ .

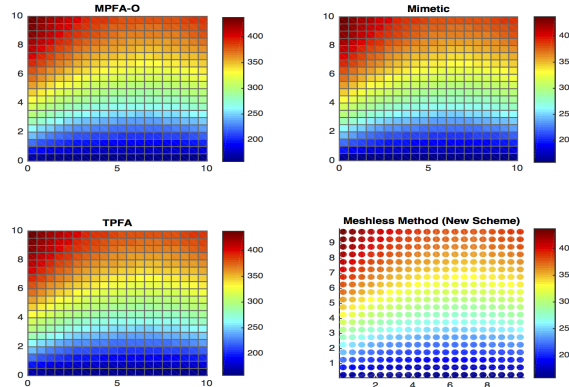
DoF	Brookshaw (4.28)	Schwaiger (4.29)–(4.32)	New Scheme (4.44)–(4.46)
25	$1.163 \cdot 10^0$	$1.078 \cdot 10^{-1}$	$1.078 \cdot 10^{-1}$
100	$1.208 \cdot 10^0$	$1.488 \cdot 10^{-2}$	$1.488 \cdot 10^{-2}$
400	$8.291 \cdot 10^{-1}$	$2.244 \cdot 10^{-3}$	$2.244 \cdot 10^{-3}$
1600	$4.831 \cdot 10^{-1}$	$4.215 \cdot 10^{-4}$	$4.215 \cdot 10^{-4}$
6400	$2.606 \cdot 10^{-1}$	$9.858 \cdot 10^{-5}$	$9.858 \cdot 10^{-5}$
25600	$1.353 \cdot 10^{-1}$	$2.502 \cdot 10^{-5}$	$2.502 \cdot 10^{-5}$

**Table 4.7:** The error of convergence for different schemes (random particle distribution) and  $f = 0.6006$ .

DoF	Brookshaw (4.28)	Schwaiger (4.29)–(4.32)	New Scheme (4.44)–(4.46)
25	$5.608 \cdot 10^1 \pm 1.019 \cdot 10^0$	$8.815 \cdot 10^{-1} \pm 4.248 \cdot 10^{-1}$	$1.242 \cdot 10^0 \pm 5.058 \cdot 10^{-1}$
100	$3.769 \cdot 10^1 \pm 5.708 \cdot 10^{-1}$	$3.454 \cdot 10^{-1} \pm 1.977 \cdot 10^{-1}$	$4.361 \cdot 10^{-1} \pm 2.425 \cdot 10^{-1}$
400	$2.154 \cdot 10^1 \pm 1.757 \cdot 10^{-1}$	$8.454 \cdot 10^{-2} \pm 5.111 \cdot 10^{-2}$	$1.525 \cdot 10^{-1} \pm 1.195 \cdot 10^{-1}$
1600	$1.159 \cdot 10^1 \pm 7.457 \cdot 10^{-2}$	$2.245 \cdot 10^{-2} \pm 1.055 \cdot 10^{-2}$	$4.563 \cdot 10^{-2} \pm 2.328 \cdot 10^{-2}$
6400	$6.027 \cdot 10^0 \pm 2.312 \cdot 10^{-2}$	$1.104 \cdot 10^{-2} \pm 7.523 \cdot 10^{-3}$	$1.848 \cdot 10^{-2} \pm 9.276 \cdot 10^{-3}$
25600	$3.054 \cdot 10^0 \pm 1.174 \cdot 10^{-2}$	$4.123 \cdot 10^{-3} \pm 2.059 \cdot 10^{-3}$	$5.879 \cdot 10^{-3} \pm 4.253 \cdot 10^{-3}$

**Table 4.8:** The error of convergence for different schemes (random particle distribution) and  $f = 1.2012$ .

DoF	Brookshaw (4.28)	Schwaiger (4.29)–(4.32)	New Scheme (4.44)–(4.46)
25	$5.177 \cdot 10^{-1} \pm 7.312 \cdot 10^{-2}$	$3.143 \cdot 10^{-1} \pm 7.543 \cdot 10^{-2}$	$4.302 \cdot 10^{-1} \pm 1.461 \cdot 10^{-1}$
100	$5.160 \cdot 10^{-1} \pm 4.035 \cdot 10^{-2}$	$5.959 \cdot 10^{-2} \pm 4.713 \cdot 10^{-3}$	$1.106 \cdot 10^{-1} \pm 1.739 \cdot 10^{-2}$
400	$4.349 \cdot 10^{-1} \pm 1.715 \cdot 10^{-2}$	$1.515 \cdot 10^{-2} \pm 1.973 \cdot 10^{-3}$	$3.015 \cdot 10^{-2} \pm 1.045 \cdot 10^{-2}$
1600	$2.745 \cdot 10^{-1} \pm 9.059 \cdot 10^{-3}$	$3.926 \cdot 10^{-3} \pm 6.865 \cdot 10^{-4}$	$1.133 \cdot 10^{-2} \pm 5.486 \cdot 10^{-3}$
6400	$1.508 \cdot 10^{-1} \pm 2.822 \cdot 10^{-3}$	$1.595 \cdot 10^{-3} \pm 8.144 \cdot 10^{-4}$	$3.187 \cdot 10^{-3} \pm 1.438 \cdot 10^{-3}$
25600	$7.958 \cdot 10^{-2} \pm 1.146 \cdot 10^{-3}$	$5.354 \cdot 10^{-4} \pm 2.036 \cdot 10^{-4}$	$9.201 \cdot 10^{-4} \pm 5.201 \cdot 10^{-4}$



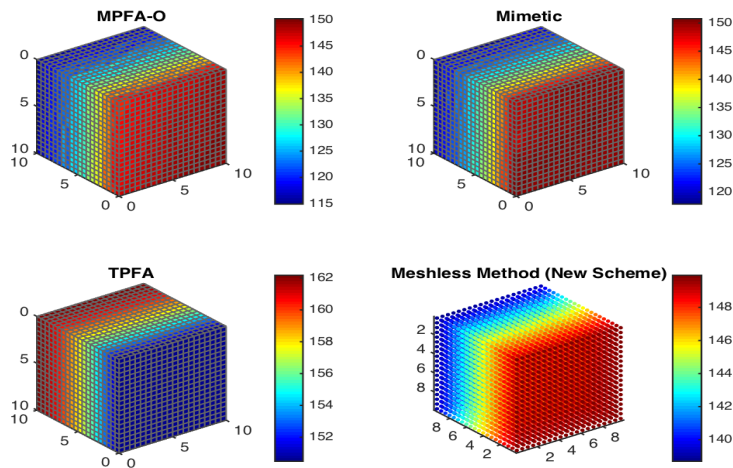
**Figure 4.7:** Comparison of solutions of the inhomogeneous mixed boundary problems for the Laplace equations. The method used are MPFA-O, Mimetic, TPFA, and Meshless methods (New Method: (4.44)–(4.46)).

### 4.6.3 Fully Anisotropic Medium

The new method (4.66) – (4.75) has been tested on a sequence of uniform and random particle distributions for homogeneous and heterogeneous anisotropic media in 2D and 3D. Physically, it is assumed that the permeability  $\mathbf{M}(\mathbf{r})$  is a symmetric, uniformly positive definite tensor in  $\Omega \subset \mathbb{R}^n$ ,  $n = 2, 3$ . In all cases, the boundary conditions of Dirichlet type and mixed conditions as defined in the previous section are considered. The numerical results are presented for the following case

$$\mathbf{M}(\mathbf{r}) = \begin{bmatrix} 2 & 50 & 20 \\ 50 & 200 & 10 \\ 20 & 10 & 300 \end{bmatrix}, \quad \mathbf{r} \in \Omega \subset \mathbb{R}^3, \quad (4.86)$$

Figure 4.8 shows the comparison of solutions of the mixed boundary value problem for the Laplace equation in 3D using MPFA-O, Mimetic, TPFA, and Meshless methods (New Method: (4.69)–(4.72)) and permeability tensor (4.86) Case (b). The computed errors were  $\|E_R\|_{\Omega}^{L^2} = 0.000 \cdot 10^0$  (MPFA),  $\|E_R\|_{\Omega}^{L^2} = 6.478 \cdot 10^{-5}$  (Mimetic),  $\|E_R\|_{\Omega}^{L^2} = 8.458 \cdot 10^{-13}$  (TPFA),  $\|E_R\|_{\Omega}^{L^2} = 5.945 \cdot 10^{-4}$  (Meshless Method). The proposed method (4.69)–(4.72) shows similar qualitative behaviour as MPFA and Mimetic but not as TPFA; however, the proposed method has a higher error compared to Mimetic. The TPFA method does not show the correct behavior and, hence, this method produces incorrect pressure distribution. In a case of heterogenous media, the following



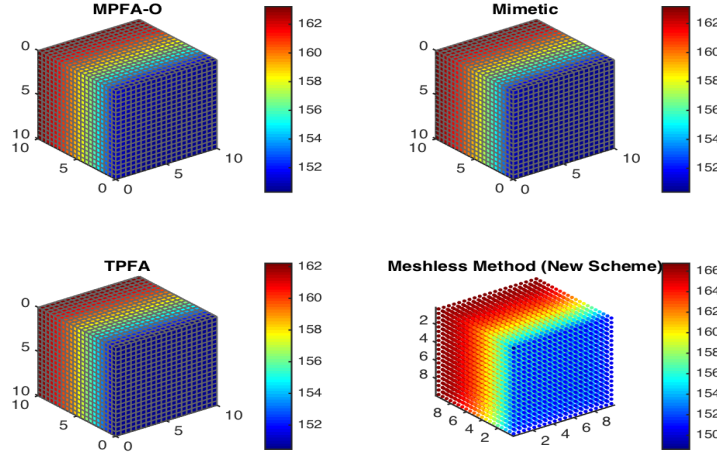
**Figure 4.8:** Comparison of solutions of the Dirichlet problem for the Laplace equation and permeability tensor (4.86) Case (c). The method used are MPFA-O, Mimetic, TPFA, and Meshless methods (New Method: (4.69)–(4.72)). Errors  $\|E_R\|_{\Omega}^{L^2} = 0.000 \cdot 10^0$  (MPFA),  $\|E_R\|_{\Omega}^{L^2} = 6.478 \cdot 10^{-5}$  (Mimetic),  $\|E_R\|_{\Omega}^{L^2} = 8.458 \cdot 10^{-13}$  (TPFA),  $\|E_R\|_{\Omega}^{L^2} = 5.945 \cdot 10^{-4}$  (Meshless Method)

tensors are considered:

$$\mathbf{M}(\mathbf{r}) = \begin{bmatrix} 10 + (x+2)^2 + y^2 & 2 + 2 \sin(xy) & 1 + \cos(xz) \\ 2 + 2 \sin(xy) & 2 & 1 + \sin(yz) \\ 1 + \cos(xz) & 1 + \sin(yz) & 20 + (z+2)^2 + y^2 \end{bmatrix}, \quad \mathbf{r} \in \Omega \subset \mathbb{R}^3, \quad (4.87)$$

The provided expressions ensure that the permeability  $\mathbf{M}(\mathbf{r})$  is a symmetric, uniformly positive definite tensors in  $\Omega \subset \mathbb{R}^n$ ,  $n = 2, 3$ . Again, the boundary conditions of Dirichlet and mixed types (as defined as in the previous section) are considered again. Figure 4.9 shows the comparison of solutions of the mixed boundary value problem for the Laplace equation in 3D using MPFA-O, Mimetic, TPFA, and Meshless methods (New Method: (4.69) – (4.72)) and heterogenous permeability tensor (4.87). The computed errors were  $\|E_R\|_{\Omega}^{L^2} = 0.000 \cdot 10^0$  (MPFA),  $\|E_R\|_{\Omega}^{L^2} = 4.060 \cdot 10^{-4}$  (Mimetic),  $\|E_R\|_{\Omega}^{L^2} = 4.948 \cdot 10^{-3}$  (TPFA),  $\|E_R\|_{\Omega}^{L^2} = 1.958 \cdot 10^{-2}$

(Meshless Method). The proposed method (4.69)–(4.72) shows similar qualitative behaviour as MPFA, TPFA and Mimetic; furthermore, the proposed method has almost identical error compared to TPFA.



**Figure 4.9:** Comparison of solutions of the Dirichlet problem for the Laplace equations and permeability tensor (4.87). The method used are MPFA-O, Mimetic, TPFA, and Meshless methods (New Method: (4.69)–(4.72)). Errors  $\|E_R\|_{\Omega}^{L^2} = 0.000 \cdot 10^0$  (MPFA),  $\|E_R\|_{\Omega}^{L^2} = 4.060 \cdot 10^{-4}$  (Mimetic),  $\|E_R\|_{\Omega}^{L^2} = 4.948 \cdot 10^{-3}$  (TPFA),  $\|E_R\|_{\Omega}^{L^2} = 1.958 \cdot 10^{-2}$  (Meshless Method)

#### 4.4.1 Monotonicity

In real life applications, the numerical domains are large and, therefore, many degree of freedom (i.e., unknowns) is required. The resulting matrix is usually sparse, but because of fill-in a direct method requires significant amount of memory and time in general case. Hence, iterative solvers are used to overcome these issues. The iterative solvers converge only if the matrix satisfies certain properties related to the property of the diagonal dominance. However, these properties are only sufficient conditions for the method to converge.

The proof of the convergence of linear meshless schemes applied to a linear elliptic boundary value problem can be done in the following steps (see, Bouchon (2007) [34], Bouchon and Peichl (2007) [35], Matsunaga and Yamamoto (2000) [197], Thomée (2001) [252]: if it is shown that the truncation error  $\varepsilon$  tends to 0 as the maximum smoothing length  $\max_{I \in \mathcal{N}} h_I$  goes to 0, then the linear system  $\mathbf{A}\delta u = \varepsilon$  that couples the variable error  $\delta u$  with  $\varepsilon$  proves the convergence of the schemes, given that the matrix of the discretized meshless operator is monotone.

**Definition 4.17.** A square matrix  $\mathbf{A} = (a_{ij})_{1 \leq i \leq n, 1 \leq j \leq n} \in \mathbb{R}^{n \times n}$  is called monotone if it is inverse positive  $\mathbf{A}^{-1} \geq 0$ . Inverse positive refers to the component wise.

The monotone matrix has always attracted researches in many fields (e.g., Bramble and Hubbard (1964) [38], Fujimoto and Ranade (2004) [93], Bouchon and Peichl (2007) [35], LeVeque and Li (1994) [161], Wiegmann and Bube (2000) [276]). Generally speaking, meshless multi-point flux approximation matrices are not  $M$ -matrices. However, the scheme converges to the solution of the continuous problem (1) and the entries of the matrix  $a_{ij}$  seem to be insignificantly deviated from the  $M$ -matrix structure. In this thesis, the perturbation approach will be employed to characterize the monotone matrices (Alfa *et al.* (2002) [7], Elsner (1997) [88], Bouchon (2007) [34], Haynes *et al.* (2007) [108], Xue and Jiang (1995) [277]). Usually  $\mathbf{A} \in \mathbb{R}^{n \times n}$  is shown to be monotone by showing that it is an  $M$ -matrix (Bouchon, 2007 [34]). There are over 50 various equivalent definitions of  $M$ -matrix (Bermann and Plemmons, 1979 [29]).

**Definition 4.18.** A square matrix  $\mathbf{A} = (a_{ij})_{1 \leq i \leq n, 1 \leq j \leq n} \in \mathbb{R}^{n \times n}$  is called  $M$ -matrix if  $a_{ij} \leq 0 \forall i \neq j$ ,  $a_{ii} > 0 \forall i$  and  $\mathbf{A}$  is strictly diagonally dominant matrix

The  $\mathcal{M}$ -matrix is monotone since its inverse is positive, i.e.  $\mathbf{A}^{-1} \geq 0$ . Furthermore, the monotone schemes do satisfy a discrete maximum principle producing solutions without spurious oscillations.

It is clear that the new scheme (4.44)–(4.46) can be written in the form (4.4), where meshless transmissibility between particles  $\mathbf{r}_J$  and  $\mathbf{r}_I$  can be defined as  $T(\mathbf{r}_J, \mathbf{r}_I) = \frac{\bar{\Gamma}_{\beta\beta}^{-1}}{n} (m_I + m_J) \bar{T}_{IJ}$  with:

$$\bar{T}_{IJ} = V_{\mathbf{r}_J} \left\{ \frac{(\mathbf{r}_J - \mathbf{r}_I) \cdot \nabla \bar{W}(\mathbf{r}_J - \mathbf{r}_I, \tilde{h}_{IJ})}{\|\mathbf{r}_J - \mathbf{r}_I\|^2} - \nabla_{\alpha}^* \bar{W}(\mathbf{r}_J - \mathbf{r}_I, \tilde{h}_{IJ}) \tilde{\mathbf{N}}^{\alpha} \right\}, \quad (4.88)$$

where  $\tilde{\mathbf{N}}^{\alpha}(\mathbf{r}_I)$  is defined by (4.30). Applying the relation (2.35) valid for kernel gradients (2.31), (2.33), (2.34) and the definition of the corrected kernel gradient (2.36), (2.37) leading to

$$\bar{T}_{IJ} = \frac{V_{\mathbf{r}_J}}{\tilde{h}_{IJ} \|\mathbf{r}_J - \mathbf{r}_I\|} G(z_J, \mathbf{r}_I) \left[ 1 - \tilde{\mathbf{N}}^{\alpha}(\mathbf{r}_I) \mathbf{C}_{\alpha\beta}(\mathbf{r}_I) (\mathbf{r}_J^{\beta} - \mathbf{r}_I^{\beta}) \right]. \quad (4.89)$$

The sign of the transmissibility coefficient is described by the the following Lemma.

**Lemma 4.19.** *If matrix  $\bar{\Gamma}_{ij}(\mathbf{r}_I)$  is strictly diagonally dominant matrix then the coefficients  $T(\mathbf{r}_J, \mathbf{r}_I)$  are positive in the following cases  $\forall \mathbf{r}_J$ :*

(a) Case  $\Gamma_{\alpha\beta}^*(\mathbf{r}_I) \neq 0$ : if we have the following relation  $\forall \mathbf{r}_J, \mathbf{r}_K \in \Omega_{\mathbf{r}_I, \tilde{h}_I}$

$$\text{sgn} \left[ 1 - \tilde{\mathbf{N}}(\mathbf{r}_I) \mathbf{C}(\mathbf{r}_I) (\mathbf{r}_J - \mathbf{r}_I) \right] = \text{sgn} \left[ 1 - \tilde{\mathbf{N}}(\mathbf{r}_I) \mathbf{C}(\mathbf{r}_I) (\mathbf{r}_K - \mathbf{r}_I) \right], \quad (4.90)$$

where  $\text{sgn}$  is the sign function.

(b) Case  $\Gamma_{\alpha\beta}^*(\mathbf{r}_I) = 0$ : if we have the following relation  $\forall \mathbf{r}_J \in \Omega_{\mathbf{r}_I, \tilde{h}_I}$

$$\left[ 1 - \tilde{\mathbf{N}}(\mathbf{r}_I) \mathbf{C}(\mathbf{r}_I) (\mathbf{r}_J - \mathbf{r}_I) \right] > 0. \quad (4.91)$$

*Proof.* Taking into account (4.47), (4.48), (4.49) and Lemma 4.5, we need to ensure that  $\bar{\Gamma}_{\beta\beta}^{-1}/n$  and  $\bar{T}_{IJ}$  are of the same sign. This can be achieved by the conditions of the Lemma 4.19.  $\square$

It is clear that the sufficient conditions (4.90) and (4.91) are fulfilled for the homogeneous and symmetrical particles distribution due to  $\tilde{\mathbf{N}}(\mathbf{r}_I) = 0$ . In general, one can note that

$$\tilde{\mathbf{N}}(\mathbf{r}_I) \mathbf{C}(\mathbf{r}_I) = \|\boldsymbol{\xi}_I\| \|\Delta \mathbf{r}_{JI}\| \cdot \cos(\boldsymbol{\xi}_I, \Delta \mathbf{r}_{JI}), \quad (4.92)$$

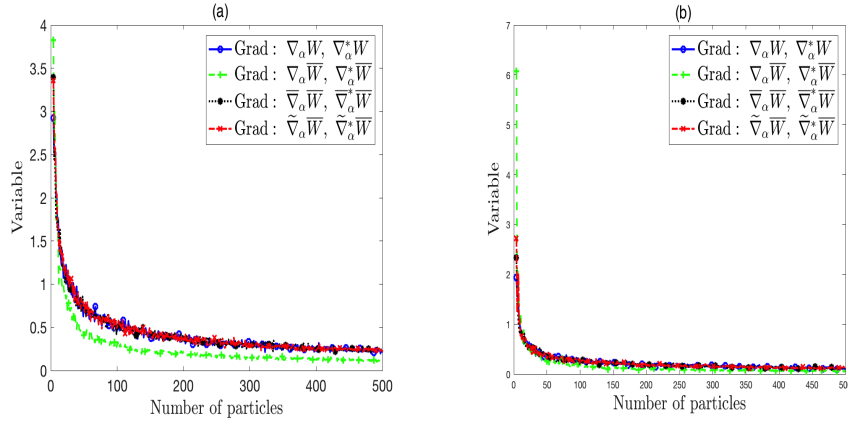
where  $\boldsymbol{\xi}_I^{\beta}$  is the vector  $\tilde{\mathbf{N}}^{\alpha}(\mathbf{r}_I) \mathbf{C}(\mathbf{r}_I)_{\alpha\beta}$ ,  $\Delta \mathbf{r}_{JI}$  is the vector  $(\mathbf{r}_J - \mathbf{r}_I)$ ,  $\cos(\boldsymbol{\xi}_I, \Delta \mathbf{r}_{JI})$  is the *cos* of angle between  $\boldsymbol{\xi}_I^{\beta}$  and  $\Delta \mathbf{r}_{JI}$ . The maximum of absolute values in (4.92) is achieved when vectors  $\boldsymbol{\xi}_I^{\beta}$  and  $\Delta \mathbf{r}_{JI}$  are collinear. Figure 4.10 shows the mean value distribution of  $\|\boldsymbol{\xi}_I\|$  and its dispersion as a function of neighboring particles in a unit circle. The smoothing length for all particles  $\tilde{h}_I = 1 \forall I$  and  $f = 0.5005$  are assumed. The 50 random configurations of the neighboring particles distribution are considered starting from 4 to 500 neighboring particles in 2D. It is clear from the Fig. 4.10 that sufficient conditions (4.90) and (4.91) are fulfilled in statistical sense for heterogeneous particles distribution for large number of neighboring particles. A consequence of the Lemma 4.19 is the statement of the next Theorem.

**Theorem 4.20.** *The proposed discretization scheme (4.44)–(4.46) subject to the conditions of the Lemma 4.19 is monotone for the medium with the scalar heterogeneous  $-m(\mathbf{r})$  coefficients.*

The Lemma 4.19 provides a sufficient (not necessary) conditions for the monotonicity of the proposed new discretization scheme (4.44)–(4.46).

#### 4.4.2 von Neumann stability analysis

For linear PDEs, there is the Lax-equivalence theorem which connects the consistency and stability with the convergence. The idea of the von Neumann stability analysis is to study the growth of waves  $\lambda e^{i\mathbf{k} \cdot \mathbf{r}}$  (similar



**Figure 4.10:** (a) The mean value distribution of  $\|\xi_I\|$  for 50 random configurations; (b) The dispersion  $\sigma(\|\xi_I\|)$  of the  $\|\xi_I\|$  distribution for 50 random configurations;

to Fourier methods). After applying one of the discretization methods above to the Laplace operator (4.1), the following relation can be written:

$$\frac{\{\mathbf{u}\}^{n+1} - \{\mathbf{u}\}^n}{\tau} - \mathbf{L}^{\tilde{h}}[\{\mathbf{u}\}^n] = \{\mathbf{b}\}, \quad (4.93)$$

where  $\tau$  is the iteration parameter (e.g., time step),  $n$  is the iteration index (e.g., time index),  $\{\mathbf{u}\}^n = (\mathbf{u}_1^n, \dots, \mathbf{u}_N^n)$  is a vector of all  $N$  particle values  $\mathbf{u}_i^n$ ,  $i = 1, \dots, N$ ,  $\{\mathbf{b}\} = (\mathbf{b}_1, \dots, \mathbf{b}_N)$  is the right-hand side vector. The expression (4.93) may represent, for example, discretization of the parabolic PDE or an iterative solver of the linear system of equations arising from discretization of elliptic boundary value problem. Substituting into the left-hand side of the relation (4.93) the following form of perturbation

$$\mathbf{u}_j^n = \lambda^n e^{i\mathbf{k}_j \cdot \mathbf{r}_j} = \lambda^n \cdot \prod_{l=1}^n e^{i\mathbf{k}_j^l \cdot \mathbf{x}_j^l} \quad (4.94)$$

leads to the expression for the von Neumann growth factor subject to (4.93) and linear Laplace operator:

$$\lambda_j(\tau) = 1 + \tau \cdot e^{-i\mathbf{k}_j \cdot \mathbf{r}_j} \cdot \mathbf{L}^{\tilde{h}}[\{e^{i\mathbf{k} \cdot \mathbf{r}}\}], \mathbf{r} \in \mathbb{R}^n, n = 1, 2, 3; \quad (4.95)$$

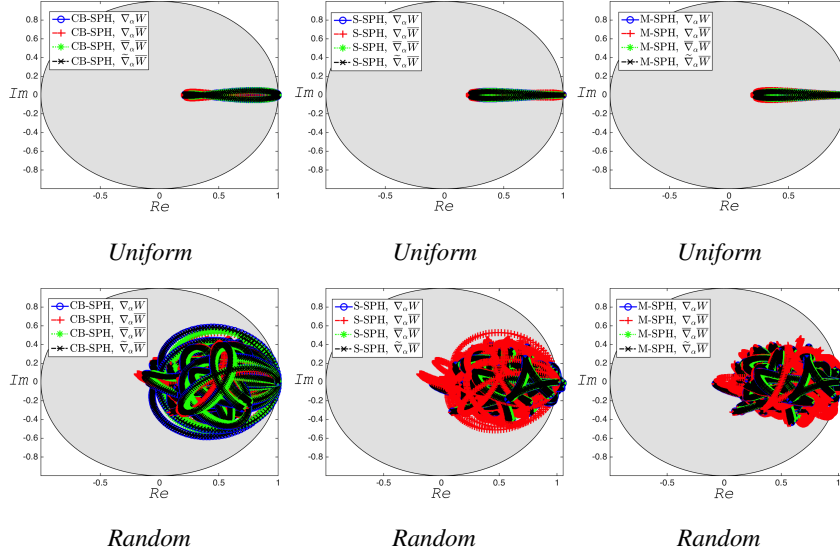
where  $\{e^{i\mathbf{k} \cdot \mathbf{r}}\} = (e^{i\mathbf{k}_1 \cdot \mathbf{r}_1}, \dots, e^{i\mathbf{k}_N \cdot \mathbf{r}_N})$  and  $\lambda_j(\tau)$  is the von Neumann growth factor. For the discretization to be stable, it is required that  $|\lambda_j(\tau)| \leq 1, \forall j$ . The von Neumann growth factor is shown for three main discretization schemes: Corrected Brookshaw's scheme (CB-SPH) (4.28), Schwaiger's scheme (S-SPH) (4.29)–(4.32) and new approximation (M-SPH) (4.44)–(4.46) for uniform and pseudo random particle distribution with  $\tau = 0.25$  and  $\mathbf{M}^{\alpha\beta}(\mathbf{r}) = \delta_{\alpha\beta}$  (see, Figures 4.11). In case of uniform particle distribution, the von Neumann growth factor clusters around the real axis for all schemes and satisfies the requirement  $|\lambda_j(\tau)| \leq 1, \forall j$ . In case of pseudo random particle distribution, the von Neumann growth factor has both real and imaginary parts forming complex shape but satisfying the requirement  $|\lambda_j(\tau)| \leq 1, \forall j$  almost everywhere (i.e., it could be some problems at the boundary particles).

## §4.5 SPE10

In addition, we investigate the accuracy of the numerical schemes using a well-known SPE10 benchmark [64] with the Laplace equation:

$$\begin{aligned} \mathbf{L}(\mathbf{u}) &= -\nabla(\mathbf{M}(\mathbf{r}) \nabla \mathbf{u}(\mathbf{r})) = 0, \forall \mathbf{r} \in \Omega \subset \mathbb{R}^n, \\ \mathbf{M}^{\alpha\beta}(\mathbf{r}) &= K^{\alpha\beta}(\mathbf{r}), K^{\alpha\beta}(\mathbf{r}) = 0 \forall \alpha \neq \beta; \alpha, \beta = 1, \dots, n; \end{aligned} \quad (4.96)$$

where  $\mathbf{u}(\mathbf{r})$  is the unknown pressure field,  $K^{\alpha\beta}(\mathbf{r})$  is the diagonal permeability field. The original model contains 85 layers, where layers from 1 to 35 have smooth permeability with lognormal distribution and layers



**Figure 4.11:** von Neumann growth factor for different discretization schemes. Corrected Brookshaw’s scheme (CB-SPH) is given by (4.28) with the correction multiplier, while Schwaiger’s scheme (S-SPH) is given by (4.29)–(4.32). New approximation (M-SPH) considered here are the SPH form (4.44) – (4.46). Four different options of computing kernel gradients (i.e.,  $\nabla_\gamma W$ ,  $\nabla_\alpha \bar{W}$ , and corrected kernel gradients (i.e.,  $\bar{\nabla}_\gamma^* W$ ,  $\nabla_\alpha^* \bar{W}$ ,  $\bar{\nabla}_\alpha^* \bar{W}$ , and  $\bar{\nabla}_\alpha^* \bar{W}$ ) are shown.

36 to 85 have channelized formations that are considered to be significantly more challenging for numerical simulations. The subset of this model is defined by the global Cartesian indices  $I, J, K$ . The 85 layer was used as a permeability field for 2D simulation with Cartesian indices  $I = 1 : 60$  and  $J = 1 : 60$ . In 3D, the subsection Cartesian indices  $I = 1 : 60$ ,  $J = 1 : 60$ , and  $K = 1 : 60$ . The permeability fields  $K^{11}$  for both cases are shown in Figure 4.12.

The boundary conditions correspond to the unit pressure drop over the entire domain in  $J$ -direction (i.e.,  $y_{min} = 0$  and  $y_{max} = 1$ ). The numerical results using new scheme for the SPE10 cases are presented in Figure 4.13. The relative error distribution is also shown for 2D and 3D cases, where the error is computed using (4.81) and numerical solution based on TPFA. Figures 4.14 and 4.15 compare the convergence rates of the various discretizations subject to different preconditioners. Furthermore, if we notice the convergence comparison for this test in Figures 4.14 and 4.15, the proposed new method offers similar convergence as compared to the Schwaiger’s scheme (4.29)–(4.32)). The reason for such convergence is the similarity between condition numbers of the linear system of equations resulting from these methods.

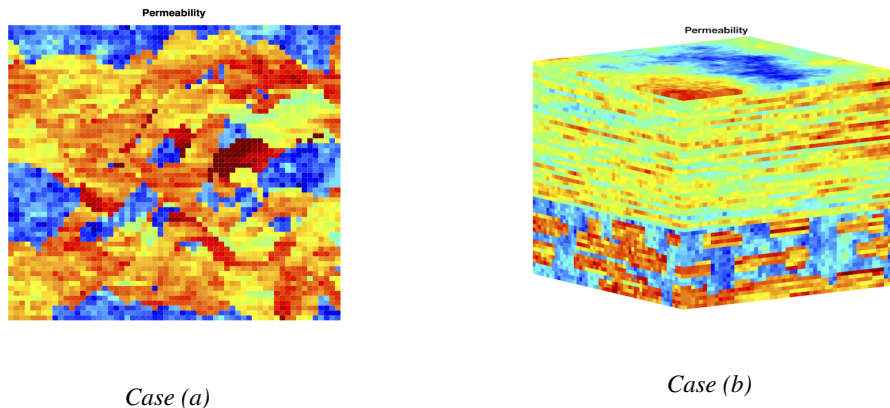
Another interesting observation in this numerical test is the small values of the relative error between the TPFA solution and proposed new method for both 2D and 3D cases. This observation exhibits the efficiency of the proposed meshless discretization scheme, which explains the higher accuracy of linear reproduction.

## §4.7 Conclusion

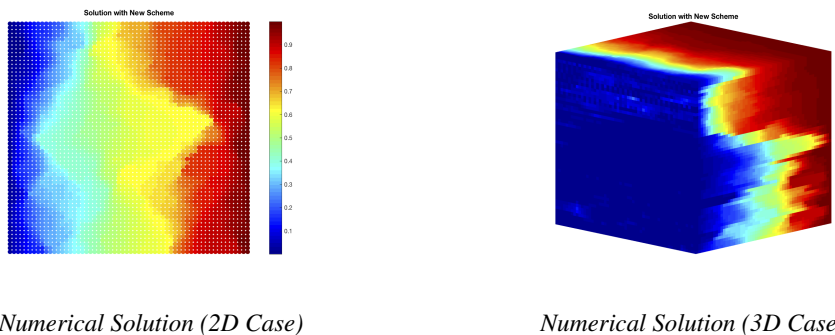
In this chapter, the new stable SPH discretization of the elliptic operator for heterogeneous media is proposed. The scheme has the two-point flux approximation nature and can be written in the form of (4.2). Using this structure, it was possible to make some theoretical monotonicity analysis, which is difficult to perform for other schemes (e.g., Schwaiger’s method). The paper also discusses the monotonicity and convergence properties of the new proposed scheme. The sufficient monotonicity condition is also formulated leading to the constraint on the kernel shape and particles distribution (see, Lemma 4.19 and Theorem 4.20). Furthermore, it follows from the Taylor’s series analysis that proposed scheme is the optimum one in this class (4.2) for a diagonal matrix of the operator coefficients. In addition, the proposed scheme allows to apply upwinding strategy during the solution of nonlinear PDEs.

The new scheme is based on a gradient approximation commonly used in thermal, viscous, and pressure

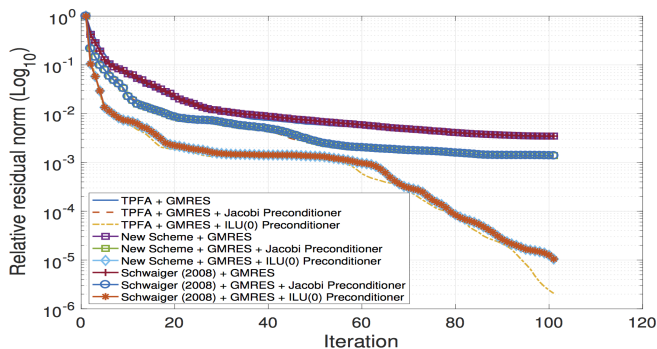




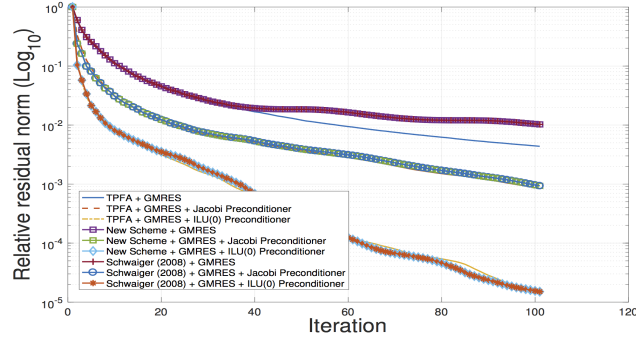
**Figure 4.12:** The lognormal permeability field in the SPE10 benchmark test. Case (a)  $60 \times 60$  cells of 85 layer. Case (b) subsection of the SPE10 model defined by  $60 \times 60 \times 60$  cells.



**Figure 4.13:** Numerical solution obtained with the new scheme for the SPE10 cases. The relative error distribution is also shown for 2D and 3D cases, where error is computed using (4.81) and numerical solution based on TPFA. The maximum relative errors in 2D and 3D are 0.07% and 0.4%, respectively



**Figure 4.14:** Comparison of the convergence rate of the GMRES iterative method with and without preconditioner for different numerical discretization methods (TPFA, New Scheme (4.44)–(4.46), Schwaiger (4.29)–(4.32)). The linear system of equations is built using 2D case.



**Figure 4.15:** Comparison of the convergence rate of the GMRES iterative method with and without preconditioner for different numerical discretization methods (TPFA, New Scheme (4.44)–(4.46), Schwaiger (4.29)–(4.32)). The linear system of equations is built using 3D case.

projection problems and can be extended to include higher-order terms in the appropriate Taylor series. The proposed new scheme is combined with mixed corrections which ensure linear completeness. The mixed correction utilizes Shepard Functions in combination with a correction to derivative approximations. Incompleteness of the kernel support combined with the lack of consistency of the kernel interpolation in conventional meshless method results in fuzzy boundaries. In the presented meshless method, the domain boundary conditions and internal field variables are approximated with the default accuracy of the method. The resulting new scheme offers a higher order of accuracy, but also minimize the impact of the particle deficiency (kernel support incompleteness) problem. Furthermore, different kernel gradients and their impact on the property of the scheme and accuracy are discussed. The model was tested by solving an inhomogeneous Dirichlet and mixed boundary value problems for the Laplacian equation with good accuracy confirming our theoretical results. The accuracy of Schwaiger’s scheme and new scheme is the same for homogeneous particle distribution and different for the distorted particles. The stability analysis shows that von Neumann growth factor has both real and imaginary parts forming complex shape for general particle distribution but satisfying the stability requirement almost everywhere.

As was previously mentioned in the introduction, several methods have been proposed to address the difficulties involved in calculating second-order derivatives with SPH. In contrast to the present formulation, many of these methods achieve a high accuracy through fully calculating the Hessian or requiring that the discrete equations exactly reproduce quadratic functions. The primary attraction of the present method is that it provides a weak formulation for Darcy’s law which can be of use in further development of meshless methods. The SPH model was previously used to model three-dimensional miscible flow and transport in porous media with complex geometry, and we are planning to use this model in future work for large (field) scale simulation of transport in porous media with general permeability distributions.

---

## MESHLESS RELAXED MULTISCALE METHODS

---

**P**RECONDITIONING can be used to damp slowly varying error modes in the linear solver residuals, corresponding to extreme eigenvalues. Existing multiscale solvers use a sequence of aggressive restriction, coarse-grid correction and prolongation operators to handle low-frequency modes on the coarse grid. High-frequency errors are then resolved by employing a smoother on fine grid. In reservoir simulations, the Jacobian system is usually solved by FGMRES method with two-level Constrained Pressure Residual (CPR) preconditioner. In this chapter, a parallel fully implicit smoothed particle hydrodynamics (SPH) based multiscale method for solving pressure system is presented. The prolongation and restriction operators in this method are based on a SPH gradient approximation (instead of solving localized flow problems) commonly used in the meshless community for thermal, viscous, and pressure projection problems. This method has been prototyped in a commercially available simulator. This method does not require a coarse partition and can be applied to general unstructured topology of the fine scale. The SPH based multiscale method provides a reasonably good approximation to the pressure system and speeds up the convergence when used as a preconditioner for an iterative fine-scale solver. In addition, it exhibits expected good scalability during parallel simulations. Numerical results are presented and discussed. <sup>1</sup>

### §5.1 Introduction

---

Academia and the corporate sectors are moving towards exascale simulations with highly complex properties of the underlying numerical domain (e.g., geology, fracture network, micro-inclusions), where it is required to

---

<sup>1</sup>This chapter is based on the following publications:

1. Cusini, M., **Lukyanov, A. A.**, Natvig, J. and Hajibeygi, H., *Constrained Pressure Residual Multiscale (CPR-MS) Method*, Journal Computational Physics, Volume 299, Issue C, 2015, PP. 472-486.
2. van der Linden, J., Jonsthovel, T. B., **Lukyanov, A. A.**, and Vuik, C., *The Parallel Subdomain-Levelset Deflation Method in Reservoir Simulation*, Journal Computational Physics, Volume 304, Issue C, 2016, PP. 340-358.
3. **Lukyanov, A. A.**, van der Linden, J., Jonsthovel, T. B. and Vuik, C., *Meshless Subdomain Deflation Vectors in the Preconditioned Krylov Subspace Iterative Solvers*, ECMOR XIV - 14th European Conference on the Mathematics of Oil Recovery, 10.3997/2214-4609.20141773.
4. **Lukyanov, A. A.**, Vuik, C., *Parallel Fully Implicit Smoothed Particle Hydrodynamics Based Multiscale Method*, ECMOR XV - 15th European Conference on the Mathematics of Oil Recovery.

compute an accurate solution with the reasonable time. Hence, current computational problems deal with the high resolutions simulations, which contain billions of degrees of freedom (i.e., unknowns). Existing modern computational resources stimulate the development of novel solver techniques tailored to these problems. At the same time, specialized parallel and multicore architectures have driven the implementation of these new methods with unprecedented performance expectations.

### 5.1.1 Commercial reservoir simulators

Commercial reservoir simulators usually uses the Newton-Raphson method to solve the non-linear governing equations for a given timestep. The corresponding Jacobian matrix and linear system are solved by the Flexible Generalized Minimum Residual Method (FGMRES) (see, Saad and Schultz, 1986 [234]) preconditioned by the Constrained Pressure Residual (CPR) preconditioner (see, e.g., Wallis (1983,1985) [271], [272], Cao *et al.* (2005) [48]). CPR decouples the linear system into two sets of equations, exploiting the specific properties of the pressure equation and transport equations. The former is solved with an Algebraic Multigrid (AMG) preconditioner (see, Ruge (1987) [232]), while the fully coupled system is solved using an ILU( $k$ ) type preconditioner.

A global linearization process results in sparse large linear systems of equations in the following form:

$$\mathbf{A}x = b \text{ or } \begin{bmatrix} \mathbf{A}_{pp} & \mathbf{A}_{ps} \\ \mathbf{A}_{sp} & \mathbf{A}_{ss} \end{bmatrix} \begin{bmatrix} x_p \\ x_s \end{bmatrix} = \begin{bmatrix} b_p \\ b_s \end{bmatrix} \quad (5.1)$$

where  $\mathbf{A}_{pp}$  represents the pressure block coefficients,  $\mathbf{A}_{ss}$  represents the non-pressure block coefficients,  $\mathbf{A}_{ps}$  and  $\mathbf{A}_{sp}$  represent the respective coupling coefficients,  $x_p$  is associated with the pressure (primary) variables,  $x_s$  is associated with the other (secondary) variables. By solving the parabolic part of the system (or elliptic for incompressible flow) as a separate inner stage of the CPR method, this results in an improved overall convergence rate for the fully coupled linear system. This requires to form an approximation of the pressure equations. The pressure equation is constructed by an IMPES-like reduction of the equation (5.1) where both sides of (5.1) are multiplied by a matrix of the form:

$$\mathbf{M}_1 = \begin{bmatrix} \mathbf{I} & -\mathbf{Q} \\ \mathbf{0} & \mathbf{I} \end{bmatrix} \quad (5.2)$$

where

$$\mathbf{Q} = \mathbf{A}_{ps}\mathbf{A}_{ss}^{-1} \approx \text{colsum}(\mathbf{A}_{ps}) \cdot \text{colsum}(\mathbf{A}_{ss})^{-1} \quad (5.3)$$

The pressure system can be extracted as follows

$$\mathbf{A}_{pp}^* \Delta x_p \approx b_p^*, \quad \mathbf{A}_{pp}^* = \mathbf{C}^T \mathbf{M}_1 \mathbf{A} \mathbf{C}, \quad \mathbf{C}^T = [\mathbf{I} \quad \mathbf{0}] \quad (5.4)$$

The robustness of CPR method depends on the quality of the pressure matrix  $\mathbf{A}_{pp}^* = \mathbf{C}^T \mathbf{M}_1 \mathbf{A} \mathbf{C}$ . Several methods can be used that produce  $\mathbf{A}_{pp}^*$ : (a) Quasi-IMPES (b) True-IMPES. Equation (5.4) is the pressure equation. It forms an approximation of the parabolic (or elliptic for incompressible flow) part of the discrete operator and is considered separately from the remaining hyperbolic part. The entire process for a given time step is schematically illustrated by the pseudocode 1 and it was shown to be extremely robust in terms of algorithmic efficiency (see, Cao *et al.*, 2005 [48]).

However, there are still challenges to overcome in implementing a near-ideal scalable AMG solver (i.e., compute of  $(\mathbf{A}_{pp}^*)^{-1}$ ). Also, the second stage of CPR preconditioning often includes some variant of an incomplete LU factorization (i.e., compute of the matrix  $\mathbf{M}_2$  in the pseudocode 1), which again is non-trivial to parallelize. As a result, the linear solver is still far from near-ideal scalability. To overcome this problem, the deflation AMG solvers for highly ill-conditioned reservoir simulation problems were considered (see, Klie *et al.*, 2007 [143]). However, the manual construction of the deflation vectors is time consuming and will most likely lead to sub-optimal results.

---

**Algorithm 1** Right-Preconditioned two stage CPR-GMRES

---

```

1: Setup  $x_0$  (e.g.,  $x_0 = 0$ )
2: Compute  $r_0 = (b - \mathbf{A}x_0)$ ,  $\beta = \|r_0\|_2$ , and  $v_1 = r_0/\beta$ .
3: Compute  $\mathbf{A}_{pp}^* = \mathbf{C}^T \mathbf{M}_1 \mathbf{A} \mathbf{C}$ 
4: for  $j = 1, 2, \dots, m$  do
5:    $w_j = \mathbf{A} \left[ \mathbf{M}_2^{-1} \left( \mathbf{I} - \mathbf{A} \mathbf{C} (\mathbf{A}_{pp}^*)^{-1} \mathbf{C}^T \mathbf{M}_1 \right) + \mathbf{C} (\mathbf{A}_{pp}^*)^{-1} \mathbf{C}^T \mathbf{M}_1 \right] v_j$ 
6:   for  $i = 1, \dots, j$  do
7:      $h_{i,j} = (w_j, v_i)$ 
8:      $w_j = w_j - h_{i,j} v_i$ 
9:   end for
10:   $h_{j+1,j} = \|w_j\|_2$ 
11:  if  $h_{j+1,j} = 0$  or converged then
12:    set  $m = j$  and go to 16
13:  end if
14:   $v_{j+1} = w_j/h_{j+1,j}$ 
15: end for
16: Fill  $\bar{H}_m = \{h_{i,j}\}$  for  $1 \leq i \leq m+1, 1 \leq j \leq m$ .
17: Compute the minimizer  $u_m$  of  $\|\beta e_1 - \bar{H}_m u\|_2$  and set  $x_m = x_0 + \mathbf{M}_2^{-1} \mathbf{V}_m u_m$ .
18: if converged then return else set  $x_0 = x_m$  and go to 2

```

---

### 5.1.2 Existing Solution Strategies

To improve the AMG robustness, Klie *et al.* (2007) [143] tried to consider deflation AMG solvers for highly ill-conditioned reservoir simulation problems. However, the manual construction of the deflation vectors is a time consuming process and will most likely lead to sub-optimal results (see, van der Linden *et al.*, 2015 [260]). However, the deflation strategy (which has a lower algebraic complexity and is inexpensive to set up) may lead to a robust alternative of AMG in general. Furthermore, the deflation strategy also (strongly) scalable which can be combined with the robust preconditioners. Deflation was first proposed for symmetric systems and the CG method by Nicolaidis (1987) [221] and Dostal (1988) [81]. Both construct a deflation subspace consisting of deflation vectors to deflate problematic eigenvalues from the linear system. A plethora of widely used deflation algorithms have been developed since, differing primarily in the application of the deflation operator (e.g. as a preconditioner or projection preconditioner) and the method to construct the deflation vectors (see, Frank and Vuik, 2001 [91]; Vuik *et al.*, 2002 [270]; Tang and Vuik, 2007 [249], [250], [247]; Jonsthoel *et al.* (2009,2011) [122], [121]; van der Linden, 2015 [260]).

Also, as alternative to AMG solver for the pressure system, two-level multiscale solvers (MS) have received considerable attention in the literature over the past decades (see, e.g., Hou and Wu, 1997 [110]; Jenny *et al.*, 2003 [115]; Lunati and Jenny, 2006 [192]; Hajibeygi *et al.*, 2008 [105]; Efendiev and Hou, 2009 [87]; Lunati *et al.*, 2011 [193]; Zhou and Tchelep, 2012 [281]; Cortinovis and Jenny, 2014 [71]; Wang *et al.*, 2014 [273]; Cusini *et al.*, 2015 [74]; Moyner and Lie, 2016 [214]).

Existing multiscale solvers use a sequence of aggressive restriction, coarse-grid correction and prolongation operators to handle low-frequency modes on the coarse grid. High-frequency errors are then resolved by employing a smoother on the fine grid, which could be expensive if large number of smoothing iterations is required in the Newton-Raphson step. This is usually the case when multiscale solvers are used as a linear solver with a very small tolerance. However, both AMG and MS methods are used incompletely, i.e. 1 V cycle of AMG and one step of MS. In all cases, the goal is to construct a relatively good approximate pressure solution before computing remaining variables and applying a second stage preconditioner.

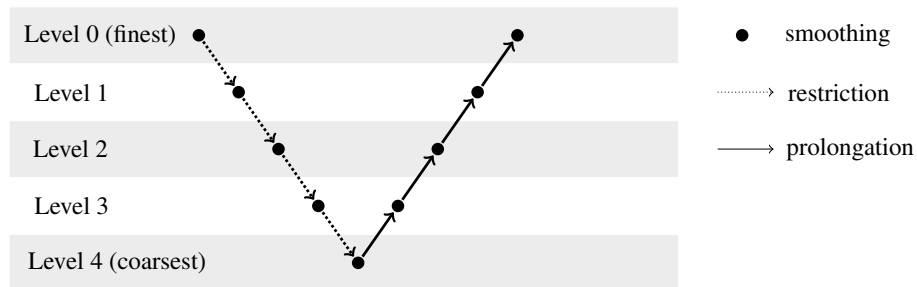
The multiscale solvers seem to be naturally scalable and can be used as a preconditioner. However, usage of the smoothers on the fine grid and solution of the coarse system form a bottleneck in constructing embarrassingly parallel algorithm. Hence, to reduce the impact of the smoothers on the fine grid, the quality of the pressure solution after one step of MS should be of acceptable accuracy. Furthermore, the combination of a multiscale solver and the deflation method can also be constructed to improve the quality of the pressure solution.

### 5.1.3 Multiscale, Multilevel, Multigrid and Deflation Methods

There are a number of common and fundamental features in currently used state-of-the-art methods. Given the fine-scale system of the governing equations, (two-level and multi-level) multiscale, multilevel, (algebraic and geometric) multigrid and deflation solvers construct a coarse-scale system by applying (one or several depending on the number of coarsing levels) restriction  $\mathbf{R}$  and prolongation  $\mathbf{P}$  operators, solve the solution at coarse level, and then prolong (interpolate) it back to the original fine-scale system by using (one or several depending on the number of coarsing levels) prolongation operators  $\mathbf{P}$ . This can be applied a pre-defined number of times as

$$\mathbf{A}^{k+1} = \mathbf{R}^k \mathbf{A}^k \mathbf{P}^k \quad (5.5)$$

where  $k$  is the level of the appropriate step of multiscale, multilevel, multigrid, and deflation methods,  $\mathbf{A}^{k+1}$  is the matrix on the next level (for the pressure system),  $\mathbf{R}^k$ ,  $\mathbf{P}^k$  are the restriction and prolongation operators at the level  $k$ . Hence, the level  $k$  has a different meaning depending on the selected method. For example, for deflation method this corresponds to a different deflated eigenspace. Typical V-cycle scheme of five levels for (multilevel-) multiscale, multigrid, and multilevel deflated method is shown in Figure 5.1.



**Figure 5.1:** Typical V-cycle scheme of five levels for (multilevel-) multiscale, multigrid, and multilevel deflated method.

Naturally, some generalization (multilevel-) multiscale, multigrid, and multilevel deflated method can be constructed using a  $W$ -cycle. It is obvious how this works in case of (multilevel-) multiscale and multigrid methods. The non-trivial multilevel deflated method can be constructed as follows. Let  $\mathbf{A}^k \in \mathbb{R}^{n \times n}$  be the non-symmetric linear system matrix at the level  $k$ . Then we define the matrix at the next level (coarse matrix). Similar to the (multilevel-) multiscale, multigrid methods, the matrix  $\mathbf{A}^{k+1} \in \mathbb{R}^{d \times d}$  is defined using either Galerkin (note that non-Galerkin projection can also be applied, see Falgout and Schroeder (2014) [89]) as

$$\mathbf{A}^{k+1} = \mathbf{R}^k \mathbf{A}^k \mathbf{P}^k, \quad (5.6)$$

and the deflation matrices at the level  $k$  (i.e.,  $\mathbf{D}_1^k$  and  $\mathbf{D}_2^k$ ) are defined as

$$\begin{aligned} \mathbf{D}_1^k &= \mathbf{I} - \mathbf{A}^k \mathbf{P}^k (\mathbf{A}^{k+1})^{-1} \mathbf{R}^k, \\ \mathbf{D}_2^k &= \mathbf{I} - \mathbf{P}^k (\mathbf{A}^{k+1})^{-1} \mathbf{R}^k \mathbf{A}^k. \end{aligned} \quad (5.7)$$

where  $\mathbf{A}^1 = \mathbf{A}$  is the original fine scale matrix. The  $(\mathbf{A}^{k+1})^{-1}$  is constructed to avoid a direct inversion of the matrix and expensive matrix-matrix product in the expression  $(\mathbf{A}^{k+1})^{-1} \mathbf{R}^k$ . This is achieved by doing an user defined number pre- and a post-smoothing (e.g., Gauss-Seidel (GS) or ILU(0)) steps similar to Multigrid Solver (see, Lukyanov *et al.*, 2014 [190]). Finally, the solution to the original linear system can be found using the relation:

$$x = \sum_{i=1}^k \mathbf{P}^i (\mathbf{A}^{i+1})^{-1} (\mathbf{R}^i)^\top b + \prod_{i=1}^k \mathbf{D}_2^i \hat{x} \quad (5.8)$$

where  $\hat{x}$  is a solution of the 'deflated system':

$$\prod_{i=1}^k \mathbf{D}_1^i \mathbf{A} \hat{x} = \prod_{i=1}^k \mathbf{D}_1^i b \quad (5.9)$$

The prolongation  $\mathbf{P}^i$  and restriction  $\mathbf{R}^i$  operators in deflation method are defined using the deflation matrix,  $\mathbf{Z}^i$  (by no limiting example) as follows

$$\mathbf{P}^i = \mathbf{Z}^i, \mathbf{R}^i = (\mathbf{Z}^i)^\top \quad (5.10)$$

where  $\mathbf{Z}^i$  is the the deflation matrix between levels  $i$  and  $i + 1$ . Let us recall that the prolongation operator  $\mathbf{P}$  in multiscale methods such as the multiscale finite element (MSFE) and multiscale finite volume (MSFV) are constructed based on local solutions (basis functions) of the fine-scale problem with different boundary conditions. The local support for the basis functions are obtained by first imposing a coarse grid ( $\check{\Omega}_k$ ) on the given fine-grid cells. The coarse grid operator is then constructed using Galerkin condition (5.5). The restriction operator, i.e., mapping fine scale to coarse scale, can be obtained by using either a finite element (MSFE) or finite volume (MSFV) methods as per terminology of the reservoir simulation community. The former employs a transpose of the prolongation operator, i.e.,

$$\mathbf{R}_{\text{FE}} = \mathbf{P}^\top, \quad (5.11)$$

There is a clear similarity in constructing a coarse system between multiscale (MSFE, MSFV) and deflation method. The high-frequency errors at the fine scale in multiscale (MSFE, MSFV) are then resolved by employing a smoother on the fine grid. The equivalent step in a deflation method is the solution of the 'deflated system' defined by the equation (5.9). It is clear that the direct solution step of the 'deflated system' can be substituted by performing smoothing iterations using either the original matrix  $\mathbf{A}$  or deflated matrix  $(\prod_{i=1}^k \mathbf{D}_1^k \mathbf{A})$ . Hence, the primary difference between (two-level or multi-level) multiscale and (two-level or multi-level) deflation method is the selection of the restriction and prolongation operators. Multiscale methods have been developed to describe local heterogeneities within the sub-domains in the coarse system by using purely locally-supported basis functions. The deflation methods use a different strategy in constructing the restriction and prolongation operators based on the detailed analysis of the underlying spectrum of the preconditioned matrix.

In recent years, the multiscale restriction smoothed basis (MsRSB) method was introduced (see, Moyner and Lie, 2016 [214]) to overcome the geological complexities and the use of complex grid geometries required to compute the underlying basis functions. Below, it will be shown that the basis functions employed by MsRSB method have been extensively used in the deflation methods for various applications, see Tang and Vuik (2007) [247], [249], [250], Frank and Vuik (2001) [91], Vuik *et al.* [270], van der Linden *et al.* (2015) [260].

## § 5.2 Multiscale Restriction vs. Deflation

Preconditioning can be used to damp slowly varying error modes in the linear solver residuals, often corresponding to extreme eigenvalues. Existing multiscale solvers use a sequence of aggressive restriction, coarse-grid correction and prolongation operators to handle low-frequency modes on the coarse grid. High-frequency errors are then resolved by employing a smoother on fine grid. Below, the deflation theory is briefly described, which will be used to contract various preconditioners.

### 5.2.1 Deflation Theory

It has been noticed in different applications by Barnard *et al.* (1967) [21], Rahola and Tissari (2002) [229], Dolean *et al.* (2014) [80], Tang and Vuik (2007) [247], Vuik *et al.* (1999, 2001) [268], [269] that a deflation method greatly facilitates the iterative solution of the problem and overcome the divergence issues. The deflation methods for symmetric positive definite problems is comprehensively described in Tang and Vuik(2007) [247], [250]. In this paper, the basic properties of the deflation method for the non-symmetric and non-singular case are presented. For more details, the following papers by Frank and Vuik (2001) [91], Vuik *et al.* (2002) [270] can be used. Let us assume that the information about slow modes affecting convergence behavior is available for a system (5.4). For incompressible fluid flow in homogenous porous media or for homogeneous electromagnetic problems with Neumann boundary conditions, these slow model corresponds to constant vectors of the null space of the corresponding operator (e.g., Laplace operator). In this case, we can deflate this singularity (assuming that the sum of the solution vector is zero) by modifying the coefficient matrix as follows (Barnard *et al.*, 1967 [21]):

$$\mathbf{A} + \beta e e^\top \quad (5.12)$$

where  $e = 1/\sqrt{N}(1, 1, \dots, 1)^\top$  is the normalized vector of the null space. The deflation in this case has the effect that the zero eigenvalue is shifted to the value  $\beta$  and the rest of eigenvalues remain unchanged. In the rest of the thesis, we consider only non-singular matrix.

Let  $\mathbf{A} \in \mathbb{R}^{n \times n}$  be the non-singular and non-symmetric linear system matrix, and assume that the deflation matrix (deflation space)  $\mathbf{Z} \in \mathbb{R}^{n \times d}$  with  $d$  deflation vectors is given (we assume that  $\mathbf{Z}$  has a rank  $d$ ).

Following work of Dolean *et al.* (2014) [80], we can consider minimization problem for a general non-singular matrix  $\mathbf{A}$ :

$$\min_{\gamma} (y + \mathbf{Z}\gamma - \mathbf{A}^{-1}b)^{\top} (\mathbf{A}[y + \mathbf{Z}\gamma] - b), \quad (5.13)$$

where  $y$  is the approximate solution. This problem corresponds to finding the best correction  $\mathbf{Z}\gamma$  in the vector space spanned by the columns of  $\mathbf{Z}$  matrix to a given approximate solution. The solution to this problem is defined as

$$\gamma = [\mathbf{Z}^{\top} \mathbf{A} \mathbf{Z}]^{-1} \mathbf{Z}^{\top} (b - \mathbf{A}y) - \mathbf{Z}^{\top} \mathbf{A} (\mathbf{A}^{-1}b - y). \quad (5.14)$$

Hence, the corrected solution  $\tilde{x} = y + \mathbf{Z}\gamma$  is

$$\tilde{x} = (\mathbf{I} - \mathbf{Z}\mathbf{E}^{-1}\mathbf{Z}^{\top} \mathbf{A}) y + \mathbf{Z}\mathbf{Z}^{\top} \mathbf{A}^{\top} (y - x) + \mathbf{Z}\mathbf{E}^{-1}\mathbf{Z}^{\top} b \quad (5.15)$$

where  $x$  is the true solution and we define the matrix  $\mathbf{E} \in \mathbb{R}^{d \times d}$  as

$$\mathbf{E} = \mathbf{Z}^{\top} \mathbf{A} \mathbf{Z}, \quad (5.16)$$

In a limiting case when  $\tilde{x} = y = x$ , we arrive to the following identity

$$x = (\mathbf{I} - \mathbf{Z}\mathbf{E}^{-1}\mathbf{Z}^{\top} \mathbf{A}) x + \mathbf{Z}\mathbf{E}^{-1}\mathbf{Z}^{\top} b = (\mathbf{I} - \mathbf{P}_1)x + \mathbf{P}_1 x \quad (5.17)$$

where we introduce a first deflation matrix  $\mathbf{P}_1$  as follows

$$\mathbf{P}_1 = \mathbf{I} - \mathbf{Z}\mathbf{E}^{-1}\mathbf{Z}^{\top} \mathbf{A}. \quad (5.18)$$

Here we used the fact that  $(\mathbf{I} - \mathbf{P}_1)x = \mathbf{Z}\mathbf{E}^{-1}\mathbf{Z}^{\top} \mathbf{A} x = \mathbf{Z}\mathbf{E}^{-1}\mathbf{Z}^{\top} b$ , which eliminates dependency on  $x$ . It is important to note that deflation method requires inversion of the matrix  $\mathbf{E}$ . This should be relatively cheap other wise this method will be very slow. This condition can be achieved if (1) we have a case  $d \ll n$  or (2) we can pre-compute the factorization of the matrix  $\mathbf{E}$  which can be used in multiple solutions with different right hand sides. We will comeback to this condition during the numerical modeling. Considering another limiting case when  $\mathbf{A}\tilde{x} = b$  we can obtain using (5.15) the following condition

$$\mathbf{P}_2 b = \mathbf{P}_2 \mathbf{A} y + \mathbf{A} \mathbf{Z} \mathbf{Z}^{\top} \mathbf{A}^{\top} (y - x) \quad (5.19)$$

where we introduce a second deflation matrix  $\mathbf{P}_2$  as follows

$$\mathbf{P}_2 = \mathbf{I} - \mathbf{A} \mathbf{Z} \mathbf{E}^{-1} \mathbf{Z}^{\top}, \quad (5.20)$$

Furthermore, it can be easily shown that if  $y$  is a solution of the 'deflated system' as

$$\mathbf{P}_2 \mathbf{A} y = \mathbf{P}_1 b \quad (5.21)$$

then  $y = x$  assuming that the matrix  $\mathbf{A} \mathbf{Z} \mathbf{Z}^{\top} \mathbf{A}^{\top}$  is non-singular. It is clear that 'deflated system' is singular since  $\mathbf{Z}$  is in the null space of  $\mathbf{P}_2 \mathbf{A}$ . It is not a problem since projection is applied to both sides of the nonsingular system. This problem has been discussed in details in (Frank and Vuik, 2001 [91]; Vuik *et al.*, 2002 [270]). Furthermore, we can always apply the method described in (5.12) to the 'deflated system' bringing this to a nonsingular matrix

$$\mathbf{P}_2 \mathbf{A} + \beta \mathbf{Z} \tilde{\mathbf{Z}}^{\top} \text{ or } \mathbf{P}_2 \mathbf{A} + \beta \mathbf{Z} \mathbf{Z}^{\top} \quad (5.22)$$

where  $\beta$  is the shifting parameter and  $\tilde{\mathbf{Z}}^{\top} = (\mathbf{Z}^{\top} \mathbf{Z})^{-1} \mathbf{Z}^{\top}$ ,  $\tilde{\mathbf{Z}}^{\top} \mathbf{Z} = \mathbf{I}$ . Although, these corrections do not give significant impact on Krylov subspace iterative solvers. In conclusion, the solution to the original linear system can be approximated using the relation once the 'deflated system' system (5.21) is accurately solved as follows:

$$\tilde{x} = \mathbf{Z}\mathbf{E}^{-1}\mathbf{Z}^{\top} b + \mathbf{P}_2 y \quad (5.23)$$

This idea has been exploited in several papers. We have not yet defined the deflation subspace. Some attempts to construct a deflation subspace *a priori* that effectively represents the slowest modes have been made in the past (Mansfield, 1990 [194]; Mansfield, 1991 [195]; Nicolaidis, 1987 [221]; Tang and Vuik, 2007 [247]; Frank and Vuik, 2001 [91]; Vuik, 2002 [270]).



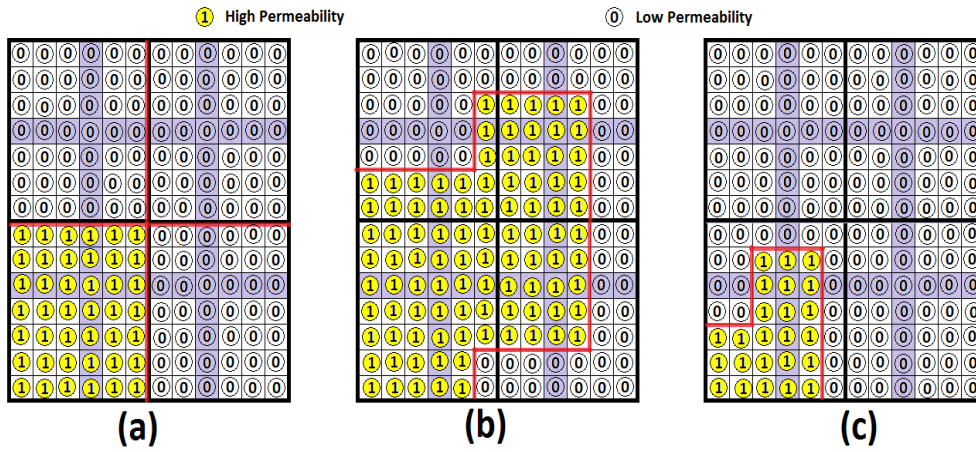


Figure 5.2: Subdomain (a), levelset (b) and subdomain-levelset deflation (c).

### 5.2.2 Multiscale Restriction Smoothed Basis and Deflation Vectors

In both methods (i.e., MsRSB and Deflation), the discretized computational domain  $\Omega$  is first decomposed into  $d$  non-overlapping subdomains  $\bar{\Omega}_j$  with  $j \in \{1, \dots, d\}$ . The deflation vector  $\bar{Z}_j$  forms  $j$ -th column of the deflation operator  $\mathbf{Z}$  or initial basis functions  $\mathcal{P}_j^0$  of MsRSB method, corresponding to  $\bar{\Omega}_j$  and it is defined as (see, Frank and Vuik, 2001 [91]; Tang, 2008 [248]; vanderLinden, 2015 [260]; Moyner and Lie, 2016 [214]; Shah *et al.*, 2016 [239])

$$(\mathcal{P}_j^0)_i = (\bar{Z}_j)_i = \begin{cases} 1, & x_i \in \bar{\Omega}_j \\ 0, & x_i \in \Omega \setminus \bar{\Omega}_j, \end{cases} \quad (5.24)$$

where  $x_j$  is a fine-scale grid cell center. Based on the above definition,  $\bar{Z}_j$  and  $\mathcal{P}_j^0$  are piecewise-constant vectors or functions (equal to a constant value of one inside the corresponding coarse domain  $\bar{\Omega}_j$ ), disjoint and orthogonal. For this choice of the deflation subspace, the deflation projectors  $\mathbf{P}_1$  and  $\mathbf{P}_2$  essentially agglomerate each subdomain in a single cell. Hence, the subdomain deflation and MsRSB are closely related to domain-decomposition methods and multigrid (see, Frank and Vuik, 2001 [91]). For problems in the bubbly flow, the span of the deflation vectors (5.24) approximates the span of the eigenvectors corresponding to the smallest eigenvalues (Tang and Vuik, 2007 [250]). In our case, as studied by Vuik *et al.* (2002) [270], the subdomains can be defined using the underlying heterogeneity, e.g., a low-permeable region can be separated from the high-permeable regions and form  $d$  decompositions. As it was noted in Vermolen *et al.* (2004) [264], it is better to use no overlap subdomains. This fact leads to the weighted overlap method, which mimics average and no overlap in the case of no contrasts and large contrasts, respectively. It is shown that the overlap is crucial in approximating the eigenvectors corresponding to the extreme eigenvalues.

In highly heterogeneous computational domain with large jumps in the permeability field, the subdomain-levelset deflation can be used (see, Tang and Vuik, 2007 [250]). In this case where subdomain deflation does not take jumps into account, the subdomain-levelset deflation identifies different regions in the domain with similar properties. A simple example is given in Figure 5.2. The fine grid is  $12 \times 14$  with the coarse grid  $2 \times 2$  are shown in Figure 5.2. In each case, the values shown on the fine cells correspond to the values in the first deflation vector. In the middle and right figure, the border between the yellow circles (high permeability) and white circles (low permeability) exemplifies a sharp contrast in the matrix coefficient. The figures show the following:

- In the left figure, subdomain deflation is used. The red solid line divides the domain into the four subdomains  $\bar{\Omega}_1, \bar{\Omega}_2, \bar{\Omega}_3$  and  $\bar{\Omega}_4$ . Each subdomain corresponds to a unique deflation vector.
- In the middle figure, levelset deflation is used. This time, the red solid line coincides with the contrast in the matrix coefficient. As a result, we get the two domains  $\bar{\Omega}_1$  and  $\bar{\Omega}_2$ .

- In the right figure, subdomain-levelset deflation is used. The subdomain division is determined using certain criteria, which in this example leads to the division red solid line between  $\bar{\Omega}_1$  and  $\bar{\Omega}_2$ . Within each subdomain, levelset deflation uses the jump between the high permeability and low permeability cells to obtain the subdomains  $\bar{\Omega}_1, \bar{\Omega}_2, \bar{\Omega}_3$  and  $\bar{\Omega}_4$ .

In this thesis, the subdomain-levelset deflation concept is used. We highlight the fact that the algorithm is particularly suitable for a parallel implementation. We can apply the levelset deflation method to each subdomain (coarse cells), and append the deflation vectors with zeros for all cells outside the neighboring subdomains. Furthermore, it is important to note that deflation vectors can be constructed based on the jump in the PVT data (e.g., bubbly flow considered in Tang and Vuik (2007) [250]). For example, during the polymer flooding the aqueous viscosity changes drastically in the presence of polymer. Hence, the deflation vectors can be constructed based on the location of the polymer within the reservoir.

Although we have identified a full analogy between deflated vectors  $\mathbf{Z}$  and initial basis functions  $\mathcal{P}_j^0$  of MsRSB method, the final restriction-smoothed basis functions are computed by employing a modified form of the damped-Jacobi smoothing approach:

$$\delta\mathcal{P}_k^\eta = -\omega\mathbf{D}^{-1}\mathbf{A}\mathcal{P}_k^\eta \quad (5.25)$$

where  $\mathbf{A}$  is the fine-scale matrix,  $\mathbf{D} = \text{diag}(\mathbf{A})$  is the diagonal part of the matrix  $\mathbf{A}$ . The final update for prolongation operator is defined as

$$\mathcal{P}_k^{\eta+1} = \mathcal{P}_k^\eta + \delta\hat{\mathcal{P}}_k^\eta \quad (5.26)$$

where  $\delta\hat{\mathcal{P}}_k^\eta$  is the restricted iterative increments (see, Moyner and Lie (2016) [214], Shah *et al.* [239]). To ensure that basis functions have local support, the increments  $\delta\mathcal{P}_k^\eta$  is restricted to have nonzero values only inside  $\Omega_k$  leading to the definition of the  $\delta\hat{\mathcal{P}}_k$ . Finally, the basis functions (5.25)-(5.26) of the MsRSB method can be written in the abstract form as:

$$\mathcal{P}_k = \mathbf{M}_{MsRSB}^{\frac{1}{2}}\mathcal{P}_k^0 \quad (5.27)$$

where  $\mathbf{M}_{MsRSB}^{\frac{1}{2}}$  is the predefined smoothing matrix of MsRSB method defined by (5.25)-(5.26) and restriction expression (see, Moyner and Lie (2016) [214], Shah *et al.* [239]).

#### Remarks

- The proposed method is similar to smoothed aggregation-based multigrid methods (see, Vanek (1992) [262]; Vanek *et al.* (1996) [263])
- A deflation technique applied to a preconditioned system with preconditioner  $\mathbf{M}^{-1}$  at different level  $k$

$$\begin{aligned} \tilde{\mathbf{D}}_1^k &= \mathbf{I} - \tilde{\mathbf{A}}^k \tilde{\mathbf{P}}^k \left( \tilde{\mathbf{A}}^{k+1} \right)^{-1} \tilde{\mathbf{R}}^k, \quad \tilde{\mathbf{D}}_2^k = \mathbf{I} - \tilde{\mathbf{P}}^k \left( \tilde{\mathbf{A}}^{k+1} \right)^{-1} \tilde{\mathbf{R}}^k \tilde{\mathbf{A}}^k, \\ \tilde{\mathbf{A}}^{i+1} &= \tilde{\mathbf{R}}^i \tilde{\mathbf{A}}^i \tilde{\mathbf{P}}^i, \quad \tilde{\mathbf{P}}^i = \tilde{\mathbf{Z}}^i, \quad \tilde{\mathbf{R}}^i = \left( \tilde{\mathbf{Z}}^i \right)^\top, \quad \mathbf{Z} = \mathbf{M}^{-\frac{1}{2}} \tilde{\mathbf{Z}} \end{aligned} \quad (5.28)$$

is equivalent to preconditioning of a deflated system

$$\begin{aligned} \prod_{i=1}^k \mathbf{D}_1^i \mathbf{M}^{-1} \mathbf{A} \hat{x} &= \prod_{i=1}^k \mathbf{D}_1^i \mathbf{M}^{-1} b, \\ x &= \sum_{i=1}^k \mathbf{P}^i \left( \hat{\mathbf{A}}^{i+1} \right)^{-1} \left( \mathbf{R}^i \right)^\top (\mathbf{M}^{-1} b) + \prod_{i=1}^k \mathbf{D}_2^i \hat{x} \end{aligned} \quad (5.29)$$

Here  $\hat{\mathbf{A}}^{i+1} = \prod_{l=1}^i \mathbf{R}^l (\mathbf{M}^{-1} \mathbf{A}) \mathbf{P}^l$ ,  $\hat{x}$  is a solution of the preconditioned 'deflated system'. The matrix  $\tilde{\mathbf{Z}}$  is interpreted as a preconditioned deflation-subspace matrix (see, [248] who formulated this for a two-level deflation method applied to symmetric positive definite matrix):

$$\tilde{\mathbf{Z}} = \mathbf{M}^{\frac{1}{2}} \mathbf{Z} \quad (5.30)$$

where  $\mathbf{M}$  is the specified preconditioner. Comparison of the equation (5.30) with the equation (5.27) and taking into account that  $\mathcal{P}_j^0 = \bar{Z}_j$  leads to the fact that two-level (preconditioned with the matrix  $\mathbf{M}_{MsRBS}^{\frac{1}{2}}$ ) deflation projection with the post smoothing used in MsRBS should give identical results with MsRBS. Commonly, the deflation matrix (matrix of basis functions)  $\mathbf{Z}$  is applied to preconditioned matrix  $\mathbf{M}^{-1}\mathbf{A}$  and, hence, the smoothing (5.30) is not applied since it is equivalent to have twice preconditioning of the matrix  $\mathbf{A}$ .

- Localization can be constructed using any partition of unity (PU) functions  $\{\varphi_i\}$  with  $\Omega_i = \text{supp}(\varphi_i)$  at any level  $k$  as follows

$$p = \sum_{i=1}^N \varphi_i p_i = \sum_{i=1}^N \left( \varphi_i p_{\text{smooth}}^i + \varphi_i p_{\text{jump}}^i + \varphi_i p_{\text{singular}}^i \right) \quad (5.31)$$

where  $p_{\text{smooth}}^i$  is the smooth part of the solution,  $p_{\text{singular}}^i$  is the part of the solution with singularity,  $p_{\text{jump}}^i$  is the part of the solution with the jumps, and functions  $\varphi_i$  play the role of “glue”.

### 5.2.3 Meshless Deflation Vectors

The meshless deflation vectors (basis functions) utilize some advantages of the existing multiscale schemes and meshless methods. In light of this, the meshless deflation vectors (basis functions) are constructed using two sets of computational points (see, Lukyanov *et al.* (2014) [190]):

1. Fine points set  $S_F$  (e.g., cell centers of underlying mesh) consisting of  $N_F$  patches, i.e.  $\Omega = \text{span} \{ \bar{\Omega}_{\mathbf{r}_I, \bar{h}} / I = 1, \dots, N_F \}$ , which are interior to the support of the kernel  $\bar{W}(\mathbf{r} - \mathbf{r}_I, \bar{h})$ , i.e.  $\Omega_{\mathbf{r}, \bar{h}} = \text{supp} \bar{W}(\mathbf{r} - \boldsymbol{\xi}, \bar{h})$ ,  $N_F$  is the number of points,  $h_F$  is the fine scale diameter (or smoothing length);
2. Coarse points set  $S_C$  (e.g., user defined points) consisting of  $N_C$  patches, i.e.  $\Omega = \text{span} \{ \tilde{\Omega}_{\mathbf{r}_J, h} / J = 1, \dots, N_C \}$ , which are interior to the support of the  $\bar{W}(\mathbf{r}_I - \mathbf{r}, h)$  kernel, i.e.  $\Omega_{\mathbf{r}, h} = \text{supp} \bar{W}(\mathbf{r} - \boldsymbol{\xi}, h)$ ,  $N_C < N_F$  is the number of points,  $h_C$  is the coarse scale diameter (or smoothing length);

In both cases (fine and coarse), the same cubic spline for kernel function  $\bar{W}$  was used (see, Lukyanov *et al.* (2014) [190]). Following the conventional multiscale approach, the approximation of the fine scale pressure distribution  $p_F$  using coarse set values  $p_C$  is constructed as

$$p_F(\mathbf{r}) \approx \sum_{J=1}^{N_C} V_{\boldsymbol{\xi}_J} \cdot \bar{W}(\mathbf{r} - \boldsymbol{\xi}_J, h_C) \cdot p_C(\boldsymbol{\xi}_J) \quad (5.32)$$

or

$$p_F(\mathbf{r}_I) \approx \mathbf{r}_I \cdot \left( \sum_{J=1}^{N_C} V_{\boldsymbol{\xi}_J} \cdot \bar{W}(\mathbf{r}_I - \boldsymbol{\xi}_J, h_C) \mathbf{C}_1(\boldsymbol{\xi}_J) \right) + \sum_{J=1}^{N_C} [V_{\boldsymbol{\xi}_J} \cdot \bar{W}(\mathbf{r}_I - \boldsymbol{\xi}_J, h_C) \cdot \mathbf{C}_2(\boldsymbol{\xi}_J)] \quad (5.33)$$

where

$$\mathbf{C}_1(\boldsymbol{\xi}_J) = \left[ \sum_{K=1}^{N_C} V_{\boldsymbol{\xi}_K} [p_C(\boldsymbol{\xi}_K) - p_C(\boldsymbol{\xi}_J)] \nabla^* \bar{W}(\boldsymbol{\xi}_J - \boldsymbol{\xi}_K, h_C) \right] \quad (5.34)$$

$$\mathbf{C}_2(\boldsymbol{\xi}_J) = [p_C(\boldsymbol{\xi}_J) - \boldsymbol{\xi}_J \cdot \mathbf{C}_1(\boldsymbol{\xi}_J)]$$

The scheme (5.33) provides a first-order consistent prolongation from a coarse set of particles into a fine set of particles, i.e. it provides an exact solution for a linear pressure distribution at both scales. In case where coarse level points do not form a subset of fine level points, the aggressive restriction is also applied following relations (zero and first-order consistent operators) such as:

$$p_C(\mathbf{X}) \approx \sum_{J=1}^{N_F} V_{\boldsymbol{\xi}_J} \cdot \bar{W}(\mathbf{X} - \boldsymbol{\xi}_J, h_F) \cdot p_F(\boldsymbol{\xi}_J) \quad (5.35)$$

or

$$\begin{aligned}
p_C(\mathbf{r}_I) &\approx \mathbf{r}_I \cdot \left( \sum_{J=1}^{N_F} V_{\xi_J} \cdot \bar{W}(\mathbf{X}_I - \xi_J, h_F) \mathbf{G}_1(\xi_J) \right) + \\
&+ \sum_{J=1}^{N_F} [V_{\xi_J} \cdot \bar{W}(\mathbf{r}_I - \xi_J, h_F) \cdot (p_F(\xi_J) - \xi_J \cdot \mathbf{G}_2(\xi_J))]
\end{aligned} \tag{5.36}$$

where

$$\begin{aligned}
\mathbf{G}_1(\xi_J) &= \left[ \sum_{K=1}^{N_F} [p_F(\xi_K) - p_F(\xi_J)] \nabla^* \bar{W}(\xi_J - \xi_K, h_F) \right] \\
\mathbf{G}_2(\xi_J) &= [p_F(\xi_J) - \xi_J \cdot \mathbf{G}_1(\xi_J)]
\end{aligned} \tag{5.37}$$

It is important to note that relations (5.32), (5.33), (5.35), (5.36) can be written using matrix notation:

$$\begin{aligned}
\mathbf{u}_F &= \bar{\mathbf{W}}^P \cdot \mathbf{u}_C, \quad \bar{\mathbf{W}}^P : S_C \rightarrow S_F, \quad \mathbf{u}_C = \bar{\mathbf{W}}^R \cdot \mathbf{u}_F, \quad \bar{\mathbf{W}}^R : S_F \rightarrow S_C \\
\widetilde{\mathbf{W}}^R &= B_W^{-1} \bar{\mathbf{W}}^R, \quad B_W = \bar{\mathbf{W}}^R \bar{\mathbf{W}}^P, \quad \widetilde{\mathbf{W}}^R \bar{\mathbf{W}}^P = \mathbf{I}, \quad \widetilde{\mathbf{W}}^R : S_F \rightarrow S_C \\
\widetilde{\mathbf{W}}^P &= \bar{\mathbf{W}}^P B_W^{-1}, \quad B_W = \bar{\mathbf{W}}^R \bar{\mathbf{W}}^P, \quad \bar{\mathbf{W}}^R \widetilde{\mathbf{W}}^P = \mathbf{I}, \quad \widetilde{\mathbf{W}}^P : S_C \rightarrow S_F
\end{aligned} \tag{5.38}$$

where  $\bar{\mathbf{W}}^P$  and  $\widetilde{\mathbf{W}}^P$  are the prolongation operators,  $\bar{\mathbf{W}}^R$  and  $\widetilde{\mathbf{W}}^R$  are the restriction operators. In general, it is clear that  $\bar{\mathbf{W}}^R \neq (\bar{\mathbf{W}}^P)^T$ . As a result, the following options are available to construct deflation vectors for restriction and prolongation operators:

$$\begin{aligned}
(I) \quad \mathbf{P} &= \bar{\mathbf{W}}^P, \quad \mathbf{R} = (\bar{\mathbf{W}}^P)^T, \quad (II) \quad \mathbf{P} = \widetilde{\mathbf{W}}^P, \quad \mathbf{R} = \left( \widetilde{\mathbf{W}}^P \right)^T \\
(III) \quad \mathbf{P} &= \bar{\mathbf{W}}^P, \quad \mathbf{R} = \bar{\mathbf{W}}^R, \quad (IV) \quad \mathbf{P} = \bar{\mathbf{W}}^P, \quad \mathbf{R} = \widetilde{\mathbf{W}}^R, \quad (V) \quad \mathbf{P} = \widetilde{\mathbf{W}}^P, \quad \mathbf{R} = \bar{\mathbf{W}}^R \\
(VI) \quad \mathbf{P} &= (\bar{\mathbf{W}}^R)^T, \quad \mathbf{R} = \bar{\mathbf{W}}^R, \quad (VII) \quad \mathbf{P} = \left( \widetilde{\mathbf{W}}^R \right)^T, \quad \mathbf{R} = \widetilde{\mathbf{W}}^R
\end{aligned}$$

The option (I) is used in this thesis. The prolongation and restriction operators in this method are based on an SPH gradient approximation (instead of solving localized flow problems) commonly used in the meshless community for thermal, viscous, and pressure projection problems. Furthermore, the smoothing length  $h_C$  can be selected to maintain only the host particle in the compact support resulting in the basis functions defined by the equation (5.24). Hence, the meshless basis functions provide a more flexible framework for constructing deflation vectors (or basis functions).

Finally, the deflation vector  $Z_j$ , column  $j$ -th of  $\mathbf{Z}$ , corresponding to  $\bar{\Omega}_j$  is defined as

$$(Z_j)_i = \begin{cases} D_{ij}, & \mathbf{X}_i \in \bar{\Omega}_j, \quad \xi_J \in \bar{\Omega}_j \\ 0, & x_i \in \Omega \setminus \bar{\Omega}_j, \end{cases} \tag{5.39}$$

where  $\mathbf{X}_i$  is a fine-scale grid cell and  $\xi_J$  is the coarse point. As a result, the following options are available to construct deflation vectors in each subdomains  $\bar{\Omega}_j$  with  $j \in \{1, \dots, p\}$ :

$$\begin{aligned}
(I) \quad D_{ij} &= \mathbf{W}_{ij}^P, \quad i = 1, \dots, N_F; j = 1, \dots, N_C; \\
(II) \quad D_{ij} &= \mathbf{W}_{ji}^R, \quad i = 1, \dots, N_F; j = 1, \dots, N_C; \\
(III) \quad D_{ij} &= \widetilde{\mathbf{W}}_{ji}^R, \quad i = 1, \dots, N_F; j = 1, \dots, N_C; \\
(IV) \quad \mathbf{A}_C S_j &= \theta_j S_j; \quad Z_j = \mathbf{W}^P S_j, \quad \mathbf{A}_C = \widetilde{\mathbf{W}}^R \mathbf{A} \mathbf{W}^P; \\
(V) \quad \left( \widetilde{\mathbf{W}}^R \mathbf{A}^T \right) &(\mathbf{A} z_j - \gamma_j z_j) = 0; \quad z_j = \mathbf{W}^P s_j; \\
(VI) \quad \text{Combination of (II) + (III)} &: \mathbf{Z} = \{Z_j, z_j | j = 1, \dots, N_C\};
\end{aligned} \tag{5.40}$$

where  $\theta_j$  is the Ritz values,  $\gamma_j$  is the Harmonic Ritz values. Note that proposed method does not require reconstructing of any kind basis functions as in the case of conventional multi-scale methodology. During the construction of deflation vectors we need to keep only linear independent vectors (i.e.,  $\mathbf{Z}$  must have a full rank  $d$ ).

## 5.2.4 Meshless Deflation Method

The Meshless Deflation Method (MDM) can be used (instead or complementary to AMG) to solve the pressure equation (5.4). The deflation space can be constructed using methods (I)-(VI) described in (5.40). Since it is numerically inefficient to construct both  $\mathbf{W}_j^R$  and  $\mathbf{W}_j^P$ , we will construct the restriction operator as  $\bar{\mathbf{W}}_j^R = (\mathbf{W}_j^P)^\top$ . Hence, it makes sense to consider only (I), (IV), (V) described in (5.40). The method (II) is equivalent to method (I) under the assumption  $\bar{\mathbf{W}}_j^R = (\mathbf{W}_j^P)^\top$  and method (VI) provides usually a set of dependent vectors which is required additional effort to construct independent subset. Method (III) is different from the methods (I) and (II) by the factor  $(B_W^j)^{-1}$  and we did not observed any significant difference in performance between (III) and (I). For the rest of the analysis, we will consider only option (I) denote this by MsMBM. In addition, we could use (a) subdomain, (b) levelset, (c) subdomain-levelset and (d) global deflation methods. In this thesis, we will focus on subdomain and global deflation methods. Hence, we will use index "s" and "g" to denote these methods, e.g., sMsMBM and gMsMBM. It is important to note that these methods can be extended to solve the full system (5.1). Hence, a fully implicit formulation is used and resulting matrix solved with a 2-stage CPR preconditioner, where the MsMBM method is used for solving the CPR pressure system (5.4). The pseudocode for deflation method is given in Algorithm 2. The computations in line 1 involve

---

**Algorithm 2** Right-Preconditioned Meshless Deflation GMRES Based Method
 

---

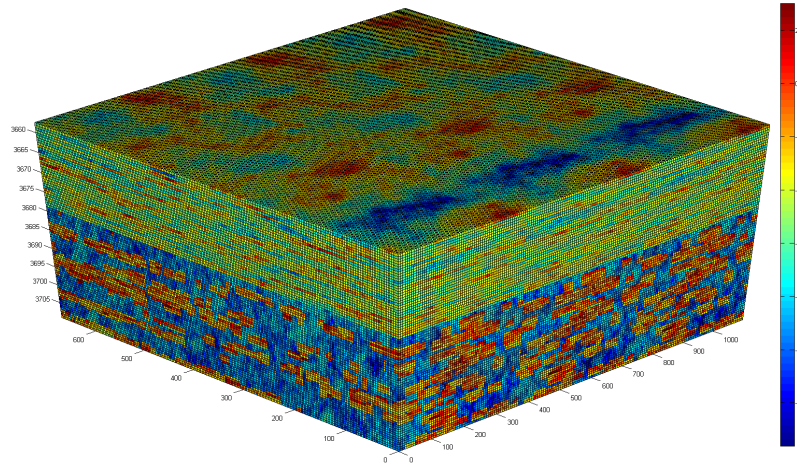
- 1: Setup meshless deflation vectors  $\mathbf{Z}$
  - 2: Setup  $\mathbf{A}_p = \mathbf{A}_{pp}^* \mathbf{M}_3^{-1}$ ,  $\mathbf{E} = \mathbf{Z}^\top \mathbf{A}_p \mathbf{Z}$ , and  $x^* = \mathbf{Z} \mathbf{E}^{-1} \mathbf{Z}^\top b$ .
  - 3: Setup  $\mathbf{P}_1 = \mathbf{I} - \mathbf{Z} \mathbf{E}^{-1} \mathbf{Z}^\top \mathbf{A}_p$  and  $\mathbf{P}_2 = \mathbf{I} - \mathbf{A}_p \mathbf{Z} \mathbf{E}^{-1} \mathbf{Z}^\top$ .
  - 4: Compute  $r_0 = \mathbf{P}_2(b - \mathbf{A}x_0)$ ,  $\beta = \|r_0\|_2$ , and  $v_1 = r_0/\beta$ .
  - 5: **for**  $j = 1, 2, \dots, m$  **do**
  - 6:      $w_j = \mathbf{P}_2 \mathbf{A}_{pp}^* \mathbf{M}_3^{-1} v_j$
  - 7:     **for**  $i = 1, \dots, j$  **do**
  - 8:          $h_{i,j} = (w_j, v_i)$
  - 9:          $w_j = w_j - h_{i,j} v_i$
  - 10:     **end for**
  - 11:      $h_{j+1,j} = \|w_j\|_2$
  - 12:     **if**  $h_{j+1,j} = 0$  **or** converged **then**
  - 13:         set  $m = j$  and **go to** 17
  - 14:     **end if**
  - 15:      $v_{j+1} = w_j/h_{j+1,j}$
  - 16: **end for**
  - 17: Fill  $\bar{H}_m = \{h_{i,j}\}$  for  $1 \leq i \leq m+1, 1 \leq j \leq m$ .
  - 18: Compute the minimizer  $u_m$  of  $\|\beta e_1 - \bar{H}_m u\|_2$  and set  $x_m = x_0 + \mathbf{M}_3^{-1} \mathbf{V}_m u_m$ .
  - 19: **if** converged **then**  $x_m = \mathbf{P}_1 x_m + x^*$  and return **else** set  $x_0 = x_m$  and **go to** 4
- 

construction of meshless deflation vectors and setting up the deflation operators, and can be executed at the beginning of the linear solver since  $\mathbf{Z}$  is available *a priori*.

The algorithm clearly illustrates the action of  $\mathbf{P}_1$  and  $\mathbf{P}_2$ . The search space is narrowed to the deflated subspace by solving the deflated system (5.21), and the standard right preconditioned GMRES algorithm 2 is used. In the case of omitting the GMRES algorithm, the aforementioned algorithm reduces to the two-level meshless multiscale method [186]. To return to the original space,  $x_m$  is multiplied with  $\mathbf{P}_1$ , and the result is added to  $x^*$ . The preconditioner  $\mathbf{M}_3$  is constructed to avoid direct inversion of the matrix and expensive matrix-matrix product in the expression  $\mathbf{A}_p = \mathbf{A}_{pp}^* \mathbf{M}_3^{-1}$ . This is achieved by doing a user defined number pre- and a post-smoothing (e.g., Gauss-Seidel (GS) or ILU(0)) steps similar to Multigrid Solver. The coarse pressure system  $\mathbf{E}v = w$  can be solved with different strategies depending on the size of the coarse pressure matrix. The size of the coarse pressure matrix is defined by the size of the model and the choice of the coarsening factors. If the size of the coarse system is small a direct solver can be used. The iterative methods are used for the large coarse system.

## 5.2.5 SPE10 simulation

In this section, we show the performance of the meshless deflation strategy using global domain based meshless deflations vectors applied to the large scale simulation. For this reason we consider a well-known SPE-10 benchmark [65]. The fine grid is  $180 \times 220 \times 85$  for a total of 3366000 cells with  $\mathcal{O}(10^6)$  degrees of freedom



**Figure 5.3:** *X-direction permeability distribution in logarithmic scale and Darcy units for SPE10 case.*

The complexity of modeling large models lies both in constructing  $\mathbf{E}^{-1}$  and solving of the deflated system  $\mathbf{P}_1 \mathbf{A} \hat{\mathbf{x}} = \mathbf{P}_1 \mathbf{b}$ . Note that even when the deflation subspace dimension is relatively low, i.e.  $d \ll n$ , solving the deflated system may still be difficult for challenging cases. On the other hand, increasing the deflation space dimension shifts the complexity to the construction of  $\mathbf{E}^{-1}$ . However, it is possible to follow up the multiscale solution strategy in this case by ignoring the solution of the deflated system. This is the case where combining significantly weaker preconditioner such as Jacobi with the deflation method leads to a very poor performance. Hence, in this case, we combined deflation method with the AMG-preconditioned deflated system.

Although, this model has a clearly layered structure (see, figure 5.3) with two layers, the proposed physics-based deflation vectors for the SPE10 are equally distributed within the numerical domain using subdomain method (see, Figure 5.2(a)). The total number of deflation vectors considered in this study is (1)  $d = 8$ , (2)  $d = 27$  and (3)  $d = 64$ . The pressure system is solved approximately (as is common in practice) in any two-stage preconditioning methods. In this case, the pressure is also solved approximately.

Table 5.1 summarizes the results for  $gMsMBM(3,8)$ ,  $gMsMBM(3,27)$ ,  $gMsMBM(3,64)$  and CPR-AMG with an AMG preconditioner. As before, we use the termination criterion of either a tolerance of  $10^{-2}$  or the maximum number of pressure solution iterations which is set to 3. Results and performance were compared with the current version of a modern reservoir simulator [235] which uses CPR preconditioning with TRUE-IMPES decoupling, 1 V-cycle of AMG for solving the CPR pressure system and ILU(0) as a second-stage fully implicit (FIM) preconditioner [235]. This reference solution strategy is referred to as CPR-AMG. The coarse grids in AMG solver are constructed by the parallel maximally independent set (PMIS) coarsening scheme with the Gauss-Seidel smoothing process. The coarse level is solved by FGMRES preconditioned by ILU(0) and maximum number of levels is limited to 50 by default settings. The results for this case were obtained in serial runs using a desktop PC with 80GB RAM with Intel Xeon E5-2697 v2 2.70GHz CPU. Note that physics-based deflation is highly parallelizable, which is the topic of ongoing research.

	gMsMBM(3,8)	gMsMBM(3,27)	gMsMBM(3,64)	CPR-AMG
Preconditioner	AMG	AMG	AMG	AMG
Non-linears	1,160	1,159	1,161	1,159
Fails	0	0	0	0
Outer linears	12,986	13,026	13,029	13,194
Inner linears	38,582	38,775	38,774	39,248
No. time steps	286	286	286	286
CPU time	65,784.7	66,035.3	66,239.4	56,916.1

**Table 5.1:** Comparison of gMsMBM(3,8) (with AMG preconditioner), gMsMBM(3,27) (with AMG preconditioner), gMsMBM(3,64) (with AMG preconditioner) and CPR-AMG for the SPE10 case.

Each method uses approximately three inner linear iterations in all pressure solves. The size of the residual at the end of each pressure solve, however, will be smaller for gMsMBM with AMG. This results in a reduction of the inner linear iterations for all deflated methods. Note that the number of non-linear iterations in this case were the same.

In this case, both the time needed for the setup of AMG and the use of deflation offsets the iteration gain, resulting in higher CPU times. We expect the combination of multiscale solver and deflation method is expected to get a better solution strategy. Further analysis of optimal deflation vectors is required for this case and it is a subject of future research. In addition, it is important to note that the difference between the inner linear iterations for gMsMBM(3,27) and gMsMBM(3,64) is negligible leading to the conclusion that the dimension of the deflated space based on subdomain method must be relatively small for this case. This example also illustrates the potential of physics-based deflation vectors. The gMsMBM achieves in this case a relatively good iteration reduction in the pressure solve. The following section describes multiscale meshless based method and its coupling with the deflation strategy.

### § 5.3 Adaptive Deflated Meshless Multiscale Solver (ADMMS)

The conventional two-grid algorithm for linear problems consists of smoothing on the fine grid, approximation of the required correction on the coarse grid (restriction step), prolongation of the coarse grid correction to the fine grid, and again smoothing on the fine grid (Wesseling, (1992) [275]). The Adaptive Deflated Meshless Multiscale Solvers (ADMMS) can be used to construct a coarse pressure system in three different ways: (1) fully deflated method coupling with the meshless multicale, (2) decoupled deflated method coupling with multiscale and (3) mixed deflated method coupling with multiscale method. The next subsections describe these methods in details.

#### 5.3.1 Fully ADMMS (F-ADMMS)

Fully ADMMS method uses prolongation  $\mathbf{P}$  and restriction  $\mathbf{R}$  operators described above applied to the deflated system (5.9) as follows

$$\mathbf{P}_1 \mathbf{R} \mathbf{A}^f \mathbf{P} \hat{p}^c = \mathbf{P}_1 \mathbf{R} b^f, \quad \hat{p}^c = (\mathbf{P}_1 \mathbf{R} \mathbf{A}^f \mathbf{P})^{-1} \mathbf{P}_1 \mathbf{R} b^f. \quad (5.41)$$

The coarse system is solved to obtain  $\hat{p}^c$  and the final solution can be reconstructed as follows

$$\begin{aligned} p^f &\approx p' = \mathbf{P} \mathbf{R} \mathbf{Z} \mathbf{D}^{-1} \mathbf{Z}^T \mathbf{R}^T \mathbf{R} b^f + \mathbf{P} \mathbf{P}_2 \hat{p}^c = \\ &= \underbrace{\left[ \mathbf{P} \mathbf{R} (\mathbf{Z} \mathbf{D}^{-1} \mathbf{Z}^T) \mathbf{R}^T \mathbf{R} + \mathbf{P} \mathbf{P}_2 (\mathbf{P}_1 \mathbf{R} \mathbf{A}^f \mathbf{P})^{-1} \mathbf{P}_1 \mathbf{R} \right]}_{\mathbf{M}_{F-ADMMS}^{-1}} b^f, \end{aligned} \quad (5.42)$$

$$\mathbf{D} = \mathbf{Z}^T \mathbf{R}^T (\mathbf{R} \mathbf{A}^f \mathbf{P}) \mathbf{R} \mathbf{Z}.$$

It is important to recall Additive Schwarz Method with deflation correction discussed in [80]. The operator in this method can be written as

$$\mathbf{M}_{ASM}^{-1} = \mathbf{Z} \mathbf{D}^{-1} \mathbf{Z}^T + \sum \mathbf{R}_i^T (\mathbf{R}_i \mathbf{A} \mathbf{R}_i^T)^{-1} \mathbf{R}_i \quad (5.43)$$

where  $\mathbf{R}_i$  is the restriction operator to the overlapping domain. The structure of the operators  $\mathbf{M}_{ASM}^{-1}$  and  $\mathbf{M}_{F-ADMMS}^{-1}$  are different due to the presence of deflation projector operators  $\mathbf{P}_1$  and  $\mathbf{P}_2$ .

### 5.3.2 Decoupled ADMMS (D-ADMMS)

In light of the structure of the operators  $\mathbf{M}_{ASM}^{-1}$ , it is possible to use the decoupled ADMMS method (D-ADMMS) constructed as follows

$$p^f \approx p' = \underbrace{\left[ \mathbf{P}\mathbf{R}(\mathbf{Z}\mathbf{D}^{-1}\mathbf{Z}^T)\mathbf{R}^T\mathbf{R} + \mathbf{P}(\mathbf{R}\mathbf{A}^f\mathbf{P})^{-1}\mathbf{R} \right]}_{\mathbf{M}_{D-ADMMS}^{-1}} b^f, \quad \mathbf{D} = \mathbf{Z}^T\mathbf{R}^T(\mathbf{R}\mathbf{A}^f\mathbf{P})\mathbf{R}\mathbf{Z}. \quad (5.44)$$

This is the most trivial way of coupling deflation method with the multiscale solver.

### 5.3.3 Mixed ADMMS (M-ADMMS)

Mixed ADMMS employs an enriched set of basis functions to map between fine and coarse scales. This extended set involves the conventional multiscale local basis functions and globally constructed deflation vectors. Hence, the global prolongation operator  $\mathbf{P}$  is constructed such that it consists of original prolongation operator and deflation operator

$$\hat{\mathbf{P}} = [\mathbf{P}; \mathbf{Z}]. \quad (5.45)$$

Furthermore, there is only one option in the case for the restriction operator  $\mathbf{R}$  defined as

$$\mathbf{R} = \hat{\mathbf{P}}^T = ([\mathbf{P}; \mathbf{Z}])^T. \quad (5.46)$$

The multiscale procedure in this can be written as

$$p^f \approx \underbrace{\hat{\mathbf{P}}(\hat{\mathbf{P}}^T\mathbf{A}^f\hat{\mathbf{P}})^{-1}\hat{\mathbf{P}}^T}_{\mathbf{M}_{M-ADMMS}^{-1}} b^f. \quad (5.47)$$

The mixed adaptive deflated multiscale operator  $\mathbf{M}_{M-ADMMS}^{-1}$  is clearly different from the operators  $\mathbf{M}_{ASM}^{-1}$ ,  $\mathbf{M}_{D-ADMMS}^{-1}$  and  $\mathbf{M}_{F-ADMMS}^{-1}$ . There are two types of coarse system in the proposed methods: (a) the deflated coarse system with the matrix  $\mathbf{D}$  and (b) the multiscale coarse system with the matrix  $\bar{\mathbf{A}}_c = \mathbf{R}\bar{\mathbf{A}}\mathbf{P}$ , where  $\bar{\mathbf{A}}$  is the fine scale matrix. All presented above methods strongly depend on the underlying construction of the deflation vectors. The different ways of constructing deflation vectors are describe in the next section.

In real applications, the deflation vectors are constructed approximately. Hence any numbers of pre- and post-smoothing  $\omega$  iterations can be performed to eliminate any undesirable frequencies (e.g., Gauss-Seidel (GS) or ILU(0)) steps similar to Multigrid Solvers as  $w_{i+1}^f = \mathbf{S}^{-1}(\mathbf{A}^f, v^f, w_i^f, w_0^f, \omega)$ :

$$w_{i+1}^f = w_i^f + \mathbf{S}^{-1} \cdot (v^f - \mathbf{A}^f w_i^f), \quad i = 1, \dots, \omega; \quad (5.48)$$

where  $v^f$  is the given vector,  $w_{\omega+1}^f$  is the output vector,  $w_0^f$  is the initial guess,  $\mathbf{S}$  is the smoothing operator. Furthermore, it is naturally to use  $\mathbf{M}_{M-ADMMS}^{-1}$  and  $\mathbf{M}_{F-ADMMS}^{-1}$  as a preconditioner with some iterative accelerator (e.g., Krylov's type accelerator).

### 5.3.4 Multiscale Meshless Based Method

The linear system of equations (primary focus is the pressure equations) with the matrix  $\mathbf{A}_F$  and right hand side  $b_F$  can be difficult to solve, if its condition number  $k = \|\mathbf{A}_F\| \|\mathbf{A}_F^{-1}\|$  is large. This motivates the concept of preconditioning. Let  $\mathbf{V}$  be an approximation of  $\mathbf{A}^{-1}$ , which is easy to construct and to solve for a given input. Hence, we can write a simple Richardson iteration scheme with the predefined number of application of the multilevel multiscale meshless based preconditioner:

$$[p_F]^{m+1} = [p_F]^m + \mathbf{V} \cdot (b_F - \mathbf{A}_F [p_F]^m) \quad (5.49)$$



where  $m$  is the iteration index,  $[p_F]^m$  is the pressure vector at the iteration  $m$ ,  $\mathbf{V}$  is the left multiscale meshless based preconditioner defined as an operational object. A meshless multiscale preconditioner  $\mathbf{V}$  is constructed as follows for a given input  $v_F$  and output  $z_F$  using a two-level case by no limiting example:

$$[z_F] = \mathbf{P} (\mathbf{A}_C)^{-1} \mathbf{R} [v_F], \quad \mathbf{A}_C = \mathbf{R} \mathbf{A}_F \mathbf{P} \quad (5.50)$$

$$[w_F] = [z_F] + \mathbf{S}_\gamma^{-1} \cdot ([v_F] - \mathbf{A}_F [z_F]) \quad (5.51)$$

where  $\mathbf{S}_\gamma^{-1}$  is the smoothing operator (e.g., Gauss-Seidel (GS) or ILU( $k$ ) or BILU( $k$ ) smoothing method or Krylov-space accelerator) applied  $\gamma$  times. The multiscale meshless based method involves setting up the restriction and prolongation operators, which can be constructed at the beginning of the simulations.

## §5.4 Numerical Experiments

In this section, the performance of deflated and decoupled ADMMS solver techniques described above is discussed. Several test cases such as "Islands" model problem and Fractured reservoir, SPE10 layer and some real industrial test cases are considered. It is clear from the construction of the above methods that they have a low algebraic complexity compared to fully ADMMS and mixed ADMMS. This was a primary reason to keep our focus on deflated and decoupled ADMMS solvers.

### 5.4.1 "Islands" model problem

The Cartesian grid  $100 \times 100$  with the physical size of  $10 \times 10$  meters squared and 64 high-permeability islands distributed symmetrically with respect to the centre of the domain (see Fig. 5.4) is considered during the numerical analysis:

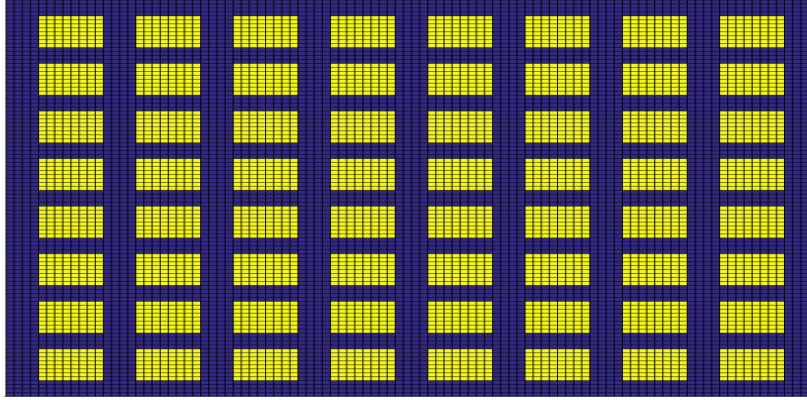


Figure 5.4: Numerical domain: 2D example with 64 high heterogeneities islands.

The incompressible single phase fluid model with viscosity  $1 \text{ cP}$  and density  $1014 \text{ kg/m}^3$  is used to test the solver performance. The flux and pressure boundary conditions are used where a Neumann condition with total inflow of  $5000 \text{ m}^3/\text{day}$  on the left side and a Dirichlet condition with fixed pressure of  $50 \text{ bar}$  on the right side are applied. The fluid flow is driven by the fluid source at the south-west corner and a fluid sink at the north-east corner of the model. The source terms have a rate such that a unit time corresponds to the injection of one pore volume of fluids. For the numerical analysis we use the matrix obtained from the last time step which is of the  $10000 \times 10000$  matrix size with 49600 non-zero entries.

**Deflation.** For method validation the following deflation matrices are used:

1.  $\mathbf{Z}_1$  - *physics-based deflation*: contains 64 vectors of the size 10000, where each vector represents only one high-permeability island, specifically 1 in the corresponding island coordinates and 0 otherwise;
2.  $\mathbf{Z}_{mms}$  - *meshless multiscale basis functions*: contains meshless multiscale basis functions as columns;
3.  $\mathbf{Z}_{db}$  - *domain-based*: similar to the *physics-based deflation* approach, but here we put 1 into all cells, which belong to the certain subdomain, and 0 into all other cells;

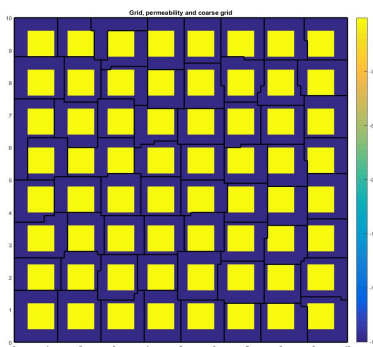
4.  $\mathbf{Z}_{mix}$  - *mixed deflation*: consists of vectors obtained from different approaches (e.g. physics-based deflation and meshless multiscale basis functions);
5.  $\mathbf{Z}_t$  - *theoretical*: consists of determined beforehand number of the exact eigenvectors corresponding to the smallest magnitude eigenvalues.

The classical GMRES method (without deflation and meshless multiscale additions) requires 500 iterations to solve the pressure equation subject to the tolerance  $10^{-7}$ . The numerical simulations with ADMMS methods outperform GMRES as expected. The numerical results are presented for the right-preconditioned setup, where the preconditioners were decoupled, fully and mixed modifications respectively. It is important to note in all tables below that the numbers in brackets indicate numbers of vectors in the corresponding matrix. For our reference, we computed the number of iterations for the solution of the pressure system using deflation matrix  $\mathbf{Z}_t$  based on the extreme eigenvalues. This is the most efficient way to deflate extreme eigenvalues which is the primary source of the slow convergence rate (see table 5.2). For the fast solution of the linear system, it

**Table 5.2:** Numerical results: linear solver iterations using  $\mathbf{Z}_t$ .

Deflation Matrix	No. Iterations
$\mathbf{Z}_t(16)$	181
$\mathbf{Z}_t(32)$	142
$\mathbf{Z}_t(64)$	57
$\mathbf{Z}_t(65)$	51

is important to be able to determine the best option for the deflation matrix, which can be easily and cheaply constructed. In light of this, the domain decomposition based on 3 METIS-based variants of grid partitioning (i.e., 16, 32 and 64 subdomains) are employed to construct the approximation of deflation vectors:



**Figure 5.4:** Application of the METIS-based grid partitioning: partitioning into 64 subdomains.

For these cases the required number of iterations for GMRES, right-preconditioned only by deflation consisting of multiscale basis functions or domain-based vectors, are presented in the table 5.3:

Deflation Matrix	No. Subdomains		
	16	32	64
$\mathbf{Z}_1$	358	279	103
$\mathbf{Z}_{mms}$	238	193	37
$\mathbf{Z}_{db}$	285	256	59
$\mathbf{Z}_{mix}[\mathbf{Z}_1 \mathbf{Z}_{mms}]$	45	31	19
$\mathbf{Z}_{mix}[\mathbf{Z}_1 \mathbf{Z}_{db}]$	49	38	29

**Table 5.3:** Linear solver iterations using  $\mathbf{Z}_1$ ,  $\mathbf{Z}_{mms}$ ,  $\mathbf{Z}_{db}$ ,  $\mathbf{Z}_{mix}[\mathbf{Z}_1 \mathbf{Z}_{mms}]$  and  $\mathbf{Z}_{mix}[\mathbf{Z}_1 \mathbf{Z}_{db}]$ .

Note that in the corresponding deflation matrices the number of columns coincide with the chosen number of subdomains, while the mixed version contains vectors from both components. As we can see from the tables above, the best option for the deflation would be usage of mixed deflation. To investigate the performance of the meshless multiscale idea, the domain was split into the computational domain and the meshless multiscale preconditioner (MsMBM) were applied as a preconditioner operator to the GMRES method, which gives us,

No. Subdomains	No. Iterations
16	89
32	77
48	71
64	19

Table 5.4: Linear solver iterations using meshless multiscale operators.

The decoupled ADMMS method is constructed by combining deflation and multiscale operators into single preconditioner (5.44) giving the following numerical results:

Number of Subdomains	Deflation Matrix				
	$Z_1$	$Z_{mms}$	$Z_{db}$	$Z_{mix}[Z_1 Z_{mms}]$	$Z_{mix}[Z_1 Z_{db}]$
16	37	88	134	34	36
32	28	69	315	23	28
64	14	14	40	11	12

Table 5.5: Linear solver iterations of the decoupled ADMMS preconditioner.

### 5.4.2 Fractured reservoir

In this paragraph, a 2D example of the fractured reservoir is considered, where fractures play a key role in defining the fluid flow paths due to its high permeability. More specifically, 30 fractures are randomly generated and distributed over the  $100 \times 100$  domain with a homogeneous permeability which is  $10^6$  times greater than reservoir permeability (Fig. 5.5).

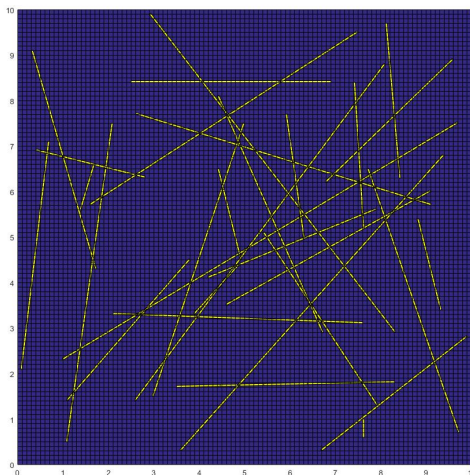


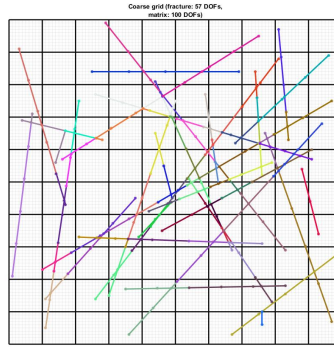
Figure 5.5: Numerical Domain: fractured reservoir.

The physical fluid properties (i.e., density and viscosity) and boundary conditions are the same as described in the previous paragraph for the "Islands" model problem. After TPFA-type discretization, a  $10277 \times 10277$  matrix were derived where the last 277 rows and columns correspond to fractures properties.

**Deflation.** For the deflation-based preconditioner we utilize these matrices:

1.  $\mathbf{Z}_1$  - *physics-based deflation*: contains 30 vectors of the size 10277, where every vector corresponds to only one fracture, especially 1 in cells crossed by this fracture and 0 otherwise;
2.  $\mathbf{Z}_{mms}$  - *meshless multiscale basis functions*: contains meshless multiscale basis functions as columns;
3.  $\mathbf{Z}_{db-g}$  - *grid-based*: here we put 1 into all cells, which belong to the certain subdomain, and 0 into all other cells;
4.  $\mathbf{Z}_{db-f}$  - *fracture-based*: similar to the *grid-based deflation* approach, but here we put 1 into all cells, which belong to the certain set of fractures pieces after grid partitioning, and 0 into all other cells;
5.  $\mathbf{Z}_{db}$  - *domain-based*: contains vectors from both  $\mathbf{Z}_{db-g}$  and  $\mathbf{Z}_{db-f}$ ;
6.  $\mathbf{Z}_{mix}$  - *mixed deflation*: consists of vectors obtained from different approaches (e.g. physics-based deflation and multiscale basis functions);
7.  $\mathbf{Z}_t$  - *theoretical*: consists of determined beforehand number of the exact eigenvectors corresponding to the smallest magnitude eigenvalues.

In the figure below there is a couple of possible ways to partition the grid:



**Figure 5.6:** Numerical domain with grid- and fracture-based partitioning: 57 fracture and 100 grid subdomains.

The standard GMRES method requires 100 iterations to solve the pressure equation with desired tolerance  $10^{-9}$ . Below, the performance of the deflation-, meshless multiscale-based and ADMMS preconditioners are presented. To obtain the reference behaviour, the theoretical type of deflation preconditioner is applied, i.e. using  $\mathbf{Z}_t(30)$ , which leads to the converge with 48 iterations. Tables 5.6 and 5.7 show the required number of the iterations for different deflation matrices:

Deflation Matrix	Grid and Fractures Partitioning					
	30 f 25 g	30 f 16 g	21 f 16 g	57 f 100 g	16 f 100 g	16 f 100 g
$Z_{mms}$	40	47	45	29	31	
$Z_{db-f}$	84	84	85	85	85	
$Z_{db-g}$	94	96	96	78	78	
$Z_{db}$	59	62	63	43	48	

**Table 5.6:** Linear solver iterations using multiscale (grid- and fractures-based) deflation. Multiscale-based deflation (f and g stand for the amount of fractures and grid subdomains respectively).

Deflation Matrix	Grid and Fractures Partitioning				
	21 f 25 g	16 f 100 g	16 f 16 g	57 f 25 g	12 f 16 g
$Z_{mix}[Z_1 Z_{mms}]$	39	28	44	38	43
$Z_{mix}[Z_1 Z_{db-g}]$	60	51	64	60	64
$Z_{mix}[Z_2 Z_{mms}]$	45	32	50	43	50
$Z_{mix}[Z_2 Z_{db-g}]$	60	51	64	60	64

Table 5.7: Linear solver iterations using mixed deflation matrix.

The performance of stand alone meshless multiscale-based preconditioner (MsMBM) is described in the Table 5.8:

Fractures and Grid partitioning	No. Iterations
16 f 25 g	61
21 f 16 g	60
16 f 100 g	48
12 f 16 g	36
9 f 16 g	33
9 f 25 g	25
9 f 100 g	20

Table 5.8: Linear solver iterations using meshless multiscale-based preconditioner.

It follows from the table 5.8 that the meshless multiscale-based preconditioner has its own considerable effect on the convergence rate. The results of applying decoupled ADMMS preconditioner (both deflation and multiscale components) are presented in Table 5.9:

Fractures and Grid partitioning	Deflation Matrix				
	$Z_1$	$Z_{mms}$	$Z_t(30)$	$Z_{mix}[Z_1 Z_{mms}]$	$Z_{mix}[Z_1 Z_{db-g}]$
9 f 16 g	35	25	19	31	35
9 f 25 g	29	27	18	25	27
9 f 100 g	26	14	18	14	23

Table 5.9: Linear solver iterations of the ADMMS preconditioner with the GMRES solver.

In conclusion, the meshless deflation vectors can significantly improve the convergence and robustness of a numerical simulator of both deflation and ADMMS methods. The overall speed in serial mode can vary between 10%-20%. Furthermore, these vectors are constructed at the beginning of simulation leading to the overall reduction in the preconditioner setup. The proposed methods are also suitable for the parallel implementation.

### 5.4.3 Real Reservoir Simulation Test Cases

In this section, the performance results of the fully implicit smoothed particle hydrodynamics (meshless) based multiscale method (MsMBM) are presented. The method has been prototyped in a commercial reservoir simulator and the method was compared against the two stage CPR-AMG-ILU(0) solver, which is the default solution strategy in majority of commercial simulators.

The test cases are classified by the number of grid cells, fluid models and time discretization. The following characteristics were compared between the default and proposed solutions.

- *Time steps*: the total number of time steps required to complete the simulation.
- *Non-linear iterations*: the number of non-linear iterations in the simulation.
- *Linear iterations*: the number of iterations used to solve the linear systems generated by the non-linear solver.
- *Linear solver time*: the amount of time needed to solve the linear systems.

- *CPU time*: the overall computational time required to complete the simulation.

Table 5.10 describes all the running five test cases ranging from relatively small (not too small) models to relatively large (not too large) real life test cases. The black oil, iso-thermal and thermal compositional models

Active cells	Dimensions	Fluid model	Implicitness	Number of phases	Number of active components
389557	$154 \times 90 \times 34$	Compositional Isothermal	AIM IMPES	3	13
348807	$238 \times 192 \times 114$	Black Oil Isothermal	Fully Implicit	3	3
348812	$238 \times 192 \times 114$	Compositional Isothermal	AIM IMPES	3	8
1722781	$18 \times 1126 \times 85$	Compositional Thermal with steam permitted	Fully Implicit	3	3
164945	not a 'box'	Compositional Thermal with steam permitted	Fully Implicit	3	3

**Table 5.10:** Basic properties of the simulated test cases.

with varying degree of heterogeneity in the reservoir grid properties are considered in this thesis to test the performance of the Multiscale Meshless Based Method (MsMBM). The names of the test cases correspond to the total number of cells in the models. Table 5.10 contains several examples where the number of active cells is lower than the number of cells suggested by the dimensions. In those cases, the domain includes a number of inactive cells. The settings for the simulation test cases are (a) Pre-smoothing - GS; (b) Post-smoothing; (c) MsMBM-GMRES( $k$ ), where  $k = 3$  and parameter  $k$  represents the number of the top level GMRES accelerations with MsMBM preconditioner; (d) Coarse Solver - AMG. The following tables and figures shows the performance results for all experimental tests including reference performance results (CPR-AMG-ILU(0)).

In general, Multiscale Meshless Based Method (MsMBM) does not change the number of time steps and non-linear iterations compared to the CPR-AMG-ILU(0) solution strategy in the considered simulations. This is due to second stage preconditioner ILU(0), which eliminates all the differences in the pressure solver, where AMG and MsMBM are applied. However, in all cases there is a significant effect on the number of linear iterations. This is a very common observations for multiscale solutions strategies (see, Lukyanov, 2014 [190]; Cusini, 2015 [74]) which leads to a larger number of linear iterations in general. This is, of course, a subject to a number of smoothing iterations on the fine scale. This indicates that the convergence rate of the multiscale method is worse than default AMG as other components of the linear solver have not changed. However, the increase in linear iterations is acceptable given the fact that the MsMBM has a more favorable CPUs in mapping information from fine to coarse level and solving this at the coarse level. The localized construction of the multiscale basis functions has strong affect on parallel scalability of multiscale method in general. Below, the CPUs time of different cases are presented.

Figure 5.7 shows the total time (CPUs) of the linear solver stage for different cases in serial runs. The MsMBM algorithm improves the results of the default method CPR-AMG-ILU(0) method in terms of total simulation time. The total simulation time is significantly reduced in all cases. Comparing the performance results of different simulations, it is clear that moderate number of cheap smoothing iterations reduces considerably the number of linear iterations and it allows a substantial speedup. If the correct settings are chosen CPR-MsMBM-ILU(0) results to be more than 20 % faster than CPR-AMG-ILU(0) in serial runs. The simulation tests clearly shows that MsMBM leads to a substantial speedup around 20% in general for serial runs. If the correct settings are chosen then the multiscale meshless based method preconditioner in the Krylov subspace iterative solvers results in a speedup relative to the reference settings (i.e., CPR-AMG-ILU(0)).

The size and complexity of modern reservoir simulation problems require vast computational resources and parallel computation. Hence, the state-of-the-art solvers, for example, the AMG preconditioner is used for parallel computing of large problems. Figure 5.8 shows preliminary results of the parallel scalability of the proposed multiscale method versus the default solver (i.e., CPR-AMG-ILU(0))

It is clear that further analysis of the method and its scalability is required to obtain the full picture about capabilities of the proposed method.

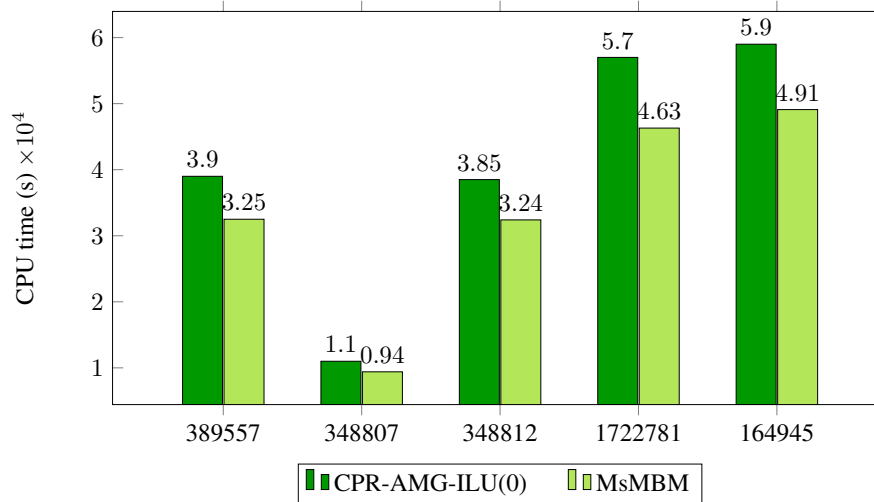


Figure 5.7: Total time of the linear solver stage for CPR-AMG-ILU(0) and MsMBM solution strategies.

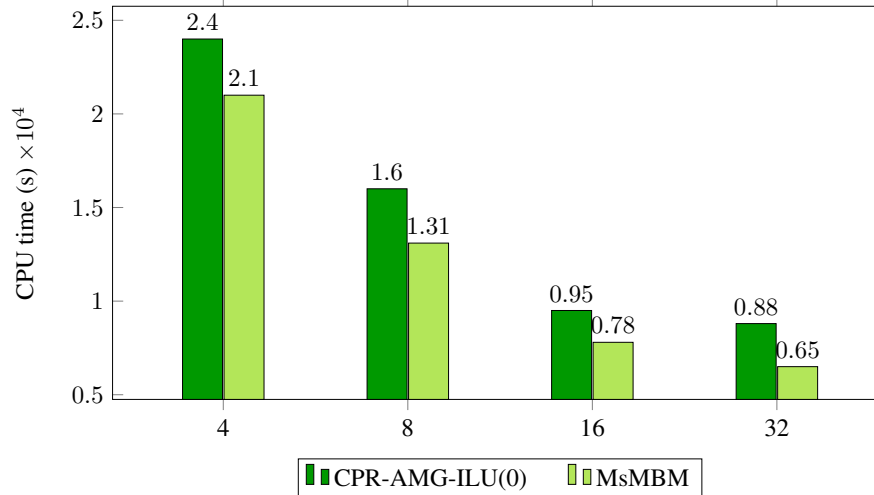


Figure 5.8: Scalability of the total time of the simulation runs for CPR-AMG-ILU(0) and MsMBM solution strategies in the case 389557.

## §5.5 Conclusions

A preconditioned Krylov subspace method such as the preconditioned FGMRES method can significantly improve the convergence and robustness of a numerical simulator. This chapter considers the preconditioned GMRES method with multilevel multiscale meshless based method for solving such pressure system. The solution technique proposed in this thesis uses a meshless approximation method to construct a priori the deflation space (or basis functions space). The analysis of the common fundamental features of different multiscale strategies are presented.

In this chapter, a parallel fully implicit smoothed particle hydrodynamics (SPH) based multiscale method for solving pressure system is presented. The prolongation and restriction operators in this method are based on a SPH gradient approximation (instead of solving localized flow problems) commonly used in the meshless community for thermal, viscous, and pressure projection problems. This method can reduce to the recently proposed MsRSB. In general, it gives more flexibility in constructing various restriction and prolongation operators.

---

This method has been prototyped in a commercially available simulator. This method does not require a coarse partition and, hence, can be applied to general unstructured topology of the fine scale. The SPH (or meshless) based multiscale method provides a reasonably good approximation to the pressure system and speeds up the convergence when used as a preconditioner for an iterative fine-scale solver. In addition, it exhibits expected good scalability during parallel simulations. Presented numerical results support theoretical and practical expectations from this method. Additional analysis of this method is required to identify the optimal parameters of this method.



---

## FUTURE RESEARCH WORK

---

### § 6.4 The Meshless Full Approximation Scheme

---

In contrast to the global linearization methods, the meshless FAS algorithm similar to the conventional FAS algorithm deals directly with the nonlinear system. The meshless FAS algorithm exploits a multi-level meshless method, error smoothing and coarse level correction, are also applicable to nonlinear problems similar to the conventional FAS method [253].

#### 6.4.1 The basics of meshless multilevel methods

Multi-level meshless methods are defect/correction methods, based on calculating a correction term from a computed residual. This process is repeated iteratively until the solution is satisfactory up to specified tolerance similar to conventional multigrid methods. Geometric multigrid methods operate with multiple grid representations of the same numerical domain whereas multi-level meshless methods operate with multiple sets of computational points. The concept is to define the problem on the finest set of points, and then interpolate (restrict) all the necessary information on to a coarser set of points similar to the conventional multigrid methods. This procedure is recursively repeated until the coarsest set of points is reached and upon which a residual equation is solved and a correction term obtained. The correction term is then recursively interpolated (prolongated) back to the finest set of points, where the approximation to the solution is corrected. An error smoothing operator (method) is applied after each restriction and prolongation operation, in order to remove the high frequency contributions to the error. Common smoothers used in multigrid methods are Jacobi-type or Gauss-Seidel-type iterations. More details on multigrid techniques can be found in [253]. Some attempts of using meshless multi-grid technique have already been made (Cummins and Rudman, 1999 [72]).

A two-level meshless method employs two sets of computational points. This has been discussed in details while constructing deflation vectors in Chapter 5. The traditional two-level algorithm for linear problems consists of smoothing on the fine grid, approximation of the required correction on the coarse grid (restriction step), prolongation of the coarse grid correction to the fine grid, and again smoothing on the fine grid. For smoothing iterations, it was applied conventional iterative methods (e.g., Gauss-Seidel, Krylov-space accelerator).

#### 6.4.2 Nonlinear Multi-Level Meshless Method: FAS

Using MMPFA method (e.g., Brookshaw (4.28) or Schwaiger (4.29)–(4.32), or New Scheme (4.44)–(4.46)) and corresponding fine set of points  $S_F$  =  $\{\mathbf{X}_I \in \mathbb{R}^n / I = 1, \dots, N_F\}$ , i.e.  $\Omega_F = \text{span} \{\bar{\Omega}_{\mathbf{X}_I, \bar{b}} / I = 1, \dots, N_F\}$ , the nonlinear discrete boundary value problem (4.96) can be written as:

$$\mathbf{N}_F(\mathbf{u}_F) = \mathbf{f}_F \quad (5.52)$$

where  $\mathbf{N}_F(\mathbf{u}_F)$  is a nonlinear fine level operator which depends on  $\mathbf{u}_F$ . Here parentheses are used to indicate

nonlinearity. The error is defined as  $\mathbf{e}_F = \mathbf{u}_F - \mathbf{v}_F$  and the residual for the approximated  $\mathbf{v}_F$  is defined as

$$\mathbf{N}_F(\mathbf{u}_F) - \mathbf{N}_F(\mathbf{v}_F) = \mathbf{r}_F \quad (5.53)$$

As described in [109], the meshless FAS method computes a coarse level correction term based on the residual equation, which using the error relation  $\mathbf{u}_F = \mathbf{v}_F + \mathbf{e}_F$  can be rewritten as

$$\mathbf{N}_F(\mathbf{v}_F + \mathbf{e}_F) - \mathbf{N}_F(\mathbf{v}_F) = \mathbf{r}_F \quad (5.54)$$

Consider this equation (5.54) on the coarsest points level with smoothing length  $h_C$ ,  $h_F$  being the smoothing length of the finer points level up, it can be written as

$$\mathbf{N}_C(\mathbf{v}_C + \mathbf{e}_C) - \mathbf{N}_C(\mathbf{v}_C) = \mathbf{r}_C \quad (5.55)$$

The coarse grid residual  $\mathbf{r}_C$  is the restriction of the fine grid residual,

$$\mathbf{r}_C = \mathbf{W}_{C,F}^R \mathbf{r}_F = \mathbf{W}_{C,F}^R (\mathbf{f}_F - \mathbf{N}_F(\mathbf{v}_F)) \quad (5.56)$$

where  $\mathbf{W}_{C,F}^R$  is the restriction operator. Similarly, the coarse level approximation  $\mathbf{v}_C$  is the restriction of the fine level approximation  $\mathbf{v}_F$ . This is in contrast to linear multigrid where it is only necessary to restrict the residual. Using these definitions equation (5.55) is written as

$$\begin{aligned} \mathbf{N}_C(\mathbf{W}_{C,F}^R \mathbf{v}_F + \mathbf{e}_C) &= \mathbf{N}_C(\mathbf{W}_{C,F}^R \mathbf{v}_F) + \mathbf{W}_{C,F}^R (\mathbf{f}_F - \mathbf{N}_F(\mathbf{v}_F)) \\ \mathbf{u}_C &= \mathbf{W}_{C,F}^R \mathbf{v}_F + \mathbf{e}_C \\ \mathbf{f}_C &= \mathbf{N}_C(\mathbf{W}_{C,F}^R \mathbf{v}_F) + \mathbf{W}_{C,F}^R (\mathbf{f}_F - \mathbf{N}_F(\mathbf{v}_F)) \end{aligned} \quad (5.57)$$

Since the right-hand side of (5.57) consists of known terms, the solution  $\mathbf{u}_H$  to this equation can be determined. Based on this solution, the coarse grid correction term is computed as  $\mathbf{e}_H = \mathbf{u}_H - \mathbf{W}_{C,F}^R \mathbf{v}_h$ . This correction term is prolonged one grid level up, where it is used to correct the solution to the residual equation at that grid level, and the process is repeated until the finest grid is reached. In the end an approximation to the nonlinear problem at the fine grid is found. Note that the linear solver is only applied at the coarsest grid and hence the Jacobian matrix is only assembled for this grid level. This implies a large memory reduction compared to the conventional techniques.

### 6.4.3 Nonlinear Meshless Coarse Level Method: FAS

One of the ways to solve non-linear governing equations is based on the Full Approximation Scheme, see Algorithm 3.

---

**Algorithm 3** Multi-Level FAS-Newton-Raphson.

---

```

1:  $l = 0$ ;
2:  $\mathbf{v}_f^l = \mathbf{w}_f^n$ ;
3: while  $\|\mathbf{r}_f(\mathbf{v}_f^l)\| \geq \varepsilon_r$  do
4:   for each level  $k$  towards coarse level do
5:     if level is not coarse then
6:       Restrict approximation and its residuals:  $\mathbf{r}_k^l = \mathbf{R} \cdot \mathbf{r}_f(\mathbf{v}_{k-1}^l)$ ,  $\mathbf{v}_k^l = \mathbf{R} \cdot \mathbf{v}_{k-1}^l$ ;
7:       Smooth:  $\mathbf{v}_k^l = \mathbf{v}_k^l - \mathbf{D}_k^{-1}(\mathbf{v}_k^l)\mathbf{r}_k^l$ ;
8:     else
9:       Solve:  $\mathbf{J}_c(\mathbf{v}_c^l)\delta\mathbf{v}_c^l = -\mathbf{r}_c^l$ ;
10:    end if
11:  end for
12:  Update coarse level solution:  $\mathbf{v}_c^{l+1} = \mathbf{v}_c^l + \delta\mathbf{v}_c^l$ ;
13:  Update coarse level residual:  $\mathbf{r}_c^{l+1} = \mathbf{r}_c(\mathbf{v}_c^{l+1})$ ;
14:  for each level towards fine level do
15:    Perform prolongation:  $\mathbf{v}_{k-1}^{l+1} = \mathbf{P} \cdot \mathbf{v}_k^{l+1}$ ,  $\mathbf{r}_{k-1}^{l+1} = \mathbf{P} \cdot \mathbf{r}_k^{l+1}$ ;
16:    Smooth:  $\mathbf{v}_{k-1}^{l+1} = \mathbf{v}_{k-1}^{l+1} - \mathbf{D}_{k-1}^{-1}(\mathbf{v}_{k-1}^{l+1})\mathbf{r}_{k-1}^{l+1}$ ;
17:  end for
18:  Smooth fine scale solution:  $\mathbf{v}_f^{l+1} = \mathbf{v}_f^{l+1} - \mathbf{D}_f^{-1}(\mathbf{v}_f^{l+1})\mathbf{r}_f^{l+1}(\mathbf{v}_f^{l+1})$ ;
19:   $l = l + 1$ ;
20: end while
21:  $\mathbf{w}^{n+1} = \mathbf{v}^l$ .

```

---

where  $\mathbf{R}$  is the restriction operator,  $\mathbf{P}$  is the prolongation operator,  $\mathbf{v}_f^l$  is the fine scale solution at  $l$ -iteration,  $\mathbf{v}_c^l$  is the coarse scale solution at  $l$ -iteration,  $\mathbf{r}_f(\mathbf{v}_f^l)$  is the fine scale non-linear residuals,  $\mathbf{D}_k(\mathbf{v}_k^l)$  is the diagonal elements of the Jacobian at level  $k$  evaluated at the point  $\mathbf{v}_k^l$ . A parallel implementation of the meshless FAS method on a distributed system is the additional subject of the future work.

# Notation

$\delta_{ij}$	delta symbol Kronecker (or unit tensor);
$\alpha_{ij}, \beta_{ij}$	first and second generalised delta symbol Kronecker;
$\mathbb{R}^n$	$n$ -dimension Riemann space;
$\mathbf{X}, \mathbf{x}$	Lagrangian coordinates, Euler coordinates;
$J_0, J$	Jacobian of reference and actual configuration respectively;
$\mathbf{u}$	displacement vector;
$\mathbf{v}, u_p$	velocity vector, particle velocity;
$U_s$	shock wave velocity;
$\rho_0, \rho$	initial and current density respectively;
$\mathbb{P}$	Lagrange stress tensor (or I-st Piola-Kirchhoff stress tensor);
$\tilde{\sigma}, \sigma_{ij}$	Cauchy stress tensor;
$\mathbb{F}$	deformation gradient;
$e$	internal energy;
$\mathbf{q}$	heat flux;
$\nabla_0, \nabla$	operator nabla of reference and actual configuration respectively;
$\tilde{\mathbf{A}}, \mathbf{A}$	any second order tensor;
$\tilde{\mathbf{A}} \cdot \tilde{\mathbf{B}} = \mathbf{A}_{ij} \mathbf{B}_{jk}$	single contraction by repeating indexes;
$\tilde{\mathbf{A}} : \tilde{\mathbf{B}} = \mathbf{A}_{ij} \mathbf{B}_{ij}$	double contraction by repeating indexes;
$\mathbf{A}_{i_1 i_1 i_3 \dots i_n} = \mathbf{A}_{i_1 i_2 i_3 \dots i_n} \delta_{i_1 i_2}$	contraction by repeating index;
$tr(\tilde{\mathbf{A}}), tr(\mathbf{A}) = \mathbf{A}_{kk}$	trace of any second order tensor $\tilde{\mathbf{A}}$ ;
$\omega_{ij}$	damage tensor;
$\omega = tr(\tilde{\omega})/3$	first damage parameter;
$\mathbf{A}'_{ij} = \mathbf{A}_{ij} - (\mathbf{A}_{kk}/3)\delta_{ij}$	deviatoric part of any second order tensor $\mathbf{A}$ ;
$ \tilde{\mathbf{A}}  =  \mathbf{A}  = \sqrt{A'_{ij} A'_{ij}}$	intensity of any second order tensor;

## Notation

---

$\alpha = \sqrt{\omega'_{ij}\omega'_{ij}}$	second damage parameter;
$\tilde{\sigma}$	effective stress tensor;
$V$	physical elementary volume;
$V^*$	volume of micropores in the physical elementary volume $V$ ;
$\bar{\sigma} = \sigma_{kk}/3$	first invariant of the stress tensor (mean stress);
$p = -\sigma_{kk}/3$	classical hydrostatic pressure;
$T$	temperature;
$\mathbf{W}_{ij}$	elastic spin tensor;
$\tilde{\varepsilon}^e$	elastic strain tensor;
$\tilde{\varepsilon}^p$	plastic strain tensor;
$F, \Psi$	free energy;
$S$	total entropy;
$S_i$	internal part of total entropy;
$S_e$	external part of total entropy;
$D$	dissipation function;
$H(\bullet)$	Heaviside function;
$\Lambda_\omega, \Lambda_\alpha, \Lambda_{ij}$	Onsager's parameters;
$\langle \bullet \rangle$	Smoothed particle hydrodynamics approximation;
$(\bullet)^\bullet = \frac{d}{dt}$	material derivative with respect to time;
$(\bullet)^\nabla$	Jaumann derivative with respect to time for the tensor components;
$\mathbf{a} \cdot \mathbf{b}$	scalar product of vectors $\mathbf{a}$ and $\mathbf{b}$ ;
$\text{div } \mathbf{a} = \nabla \cdot \mathbf{a}$	divergence of the vector $\mathbf{a}$ ;
$\text{grad } f = \nabla f$	gradient of function $f$ ;
$\otimes$	tensor product;
$\mathbf{a} \otimes \mathbf{b} = \mathbf{a}_i \cdot \mathbf{b}_j$	tensor product of of vectors $\mathbf{a}$ and $\mathbf{b}$ ;

---

---

## Bibliography

---

- [1] AARNES, J., KIPPE, V., AND LIE, K.-A. Mixed multiscale finite elements and streamline methods for reservoir simulation of large geomodels. *Adv. Water Resour.* 28, 3 (2005), 257–271.
- [2] AAVATSMARK, I. An introduction to multipoint flux approximations for quadrilateral grids. *Computational Geosciences* 6, 3-4 (2002), 405–432.
- [3] AAVATSMARK, I., BARKVE, T., BÆ, O., AND MANNSETH, T. A class of discretization methods for structured and unstructured grids in anisotropic, inhomogeneous media. In *Proc. 5th European Conference on the Mathematics of Oil Recovery, Leoben, Austria* (1996), Z. Heinemann and M. Kriebner, Eds., pp. 157–166.
- [4] AAVATSMARK, I., BARKVE, T., BÆ, O., AND MANNSETH, T. Discretization on unstructured grids for inhomogeneous, anisotropic media. part i: Derivation of the methods. *SIAM Journal on Scientific Computing* 19, 5 (1998), 1700–1716.
- [5] AAVATSMARK, I., BARKVE, T., BÆ, O., AND MANNSETH, T. Discretization on unstructured grids for inhomogeneous, anisotropic media. part ii: Discussion and numerical results. *SIAM Journal on Scientific Computing* 19, 5 (1998), 1717–1736.
- [6] AAVATSMARK, I., BARKVE, T., AND MANNSETH, T. Control-volume discretization methods for 3D quadrilateral grids in inhomogeneous, anisotropic reservoirs. *SPE Journal* 3, 2 (1998), 146–154.
- [7] ALFA, A., XUE, J., AND YE, Q. Entrywise perturbation theory for diagonally dominant M-matrices with applications. *Numerische Mathematik* 90, 3 (2002), 401–414.
- [8] ARAVAS, N., AND MCMEEKING, R. Finite element analysis of void growth near a blunting crack tip. *Journal of the Mechanics and Physics of Solids* 33, 1 (1985), 25–49.
- [9] ARAVAS, N., AND MCMEEKING, R. Microvoid growth and failure in the ligament between a hole and blunt crack tip. finite element analysis of void growth near a blunting crack tip. *International Journal of Fracture* 29, 1 (1985), 21–38.
- [10] ASTAFJEV, V., RADAYEV, Y., AND STEPANOVA, L. *Nonlinear fracture mechanics*. Samara: Izd. "Samarski Univ.", 2001.
- [11] ATLURI, S., CHO, J., AND KIM, H. Analysis of thin beams, using the meshless local Petrov-Galerkin (MLPG) method, with generalized moving least squares interpolation. *Computational Mechanics* 24, 5 (1999), 334–347.
- [12] ATLURI, S., AND SHEN, S. The meshless local Petrov-Galerkin (MLPG) method. Tech. rep., Tech. Science Press. USA, 2002.

## Bibliography

---

- [13] ATLURI, S., AND SHEN, S. The basis of meshless domain discretization: the meshless local Petrov - Galerkin (MLPG) method. *Advances in Computational Mathematics* 23, 1-2 (2005), 73–93.
- [14] ATLURI, S., AND ZHU, T. A new meshless local Petrov-Galerkin (MPLG) approach in computational mechanics. *Computational Mechanics* 22, 2 (1998), 117–127.
- [15] BAI, Y., BAI, J., LI, H., KE, F., AND XIA, M. Damage evolution, localization and failure of solids subjected to impact loading. *Int. J. Impact. Eng.* 24, 6-7 (2000), 685–701.
- [16] BAMMAN, D. A damage model for ductile metals. *Nuclear Engineering and Design* 116, 3 (1989), 355–362.
- [17] BAMMAN, D., CHIESA, M., McDONALD, A., KAWAHARA, W., DIKE, J., AND REVELLI, V. Prediction of ductile failure in metal structures, in failure criteria and analysis in dynamic response. *ASME AMD.* 107 (1990), 7–12.
- [18] BAMMANN, D., AND AIFANTIS, E. A model for finite-deformation plasticity. *Acta Mechanica* 69, 1-4 (1987), 97–117.
- [19] BAO, Y., ARUN, R., AND DODDS, R. Simulation of ductile crack growth in thin aluminum panels using 3d surface cohesive elements. *International Journal of Fracture* 110 (2001), 21–45.
- [20] BARDER, T., SEAMAN, L., CREWDSON, R., AND CURRAN, D. Dynamic fracture criteria for ductile and brittle metals. *J. Mater.* 7, 3 (1972), 393–401.
- [21] BARNARD, A., DUCK, I., LYNN, M., AND TIMLAKE, W. The application of electromagnetic theory to electrocardiology ii. numerical solution of the integral equations. *Biophysical journal* 7, 5 (1967), 463–491.
- [22] BASTE, S., AND AUDOIN, B. On internal variables in anisotropic damage. *Eur. J. Mech. A/Solids* 10, 6 (1991), 587–606.
- [23] BELYTSCHKO, T., FISH, J., AND ENGLEMAN, B. A finite element with embedded localization zones. *Comput. Meth. Appl. Mech. Engng.* 70, 1 (1988), 59–89.
- [24] BELYTSCHKO, T., KRONGAUZ, Y., DOLBOW, J., AND GERLACH, C. On the completeness of meshfree particle methods. *International Journal for Numerical Methods in Engineering* 43, 5 (1998), 785–819.
- [25] BELYTSCHKO, T., KRONGAUZ, Y., ORGAN, D., FLEMING, M., AND KRYSL, P. Meshless methods: an overview and recent developments. *Computer Methods in Applied Mechanics and Engineering* 139, 1-4 (1996), 3–47.
- [26] BELYTSCHKO, T., AND LIN, J. A three-dimensional impact-penetration algorithm with erosion. *Computers and Structures* 25, 1 (1987), 95–104.
- [27] BELYTSCHKO, T., LIU, W., AND MORAN, B. *Nonlinear Finite Elements for Continua and Structures*. John Wiley Sons, New York, 2000.
- [28] BELYTSCHKO, T., LU, Y., AND GU, L. Element-free galerkin methods. *Int. J. for Numerical Meth. in Engineering* 37, 2 (1994), 229–256.
- [29] BERMAN, P., AND PLEMMONS, R. *Nonnegative Matrices in the Mathematical Sciences*. Academic Press, 2006.
- [30] BETTEN, J. Net-stress analysis in creep mechanics. *Ingenieur-Archiv.* 52, 6 (1982), 405–419.
- [31] BETTEN, J. Damage tensors in continuum mechanics. *J. Mec. Theor. Appl.* 2 (1983), 13–32.
- [32] BONET, J., AND KULASEGARAM, S. Correction and stabilization of smooth particle hydrodynamics methods with applications in metal forming simulations. *International Journal for Numerical Methods in Engineering* 47, 6 (2000), 1189–1214.
- [33] BONET, J., AND LOK, T. Variational and momentum preservation aspects of smooth particle hydrodynamic formulations. *Computer Methods in Applied Mechanics and Engineering* 180, 1-2 (1999), 97–115.

- [34] BOUCHON, F. Monotonicity of some perturbations of irreducibly diagonally dominant M-matrices. *Numerische Mathematik* 105, 4 (2007), 591–601.
- [35] BOUCHON, F., AND PEICHL, G. A second order immersed interface technique for an elliptic neumann problem. *Numerical Methods for Partial Differential Equations* 23, 2 (2007), 400–420.
- [36] BOURNE, N., AND III, G. G. Equation of state of polytetrafluoroethylene. *Journal of Applied Physics* 93 (2003), 8966–8969.
- [37] BOURNE, N., AND STEVENS, G. A gas gun for plane and shear loading of inert and explosive targets. *Rev. Sci. Instrum.* 72, 4 (2001), 2214–2218.
- [38] BRAMBLE, J., AND HUBBARD, B. On a finite difference analogue of an elliptic boundary problem which is neither diagonally dominant nor of non-negative type. *Studies in Applied Mathematics* 43, 1-4 (1964), 117–132.
- [39] BRANDT, A. Multi-level adaptive solutions to boundary value problems. *Mathematics of Computaton* 31, 138 (1977), 333–390.
- [40] BREITKOPF, P., AND HUERTA, A. Meshless particle based approaches in computational mechanics. 176.
- [41] BROOKSHAW, L. A method of calculating radiative heat diffusion in particle simulations. *Proceedings of the Astronomical Society of Australia* 6, 2 (1985), 207–210.
- [42] BROWN, P., AND SAAD, Y. Hybrid krylov methods for nonlinear systems of equations. *SIAM Journal on Scientific and Statistical Computing* 11, 3 (1990), 450–481.
- [43] BRUHNS, O., AND SCHIESSE, P. A continuum model of elastic-plastic materials with anisotropic damage by oriented microvoids. *Eur. J. Mech. A/Solids* 15, 3 (1996), 367–396.
- [44] BRUNIG, M. An anisotropic ductile damage model based on irreversible thermodynamics. *International Journal of Plasticity* 19, 10 (2003), 1679–1713.
- [45] BRUNIG, M. Numerical analysis of anisotropic ductile continuum damage. *Computer Methods in Applied Mechanics and Engineering* 192, 26-27 (2003), 2949–2976.
- [46] CAI, X.-C., KEYES, D., AND MARCINKOWSKI, L. Nonlinear additive schwarz preconditioners and applications in computational fluid dynamics. *International Journal of Numerical Methods in Fluid Mechanics* 40, 12 (2002), 1463–1470.
- [47] CAMPBELL, P. Some new algorithms for boundary value problems in smooth particle hydrodynamics. Tech. rep., Mission Research Corp.: Albuquerque, NM, 1989.
- [48] CAO, H., TCHELEPI, H., WALLIS, J., AND YARDUMIAN, H. Constrained residual acceleration of conjugate residual methods. *SPE Annual Technical Conference and Exhibition* (2005).
- [49] CARROLL, M., AND HOLT, A. Static and dynamic pore-collapse relations for ductile porous materials. *J. Appl. Phys.* 43 (2003), 1626–1636.
- [50] CHABOCHE, J. Anisotropic creep damage in the framework of continuum damage mechanics. *Nuclear Engineering and Design* 79, 3 (1984), 309–319.
- [51] CHABOCHE, J. Continuum damage mechanics: Part i – general concepts. *Journal of Applied Mechanics* 55, 1 (1988), 59–64.
- [52] CHABOCHE, J. Continuum damage mechanics: Part ii – damage growth, crack initiation, and crack growth. *Journal of Applied Mechanics* 55, 1 (1988), 65–72.
- [53] CHAN, T., AND JACKSON, K. Nonlinearly preconditioned krylov subspace methods for discrete newton algorithms. *SIAM Journal on Scientific and Statistical Computing* 5, 3 (1984), 533–542.



## Bibliography

---

- [54] CHANIOTIS, A., POULIKAKOS, D., AND KOUMOUTSAKOS, P. Remeshed smoothed particle hydrodynamics for the simulation of viscous and heat conduction flows. *Journal of Computational Physics* 182 (2002), 67–90.
- [55] CHEN, J., AND BERAUN, J. A generalized smoothed particle hydrodynamics method for nonlinear dynamic problems. *Computer Methods in Applied Mechanics and Engineering* 190, 1-2 (2000), 225–239.
- [56] CHEN, J., BERAUN, J., AND CARNEY, T. A corrective smoothed particle method for boundary value problems in heat conduction. *International Journal for Numerical Methods in Engineering* 46, 2 (1999), 231–252.
- [57] CHEN, J., BERAUN, J., AND JIH, C. Completeness of corrective smoothed particle method for linear elastodynamics. *Computational Mechanics* 24, 4 (1999), 273–285.
- [58] CHEN, J., BERAUN, J., AND JIH, C. An improvement for tensile instability in smoothed particle hydrodynamics. *Computational Mechanics* 23 (1999), 279–287.
- [59] CHEN, J., BERAUN, J., AND JIH, C. A corrective smoothed particle method for transient elastoplastic dynamics. *Computational Mechanics* 27 (2001), 177–187.
- [60] CHEN, Q.-Y., WAN, J., YANG, Y., AND MIFFLIN, R. A new multipoint flux approximation for reservoir simulation. In *Proc. SPE Reservoir Simulation Symposium, Houston* (2007), p. 106464.
- [61] CHEN, Z., AND HOU, T. A mixed finite element method for elliptic problems with rapidly oscillating coefficients. *Mathematics of Computation* 72 (2003), 541–576.
- [62] CHEREPANOV, G. *Mechanics of brittle fracture*. Moskva: Nauka, 1974.
- [63] CHOW, C., AND WANG, J. An anisotropic theory of continuum damage mechanics for ductile fracture. *Eng. Frac. Mech.* 27 (1987), 547–558.
- [64] CHRISTIE, M. A., AND BLUNT, M. J. Tenth spe comparative solution project: A comparison of up-scaling techniques. *SPE 66599, presented at the SPE Symposium on Reservoir Simulation, Houston, February* (2001).
- [65] CHRISTIE, M. A., AND BLUNT, M. J. Tenth spe comparative solution project: A comparison of up-scaling techniques. *Presented at SPE Reservoir Simulation Symposium, Houston, TX, 11-14 February SPE-66599-MS* (2001).
- [66] CLEARY, P., AND MONOGHAN, J. Conduction modelling using smoothed particle hydrodynamics. *Journal of Computational Physics* 148 (1999), 227–264.
- [67] COCHRAN, S., AND BANNER, D. Spall studies in uranium. *Journal of Applied Physics* 48 (1977), 2729–2737.
- [68] COCKS, A. Inelastic deformation of porous materials. *J. Mech. Phys. Solids* 24 (1989), 693–715.
- [69] COLIN, F., EGLI, R., AND LIN, F. Computing a null divergence velocity field using smoothed particle hydrodynamics. *Journal of Computational Physics* 217 (2006), 680–692.
- [70] CORTES, R. The growth of microvoids under intense dynamic loading. *Int. J. Solids Struct.* 29 (1992), 1339–1349.
- [71] CORTINOVIS, D., AND JENNY, P. Iterative galerkin-enriched multiscale finite-volume method. *J. Comp. Phys.* 277 (2014), 248–267.
- [72] CUMMINS, S., AND RUDMAN, M. An SPH projection method. *Journal of Computational Physics* 152 (1999), 584–607.
- [73] CURRAN, D., AND SEAMAN, L. Dynamic failure of solids. *Physics Reports* 147, 5-6 (1987), 253–388.
- [74] CUSINI, M., LUKYANOV, A., NATVIG, J., AND HAJIBEYGI, H. Constrained pressure residual multi-scale (cpr-ms) method. *Journal of Computational Physics* 299 (2015), 472–486.

- [75] DAVISON, L., AND STEVENS, A. Continuum measures of spall damage. *J. Appl. Phys.* 43 (1972), 988–994.
- [76] DE STERCK, H. Steepest descent preconditioning for nonlinear GMRES optimization. *Numerical Linear Algebra with Applications* 20, 3 (2013), 453–471.
- [77] DEMBO, R., EISENSTAT, S., AND STEIHAUG, T. Inexact newton methods. *SIAM Journal on Numerical Analysis* 19, 2 (1982), 400–408.
- [78] DENNIS, J., AND MORE, J. Quasi-newton methods, motivation and theory. *SIAM Review* 19 (1977), 46–89.
- [79] DER VORST, H. V. Bi-CGSTAB: a fast and smoothly converging variant of Bi-CG for solution of non-symmetric linear system. *SIAM Journal on Scientific and Statistical Computing* 13, 2 (1992), 631–644.
- [80] DOLEAN, V., JOLIVET, P., NATAF, F., SPILLANE, N., AND XIANG, H. Two-level domain decomposition methods for highly heterogeneous darcy equations. connections with multiscale methods. *Oil Gas Science and Technology - Rev. IFP Energies nouvelles* 69, 4 (2014), 731–752.
- [81] DOST’AL, Z. Conjugate gradient method with preconditioning by projector. *Int. J. of Computer Mathematics* 23 (1988), 315–323.
- [82] DUARTE, C., AND ODEN, J. An hp adaptive method using clouds. *Computer Methods in Applied Mechanics and Engineering* 139 (1996), 237–262.
- [83] EDWARDS, M. Symmetric positive definite general tensor discretization operators on unstructured and flow based grids. In *Proc. 8th European Conference on the Mathematics of Oil Recovery, Freiberg, Germany, EAGE* (2002), p. E04.
- [84] EDWARDS, M. Unstructured, control-volume distributed, full-tensor finite volume schemes with flow based grids. *Computational Geosciences* 6 (2002), 433–452.
- [85] EDWARDS, M., AND ROGERS, C. A flux continuous scheme for the full tensor pressure equation. In *Proc. 4th European Conference on the Mathematics of Oil Recovery, Norway, Vol. D.* (1994).
- [86] EDWARDS, M., AND ROGERS, C. Finite volume discretization with imposed flux continuity for the general tensor pressure equation. *Computational Geosciences* 2 (1998), 259–290.
- [87] EFENDIEV, Y., AND HOU, T. *Multiscale Finite Element Methods: Theory and Applications*. Springer, 2009.
- [88] ELSNER, L. Bounds for determinants of perturbed M-matrices. *Linear Algebra and its Applications* 257 (1997), 283–288.
- [89] FALGOUT, R., AND SCHROEDER, J. Non-galerkin coarse grids for algebraic multigrid. *SIAM Journal on Scientific Computing* 36, 3 (2014), 309–334.
- [90] FANG, J., AND PARRIAUX, A. A regularized lagrangian finite point method for the simulation of incompressible viscous flows. *Journal of Computational Physics* 227, 20 (2008), 8894–8908.
- [91] FRANK, J., AND VUIK, C. On the construction of deflation-based preconditioners. *SIAM Journal on Scientific Computing* 23, 2 (2001), 442–462.
- [92] FREUND, R. A transpose-free quasi-minimal residual algorithm for non-hermitian linear systems. *SIAM Journal on Scientific Computing* 14, 2 (1993), 470–482.
- [93] FUJIMOTO, T., AND RANADE, R. Characterization of inverse-positive matrices: The Hawkins-Simon condition and the Le Chatelier-Braun principle. *Electronic Journal of Linear Algebra* 11 (2004), 59–65.
- [94] FULK, D., AND QUINN, D. An analysis of 1-d smoothed particle hydrodynamics kernels. *Journal of Computational physics* 126, 1 (1996), 165–180.

## Bibliography

---

- [95] GAO, X., WANG, T., AND KIM, J. On ductile fracture initiation toughness: Effects of void volume fraction, void shape and void distribution. *International Journal of Solids and Structures* 42, 18-19 (2005), 5097–5117.
- [96] GINGOLD, R., AND MONAGHAN, J. Smoothed particle hydrodynamics: Theory and applications to non-spherical stars. *Monthly Notices of the Royal Astronomical Society* 181 (1977), 375–389.
- [97] GLANSDORFF, P., AND PRIGOGINE, I. *Thermodynamic theory of structure, stability and fluctuations*. Wiley, 1971.
- [98] GLANSDORFF, P., AND PRIGOGINE, I. *Thermodynamics of Structure, Stability and Fluctuations*. Wiley-Interscience, New York, 1971, ch. Chapter II, p. 14.
- [99] GU, Y., AND LIU, G. A local point interpolation method for static and dynamic analysis of thin beams. *Computer Methods in Applied Mechanics and Engineering* 190 (2001), 5515–5528.
- [100] GU, Y., AND LIU, G. A meshless local petrov-galerkin (mlpg) formulation for static and free vibration analysis of thin plates. *Computer Modeling in Engineering and Sciences* 2 (2001), 463–476.
- [101] GU, Y., AND LIU, G. A meshless local petrov-galerkin (mlpg) method for free and forced vibration analysis for solids. *Computational Mechanics* 27 (2001), 188–198.
- [102] GU, Y., AND LIU, G. A boundary radial point interpolation method (brpim) for 2-d structural analyses. *Structural Engineering and Mechanics* 15 (2002), 535–550.
- [103] GULLERUD, A., DODDS, R., HAMPTON, R., AND DAWICKE, D. 3D modeling of ductile crack growth in thin sheet metals: computational aspects and validation. *Engineering Fracture Mechanics* 63, 4 (1999), 347–374.
- [104] HAJIBEYGI, H., BONFIGLI, G., AND HESSE, M. Iterative multiscale finite-volume method. *Journal of Computational Physics* 227 (2008), 8604–8621.
- [105] HAJIBEYGI, H., BONFIGLI, G., HESSE, M. A., AND JENNY, P. Iterative multiscale finite-volume method. *J. Comput. Phys.* 227 (2008), 8604–8621.
- [106] HAJIBEYGI, H., AND JENNY, P. A general multiscale finite-volume method for compressible multiphase flow in porous media. *Proceedings of the 11th European Conference on the Mathematics of Oil Recovery (ECMOR XI), Bergen, Norway* (2008).
- [107] HAJIBEYGI, H., AND JENNY, P. Multiscale finite-volume method for parabolic problems arising from compressible multiphase flow in porous media. *J. Comput. Phys.* 228 (2009), 5129–5147.
- [108] HAYNES, R., TRUMMER, M., AND KENNEDY, S. Persistently positive inverses of perturbed m-matrices. *Linear Algebra and its Applications* 422 (2007), 742–754.
- [109] HENSON, V. Multigrid methods for nonlinear problems: An overview. Tech. rep., Center for applied scientific computing, Lawrence Livermore National Laboratory, 2002.
- [110] HOU, T., AND WU, X. A multiscale finite element method for elliptic problems in composite materials and porous media. *Journal of Computational Physics* 134, 1 (1997), 169–189.
- [111] HU, X., AND ADAMS, N. A multi-phase SPH method for macroscopic and mesoscopic flows. *Journal of Computational Physics* 213, 2 (2006), 844–861.
- [112] III, G. G., BOURNE, N., ZOCHER, M., MAUDLIN, P., AND MILLETT, J. Influence of crystallographic anisotropy on the hopkinson fracture “spallation” of zirconium. In *Shock Compression of Condensed Matter-1999*, AIP Press, Woodbury, NY (2000), pp. 509–512.
- [113] III, G. G., LOPEZ, M., BOURNE, N., MILLETT, J., AND VECCHIO, K. Influence of microstructural anisotropy on the spallation of 1080 eutectoid steel. In *Shock Compression of Condensed Matter-2001*, AIP Press, Melville, NY (2002), pp. 479–483.
- [114] IL’USHIN, A. About one theory of long duration material strength. *Izv. AN SSSR MTT* 3 (1967), 21–35.

- [115] JENNY, P., LEE, S., AND TCHELEPI, H. Multi-scale finite-volume method for elliptic problems in subsurface flow simulation. *J. Comput. Phys.* 187 (2003), 47–67.
- [116] JENNY, P., LEE, S., AND TCHELEPI, H. Adaptive fully implicit multi-scale finite-volume method for multi-phase flow and transport in heterogeneous porous media. *Journal of Computational Physics* 217 (2006), 627–641.
- [117] JIRASEK, M. Nonlocal models for damage and fracture: Comparison of approaches. *International Journal of Solids and Structures* 35, 31-32 (1998), 4133–4145.
- [118] JOHNSON, G., AND COOK, W. Fracture characteristics of three metals subjected to various strains, strain rates, temperatures and pressures. *Eng. Fract. Mech.* 21 (1985), 31–48.
- [119] JOHNSON, G., STRYK, R., AND BEISSEL, S. SPH for high velocity impact computations. *Computational Methods in Applied Mechanical Engineering* 139, 1 (1996), 347–373.
- [120] JOHNSON, J., III, G. G., AND BOURNE, N. Effect of pulse duration and strain rate on incipient spall fracture in copper. *J. Appl. Phys.* 86 (1999), 4892–4901.
- [121] JÖNSTHÖVEL, T., VAN GIJZEN, M., MACLACHLAN, S., SCARPAS, A., AND VUIK, C. Comparison of the deflated preconditioned conjugate gradient method and algebraic multigrid for composite materials. *Computational Mechanics* (nov 2011), 1–13.
- [122] JÖNSTHÖVEL, T., VAN GIJZEN, M., VUIK, C., KASBERGEN, C., AND SCARPAS, A. Preconditioned conjugate gradient method enhanced by deflation of rigid body modes applied to composite materials. *Computer Modeling in Engineering and Sciences* 47 (2009), 97–118.
- [123] JU, J. On energy-based coupled elastoplastic damage theories: Constitutive modeling and computational aspects. *Int. J. Solids Struct.* 25 (1989), 803–833.
- [124] JU, J. Isotropic and anisotropic damage variables in continuum damage mechanics. *J. Engineering Mechanics* 116 (1990), 2764–2770.
- [125] JUBELGAS, M., SPRINGEL, V., AND DOLAG, K. Thermal conduction in cosmological SPH simulations. *Monthly Notices of the Royal Astronomical Society* 351, 2 (2004), 423–435.
- [126] KACHANOV, L. On rupture time under condition of creep. *Moscow, Izvestia Akademi Nauk USSR, Otd. Techn. Nauk* 8 (1958), 26–31.
- [127] KACHANOV, L. *Basics of the plasticity theory*. Moscow: Nauka, 1969.
- [128] KACHANOV, L. *Basics of the fracture mechanics*. Moscow: Nauka, 1974.
- [129] KACHANOV, L. *Introduction to Continuum Damage Mechanics*. Dordrecht, Boston: Martinus Nijhoff, 1986.
- [130] KANEL, G. Some new data on deformation and fracture of solids under shock-wave loading. *Journal of the Mechanics and Physics of Solids* 46 (1998), 1869–1886.
- [131] KANEL, G., IVANOV, M., AND PARSHIKOV, A. Computer simulation of the heterogeneous materials response to the impact loading. *International Journal of Impact Engineering* 17, 1-3 (1995), 455–464.
- [132] KANEL, G., RAZORENOV, S., BOGATCH, A., UTKIN, A., AND FORTOV, V. Spall fracture properties of aluminum and magnesium at high temperatures. *Journal of Applied Physics* 79, 11 (1996), 8310–8317.
- [133] KANEL, G., RAZORENOV, S., AND FORTOV, V. Spall strength of metals in wide diapason of impact shock loading amplitude. *Dokl. AN SSSR* 294, 2 (1987), 350–352.
- [134] KANEL, G., RAZORENOV, S., AND UTKIN, A. *High pressure shock compression of solids, II*. Berlin: Springer, 1996, ch. Spallation in solids under shock-wave loading: analysis of dynamic flow, methodology of measurements and constitutive factors, pp. 1–24.
- [135] KELLEY, C. *Iterative Methods for Linear and Nonlinear Equations*. SIAM, Philadelphia, 1995.

## Bibliography

---

- [136] KIM, J., AND GAO, X. A generalized approach to formulate the consistent tangent stiffness in plasticity with application to the GLD porous material model. *International Journal of Solids and Structures* 42, 1 (2005), 103–122.
- [137] KIM, J., GAO, X., AND SRIVATSAN, T. Modeling of crack growth in ductile solids: a three-dimensional analysis. *International Journal of Solids and Structures* 40, 26 (2003), 7357–7374.
- [138] KIM, J., GAO, X., AND SRIVATSAN, T. Modeling of void growth in ductile solids: effects of stress triaxiality and initial porosity. *Engineering Fracture Mechanics* 71, 3 (2004), 379–400.
- [139] KISELEV, A. Mathematical modelling of dynamic deformation and combined microfracture thermoelastoviscoplastic medium. *Vest. Moskovskogo Universiteta. Matem. Mech.* 6 (1998), 32–40.
- [140] KISELEV, A., AND LUKYANOV, A. Mathematical modeling of dynamic processes of irreversible deforming, micro- and macrofracture of solids and structures. *International Journal of Forming Processes* 5 (2002), 359–362.
- [141] KISELEV, A., AND YUMASHEV, M. Mathematical model of deformation and fracture of solid fuel under impact loading. *J. Applied Mechanics and Technical Physics* 6 (1992), 126–134.
- [142] KLAUSEN, R., AND RUSSELL, T. Relationships among some locally conservative discretization methods which handle discontinuous coefficients. *Computational Geosciences* 8, 4 (2004), 341–377.
- [143] KLIE, H., WHEELER, M., STUEBEN, K., AND CLEES, T. Deflation and solvers for highly ill-conditioned reservoir simulation problems. *SPE Reservoir Simulation Symposium*, doi:10.2118/105820-MS (2007).
- [144] KNOLL, D., AND KEYES, D. Jacobian-free newton-krylov methods: a survey of approaches and applications. *Journal of Computational Physics* 193 (2004), 357–397.
- [145] KONDAUROV, V. *Nauch. trudi instituta teplofiziki ekstremal'nykh sostoyanii, OIVT RAN* 3. Moskva: OIVT RAN, 2000, ch. Tensor model of continual fracture of solid bodies.
- [146] KONDAUROV, V., AND FORTOV, V. *Basics of the thermodynamic of condensate matter*, vol. I. Moskva, 2002.
- [147] KRAJČINOVIC, D. Constitutive equations for damaging materials. *J. Appl. Mech.* 50 (1983), 355–360.
- [148] KRAJČINOVIC, D. *Damage Mechanics*. Amsterdam: Elsevier Science B. V., 1996.
- [149] KRAJČINOVIC, D., AND FONSEKA, G. The continuous damage theory of brittle materials. part 1: General theory. *J. Appl. Mech.* 48 (1981), 809–815.
- [150] KRAJČINOVIC, D., AND FONSEKA, G. The continuous damage theory of brittle materials. part i: General theory. *J. Appl. Mech.* 48 (1981), 809–815.
- [151] KRYSL, P., AND BELYTSCHKO, T. Analysis of thin plates by the element-free galerkin method. *Computational Mechanics* 17 (1996), 26–35.
- [152] KUKUDZHANOV, B. Microscopic model of inelastic material fracture and its application to the investigation of deformation localisation. *Izv. RA. MTT.* 5 (1999).
- [153] LECKIE, F., AND HAYHURST, D. Constitutive equations for creep rupture. *Acta Metallurgica* 25, 9 (1977), 1059–1070.
- [154] LEE, E.-S., MOULINEC, C., XU, R., VIOLEAU, D., LAURENCE, D., AND STANSBY, D. Comparison of weakly compressible and truly incompressible algorithms for the SPH mesh free particle method. *Journal of Computational Physics* 227 (2008), 8417–8436.
- [155] LEE, S., DURLOFSKY, L., LOUGH, M., AND CHEN, W. Finite difference simulation of geologically complex reservoirs with tensor permeabilities. *SPE Reservoir Evaluation Engrg.* 1 (1998), 567–574.
- [156] LEE, S., JENNY, P., AND TCHELEPI, H. A finite-volume method with hexahedral multiblock grids for modeling flow in porous media. *Computational Geosciences* 6, 3-4 (2002), 353–379.

- [157] LEE, S., WOLFSTEINER, C., AND TCHELEPI, H. Multiscale finite-volume formulation for multiphase flow in porous media: black oil formulation of compressible, three-phase flow with gravity. *Computational Geosciences* 12, 3 (2008), 351–366.
- [158] LEMAITRE, J. *A Course on Damage Mechanics*. Berlin: Springer-Verlag, 1992.
- [159] LEMAITRE, J. *A Course on Damage Mechanics*. second ed. Springer, Berlin, 1996.
- [160] LEMAITRE, J., AND CHABOCHE, J. *Mechanics of Materials*. Cambridge University Press, Cambridge, 1990.
- [161] LEVEQUE, R., AND LI, Z. The immersed interface method for elliptic equations with discontinuous coefficients and singular sources. *SIAM Journal on Numerical Analysis* 31, 4 (1994), 1019–1044.
- [162] LI, S., HAO, W., AND LIU, W. Numerical simulation of large deformation of thin shell structures using meshfree methods. *Computational Mechanics* 25 (2000), 102–116.
- [163] LI, S., AND LIU, W. Meshfree and particle methods and their applications. *Applied Mechanics Review* 55 (2002), 1–34.
- [164] LI, S., AND LIU, W. *Meshfree Particle Methods*. Springer-Verlag, Berlin, 2003.
- [165] LIE, K.-A. *An Introduction to Reservoir Simulation Using MATLAB: User guide for the Matlab Reservoir Simulation Toolbox (MRST)*. SINTEF ICT, 2014.
- [166] LIE, K.-A. *An Introduction to Reservoir Simulation Using MATLAB*. SINTEF ICT, Departement of Applied Mathematics Oslo, Norway, 2016.
- [167] LISZKA, T., AND ORKISZ, J. The finite difference method at arbitrary irregular grids and its applications in applied mechanics. *Computers and Structures* 11 (1980), 117–142.
- [168] LIU, G. *Impact Response of Materials and Structures*. Oxford, 1999, ch. Mesh Free Method for stress analysis for solids, pp. 475–480.
- [169] LIU, G. *A point assembly Mesh Free Methods: moving beyond the finite element method*. CRC Press, Boca Raton., 2002.
- [170] LIU, G., AND GU, Y. A local point interpolation method for stress analysis of two-dimensional solids. *Structural Engineering and Mechanics* 11 (2001), 221–236.
- [171] LIU, G., AND GU, Y. A local radial point interpolation method (lr-pim) for free vibration analysis of 2-d solids. *Journal of sound and vibration* 246 (2001), 29–46.
- [172] LIU, G., AND GU, Y. A meshfree method: meshfree weak-strong (mws) form method, for 2-d solids. *Computational Mechanics* 33 (2003), 2–14.
- [173] LIU, G., AND LIU, M. *Smoothed Particle Hydrodynamics: a meshfree particle method*. World Scientific Publishing Co. Pte. Ltd., 2004.
- [174] LIU, M., AND LIU, G. *Particle Hydrodynamics: A Meshfree Particle Method*. World Scientific Publishing Co. Pte. Ltd., 2003.
- [175] LIU, M., LIU, G., AND LAM, K. Computer simulation of high explosive explosion using smoothed particle hydrodynamics methodology. *Comput. Fluids* 32 (2003), 305–322.
- [176] LIU, W., AND JUN, S. Multiple-scale reproducing kernel particle method for large deformation problems. *International Journal for Numerical Methods in Engineering* 41 (1998), 1339–1362.
- [177] LIU, W., JUN, S., AND ZHANG, F. Reproducing kernel particle methods. *International Journal for Numerical Methods in Fluids* 20 (1995), 1081–1106.
- [178] LU, T., AND CHOW, C. On constitutive equations of inelastic solids with anisotropic damage. *Theoretical and Applied Fracture Mechanics* 14 (1990), 187–218.

## Bibliography

---

- [179] LUBARDA, V., AND KRAJCIKOVIC, D. Damage tensor and the crack density distribution. *International Journal of Solids and Structures* 30, 20 (1993), 2859–2877.
- [180] LUCCIONI, B., AND OLLER, S. A directional damage model. *Computer Methods in Applied Mechanics and Engineering* 192, 9-10 (2003), 1119–1145.
- [181] LUCY, L. A numerical approach to testing the fission hypothesis. *The Astronomical Journal* 82 (1977), 1013–1024.
- [182] LUKYANOV, A. Prediction of failure in metal structures based on thermodynamics of irreversible process. In *Proceeding IPC, ASME*. (2004).
- [183] LUKYANOV, A. Numerical modelling of the material failure under shock loading using particle method. *Izvestiya Tula State University. Estestvennonauchn. Ser. I* (2007), 54–65.
- [184] LUKYANOV, A. Constitutive behaviour of anisotropic materials under shock loading. *Int. J. of Plasticity* 24, 1 (2008), 140–167.
- [185] LUKYANOV, A. Meshless upscaling method and its application to a fluid flow in porous media.
- [186] LUKYANOV, A. Adaptive fully implicit multi-scale meshless multi-point flux method for fluid flow in heterogeneous porous media. *ECMOR XIII Conference Proceedings, Biarritz, France* (2012).
- [187] LUKYANOV, A. Modeling the effect of orientation on the shock response of a damageable composite material. *J. Applied Physics* 112 (2012), 084908.
- [188] LUKYANOV, A., AND PENJKOV, V. Numerical simulation of solids deformation by a meshless method. *Vestn. Samar. Gos. Univ. Estestvennonauchn. Ser. 6*, 56 (2007), 62–70.
- [189] LUKYANOV, A., AND SEGLETES, S. Frontiers in the constitutive modeling of anisotropic shock waves. *Applied Mechanics Reviews* 64, 4 (2012), 040802.
- [190] LUKYANOV, A., VAN DER LINDEN, J., JONSTHOVEL, T., AND VUIK, C. Meshless subdomain deflation vectors in the preconditioned krylov subspace iterative solvers. In *ECMOR XIV - 14th European Conference on the Mathematics of Oil Recovery* (2014), EAGE.
- [191] LUKYANOV, A. A., AND VUIK, C. *Meshfree Methods for Partial Differential Equations*. 2017, ch. Meshless Multi-Point Flux Approximation, pp. 67–84.
- [192] LUNATI, I., AND JENNY, P. Multiscale finite-volume method for compressible multiphase flow in porous media. *Journal of Computational Physics* 216, 2 (2006), 616–636.
- [193] LUNATI, I., TYAGI, M., AND LEE, S. An iterative multiscale finite volume algorithm converging to the exact solution. *Journal of Computational Physics* 230 (2011), 1849–1864.
- [194] MANSFIELD, L. On the conjugate gradient solution of the schur complement system obtained from domain decomposition. *SIAM J. Numer. Anal.* 27, 6 (1990), 1612–1620.
- [195] MANSFIELD, L. Damped jacobi preconditioning and coarse grid deflation for conjugate gradient iteration on parallel computers. *SIAM J. Sci. Stat. Comput.* 12, 6 (1991), 1314–1323.
- [196] MARRONE, S., COLAGROSSI, L., AND GRAZIANI, G. Fast free-surface detection and level-set function definition in SPH solvers. *Journal of Computational Physics* 229 (2010), 3652–3663.
- [197] MATSUNAGA, N., AND YAMAMOTO, T. Superconvergence of the Shortley–Weller approximation for Dirichlet problems. *Journal of Computational and Applied Mathematics* 116, 2 (2000), 263–273.
- [198] MAUGIN, G. *The Thermodynamics of Plasticity and Fracture*. Cambridge University Press, Cambridge, 1992.
- [199] MAVRIPLIS, D. Multigrid strategies for viscous flow solvers on anisotropic unstructured meshes. *Journal of Computational Physics* 145, 1 (1998), 141–165.

- [200] MAVRIPLIS, D. An assessment of linear versus non-linear multigrid methods for unstructured mesh solvers. *Journal of Computational Physics* 175, 1 (2002), 302–325.
- [201] MEIJERINK, J., AND DER VORST, H. V. An iterative solution method for linear systems of which the coefficient matrix is a symmetric M-matrix. *Mathematics of Computation* 31, 137 (1977), 148–162.
- [202] METROPOLIS, N., AND ULAM, S. The monte carlo method. *Journal of American Statistical Association* 44 (1949), 335–341.
- [203] MEYERS, M. *Dynamic Behavior of Materials*. John Wiley and Sons. Inc., 1994.
- [204] MEZIERE, Y., MILLETT, J., AND BOURNE, N. Equation of state and mechanical response of NiTi during one-dimensional shock loading. *Journal of Applied Physics* 100, 3 (2006), 033513.
- [205] MILLETT, J., AND BOURNE, N. Lateral stress measurements in a shock loaded alumina: Shear strength and delayed failure. *Journal of Materials Science* 36, 14 (2001), 3409–3414.
- [206] MILLETT, J., BOURNE, N., AND III, G. G. Behavior of the shape memory alloy NiTi during one-dimensional shock loading. *Journal of Applied Physics* 92 (2002), 3107–3110.
- [207] MLACNIK, M., AND DURLOFSKY, L. Unstructured grid optimization for improved monotonicity of discrete solutions of elliptic equations with highly anisotropic coefficients. *Journal of Computational Physics* 216 (2006), 337–361.
- [208] MONAGHAN, J. Kernel estimates as a basis for general particle methods in hydrodynamics. *J. Comput. Phys.* 46 (1982), 429–453.
- [209] MONAGHAN, J. Smoothed particle hydrodynamics. *Annual Reviews in Astronomy and Astrophysics* 30 (1992), 543–574.
- [210] MONAGHAN, J. Simulating free surface flows with SPH. *Journal of Computational Physics* 110 (1994), 399–406.
- [211] MONAGHAN, J., AND LATTANZIO, J. A refined particle method for astrophysical problems. *Astronomy and Astrophysics* 149 (1985), 135–143.
- [212] MORRIS, J. A study of the stability properties of smooth particle hydrodynamics. *Publications of the Astronomical Society of Australia* 13 (1996), 97–102.
- [213] MORRIS, J., FOX, P., AND ZHU, Y. Modeling low reynolds number incompressible flows using SPH. *Journal of Computational Physics* 136 (1997), 214–226.
- [214] MOYNER, O., AND LIE, K. A multiscale restriction-smoothed basis method for high contrast porous media represented on unstructured grids. *Journal of Computational Physics* 304 (2016), 46–71.
- [215] MURAKAMI, S. Notion of continuum damage mechanics and its application to the anisotropic creep damage theory. *Journal of Engineering Materials and Technology* 105, 2 (1983), 99–105.
- [216] MURAKAMI, S. *Continuum Damage Mechanics – Theory and Applications*. Wien: Springer-Verlag, 1987, ch. Anisotropic Aspect of Material Damage and Application of Continuum Damage Mechanics, pp. 91–133.
- [217] MURAKAMI, S. *Multigrid Methods*. Society for Industrial and Applied Mathematics, Philadelphia, Pennsylvania, 1987, ch. Algebraic Multigrid, pp. 91–133.
- [218] MURAKAMI, S. Mechanical modelling of material damage. *Journal of Applied Mechanics* 55, 2 (1988), 280–286.
- [219] MURAKAMI, S., AND OHNO, N. *Creep in Structures*. Berlin:Springer-Verlag, 1981, ch. A continuum Theory of Creep and Creep Damage, pp. 422–444.
- [220] NAYROLES, B., TOUZOT, G., AND VILLON, P. Generalizing the finite element: diffuse approximation and defuse elements. *Computational Mechanics* 10 (1992), 307–318.



## Bibliography

---

- [221] NICOLAIDES, R. Deflation of conjugate gradients with applications to boundary value problems. *SIAM Journal on Numerical Analysis* 24, 2 (1987), 355–365.
- [222] OIAN, E., HEIMSUND, B.-O., EIGESTAD, G., AND AAVATSMARK, I. Control volume discretisation on non-matching meshes in 3D. In *Proc. 10th European Conference on the Mathematics of Oil Recovery, Amsterdam, EAGE*. (2006), p. B015.
- [223] PAN, W., KIM, K., PEREGO, M., TARTAKOVSKY, A., AND PARKS, M. Modeling electrokinetic flows by consistent implicit incompressible smoothed particle hydrodynamics. *Journal of Computational Physics* 334 (2017), 125–144.
- [224] POIRIER, J.-P. *Introduction to the Physics of the Earth's Interior*. 2000.
- [225] RABOTNOV, Y. *Sb. "Voprosi prochnosti materialov i konstrukcii"*. Moskva.: Izd. AN SSSR, 1959, ch. About mechanism of long duration fracture, pp. 5–7.
- [226] RABOTNOV, Y. *Progress in Appl. Mech. The Prager Anniversary Volume*. MacMillan, New York, 1963, ch. On the Equations of State for Creep, pp. 307–315.
- [227] RADAYEV, Y. Thermodynamical model of anisotropic damage growth. part ii. canonical damage growth rate equation and theory of damage invariants. *J. Non-Equilib. Thermodynam.* 21 (1996), 197–222.
- [228] RADAYEV, Y., MURAKAMI, S., AND HAYAKAWA, K. Mathematical description of anisotropic damage state in continuum damage mechanics. *Trans. Japan Soc. Mech. Engn.* 60A. (1994), 68–76.
- [229] RAHOLA, J., AND TISSARI, S. Iterative solution of dense linear system arising from the electrostatic integral equation in meg. *Phys. Med. Biol.* 47 (2002), 967–975.
- [230] RANGLES, P., AND LIBERSKY, L. Smoothed Particle Hydrodynamics: Some recent improvements and applications. *Computer Methods in Applied Mechanics and Engineering* 139, 1-4 (1996), 375–408.
- [231] RANGLES, P., AND LIBERSKY, L. Smoothed particle hydrodynamics: some recent improvements and applications. *Computational Methods in Applied Mechanical Engineering* 139 (1996), 375–408.
- [232] RUGE, J., AND STUBEN, K. Algebraic multigrid (amg). In *Multigrid Methods*, S. McCormick, Ed., vol. 3. SIAM, Philadelphia, PA, 1987, pp. 73–130.
- [233] SAAD, Y. *Iterative Methods for Sparse Linear Systems*. SIAM, Philadelphia, USA, 2003.
- [234] SAAD, Y., AND SCHULTZ, M. Gmres: a generalized minimal residual algorithm for solving nonsymmetric linear systems. *SIAM J. Sci. Stat. Comput.* 7 (1986), 856–869.
- [235] SCHLUMBERGER, CHEVRON, AND TOTAL. Intersect version 2013.1, 2013, technical description.
- [236] SCHWAIGER, H. An implicit corrected SPH formulation for thermal diffusion with linear free surface boundary conditions. *International Journal for Numerical Methods in Engineering* 75 (2008), 647–671.
- [237] SEDOV, L. *A Course in Continuum Mechanics*. Groningen: Wolters-Noordhoff, 1972.
- [238] SEIBOLD, B. *M-Matrices in meshless finite difference methods*. Dissertation, Department of Mathematics. University of Kaiserslautern, 2006.
- [239] SHAH, S., MOYNER, O., TENE, M., LIE, K.-A., AND HAJIBEYGI, H. The multiscale restriction smoothed basis method for fractured porous media (f-msrb). *Journal of Computational Physics* 318 (2016), 36–57.
- [240] SILLING, S. Reformulation of elasticity theory for discontinuities and long-range forces. *Journal of the Mechanics and Physics of Solids* 48, 1 (2000), 175–209.
- [241] STEINBERG, D. Equation of state and strength properties of selected materials. Tech. rep., Lawrence Livermore National Laboratory. Livermore. CA, 1991.
- [242] STEINMANN, P., AND CAROL, I. A framework for geometrically nonlinear continuum damage mechanics. *Int. J. Eng. Sci.* 36 (1998), 1793–1814.

- [243] STOFFEL, M. An experimental method to validate viscoplastic constitutive equations in the dynamic response of plates. *Mechanics of Materials* 37 (2005), 1210–1222.
- [244] STOUGHTON, T., AND YOON, J. A pressure-sensitive yield criterion under a non-associative flow rule for sheet metal forming. *International Journal of Plasticity* 20, 4 (2004), 705–731.
- [245] TANG, J., MACLACHLAN, S., NABBEN, R., AND VUIK, C. A comparison of two-level preconditioners based on multigrid and deflation. *SIAM. J. Matrix Anal. and Appl.* 31 (2010), 1715–1739.
- [246] TANG, J., NABBEN, R., VUIK, C., AND ERLANGGA, Y. Comparison of two-level preconditioners derived from deflation, domain decomposition and multigrid methods. *Journal of Scientific Computing* 39 (2009), 340–370.
- [247] TANG, J., AND VUIK, C. Acceleration of preconditioned krylov solvers for bubbly flow problems. In *Computational Science - ICCS 2007*, Y. Shi, G. Albada, J. Dongarra, and P. Sloot, Eds., vol. 4487 of *Lecture Notes in Computer Science*. Springer Berlin Heidelberg, 2007, pp. 874–881.
- [248] TANG, J. M. Two-level preconditioned conjugate gradient methods with applications to bubbly flow problems. *PhD Thesis TU Delft* (2008).
- [249] TANG, J. M., AND VUIK, C. Efficient deflation methods applied to 3-D bubbly flow problems. *Electronic Transactions on Numerical Analysis* 26 (2007), 330–349.
- [250] TANG, J. M., AND VUIK, C. New variants of deflation techniques for pressure correction in bubbly flow problems. *Journal of Numerical Analysis, Industrial and Applied Mathematics* 2 (2007), 227–249.
- [251] TCHELEPI, H., JENNEY, P., LEE, S., AND WOLFSTEINER, C. An adaptive multiphase multiscale finite volume simulator for heterogeneous reservoirs. In *Reservoir Simulation Symposium, 31 January-2 February 2005, Woodlands, Texas* (2005), p. 93395.
- [252] THOMÉE, V. From finite differences to elements. A short history of numerical analysis of partial differential equations. *Journal of Computational and Applied Mathematics* 128, 1-2 (2001), 1–54.
- [253] TROTTEMBERG, U., OOSTERLEE, C., AND SCHUELLER, A. *Multigrid*. Elsevier Academic Press, 2001.
- [254] TVERGAARD, V. Influence of voids on shear band instabilities under plane strain conditions. *Int. J. Fract.* 17 (1981), 389–407.
- [255] TVERGAARD, V. On localization in ductile materials containing spherical voids. *Int. J. Fract.* 18 (1982), 237–252.
- [256] TVERGAARD, V. Material failure by void growth to coalescence. *Adv. Appl. Mech.* 27 (1990), 83–151.
- [257] TVERGAARD, V., AND HUTCHINSON, J. Two mechanisms of ductile fracture: void by void growth versus multiple void interaction. *Int. J. Solids Struct.* 39 (2002), 3581–3597.
- [258] TVERGAARD, V., AND NEEDLEMAN, A. Analysis of the cup-cone fracture in a round tensile bar. *Acta Metall.* 32 (1984), 157–169.
- [259] VAKULENKO, A., AND KACHANOV, L. Continual theory of medium with cracks. *Izv. AN SSSR MTT* 4 (1971), 159–166.
- [260] VAN DER LINDEN, J., JÖNSTHÖVEL, T. B., LUKYANOV, A. A., AND VUIK, C. The parallel subdomain-levelset deflation method in reservoir simulation. *Journal of Computational Physics* 304, 1, 340–358.
- [261] VAN DER SLUIS, A., AND VAN DER VORST, H. The rate of convergence of conjugate gradients. *Numerische Mathematik* 48, 5 (1986), 543–560.
- [262] VANEK, P. Acceleration of convergence of a two-level algorithm by smoothing transfer operator. *Appl. Math.* 37 (1992), 265–274.
- [263] VANEK, P., MANDEL, J., AND BREZINA, M. Algebraic multigrid by smoothed aggregation for second and fourth order elliptic problems. *Computing* 56, 2 (1996), 179–196.

## Bibliography

---

- [264] VERMOLEN, F., VUIK, C., AND SEGAL, A. Deflation in preconditioned conjugate gradient methods for finite element problems. In *M. Křížek, P. Neittaanmäki and R. Glowinski and S. Korotov editors, Conjugate Gradient and Finite Element Methods. Springer, Berlin, 2004* (2004), 103–129.
- [265] VLADIMIROV, V. *Generalized Functions in Mathematical Physics*. Mir, USSR, 1979.
- [266] VOYIADJIS, G., AND KATTAN, P. A plasticity-damage theory for the large deformation of solids. Part i: Theoretical formulation. *International Journal of Engineering Science* 30, 9 (1992), 1089–1108.
- [267] VOYIADJIS, G., AND PARK, T. Anisotropic damage effect tensors for the symmetrization of the effective stress tensor. *Journal of Applied Mechanics* 64, 1 (1997), 106–110.
- [268] VUIK, C., SEGAL, A., AND MEIJERINK, J. An efficient preconditioned CG method for the solution of a class of layered problems with extreme contrast in the coefficients. *Journal of Computational Physics* 152, 1 (1999), 385–403.
- [269] VUIK, C., SEGAL, A., MEIJERINK, J., AND WIJMA, G. The construction of projection vectors for a deflated ICCG method applied to problems with extreme contrasts in the coefficients. *Journal of Computational Physics* 172, 2 (2001), 426–450.
- [270] VUIK, C., SEGAL, A., YAAKOUBI, L., AND DUFOUR, E. A comparison of various deflation vectors applied to elliptic problems with discontinuous coefficients. *Applied Numerical Mathematics* 41, 1 (2002), 219–233.
- [271] WALLIS, J. Incomplete gaussian elimination as a preconditioning for generalized conjugate gradient acceleration. In *SPE Reservoir Simulation Symposium* (Houston, Texas, USA, 15-18 November 1983), Society of Petroleum Engineers.
- [272] WALLIS, J. Constrained residual acceleration of conjugate residual methods. *SPE Reservoir Simulation Symposium*, 1 (1985), doi:10.2118/13536-MS.
- [273] WANG, Y., HAJIBEYGI, H., AND TCHELEPI, H. Algebraic multiscale solver for flow in heterogeneous porous media. *Journal of Computational Physics* 259 (2014), 284–303.
- [274] WASHIO, T., AND OOSTERLEE, C. Krylov subspace acceleration for nonlinear multigrid schemes with application to recirculating flow. *SIAM Journal on Scientific Computing* 21 (2000), 1670–1690.
- [275] WESSELING, P. *An introduction to multigrid methods*. John Wiley Sons Ltd., 1992.
- [276] WIEGMANN, A., AND BUBE, K. The explicit-jump immersed interface method: finite difference methods for pdes with piecewise smooth solutions. *SIAM Journal on Numerical Analysis* 37, 3 (2000), 827–862.
- [277] XUE, J., AND JIANG, E. Entrywise relative perturbation theory for nonsingular M-matrices and applications. *BIT Numerical Mathematics* 35, 3 (1995), 417–427.
- [278] YAGAWA, G., AND YAMADA, T. Free mesh method: a new meshless finite element method. *Computational Mechanics* 18 (1996), 383–386.
- [279] YAGAWA, G., AND YAMADA, T. Meshless method on massively parallel processor with application to fracture mechanics. *Key Engineering Materials* 145-149 (1998), 201–210.
- [280] ZHANG, S., KUWABARA, S., SUZUKI, T., KAWANO, Y., MORITA, K., AND FUKUDA, K. Simulation of solid-fluid mixture flow using moving particle methods. *Journal of Computational Physics* 228 (2009), 2552–2526.
- [281] ZHOU, H., AND TCHELEPI, H. Two-stage algebraic multiscale linear solver for highly heterogeneous reservoir models. *SPE Journal* 17, 2 (2012), 523–539.
- [282] ZHU, Y., AND FOX, P. Smoothed particle hydrodynamics model for diffusion through porous media. *Transport Porous Media* 43, 3 (2001), 441–471.
- [283] ZHU, Y., FOX, P., AND MORRIS, J. A pore-scale numerical model for flow through porous media. *International Journal for Numerical and Analytical Methods in Geomechanics* 23, 9 (1999), 881–904.

